THE I-BAND TULLY-FISHER RELATION
AND
LARGE-SCALE MOTIONS IN THE UNIVERSE

Thesis by
Mingsheng Han

In Partial Fulfillment of the Requirements
for the Degree of
Doctor of Philosophy

California Institute of Technology
Pasadena, California

1991

submitted May 1991

ACKNOWLEDGEMENTS

I would like first to thank my advisor, Dr. Jeremy Mould, for his generous guidance, advice and help throughout the years. In some sense, Jeremy is not only my thesis advisor, but he is also an excellent advisor on non-scientific affairs; I am grateful to Jeremy for his always being there to answer any questions, from how to get to Palomar (his advice was "drive carefully") to how the Great Attractor pulls the Hydra-Centaurus supercluster towards it; and in particular, I am greatly indebted to Jeremy for his understanding and great tolerance to my long-term absence from work two years ago when disasters happened in my home country.

I would also like to thank Drs. Bev Oke and Xiang-Tao He, who introduced me to Caltech in the first place. It is also Dr. Bev Oke who first showed me how to do photometry using CCDs and how to display a cosmos picture on a graphic device using FIGARO —- an enjoyable data reduction package on which my thesis heavily lies. I am also grateful to Bev for his help during the completion of my thesis. But I feel I owe Bev a big apology for not finishing his distant cluster project before being attracted to Jeremy's "Great Attractor" project.

It is a pleasure to thank all the staff of Palomar Observatory, in particular the engineering staff, Mike Doyle, Fred Harris, John Henning, David Levy, and Dave Tennant, for their help with the instruments and software at the 60-inch telescope during my runs there in the past three years. Special thanks to the Carnegie Institute of Washington for giving me plenty of observing time at the Las Campanas Observatory in the spring of 1988. Thanks also go to the night assistants at both Palomar and Las Campanas observatories, especially to Skip Staples, who was the night assistant for most of my runs at Palomar, and witnessed how my one-year observing project was finally finished in three years; to Oscar Duhalde, the night assistant at the LCO, who told me his interesting story of discovering the supernova 1987A; to Alberto Zuniga, who almost succeeded in persuading me to visit the Easter Island.

I would like to thank Dr. Keith Shortridge, the creator of FIGARO, Dr. Tim Pearson, the creator of PGPLOT, and Dr. Mike Cawson, the creator of GASP; their fine programs made my data reduction so efficient and enjoyable. I also thank Dr. Judy Cohen, George Djorgovski, Chris Lee, Sam Southard, Cheryl Dong and all the local computer experts for their contributions in building up the excellent computation environment for the department, without which I can hardly imagine how this thesis could be done.

I am grateful to Dr. Greg Bothun for sending his computer-readable cluster sample on which my thesis project is largely based. I thank Dr. Dave Burstein for providing the Galactic reddening data of my thesis galaxies, and also for numerous illuminating discussions on various subjects. During the completion of this thesis, I have also benefited greatly in many aspects, from computer stuff to detailed scientific ideas, through the help and intriguing discussions from/with a lot of people here and there; in particular, I thank Drs. George Djorgovski, Sandra Faber, James Schombert, Michael Strauss, Zhong Wang, Jeff Willick, and my fellow graduate students, Alain Picard, Josh Roth and Lin Zuo. Thanks also go to all the professors, postdocs and graduate students from whom I have learned so much in the past six years either from their classes, their works or their ways of working; I extend my thanks and salute to, above all I have mentioned, Drs. Peter Goldrich, Roger Blandford, Sterl Phinney, Tony Readhead, Wal Sargent, Nick Scoville, K. Y. Lo, Marshall Cohen, Maarten Schmit and Shri Kulkarni; my salute and good wishes also go to my fellow students, old and young generations, Jim McCarthy, Blaise Canzian, Haiming Wang, Steve Myers, Karl Stapelfeldt, Dabbei Padgett, Tom Herbig, Nick Weir, Wenge Xu, Jose Navarro, Chris Tinney, Helen Johnston, Irwin Horowitz, Dave Thompson, and Lin Yan.

It is a pleasure to thank Michael Strauss, Josh Roth and the examining committee members, Jeremy Mould, Roger Blandford, George Djorgovski and Nick Scoville, for their valuable comments on the manuscript of this thesis, which greatly clarified

and smoothed the expression of the thesis.

I would also like to thank all my friends outside the Astronomy society for all the joys we have had together throughout those days. I won't forget the enjoyable times when we were on the mountain, on the beach, and on the volleyball court; I regret not fulfilling our wish to win the GSC Volleyball Championship, even in the B-league.

Finally, I would like to thank my parents and sisters for their support, love and encouragement. With great pleasure, I dedicate this work to my parents.

ABSTRACT

The ultimate goal of this thesis is to better understand the large-scale motions in the universe on scales beyond the Local-Supercluster, and also to better understand the Tully-Fisher relation as a distance indicator. Sixteen clusters of galaxies in redshifts range from 3000–10000 $kms^{-1}$are studied as test points of the large-scale velocity field, using the I-band Tully-Fisher relation as distance indicator. A complete observational procedure and techniques of measuring cluster distance using the Tully-Fisher relation is investigated in detail, which involves many general topics in the photometric studies of galaxies. Major discussions and results in the thesis are summarized as:

1. CCD surface photometry is described in detail. Errors and various effects (extinction, cosmological and seeing) on surface photometry are discussed. I-band surface photometry is carried out for some 280 galaxies in the thesis sample.

2. The problem of internal absorption in spiral galaxies is investigated; new magnitude and isophotal-diameter corrections for internal absorption are derived.

3. Different techniques for deriving cluster distances using Tully-Fisher relation are compared; distance bias due to sample selection effects is discussed at length; a Maximum-Likelihood method is given which is able to handle the sample selection effects.

4. Global photometric properties of the cluster galaxies are examined; the problem of second parameter in the TF relation is investigated; a physical explanation for the TF relation and its dispersion is proposed.

5. The peculiar velocity field as traced by the sample clusters is found to be highly non-random, and appears to be a coherent flow towards the general direction of the Great Attractor, with a flow amplitude of some 400$\sim$600 kms^{-1}at the position of the Local Group.

To My Parents

TABLE OF CONTENTS

Had I been present at the creation, I would have given some useful hints for the better ordering of the Universe.

—— Alfonso the Wise, King of Castile

Thesis Organization

Chapter 1: presents a short review of the current status of the study of large-scale motions in the universe, and briefly discusses the relevant practical problems.

Chapter 2: describes the galaxy sample of this thesis, the observation, and the procedure of data reduction—surface photometry.

Chapter 3: investigates various effects on surface photometry, namely, the cosmological effects, seeing effects, Galactic absorption effects and internal absorption effects.

Chapter 4: investigates the internal absorption problems in detail, and derives magnitude, color and diameter corrections for internal absorption.

Chapter 5: presents the final derived data of the sample galaxies.

Chapter 6: studies the Tully-Fisher (TF) relation of the sample cluster galaxies; compares different methods for deriving distances using the TF relation; and predicts relative distances of the sample clusters. A formal Maximum Likelihood technique, being able to deal with sample biases, is also presented.

Chapter 7: illustrates the global photometric properties of the sample galaxies; discusses the underlying physics of the TF relation and investigates the problem of second parameters in the TF relation.

Chapter 8: investigates the large-scale motions in the universe as implied by the sample clusters.

Appendix: Presents the manual of a computer program developed for the data reduction of this thesis, which is currently a public program in the Astronomy Department of Caltech.

CHAPTER I

INTRODUCTION

The formation of galaxies and large scale structures in the universe is one of the most fundamental problems in modern cosmology. Although great efforts have been made in the past 20 years, our understanding of the formation and evolution of galaxies and large scale structures is still very premature (Rees 1989). It seems that the current generally adopted picture of galaxy and structure formation is a gravitational amplification of an initial small density fluctuation somehow imprinted in the early universe. A favored theoretical scenario is that of structure formation from scale-invariant adiabatic fluctuations in a flat (inflationary) universe dominated by cold dark matter (Blumenthal *et al.* 1984). This model showed some success in explaining the observations on small scales (Davis *et al.* 1985; Bardeen *et al.* 1986; White *et al.* 1987). However, recent observations of large scale streaming (Lynden-Bell *et al.* 1988; Aaronson *et al.* 1989; Collins, Joseph & Robertson 1986, Willick 1990), and also the extremely inhomogeneous galaxy distribution on scales larger than 100Mpc (Broadhurst *et al.* 1990) disagree with the CDM predictions (Vittorio & Silk 1985; Melott 1987; Blumenthal, Dekel & Primack 1988; Groth *et al.* 1989; Gorski *et al.* 1989; Bertschinger & Juszkiewicz 1988; but see Kaiser 1988 and 1991; Kaiser & Lahav 1989). Although there are still large uncertainties in the picture of apparent large scale motions, the tentative evidence does seem to provide a critical constraint on the theories of formation and evolution of galaxies and large scale structures. Cosmologists might consider constructing new scenarios that are able to produce more power at large scales (Peebles 1987; Bardeen *et al.* 1987; Blumenthal *et al.* 1988). Observers, on the other hand, are devoting more effort to provide more complete and accurate empirical descriptions of large scale structures and motions in the universe.

The term *large scale motions*, or *peculiar velocities* usually refers to the deviation of galaxies or clusters of galaxies from isotropic Hubble expansion, or a motion relative to the the Cosmic Microwave Background (CMB). The dipole anisotropy in the CMB has conventionally been interpreted as the result of a peculiar motion of the Local Group (LG) at a velocity of about 600 km/s relative to the CMB (Lubin, Epstein & Smoot 1983; Fixsen, Cheng & Wilkinson 1983; Lubin *et al.* 1985; Smoot *et al.* 1991). The study of peculiar motions on large scales can be traced back to Rubin (1976a,b), however, it has become one of the most active fields in observational cosmology only in recent years, when relatively accurate distance measurements for distant galaxies became possible. The Tully-Fisher (TF) relation (Tully & Fisher 1977; Aaronson, Huchra & Mould 1979) for spiral galaxies and the $D_n - \sigma$ relation (Dressler 1987) for elliptical galaxies are the two key secondary distance indicators in the recent investigations of large scale motions.

Lilje, Yahil & Jones (1986) detected a quadrupolar component in the velocity field of the LSC, which implied that the LG's motion relative to CMB was a result of Virgo infall motion and a bulk Local Supercluster (LSC) motion towards the Hydra-Centaurus supercluster, presumably due to the gravitational force of this supercluster. Aaronson *et al.* (1986), by measuring the peculiar velocities of 10 clusters in redshift range from 4000 km/s to 10000 km/s using the IRTF relation, claimed that these clusters are at rest with respect to the CMB, they also concluded that the LSC had a large peculiar motion in the direction of Hydra-Centaurus supercluster. Similar conclusions have also been reached by Shaya (1984) and Tammann & Sandage (1985).

An exciting and perhaps surprising result came out of the study of the peculiar motions of 400 elliptical galaxies within 6000 km/s using the $D_n - \sigma$ relation by seven astronomers (later known as "Seven Samurai"). They concluded that the large scale motion in the local universe is dominated by a "Great Attractor" (GA) located at $l = 307°$, $b = 9°$ at distance of 4350 km/s and mass about $5 \times 10^{16} M_\odot$ (Dressler *et al.*

1987; Burstein *et al.* 1987; Lynden-Bell *et al.* 1988). In this attractive model, the LG has an infall velocity of about 500 km/s, and the Hydra-Centaurus supercluster itself is also participating the infall. Later work of the 7 Samurai mildly revised the GA model and provided additional support for it (Faber & Burstein 1988; Dressler & Faber 1990a, 1990b; Burstein, Faber & Dressler 1990). To actually "observe" the GA, a survey of radial velocities of elliptical galaxies in the GA region has been carried out (Dressler 1988, 1991), and there does seem to have a large concentration of galaxies in that direction and at about the distance predicted by the GA model. However, Jahoda & Mushotzky (1989) concluded, from study of the X-ray emission in the GA region, that the GA of a mass $\sim 10^{16} M_{\odot}$ can not be composed of rich clusters of galaxies.

Han & Mould (1990) studied the velocity field in the LSC and showed that the CMB dipole can be well explained by a GA + Virgo bi-infall model. Staveley-Smith & Davies (1990), from an all sky survey of spiral galaxies within 5000 km/s, concluded that no single attractor was able to explain all the motions observed in nearby galaxies, and the Centaurus cluster appears to have the dominant effect. Aaronson *et al.* (1989) and Mould *et al.* (1991) measured the peculiar motions of more clusters in the south sky; their data appears to support the general concept of the GA. Willick (1990), using R-band TF relation, measured the peculiar motions of 376 spiral galaxies in the Perseus-Pisces supercluster, which lies on the opposite side of the sky from the GA. He found that the P-P supercluster has a negative peculiar velocity of about 450 km/s, which can not be accounted for by the GA model. A survey of peculiar velocities of spiral galaxies in the GA region was also carried out by Mathewson, Ford & Buchhorn (1991); this survey, when combined with the P-P survey of Willick, seems to indicate a bulk flow motion of 500 km/s towards the direction of CMB dipole apex on scale of 20000 km/s (Mathewson, Ford & Buchhorn 1991). Collins, Joseph & Robertson (1986) have also reported a detection of bulk flow motion, but with even larger amplitude and in a slightly different direction. Lucey & Carter (1988) measured the peculiar motions of several

southern clusters, using first ranked galaxies as distance indicator, they did not see a large scale motion.

Other than the method of directly measuring peculiar velocities using a distance indicator, there are other approaches to understanding the large scale motions. One of them is the study of the dipole moment of galaxy surface brightness distribution in a (complete sky coverage) galaxy sample (e.g., Yahil *et al.* 1986; Lahav *et al.* 1988; Lynden-Bell, Lahav & Burstein 1988). These investigations do not seem, in general, to agree well with the idea of GA model or a large scale bulk flow picture. Another approach is that of Strauss & Davis (1989), Yahil (1989), and Strauss (1990) (see also Rowan-Robinson *et al.* 1990); these authors have carried out an extensive survey of radial velocities for all the IRAS galaxies brighter than a given limit, which enables them to construct a self-consistent model of (gravitationally induced) velocity and density fields, assuming IRAS galaxies trace mass. This model agrees well with the GA model on small scales (within about 1500 km/s), but fails to predict the large scale motions implied by the GA model (Gunn 1989; Burstein 1990). Complementary to the idea of Strauss *et al.*, which is basically to predict the (gravitational) peculiar velocity field by measuring the responsible mass distribution, Bertschinger & Dekel (1989, 1990), Dekel & Bertschinger (1990) and Dekel, Bertschinger & Faber (1990) have developed a method which is able to construct the 3-D potential, velocity and density fields from the observed 1-D peculiar velocity field, by assuming the smoothed velocity field to be a potential flow. Interesting velocity, potential and mass density fields within 6000 km/s in the real universe have been constructed by applying this method to a sample of galaxies which have peculiar velocities measured by the $D_n - \sigma$ and the IRTF relations (Bertschinger *et al.* 1990).

In sum, I think it is fair to say that a consistent picture of large scale motions in the universe has not yet achieved, although the GA model is seeing more popularity (see Gunn 1988 and Burstein 1990 for recent reviews). It should also be noted

that most of the investigations of large scale motions so far rely on the distance indicators of the TF relation and the $D_n - \sigma$ relation, and a generally good agreement between these two relations has been reported by Faber & Burstein (1988), Dressler & Faber (1990) and Aaronson *et al.* (1989) (but this may largely rely on those galaxies or clusters of galaxies seen in the GA direction). The reason for the existing discrepancies between different studies are not well understood, though one may be able to list a number of reasons for or against a particular result. In general, we may consider the reliability or accuracy of the measurement of large scale motions is determined by the combination of three factors: (1) the quality of the dataset (its completeness, and observational errors), (2) the quality of the distance indicator (universality, intrinsic scatter), and (3) the quality of data analyzing technique (including the justification of any specific assumptions made for the analysis). The universality of distance indicators has been a major concern in the study of large scale motions (Djorgovski, de Carvalho & Han 1989; Silk 1989). A number of empirical studies, however, reveal no strong environmental dependences of either the TF relation (Bothun *et al.* 1984; Mould, Han & Bothun 1989; Biviano *et al.* 1990), or the $D_n - \sigma$ relation (Burstein, Faber & Dressler 1990), indicating that these relations are qualified as a distance indicator. Although the TF relation and the $D_n - \sigma$ relation show no gross variation from place to place, they are not perfectly tight due to observational and intrinsic scatters. On the other hand, a real galaxy sample is alway incomplete due to selection limits. The very properties of non-zero scatter of distance indicator and the incompleteness of a real dataset raise another serious question in the study of large scale motions: bias. A familiar example of such bias is the Malmquist effects (Teerikorpi 1984, 1986; Bottinelli *et al.* 1986; Giraud 1987). Roth (1990) showed, using Monte Carlo experiment, that Malmquist bias could produce a fake infall flow into an overdense region; this effect brings complication in confirming an infall of galaxies from the back side of GA (Burstein, Faber & Dressler 1990). In principle, these kinds of biases can be removed by using the right data analyzing technique, which, unfortunately, is not

an easy job in practice; the difficulty usually comes from a poor understanding of sample completeness and the real distribution of galaxies in space. Examples of dealing with bias in large scale motion studies are found in Staveley-Smith & Davies (1990), and Lynden-Bell *et al.* (1988). A formally complete Maximum Likelihood method for this problem has been given by Han & Mould (1990).

Further investigations are certainly needed to get a clear picture of the large scale motions in the universe. Improving distance measurements is particularly necessary in future studies; it is also important to enlarge observational material and seek different approaches towards the problem. This thesis just aims to better understand the large scale motions in the universe, and also to better understand the TF relation as a distance indicator. A sample of nearby clusters of galaxies is taken as tracer of the large scale velocity field, and the I-band TF relation is investigated and employed as a distance indicator. For the purpose of studying large scale motions, using clusters as test points of the velocity field can greatly reduce uncertainties in distance measurements, and thus yields better estimations of peculiar velocities. The current cluster sample is a combination of those of Aaronson *et al.* (1986, 1989), who investigated the peculiar motions of these clusters using H-band TF relation. Compared with the conventional H-band TF relation (based on aperture photometry), the I-band TF relation based on CCD surface photometry is greatly preferred (Bothun & Mould 1987).* This is because, we are able to measure detailed luminosity distributions of galaxies with CCD detectors, i.e., to determine accurate total magnitude and isophotal magnitudes at any given level.

---

* Bothun and Mould (1987) pointed out two major disadvantages for I-band TF relation as compared with H-band TF relation: 1) noisier sky, and 2) larger internal extinction. However, sky background can be better evaluated using a CCD detector than from an IR photometer. As for the second point, it will be shown in this thesis that the conventional way of scaling the internal absorption from one band to another, as often seen in literature, is not correct.

Surface photometry also allows a more reliable estimation of inclination, which is important for the edge-on correction of rotation velocity-width. Compared with other optical bands at shorter wavelengths, the I-band is favored for the study of the TF relation, because it is less affected by the variation of star formation rates, and better traces the underlying disk mass. Pierce (1988) studied the I-band TF relation of the Virgo and Ursa Major clusters and found a very small scatter in the relation (see also Bothun & Mould 1987 and Mathewson, Ford & Buchhorn 1991). This thesis will provide the largest cluster sample thus far with detailed surface photometry data at I-band, suitable for the study of the TF relation and photometric properties of cluster galaxies.

REFERENCES FOR CHAPTER 1

Aaronson, M., Huchra, J. and Mould, J. M. 1979, *Ap. J.*, **229**, 1.

Aaronson, M. *et al.* 1989, *Ap. J.*, **338**, 654.

Bardeen, J. M. *et al.* 1986, *Ap. J.*, **304**, 15.

Bardeen, J. M. *et al.* 1987, *Ap. J.*, **321**, 28.

Bertschinger, E. and Juszkiewicz, R. 1988, *Ap. J.*, **334**, L59.

Bertschinger, E. and Dekel, A. 1989, *Ap. J. (Letters)*, **336**, L5.

Bertschinger, E. and Dekel, A. 1990, in *Large Scale Structure and Motions in the Universe*, ed. D.W. Lathem and L.N. da Costa (San Froncisco: A.S.P.), in press.

Bertschinger, E. *et al.* 1990, *Ap. J.*, **370**, 395.

Biviano, A. *et al.* 1990, *Ap. J. Suppl.*, **74**, 325.

Blumenthal, G. R. *et al.* 1984, *Nature*, **311**, 11.

Blumenthal, G. R., Dekel, A. and Primack, J. R. 1988, *Ap. J.*, **326**, 539.

Bothun, G. D. and Mould, J. R. 1987, *Ap. J.*, **313**, 629.

Bottinelli, L. *et al.* 1986, *Astr. Ap.*, **156**, 157.

Burstein, D. *et al.* 1987 in *Large Scale Structures of the Universe*, IAU Symposium 130, eds. J. Audouze, M. C. Pelletan and A. Szalay; p. 177.

Burstein, D. 1990, *Rep. Prog. Phy. Review.*, **53**, 421.

Burstein, D., Faber, S. M., and Dressler, A. 1990, *Ap. J.*, **354**, 18.

Collins, A., Joseph, R. D. and Robertson, N. A. 1986, *Nature*, **320**, 506.

Davis, M. *et al.* 1985, *Ap. J.* , **292**, 371.

Dekel, A. and Bertschinger, E. 1990, in *Large Scale Structure and Motions in the Universe*, ed. D.W. Lathem and L. N. da Costa (San Francisco: A.S.P.), in press.

Dekel, A., Bertschinger, E. and Faber, S. M. 1990, *Ap.J.*, **364**, 349.

Djorgovski, G., de Carvalho, R. and Han, M. 1988, in *The Extragalactic Distance Scale*, eds. S. van den Bergh and C. J. Pritchet (Provo: A.S.P.), p. 329.

Dressler, A. *et al.* 1987, *Ap. J. (Letters)*, **313**, L37.

Dressler, A., and Faber, S. M. 1990a, *Ap. J. Letters*, **354**, 13.

Dressler, A., and Faber, S. M. 1990b, *Ap. J. Letters*, **354**, L45.

Faber, S. M., and Burstein, D. 1988, in *Large Scale Motions in the Universe,* ed. V.C. Rubin and G. Coyne (Princeton University Press), p. 116.

Fixsen, D. J., Cheng, E. S., and Wilkinson, D. T. 1983, *Phys. Rev. Letters*, **50**, 620.

Giraud, E. 1987, *Astr. Ap.*, **174**, 23.

Gorski, K. *et al.* 1989, *Ap. J.*, **344**, 1.

Groth, E. J. *et al.* 1989, *Ap. J.*, **346**, 558.

Gunn, J. E. 1988, in *The Extragalactic Distance Scale*, eds. S. van den Bergh and C. J. Pritchet (Provo: A.S.P.), p. 344.

Han, M. and Mould, J. R. 1990, *Ap. J.*, **360**, 448.

Huchra, J. P. 1988, in *The Extragalactic Distance Scale*, eds. S. van den Bergh and C. J. Pritchet (Provo: A.S.P.), p. 257.

Kaiser, N. 1988, *M.N.R.A.S.*, **231**, 149.

Kaiser, N. 1991, *Ap. J.*, **366**, 388.

Lahav, O. *et al.* 1988, *M.N.R.A.S.*, **234**, 677.

Lilje, P. B., Yahil, A. and Jones, B. J. T. 1986, *Ap. J.*, **307**, 91.

Lubin, P. M., Epstein, G. L. and Smoot, G. F. 1983, *Phys. Rev. Letters*, **50**, 616.

Lubin, P. M. *et al.* 1985, *Ap. J. (Letters)*, **298**, L1.

Lynden-Bell, D. *et al.* 1988, *Ap. J.*, **326**, 19.

Lynden-Bell, D., Lahav, O. and Burstein, D. 1988, *M.N.R.A.S.*, **241**, 325.

Mathewson, D. S., Ford, V. L., and Buchhorn, M. 1991 *Ap. J. (Letters)*, in press.

Mould, J. R. *et al.* 1991, submitted to *Ap. J.*

Peebles, P. J. E. 1987 , *Nature*, **327**, 210.

Pierce, M. J. 1988, Ph. D. thesis, University of Hawaii.

Rees, M. 1989, preprint.

Roth, J. 1990, private communication.

Rowan-Robinson, M. *et al.* 1990, *M.N.R.A.S.*, **247**, 1.

Rubin, V. C. *et al.* 1976a, *A. J.*, **81**, 687.

Rubin, V. C. *et al.* 1976b, *A. J.*, **81**, 719.

Shaya, E. J. 1984, *Ap. J.*, **280**, 470.

Silk, J. 1989, *Ap. J. (Letters)*, **345**, L1.

Smoot, G. F. *et al.* 1991, *Ap. J. (Letters)*, **371**, L1.

Staveley-Smith, L. and Davies, R. D. 1989, *M.N.R.A.S.*, **241**, 787.

Strauss, M. A. and Davis, R. D. 1988, in *Large Scale Motions in the Universe,* ed. V.C. Rubin and G. Coyne (Princeton University Press), p. 255.

Strauss, M. A. 1990, Ph.D. Thesis, University of California, Berkeley.

Tammann, G. and Sandage, A. 1985, *Ap. J.*, **294**, 81.

Teerikorpi, P. 1984, *Astr. Ap.*, **141**, 407.

Tully, R. B. and Fisher, J. R. 1977, *Astr. Ap.*, **54**, 661.

Vittorio, N. and Silk, J. 1985, *Ap. J. (Letters)*, **293**, L1.

White, S. D. M. *et al.* 1987, *Ap. J.*, **313**, 505.

Willick, J. 1990, *Ap. J. (Letters)*, **351**, L5.

Yahil, A., Walker, D. and Rowan-Robinson, M. 1986, *Ap J.*, **301**, L1.

Yahil, A. 1988, in *Large Scale Motions in the Universe,* ed. V. C. Rubin and G. Coyne (Princeton University Press), p. 219.

CHAPTER II

OBSERVATION AND DATA REDUCTION

§2.1 The Sample

The galaxy sample of this thesis is basically a combination of the northern-sky cluster sample of Bothun *et al.* (1985) and the southern-sky cluster sample of Aaronson *et al.* (1989). Table 2.1 summarizes the global properties of these clusters.

Bothun's sample is a selection of cluster spirals drawn from the UGC and Zwicky catalogs, falling in the redshift range of 3000 - 11000 kms^{-1}, with declination between -1° and 38° (i.e., the range of Arecibo telescope). Aaronson's sample is a selection of cluster spirals drawn from the ESO catalog (Lauberts 1982), and falling in the redshift range of 2000 - 5000 kms^{-1}.

Although the sample galaxies were originally drawn from either a magnitude-limited catalog or a diameter-limited catalog, they all have to be $gas-rich$ enough to be detected at the HI 21 cm by Arecibo telescope (for the northern clusters) or by the Parkes telescope (for the southern clusters). The sample is therefore partially flux-limited. Effects of sample selection limits on the study of this thesis will be discussed in Chapter 6.

Photometric observations were done in the last 3 years for some 320 galaxies from the original two samples, and 284 of them were observed under photometric conditions. These 284 galaxies form the sample of this thesis. In this sample, 171 galaxies are cluster members and have high quality HI 21 cm data available from the original two samples. The HI data (21cm line-width) was reduced by the same group of authors, and is thus a homogeneous data set.

§2.2 Optical Observation

CCD images of the sample galaxies were obtained in both Cousins V and I bandpass (Cousins 1976), in the period from December 1987 to December 1989. The northern-sky galaxies were imaged with a TI CCD camera, in reimaging mode, on the 60-inch telescope of the Palomar Observatory; and the southern-sky galaxies were imaged with two very similar TI CCD cameras on, respectively, the 40-inch telescope and the 100-inch telescope of the Las Campanas Observatory. The exposure times were mostly from 10 to 15 minutes for I images, and from 5 to 10 minutes for V images.

Typically, 4 to 6 standard stars, with $V - I$ color covering that of a typical spiral galaxy, were observed each night. For the Palomar runs, the Landolt (1982) standards were used; and for the Las Campanas runs, both the Landolt standards and the E-region standards of Graham (1982) were used. The M67 standards (Schild 1983) were also observed on a few nights.

To check the consistency between Palomar and Las Campanas observations, 7 galaxies in cluster A539 were observed at both observatories. There are also some other galaxies observed several times at either Palomar Observatory, or Las Campanas Observatory. Table 2.2 lists the observational information for the sample galaxies. Column (1) gives the galaxy name; Column (2) is the date of observation in the format of "yymmdd"; Column (3) records the telescope used for the galaxy (P60 = Palomar 60-inch, C40, C100 = Las Campanas 40-inch and 100-inch); Columns (4) and (5) are the exposure time and airmass for the observation of I-image; Columns (6) and (7) are the exposure time and airmass for the V-image; Column (8) is a *photometry-quality-parameter* assigned for each galaxy during data reduction (see §2.5).

§2.3 Preliminary Reduction

The images were debiased and flat-fielded using dome flats. Each dome flat is the average of 4 individual frames. No dark subtraction was performed. After debiasing and flattening, the large-scale sky gradient was typically less than 0.5%, for Palomar observations; and less than 0.8%, for Las Campanas observations. No attempt was made to automatically correct cosmic-ray events, but in the subsequent data reduction, as described further below, each image was visually examined on a color graphic device, and any chip defects, including hot pixels, on or around the program galaxy were interpolated.

The transformation from instrumental magnitudes to Cousins photometric system was made using the following equations,

$$I = a + I_i + b(V - I) - k_I X \tag{2.1a}$$

$$V - I = c + d(V_i - I_i) - k_{V-I} X \tag{2.1b}$$

where I_i and V_i are, respectively, the I and V instrumental magnitudes. The coefficients a, b, c and d were determined for each night using the standard stars observed that night. The atmospheric extinctions were fixed at $k_I = 0.05$ mag, $k_{V-I} = 0.09$ mag, for Palomar observations; and $k_I = 0.07$ mag, $k_{V-I} = 0.1$ mag, for Las Campanas observations. These values were checked on several nights, by observing a couple of stars at different airmasses, the uncertainties are within 0.02 mag. Table 2.3 lists the coefficients of each observing night.

§2.4 Surface Photometry

Surface photometry was carried out on the I-band images using the ellipse-fitting routine, PROF, of the Galaxy Surface Photometry (GASP) package developed by Cawson (1983), and a complementary routine SFOTO, written by myself. A detailed description of SFOTO is given in the Appendix.

The ellipse-fitting routine PROF assumes that the isophotes of the galaxy can be roughly represented by ellipses, with intensities, centers, ellipticities, and position angles variable with major axis. The intensity variation $I(a, \phi)$ around the sampling ellipse of semi-major axis a can then be approximated using the Fourier series:

$$I(a, \phi) = I_0(a) + A_1 \sin\phi + B_1 \cos\phi + A_2 \sin 2\phi + B_2 \cos 2\phi \qquad (2.2)$$

here ϕ is the eccentric anomaly. For an ellipse of ellipticity ϵ and semi-major axis a, ϕ is related to the $x - y$ coordinates of a point on the ellipse in the following form,

$$\begin{aligned} x &= a \sin\phi \\ y &= a(1-\epsilon) \cos\phi \end{aligned} \qquad (2.3)$$

The fitting of equation (2.2) to a galaxy image, for Fourier coefficients, is done using the least-squares method. It is clear that if the galaxy isophotes are ellipses, the coefficients A_i and B_i will all be zeros. Nonzero values of A_1 and B_1 indicate an error in the position of the ellipse center; a nonzero A_2 indicates an error in the position angle; and nonzero B_2 indicates an error in ellipticity. Any defects in the image, such as cosmic rays, foreground stars, or star-forming regions can be masked (using SFOTO) so that the fitting program (PROF) ignores them entirely. The iteration at each radius ceases if the residual coefficients are smaller than a given threshold set by the size of the ellipse and the noise in the data, or the number of iterations is equal to the maximum number specified. The fitting starts at an user-specified initial major axis, usually 1 pixel. After each radius fit, the axis is increased by a factor, typically 1.1. and the process is repeated until one of the following conditions is satisfied: 1) the profile intensity is sufficiently close to the sky value, typically within 1 σ of the sky noise, 2) the portion of the ellipse perimeter in the masked region is larger than a given fraction, usually 40%, or 3) the profile intensity starts to rise at large radii by too much. The output of PROF is a list of mean intensities, ellipticities, position angles, and $x - y$ centers as a function of semi major axis.

Below is an outline of the complete operational procedure of doing surface photometry for the galaxies of this thesis sample.

1) The galaxy images (after debiasing and flatfielding) are interactively processed with SFOTO to produce the initial information required by PROF: the position of the program galaxy in the image, the initial guess of the parameters of the first ellipse (radius, eccentricity, and position angle), the sky value, and the regions to be ignored in the fit. SFOTO also converts the original image format (FIGARO HDS format) into the format recognized by GASP. All these are output into four separate files, according to the demand of PROF (see Appendix for details).

2) PROF then reads these output files, and does the ellipse fitting job. The fitting results, i.e., the ellipse parameters, are output to a file, NAME.PRF.

3) SFOTO is used again to convert the instrumental intensities of the fitted ellipses into brightnesses (in units of mag/arcsec^2), using the photometric transformation coefficients tabulated in Table 2.3. SFOTO also performs photometry on the galaxy through elliptical apertures, and computes the color profile and inclination of the galaxy. To do this, the defects in the image can not be ignored any more, and must be carefully interpolated. Each galaxy image is visually inspected with different stretches and magnifications on a graphic device, and defects within the interesting area around the galaxy are interpolated. SFOTO also superposes the ellipses onto the CCD frame on a display device for a visual check of the goodness of ellipse fitting by PROF, and is able to repair those which do not look like reasonable fits. It turns out that most isophotes, even those for which the maximum number of iterations was reached without passing the residual test, seem to be good enough visually. In a few cases, the last couple of isophotes are obviously a poor fit, due to large sky variation or sky contamination by a nearby bright star. Such isophotes are repaired by simply expanding the closest "good ellipse" outward to the corresponding sizes, and the mean intensities assigned to the modified ellipses are calculated within 3-pixel

wide annuli centered at the ellipses.

4) After performing the photometry, SFOTO displays the surface brightness profile and ellipticity profile. The semi-major axis range corresponding to the disk of the galaxy is then roughly estimated based on these profiles. The inclination of the galaxy is calculated using the median ellipticity of those isophotes falling in the specified radius-range, and assuming an intrinsic ellipticity of 0.8 (i.e., minor to major axial ratio of 0.2). The "disk range" is usually identified to be the outer linear part of the surface brightness profile. Attention is also paid to the outermost few ellipses, which would be excluded if their ellipticities are too low due to seeing effects or low signal-to-noise ratio. For most of our galaxies, this procedure of calculating inclination is found to be very robust to accidental errors in individual isophotes, and to the user's judgement on the range of "disk". The typical uncertainty is about 3 degrees.

The final results from SFOTO are a list of the I-band isophotal brightnesses in units of mag/arcsec^2, I-band isophotal magnitudes, differential and integrated $(V-I)$ colors as a function of major radius; and also the inclination of the galaxy and a crude estimate of the I-band luminosity concentration parameters at the levels of 20%, 30%, 50%, 70%, and 80% (more accurate concentration parameters will be calculated using extrapolated total luminosity in Chapter 5).

For most of the sample galaxies, the I-band surface photometry can be performed down to a level of 23.5 mag/arcsec^2, which corresponds to a blue surface brightness of about 26 mag/arcsec^2. The typical rms error at this level is about 0.10 mag. The sources of error in surface photometry are discussed below.

§2.5 Errors In Surface Photometry

The uncertainty in surface photometry comes from various sources, some of them may merely introduce noise in the data, some may cause systematic errors, while

others may distort the luminosity distribution of the object (a detailed discussion of various sources of accidental and systematic errors in surface photometry is given by Capaccioli & de Vaucouleurs 1983). The error or uncertainty in surface photometry is usually reflected by the formal rms errors associated with the derived quantities from the process of basic data reduction. In this thesis, the following sources have been taken into account in the estimation of such formal errors.

1) *Photometric transformation error:* this is due to the formal rms errors in the photometric transformation coefficients tabulated in table 2.3. These rms errors were basically from the uncertainties in the aperture photometry of the standard stars observed each night. These can amount an error of typically 0.02 mag.

2) *Sky subtraction error:* the uncertainty in estimating sky background comes mainly from the imperfection of flatfielding, and, in some cases, the existence of bright (or unresolved faint) stars near to the program galaxy. Intrinsic noise and variation in the sky brightness may also be a factor (Okamura 1988). Fortunately, all of our galaxies are small enough to leave plenty of "blank sky" on the CCD frame, so that the light of the galaxy itself does not bother the sky evaluation. In practice, sky is determined in two steps, 1) sampling the sky: the image is visually checked on a display device with suitable stretch, and the "blank sky" fields around the galaxy are sampled with the cursor. Each sampling gives an average sky intensity within a box of typically 10 by 10 pixels at the cursor position, denoted as s_i with rms error σ_i. 2) calculating the sky background: in this thesis, the sky background is simply taken to be the median value of the above samplings, $< s >$. The standard deviation $\sigma_{<s>}$, is typically only 0.2 to 0.5% of the sky level. The total error assigned to the estimated sky level $< s >$ is the sum of this large-scale uncertainty ($\sigma_{<s>}$) and the mean local rms error divided by $\sqrt{n}$, that is,

$$\sigma_s = \sigma_{<s>} + \sum_{i=1}^{n} \frac{\sigma_i}{n^{3/2}} \tag{2.4}$$

This error is more important at fainter surface brightness levels than at bright

levels. An inaccurate estimate of the sky level would introduce a systematic error in both the surface brightness and the isophotal magnitude. Figure 2.1 shows how an exponential profile is affected by an inaccurate determination of sky level; this example assumes a value of 4 for the ratio of galaxy-center intensity to sky intensity.

3) *Readout noise:* this is not expected to be an important source of error in surface photometry; in our data reduction, we simply used a value of 10 e^- for the readout noise of all detectors, and a value of 2 for the conversion factor from electrons to the raw CCD intensity units (counts).

4) *Photon statistics:* this is just the Poisson statistical uncertainty in both sky and galaxy photon detections.

5) *Ellipse fitting error:* this is supposed to reflect the deviation of the real azimuthal distribution of light from an ideal ellipse, which has been assumed to represent the true isophotes in the first place. Unfortunately, there is not a well defined quantity to characterize such deviation. For simplicity, the intensity variance around each ellipse was used as an indicator of the fitting error, regardless of other fitting information, such as whether the fit had passed the residual criterion, or how large were the residuals in the four Fourier coefficients of equation (2.2). This error, like σ_s, also has larger effects on fainter surface brightness levels than for bright levels, but in any case, it can hardly contribute more than half of the total error in surface brightness.

It turns out that the dominant error in surface photometry, especially at faint levels, is due to the sky subtraction error. All the above errors, except the ellipse fitting error, also contribute to the errors in isophotal magnitudes. Other possible error, not reflected in the formal errors, may come from:

1) *Image blurring:* This could be caused by seeing effects, poor focusing and poor telescope guiding. The FWHM of the Point Spread Function (PSF) is typically from 1.5 to 2.5 arcseconds for most of our images. The importance of seeing on

surface photometry has been stressed by Schweizer (1979, 1981), and confirmed by a number of other authors. Discussion of seeing and other image-distorting effects will be presented in Chapter 3.

2) *Scale conversion:* a conversion of CCD scale from pixel to arcseconds has to be made in order to measure the brightness and size of a galaxy in meaningful units. The adopted CCD scale is $0''.640$ pixel^{-1}, for Palomar 60-inch images, $0''.435$ pixel^{-1}, for Las Campanas 40-inch images, and $0''.405$ pixel^{-1}, for Las Campanas 100-inch images. These are the mean scale values of several measurements for each CCD. Each measurement consists of a couple of star-pairs in either the E-regions (Graham 1982), or the M67 cluster. The scatters were at about 5% level, which would translate an error of 0.05 mag/arcsec^2 in surface brightness of all levels, and a 5% error in radius.

3) *Image cleaning:* Most of the galaxies in the sample have bad pixels (usually cosmic ray events) or foreground stars superposed on them in the CCD frames. As explained above, these bad pixels and stars had been ignored in the process of ellipse fitting, and had been cleaned up in the process of performing photometry. Ignoring a small portion of a bad region in the fitting process might introduce errors in the fitted parameters (i.e., ellipse intensity, ellipticity and position angle). But such errors can be well ignored, both because the ignored regions are always relatively small, and because most galaxies are relatively smooth and symmetric. Even in the case of an irregular shaped galaxy, or a heavily armed galaxy, the errors would be dominated by the large deviations of the isophotes from ellipses, rather than by, if any, ignoring a small portion of it. Therefore, it is expected that the surface brightness profile and ellipticity, which were directly converted from the fitting results, are almost free of such errors. In the case of performing photometry through elliptical apertures, however, the bad regions and foreground stars have to be interpolated, rather than ignored. The interpolation mode of SFOTO has a restoring function, which allows the

user to process the interpolation for a bad region back and forth several times, until visually satisfied. An imperfect interpolation would introduce errors in the isophotal magnitudes and colors. Unfortunately, this kind of error can not be precisely quantified.

In order to give an estimate of those error sources, which were not implicitly reflected in the quoted rms errors, an alternative *photometry quality parameter* (Q), is assigned for each galaxy. This parameter, ranging from 1 to 5, with 1 indicating the highest quality, is subjectively estimated according to the author's judgment about the overall quality of photometry. The factors considered in the judgment are usually the reliability of image cleaning, contamination of the galaxy by scattered light of nearby bright stars, or a low signal-to-noise ratio of the object. It is attempted to make the parameter Q approximately reflect the photometry errors due to these factors: a value from 1 to 3 corresponds crudely to a 0 – 5 percent uncertainty, a value of 4 indicates 5 – 10 percent uncertainty, and 5 is the worst case. There are only 5 galaxies in the sample which were assigned a value of 4 or 5 for the Q parameter; these 5 galaxies are excluded from the following studies. In sum, the overall reliability of the surface photometry in this thesis is judged by both the rms formal errors and the quality parameter Q.

Additional uncertainties may be introduced when correcting surface photometry for various effects, mainly Galactic absorption and internal extinction; these effects will be discussed in Chapter 3 and Chapter 4.

§2.6 Average Profiles of Different Measurements

There are 50 galaxies in our sample that were observed twice or three times, using same or different devices. The results of surface photometry from different measurements of same object are weight-averaged as described below.

a) Rescale Profiles of Different Measurements

Let $\{g_j(r_{i,j}),\, i = 1, m_j\}$, be the observed profile of a quantity g of the j^{th} measurement ($j = 1, n$), and $\{\sigma_j(r_{i,j}),\, i = 1, m_j\}$ be its formal errors. Usually, different profiles have different numbers of points m_j; and were sampled on different radius-bases, especially in the case that the measurements were done with different devices. So the first thing to do is to re-scale the profiles of different measurements to a common radius-base (r_i, $i = 1, m$), so that the average of different measurements can be performed on this radius-base. The common radius-base is chosen to be that of the j_0^{th} measurement, if the radius of its first point, i.e., r_{1,j_0}, is the smallest of ($r_{1,j}$, $j = 1, n$); in the case that the radius of its last point, i.e., $r_{m_{j_0},j_0}$, is not the largest of ($r_{m_j,j}$, $j = 1, n$), the common radius-base is simply extended using the measurement, which has largest radius coverage. With the common radius-base thus defined, we then "re-measure" each g profile, i.e., calculate the value of g for each measurement at the radii (r_i, $i = 1, m$). This is done (where necessary) by linear interpolation of the two closest points in the original profile, and the errors associated with these "measurements" are taken to be the mean error of the two points used in the interpolation. For those points in the common radius-base which lie out of the original radius-range of a measurement, g is assigned to an arbitrary value, and will be given a zero weight in the following average.

A possible concern about the profile re-measuring procedure (i.e., linear interpolation) as just described is that it would introduce additional errors in the profile, or smear out some fine structures in the profile. The uncertainty thus introduced into the profiles, however, is believed to be very small relative to other uncertainties discussed in §2.5. Because, all our profiles were originally sampled on a radius-base with a 10% radius spacing, this means that in the inner part of a profile (the nuclei region), a 10% radius ranges from tenth of pixel to a few pixels. Considering other uncertainties in the profile (e.g., seeing effects, and measurement errors), the errors

introduced by an interpolation of the profile within such a small interval should be negligible. The outer part of a profile is usually flat and has larger uncertainties from other sources, thus it is also believed to be suitable for a linear interpolation in the outer part of a profile.

Now, for each measurement, we have a re-scaled g-profile, $\{g_j(r_i), i = 1, m\}$ with error $\{\sigma_j(r_i), i = 1, m\}$. In order to best estimate the g profile from the n measurements, which have different uncertainties. We need to weight each profile properly.

b) Weight Profiles of Different Measurements

Djorkovski (1985) discussed the problem of weighting profiles of different measurements at length. In this thesis, a relatively simple weighting scheme is employed. The factors considered for assigning a weight to a profile are, 1) errors associated with each profile, i.e., $\{\sigma_j(r_i), i = 1, m\}$; 2) seeing effects, as characterized by the parameter $s \equiv$ FWHM; and 3) the overall quality of the profile Q (see §2.5). Exposure time and sky brightness are not explicitly included in our weight, these two quantities largely determine the S/N ratio at the outer part of a profile, which is partially reflected in the formal errors of the profile (see §2.5).

The complete weight function $w_j(r)$ is assumed to be a product of three individual weight functions, which reflect the three factors mentioned above:

$$w_j(r) = w^j_\sigma(r) \cdot w^j_s(r) \cdot w^j_Q(r) \tag{2.5}$$

Our determination of the three weight functions below will be largely based on subjective, but reasonable judgements, rather than on strict statistical analyses.

The function $w^j_\sigma(r)$ is a contribution from the original profile errors, and is taken

to be the inverse of σ, i.e.,

$$w_\sigma^j(r) = \frac{1}{\sigma_j(r)} \tag{2.6a}$$

The seeing weighting function $w_s^j(r)$ is supposed to account for the relative importance of seeing effects. The detailed form of such a function depends, obviously, not only on the amount and form of seeing corrections on surface intensity as a function of radius, but also on how we define the weighting function in terms of such corrections. It is therefore clear that the question of "weighting seeing" itself is not well defined, even in principle. On the other hand, however, we do hope that a measurement with smaller seeing receives a larger weight in our average. For a real galaxy, we therefore expect the form of the seeing weight function w_s^j is such that at a constant radius, it is a decreasing function of seeing, and the decreasing rate is maximum at the galaxy center (the intensity peak) and gradually drops to zero, as radius goes to infinity. Based on this qualitative expectation, we adopt the following for a seeing weighting function

$$w_s^j(r) = 1 + \frac{(\frac{\overline{s}}{s_j})^2 - 1}{1 + e^{\frac{r - r_o}{\Delta r}}} \tag{2.6b}$$

where

$$\overline{s} = \frac{1}{n} \sum_{j=1}^{n} s_j$$

is the mean seeing of the n measurements. r_o and Δr are two parameters that control the amplitude of the weight and how it varies with radius, we adopt $r_o = 3\,\overline{s}$, and $\Delta r = 1.2\,\overline{s}$. Figure 2.2 shows the relative seeing weight functions of two measurements with seeing $s = 2''$ and $3''$.

It will be shown in §3.4, that seeing correction on surface brightness can be approximated by a power law of s (= FWHM), with s^2 being the dominant term.

Our adopted seeing weighting function (2.6b), which varies with s^{-2}, is therefore, more or less, inversely proportional to the seeing correction on surface brightness.

Finally, $w_Q^j(r)$ provides a global weight to the j^{th} measurement. We define w_Q to be inversely proportional to the square root of the global quality parameter Q, which has been assigned to each measurement (see §2.5),

$$w_Q^j(r) = \frac{1}{\sqrt{Q_j}} \tag{2.6c}$$

Recall that Q has five possible values (1 to 5), and only those measurements with $Q \leq 3$ are included in our sample. Thus w_Q^j takes one of the following three values: 1.0, 0.70, or 0.58.

Equations (2.5) and (2.6a-c) define the weighting function for each observed profile. In applying it to our data, care has to be taken for those points in the common radius-base (r_i, $i = 1, m$), at which not every measurement has an available observed value. This can be easily dealt with by introducing a switching function δ_i^j for each point, so that $\delta_i^j = 1$ at observed points, and $\delta_i^j = 0$ at unobserved points. The weighting function can then be expressed as

$$w_j(r_i) = \frac{\delta_i^j}{\sigma_j(r_i)\sqrt{Q_j}} \left[1 + \frac{(\frac{\bar{s}}{s_j})^2 - 1}{1 + e^{\frac{r - r_Q}{\Delta r}}} \right], \qquad i = 1, m;\ j = 1, n \tag{2.7}$$

c) Average the profiles

Given a weight $w_j(r)$ for each $g_j(r)$, the final average of the g-profile is

$$g(r_i) = \frac{\sum_{j=1}^{n} w_j(r_i)\, g_j(r_i)}{\sum_{j=1}^{n} w_j(r_i)}, \qquad i = 1, m \tag{2.8}$$

The formal error of the averaged profile is conservatively estimated in the same manner.

$$\sigma_g(r_i) = \frac{\sum_{j=1}^{n} w_j(r_i)\,\sigma_j(r_i)}{\sum_{j=1}^{n} w_j(r_i)}, \quad i = 1, m \tag{2.9}$$

This weighting method is applied to the observed profiles of those galaxies with more than one measurements. For color profiles, the seeing weighting function is taken to be the product of both the I-band and V-band seeing functions. The averaging process is carried out using an interactive computer program, which displays, on a graphic device, each of the original observed profiles and the mean profile given by equation (2.8), and allows the user to modify the result.

Some notes on the average of different profiles:

1) *Surface brightness profile:* the agreement between different measurements are generally within the formal error bars. But in some cases, the innermost profile of different measurements can differ by more than several sigmas, due to seeing effects; and the outermost one or two points sometimes can also have large difference, presumably due to low S/N ratio or minor sky subtraction errors. In the case that the innermost or the outermost couple of points were not sampled by all the measurements, the value of surface brightness given by equation (2.8) at these points sometimes show a noticeable shift relative to the mean trend of the profile. A slight modification were then made on these points to make them follow the mean trend.

2) *The growth curve:* the agreement between different measurements in the outer part of the profile is generally good to within 1 σ (i.e., $\lesssim$ 0.05 mag). The inner parts sometimes show large differences, which are also caused by seeing effects. As we did for the surface brightness profile, in the case that the last few points were not sampled by all the measurements and a small shift is noticed between these points and the mean profile: a small modification was then applied to

make the whole profile smoother at these points.

3) *Color profile:* large disagreement between different measurements also occurs in the inner part of the profile, which reflects the relative importance of seeing effects. As mentioned before, in weighting the $(V - I)$ color for seeing effects, I simply use the product of the seeing weighting functions for both I and V bands. Minor modifications were also applied on the innermost or outermost points, where necessary. It is interesting to note that quite a number of galaxies show a reddening effect of typically 0.1 mag in the outer parts of color profiles. This is not believed to be caused by possible sky subtraction errors for two reasons: (1) no significant blue effect is seen, and (2) the outer part of color profiles from different measurements are generally in good agreement. Possible explanations are, (1) galaxy disk is usually more extended at I-band than at V-band (sharp V disk cut off ?), and (2) the S/N ratio at the outer part of galaxies is lower for V images, because V images were always taken with shorter exposure times than I images.

4) *The ellipticity profile:* as for other profiles, the ellipticity profiles are also averaged according to equation (2.8), and agreement in the outer part of the profiles (interesting range for inclination estimation) is always very good (within typically 3°). The inclination of a multi-measured galaxy was simply taken to be the mean value of the individual inclination estimates.

REFERENCES FOR CHAPTER 2

Aaronson, M. *et al.* 1989, *Ap. J.*, **338**, 654.

Bothun, G. *et al.* 1985, *Ap. J. Suppl.*, **57,** 423.

Capaccioli, M. and de Vaucouleurs, G. 1983, *Ap. J. Suppl.*, **52**, 465.

Cawson, M. 1983, Ph.D. thesis, University of Cambridge.

Cowsins, A. W. J. 1976, *Mem. R. A. S.*, **81**, 25.

Graham, J. A. 1982, *P. A. S. P.*, **94**, 244.

Landolt, A. 1983,*A. J.*, **88**, 439.

Lauberts, A. 1982, *The ESO/Uppsala Survey of the ESO Atlas* (Munich: European Southern Observatory).

Okamura, S. 1988, *P. A. S. P.*, **100**, 524.

Schild, R. E. 1983, *P. A. S. P.*, **95**, 1021.

Schweizer, F. 1979, *Ap. J.*, **223**, 23.

Schweizer, F. 1981, *A. J.*, **86**, 662.

Figure Captions for Chapter 2

Figure 2.1: Effects of sky subtraction error on the surface brightness profile of a pure e–disk galaxy.

Figure 2.2: Relative seeing weighting functions (eq. [2.6b]) for two measurements with seeing (FWHM) of 2 and 3 units, respectively.

Table 2.1

Global Properties of Sample Clusters

Cluster	l	b	v_c	±	v_s	±	R
Pisces ..	125.8	–32.5	5274	(58)	5329	(111)	–1
A400 ...	170.3	–44.9	7154	(90)	7855	(134)	1
A539 ...	195.7	–17.7	8561	(123)	8502	(97)	1
Cancer .	202.5	28.7	4790	(89)	4376	(99)	–1
A1367 ..	234.8	73.0	6427	(73)	6511	(140)	2
Coma ..	57.2	87.9	6931	(45)	7019	(193)	2
Z74-23 ..	349.6	65.5	6025	(153)	6369	(181)	–1
A2151 ..	31.7	44.5	11077	(97)	10657	(233)	2
Pegasus .	87.8	–48.4	4078	(78)	4319	(155)	–1
A2634 ..	103.5	–36.0	8783	(115)	8693	(215)	1
Antlia ..	273.0	20.0	2667	(84)	2662	(68)	–1
Cen30 ..	302.5	21.5	2804	(52)	3160	(180)	0
Cen45 ..	302.5	21.5	4337	(35)	4478	(140)	0
E508 ...	309.2	39.2	2728	(60)	2715	(63)	–
Hydra ..	269.6	26.5	3455	(85)	3476	(140)	1
N3557 ..	282.0	22.0	2702	(79)	2753	(64)	–

l, b = galactic coordinate.

v_c = cluster mean velocity in the LG frame.

v_s = sample mean velocity in the LG frame.

R = richness class.

Table 2.2

Observation of the Sample Galaxies

Name	Date	Telescope	ET_I	X_I	ET_V	X_V	Q
(1)	(2)	(3)	(4)	(5)	(6)	(7)	(8)
PISCES							
N295	87DEC10	P60	300	1.03	300	1.04	3
N296	87DEC10	P60	300	1.05	300	1.04	1
N444	88DEC09	P60	900	1.01	600	1.02	1
N452	88DEC09	P60	500	1.09	500	1.04	2
N536	88DEC09	P60	500	1.04	300	1.05	3
N582	88DEC09	P60	600	1.09	400	1.10	1
U525	88DEC10	P60	600	1.15	300	1.17	3
U540	88DEC10	P60	600	1.22	300	1.25	2
U556	88DEC10	P60	500	1.31	300	1.27	2
U557	88DEC10	P60	800	1.40	500	1.45	2
U575	89NOV02	P60	600	1.79	300	1.69	2
	89DEC22	P60	700	1.25	500	1.21	1
U633	89NOV02	P60	600	1.86	300	1.93	2
	89DEC22	P60	600	1.50	300	1.54	1
U673	89NOV02	P60	600	2.10	300	1.95	2
	89DEC22	P60	600	1.27	400	1.31	1
U679	89DEC21	P60	600	1.23	300	1.20	1
U732	89DEC21	P60	500	1.26	300	1.29	1
U841	88DEC10	P60	500	1.43	350	1.38	1
U987	88DEC10	P60	300	1.49	200	1.52	1
U1033	89DEC21	P60	300	1.39	300	1.43	2
U1066	89DEC22	P60	300	1.30	150	1.27	2
Z501021	89DEC21	P60	450	1.53	300	1.47	1

Table 2.2 —— continued

Name (1)	Date (2)	Telescope (3)	ET_I (4)	X_I (5)	ET_V (6)	X_V (7)	Q (8)
A400							
U2285	88DEC09	P60	600	1.19	400	1.21	2
	88DEC10	P60	500	1.54	300	1.48	1
U2364	87DEC10	P60	300	1.41	300	1.38	1
U2367	89OCT27	P60	600	1.33	300	1.29	2
	89DEC20	P60	300	1.12	300	1.12	1
U2375	89OCT27	P60	600	1.39	300	1.43	2
	89DEC22	P60	600	1.40	300	1.35	1
U2405	89OCT27	P60	600	1.56	300	1.49	2
	89DEC22	P60	600	1.48	300	1.52	1
U2414	87DEC10	P60	300	1.26	300	1.27	1
U2415	87DEC10	P60	300	1.29	300	1.27	1
U2454	87DEC10	P60	300	1.30	300	1.32	1
U2509	88DEC10	P60	500	1.60	300	1.65	1
Z415055	89DEC21	P60	200	1.38	150	1.35	1
Z415058	89DEC21	P60	300	1.42	250	1.45	2
A539							
U3219	87DEC10	P60	300	1.13	300	1.14	1
U3220	87DEC10	P60	300	1.15	300	1.14	1
U3236	87DEC10	P60	300	1.16	300	1.18	2
U3248	87DEC10	P60	300	1.25	300	1.23	1
U3269	87DEC10	P60	300	1.23	300	1.24	1
U3270	87DEC10	P60	300	1.25	300	1.27	1
U3275	87DEC09	P60	300	1.31	300	1.29	1
	89DEC20	P60	900	1.12	500	1.12	1
U3282	89DEC20	P60	900	1.15	450	1.18	3
	89OCT27	P60	900	1.20	300	1.14	3

Table 2.2 —— continued

Name	Date	Telescope	ET_I	X_I	ET_V	X_V	Q
(1)	(2)	(3)	(4)	(5)	(6)	(7)	(8)
U3291	87DEC10	P60	300	1.27	300	1.25	1
Z421011	87DEC09	P60	300	1.33	300	1.36	1
Z421012	87DEC10	P60	300	1.40	300	1.37	1
Z421030	87DEC09	P60	300	1.42	300	1.39	1
CANCER							
I2288	87DEC01	P60	300	1.02	300	1.02	1
	89DEC20	P60	600	1.09	400	1.07	1
I2348	87DEC01	P60	300	1.03	300	1.03	1
N2535	88DEC10	P60	600	1.06	400	1.05	3
N2545	89DEC21	P60	200	1.15	200	1.14	1
N2570	87DEC01	P60	300	1.03	300	1.03	1
N2575	89FEB10	P60	300	1.01	250	1.02	3
N2582	88DEC10	P60	400	1.03	250	1.03	1
N2595	89DEC22	P60	300	1.03	300	1.03	3
N2596	87DEC01	P60	300	1.05	300	1.05	1
U4299	87DEC01	P60	300	1.06	300	1.05	1
	89DEC22	P60	600	1.02	300	1.02	1
U4329	87DEC01	P60	300	1.07	300	1.08	1
	89DEC20	P60	600	1.05	400	1.07	1
U4344	89DEC20	P60	600	1.12	300	1.09	1
U4361	87DEC01	P60	300	1.10	300	1.08	1
U4386	87DEC01	P60	300	1.12	300	1.14	1
U4399	87DEC01	P60	300	1.16	300	1.14	1
	89DEC20	P60	700	1.04	400	1.03	2
U4400	87DEC02	P60	300	1.49	300	1.45	1
	89DEC20	P60	900	1.05	500	1.06	2
U4405	87DEC02	P60	300	1.36	300	1.39	1

Table 2.2 —— continued

Name	Date	Telescope	ET_I	X_I	ET_V	X_V	Q
(1)	(2)	(3)	(4)	(5)	(6)	(7)	(8)
U4424	87DEC02	P60	300	1.35	300	1.32	1
	89DEC20	P60	1000	1.03	600	1.04	1
U4444	89DEC21	P60	200	1.25	200	1.26	1
U4446	87DEC02	P60	300	1.23	300	1.25	2
Z89001	89DEC22	P60	400	1.07	300	1.06	1
Z119019	88DEC10	P60	600	1.03	400	1.05	1
Z119044	87DEC02	P60	300	1.17	300	1.15	2
Z119047	89OCT27	P60	600	1.06	300	1.07	2
	89DEC20	P60	900	1.13	400	1.17	1
Z119051	87DEC02	P60	300	1.12	300	1.14	1
Z119053	87DEC02	P60	300	1.11	300	1.10	2
Z119066	88DEC10	P60	600	1.10	400	1.12	3
Z119095	87DEC02	P60	300	1.05	300	1.04	1
Z119107	87DEC02	P60	300	1.03	300	1.03	2
A1367							
I742	87DEC09	P60	300	1.24	300	1.26	1
N3697	87DEC02	P60	300	1.45	300	1.41	1
	89DEC21	P60	200	1.20	150	1.19	1
N3701	87DEC09	P60	300	1.14	300	1.12	2
N3832	88APR09	P60	300	1.02	300	1.02	1
N3840	87DEC02	P60	300	1.41	300	1.46	1
N3861	87DEC02	P60	300	1.38	300	1.35	1
N3883	87DEC09	P60	300	1.14	300	1.16	1
N3933	87DEC09	P60	300	1.16	300	1.15	1
N3947	87DEC09	P60	300	1.10	300	1.11	1
N3951	87DEC02	P60	300	1.29	300	1.31	1
U6509	89DEC22	P60	300	1.06	300	1.05	1

Table 2.2 —— continued

Name	Date	Telescope	ET_I	X_I	ET_V	X_V	Q
(1)	(2)	(3)	(4)	(5)	(6)	(7)	(8)
U6586	87DEC10	P60	300	1.27	300	1.25	1
U6686	87DEC02	P60	300	1.21	300	1.23	1
U6743	88APR09	P60	300	1.11	300	1.10	1
U6821	87DEC10	P60	300	1.19	300	1.17	1
U6837	87DEC02	P60	300	1.20	300	1.18	1
U6876	87DEC10	P60	300	1.14	300	1.16	1
U6891	87DEC02	P60	300	1.16	300	1.18	1
Z97005	88DEC10	P60	800	1.20	500	1.17	2
	89DEC22	P60	600	1.04	400	1.05	1
Z97033	88DEC10	P60	600	1.11	400	1.13	1
Z97058	89FEB10	P60	300	1.43	250	1.40	3
	89DEC20	P60	300	1.06	250	1.07	1
Z97062	89FEB10	P60	600	1.28	400	1.32	3
Z97068	88DEC10	P60	300	1.07	300	1.08	1
Z97152	89FEB10	P60	300	1.17	300	1.15	1
Z97180	89FEB10	P60	700	1.10	500	1.12	1
Z97185	89FEB10	P60	600	1.09	400	1.08	1
Z126083	89DEC21	P60	300	1.16	300	1.17	1
Z126104	88APR11	P60	500	1.10	300	1.09	2
Z127005	89FEB10	P60	700	1.02	500	1.03	1
Z127049	89FEB10	P60	600	1.03	400	1.02	2
Z127056	89FEB10	P60	600	1.03	400	1.02	1
Z127082	89FEB10	P60	600	1.03	400	1.04	2
	89DEC21	P60	400	1.15	300	1.14	1
Z127083	88APR11	P60	500	1.08	300	1.09	1
I821	89FEB12	P60	250	1.01	200	1.01	2
I842	89FEB11	P60	300	1.01	300	1.01	1
	89DEC22	P60	600	1.10	300	1.09	1

Table 2.2 —— continued

Name	Date	Telescope	ET_I	X_I	ET_V	X_V	Q
(1)	(2)	(3)	(4)	(5)	(6)	(7)	(8)
I3949	89FEB12	P60	350	1.01	300	1.01	2
I4040	89DEC20	P60	600	1.04	300	1.06	1
I4088	89FEB11	P60	300	1.00	250	1.00	1
N4966	89FEB11	P60	300	1.01	300	1.00	3
	89DEC22	P60	300	1.07	250	1.08	3
N5065	89FEB11	P60	400	1.00	300	1.01	1
N5081	89FEB12	P60	300	1.05	300	1.05	2
COMA							
U7754	89DEC21	P60	400	1.13	300	1.11	1
U7978	89FEB11	P60	400	1.08	300	1.07	1
	89DEC21	P60	300	1.19	250	1.21	1
U8013	89DEC20	P60	800	1.08	400	1.07	1
U8017	89FEB11	P60	400	1.12	300	1.13	1
U8161	89FEB11	P60	300	1.16	250	1.14	1
U8195	89FEB12	P60	600	1.20	450	1.24	1
U8229	89FEB12	P60	300	1.34	250	1.32	1
U8244	89FEB12	P60	700	1.16	500	1.14	2
Z160058	89FEB12	P60	600	1.06	400	1.08	2
Z74-23							
N5409	89FEB10	P60	400	1.11	250	1.10	1
N5416	89FEB10	P60	350	1.10	200	1.10	1
U8918	88APR11	P60	500	1.40	300	1.44	1
U8927	88APR11	P60	500	1.36	300	1.33	2
U8948	88APR11	P60	500	1.22	300	1.25	3
U8950	88APR11	P60	500	1.19	300	1.17	1

Table 2.2 —— continued

Name	Date	Telescope	ET_I	X_I	ET_V	X_V	Q
(1)	(2)	(3)	(4)	(5)	(6)	(7)	(8)
U8951	88APR11	P60	500	1.14	300	1.16	1
U8967	88APR11	P60	500	1.09	300	1.09	1
U9023	89FEB10	P60	650	1.14	450	1.16	1
U9027	88APR11	P60	500	1.08	300	1.09	1
Z74012	88APR11	P60	500	1.11	300	1.10	1
Z74035	88APR11	P60	600	1.14	400	1.15	1
A2151							
I1155	89FEB12	P60	500	1.28	350	1.26	4
I1173	89FEB10	P60	400	1.18	300	1.17	1
N6050	89FEB10	P60	600	1.11	400	1.13	1
U10085	89FEB12	P60	600	1.15	400	1.18	2
U10190	89FEB12	P60	800	1.10	600	1.08	2
U10195	89FEB12	P60	300	1.06	200	1.06	1
Z108108	89FEB10	P60	500	1.09	280	1.07	1
Z108140	89FEB10	P60	400	1.05	300	1.05	2
Z108158	89FEB12	P60	450	1.37	350	1.42	3
PEGASUS							
I1474	87DEC02	P60	300	1.21	300	1.22	1
I5309	87DEC02	P60	300	1.34	300	1.20	2
N7536	87DEC02	P60	300	1.32	300	1.35	1
N7591	87DEC02	P60	300	1.50	300	1.47	1
N7593	89DEC20	P60	500	1.38	300	1.35	3
N7631	87DEC02	P60	300	1.50	300	1.54	1
U12382	89DEC21	P60	400	1.32	250	1.34	2

Table 2.2 —— continued

Name	Date	Telescope	ET_I	X_I	ET_V	X_V	Q
(1)	(2)	(3)	(4)	(5)	(6)	(7)	(8)
U12423	89DEC21	P60	450	1.38	300	1.34	4
U12451	89DEC21	P60	500	1.45	300	1.51	2
U12467	89DEC22	P60	600	1.22	400	1.20	1
U12494	89DEC22	P60	600	1.25	300	1.27	1
U12547	89DEC22	P60	500	1.35	300	1.32	1
U12555	89DEC22	P60	600	1.40	300	1.44	1
U12561	89DEC22	P60	600	1.47	300	1.41	2
U12571	89DEC22	P60	400	1.46	300	1.50	1
A2634							
N7747	88DEC10	P60	300	1.01	200	1.01	1
U12631	88DEC10	P60	500	1.03	300	1.02	1
U12678	88DEC10	P60	600	1.05	400	1.06	2
U12701	88DEC10	P60	900	1.10	600	1.07	1
U12721	88DEC10	P60	600	1.12	400	1.14	1
U12746	88DEC10	P60	600	1.20	400	1.16	1
U12755	88DEC10	P60	500	1.22	300	1.25	1
Z476112	89DEC21	P60	500	1.24	300	1.21	5
Z477024	89DEC21	P60	600	1.25	300	1.27	2
	89DEC22	P60	600	1.40	350	1.44	1
Z477033	89DEC21	P60	600	1.36	350	1.30	1
Z498012	89DEC21	P60	600	1.47	300	1.51	1
ANTLIA							
318-4	88JAN25	C40	900	1.09	600	1.12	1
437-14	88JAN24	C40	900	1.28	600	1.35	1

Table 2.2 —— continued

Name	Date	Telescope	ET_I	X_I	ET_V	X_V	Q
(1)	(2)	(3)	(4)	(5)	(6)	(7)	(8)
437-18	88FEB08	C100	300	1.16	200	1.18	1
	88JAN27	C40	600	1.78	720	1.64	3
437-56	88JAN29	C40	900	1.23	600	1.28	1
	88FEB09	C100	300	1.00	200	1.00	1
I2531	88JAN24	C40	900	2.09	600	1.89	1
I2556	88JAN26	C40	900	1.98	600	1.82	3
	88FEB10	C100	300	1.05	200	1.06	2
I2559	88JAN26	C40	900	1.56	600	1.69	1
I2560	88JAN24	C40	900	1.66	600	1.79	2
N3223	88JAN23	C40	900	1.51	600	1.64	2
N3347A	88JAN27	C40	600	1.23	400	1.26	2
N3347B	88JAN27	C40	800	1.18	600	1.14	2
N3449	88JAN27	C40	500	1.42	300	1.37	1
CEN30							
268-44	88JAN24	C40	900	1.13	600	1.10	2
268-46	88JAN24	C40	900	1.06	600	1.08	1
269-28	88JAN27	C40	900	1.40	600	1.32	2
269-52	88JAN28	C40	900	1.24	600	1.28	1
322-42	88JAN23	C40	900	1.35	600	1.41	2
	88FEB09	C100	300	1.05	200	1.06	1
322-85	88JAN29	C40	900	1.23	600	1.19	1
323-27	88JAN26	C40	600	1.46	400	1.40	1
323-72	88JAN27	C40	900	1.17	600	1.14	1
381-14	88JAN24	C40	900	1.14	600	1.17	1
N4603	88JAN24	C40	900	1.27	600	1.23	2
N4603A	88JAN23	C40	900	1.27	600	1.22	1
N4672	88JAN25	C40	900	1.05	600	1.04	3

Table 2.2 —— continued

Name (1)	Date (2)	Telescope (3)	ET_I (4)	X_I (5)	ET_V (6)	X_V (7)	Q (8)
CEN45							
268-37	88JAN25	C40	900	1.09	600	1.11	2
322-48	88JAN23	C40	900	1.15	600	1.18	2
323-25	88JAN29	C40	900	1.12	600	1.16	1
323-39	88JAN28	C40	900	1.41	——	——	2
323-73	88JAN27	C40	900	1.23	600	1.27	1
N4679	88JAN23	C40	900	1.10	600	1.08	1
E508							
443-79	88JAN26	C40	900	1.10	600	1.08	3
507-41	88JAN27	C40	900	1.60	600	1.70	1
507-42	88JAN26	C40	800	1.24	500	1.20	2
507-67	88JAN26	C40	900	1.13	600	1.17	2
508-11	88JAN27	C40	900	1.09	600	1.11	2
508-19	88JAN27	C40	900	1.03	600	1.04	3
508-51	88JAN28	C40	900	1.10	600	1.08	2
508-7	88JAN26	C40	900	1.03	600	1.05	2
576-11	88JAN23	C40	900	1.08	600	1.10	1
576-32	88JAN28	C40	900	1.16	600	1.21	2
576-40	88JAN28	C40	900	1.04	600	1.06	2
I4237	88JAN28	C40	700	1.03	400	1.02	1
N5022	88JAN24	C40	602	1.05	600	1.04	1

Table 2.2 —— continued

Name	Date	Telescope	ET_I	X_I	ET_V	X_V	Q
(1)	(2)	(3)	(4)	(5)	(6)	(7)	(8)
HYDRA							
437-30	88JAN27	C40	700	1.46	500	1.53	1
	88FEB13	C40	397	1.08	300	1.07	1
437-34	88JAN29	C40	900	1.77	600	1.57	2
	88FEB08	C100	300	1.01	200	1.01	1
437-4	88JAN24	C40	900	1.55	600	1.46	1
437-54	88JAN29	C40	600	1.46	600	1.36	1
	88FEB08	C100	300	1.00	200	1.00	1
501-1	88JAN25	C40	900	1.20	600	1.16	2
	88FEB09	C100	300	1.02	300	1.01	1
501-2	88JAN28	C40	900	1.97	600	1.87	3
	88FEB08	C100	400	1.16	300	1.12	1
501-68	88JAN28	C40	900	1.54	600	1.42	1
	88FEB08	C100	400	1.27	300	1.21	1
501-82	88JAN26	C40	900	1.69	600	1.59	1
501-86	88JAN28	C40	900	1.21	600	1.17	1
	88FEB08	C100	300	1.39	200	1.36	1
N3463	88JAN26	C40	900	1.15	600	1.19	1
N3557							
319-11	88JAN24	C40	900	1.16	600	1.14	3
377-21	88JAN23	C40	900	1.26	600	1.21	1
377-31	88JAN25	C40	900	1.05	600	1.07	2
377-34	88JAN24	C40	900	1.32	600	1.26	2
377-40	88JAN28	C40	600	1.17	600	1.21	1
378-11	88JAN26	C40	800	1.03	400	1.04	2

Table 2.2 —— continued

Name	Date	Telescope	ET_I	X_I	ET_V	X_V	Q
(1)	(2)	(3)	(4)	(5)	(6)	(7)	(8)
378-3	88JAN25	C40	900	1.04	600	1.02	1
N3533	88JAN26	C40	900	1.36	600	1.55	1
N3568	88JAN23	C40	900	1.35	600	1.42	4
N3573	88JAN26	C40	400	1.31	300	1.27	2
South sky galaxies without HI measurement							
263-51	88JAN23	C40	900	1.40	600	1.34	2
321-10	88JAN29	C40	400	1.01	200	1.01	2
321-16	88JAN29	C40	400	1.01	200	1.02	2
321-18	88FEB09	C100	300	1.02	200	1.01	3
322-9	88FEB09	C100	150	1.03	100	1.03	1
323-42	88JAN26	C40	900	1.30	600	1.35	1
324-23	88FEB11	C40	600	1.02	400	1.02	1
377-17	88JAN29	C40	900	1.17	600	1.22	3
	88FEB10	C100	600	1.10	400	1.10	3
380-14	88FEB08	C100	400	1.01	300	1.02	1
380-29	88FEB10	C100	300	1.12	200	1.14	1
380-34	88FEB10	C100	400	1.20	300	1.18	2
380-8	88FEB09	C100	300	1.01	200	1.01	2
382-32	88FEB10	C100	300	1.02	200	1.02	1
382-4	88FEB10	C100	300	1.07	200	1.08	2
382-41	88FEB10	C100	300	1.01	200	1.01	1
382-45	88FEB10	C100	300	1.01	200	1.01	3
382-58	88FEB13	C40	600	1.55	400	1.60	1
383-2	88FEB11	C40	600	1.06	400	1.05	1
383-27	88FEB12	C40	300	1.04	300	1.03	1
383-44	88JAN29	C40	600	1.18	——	——	2

Table 2.2 —— continued

Name	Date	Telescope	ET_I	X_I	ET_V	X_V	Q
(1)	(2)	(3)	(4)	(5)	(6)	(7)	(8)
383-48	88FEB12	C40	300	1.53	200	1.59	1
383-60	88FEB12	C40	400	1.37	300	1.33	2
383-72	88FEB12	C40	500	1.14	400	1.12	1
383-88	88FEB12	C40	300	1.30	300	1.33	2
384-2	88FEB12	C40	900	1.01	600	1.00	3
437-31	88JAN28	C40	900	1.25	600	1.32	1
	88FEB08	C100	500	1.00	300	1.00	1
442-28	88FEB10	C100	600	1.10	300	1.12	3
443-21	88FEB10	C100	300	1.09	200	1.08	1
443-42	88FEB10	C100	200	1.19	150	1.18	1
443-59	88FEB10	C100	300	1.05	200	1.04	1
443-83	88FEB10	C100	300	1.03	200	1.02	1
444-47	88FEB10	C100	250	1.01	150	1.00	2
445-14	88FEB12	C40	300	1.17	300	1.19	2
445-26	88FEB13	C40	600	1.51	400	1.45	1
445-58	88FEB12	C40	300	1.27	300	1.25	1
445-81	88FEB12	C40	400	1.03	300	1.04	2
507-62	88FEB09	C100	200	1.03	100	1.02	1
510-7	88FEB13	C40	900	1.32	600	1.40	1
I1657	88JAN28	C40	600	1.58	500	1.51	1
I3290	88FEB09	C100	150	1.03	100	1.02	1
I4214	88FEB10	C100	120	1.00	60	1.00	1
I4299	88FEB12	C40	400	1.77	300	1.70	1
I4351	88FEB13	C40	400	1.22	300	1.19	1
N4112	88JAN29	C40	400	1.02	200	1.02	2
N4219	88JAN29	C40	300	1.04	150	1.04	1
N424	88JAN27	C40	600	1.72	900	1.61	1
N4980	88FEB08	C100	400	1.02	300	1.02	1

Table 2.2 —— continued

Name	Date	Telescope	ET_I	X_I	ET_V	X_V	Q
(1)	(2)	(3)	(4)	(5)	(6)	(7)	(8)
N5121A	88FEB11	C40	900	1.08	600	1.11	2
N5161	88FEB11	C40	900	1.23	600	1.30	1
	88FEB13	C40	600	1.00	400	1.01	1
N5188	88FEB11	C40	400	1.03	200	1.03	1
N5302	88FEB12	C40	400	1.09	300	1.10	1
N5398	88FEB13	C40	900	1.12	600	1.15	2

Col. 1: galaxy name.

Col. 2: observing data (yymmdd).

Col. 3: telescope (P60=Palomar 60″; C40, C100=Las Campanas 40″, 60″.

Col. 4: I-band exposure time in seconds.

Col. 5: I-airmass.

Col. 6: V-band exposure time in seconds.

Col. 7: V-airmass.

Col. 8: photometry quality parameter (see text).

Table 2.3

Photometric Thansformation Coefficients

Date (yymmdd)	a (mag)	b	c (mag)	d	k_I (mag/airmass)	k_{V-I}
Palomar / 60 inch telescope / CCD-scale = 0.640″pixel^{-1}						
87DEC01	21.505 ±0.010	−0.050 ±0.010	1.680 ±0.030	1.110 ±0.020	0.05	0.09
87DEC02	21.500 ±0.020	−0.030 ±0.030	1.635 ±0.030	1.100 ±0.020	0.05	0.09
87DEC09	21.503 ±0.029	−0.019 ±0.040	1.670 ±0.017	1.107 ±0.018	0.05	0.09
87DEC10	21.498 ±0.008	−0.018 ±0.010	1.653 ±0.010	1.096 ±0.008	0.05	0.09
88APR09	21.429 ±0.011	−0.020 ±0.010	1.588 ±0.005	1.067 ±0.005	0.05	0.09
88APR11	21.384 ±0.008	−0.022 ±0.012	1.574 ±0.027	1.042 ±0.022	0.05	0.09
88DEC09	21.420 ±0.027	−0.051 ±0.025	1.644 ±0.011	1.064 ±0.011	0.05	0.09
88DEC10	21.424 ±0.019	−0.017 ±0.015	1.634 ±0.010	1.042 ±0.008	0.05	0.09
89FEB10	21.223 ±0.012	−0.023 ±0.010	1.594 ±0.014	1.055 ±0.012	0.05	0.09
89FEB11	21.223 ±0.012	−0.023 ±0.010	1.594 ±0.014	1.055 ±0.012	0.05	0.09
89FEB12	21.223 ±0.012	−0.023 ±0.010	1.594 ±0.014	1.055 ±0.012	0.05	0.09
89DEC20	21.460 ±0.017	−0.020 ±0.016	1.530 ±0.018	1.040 ±0.016	0.05	0.09
89DEC21	21.465 ±0.020	−0.020 ±0.020	1.590 ±0.020	1.070 ±0.020	0.05	0.09
89DEC22	21.490 ±0.019	−0.034 ±0.016	1.598 ±0.018	1.079 ±0.018	0.05	0.09

Table 2.3 —— continued

Date (yymmdd)	a (mag)	b	c (mag)	d	k_I (mag/airmass)	k_{V-I}
	Las Campanas / 40 inch telescope / CCD-scale = 0.435″pixel^{-1}					
88JAN23	22.098 ±0.018	0.050 ±0.017	0.763 ±0.005	0.952 ±0.007	0.07	0.10
88JAN24	22.112 ±0.025	0.032 ±0.031	0.756 ±0.007	0.966 ±0.015	0.07	0.10
88JAN25	22.100 ±0.030	0.040 ±0.030	0.760 ±0.020	0.966 ±0.020	0.07	0.10
88JAN26	22.151 ±0.001	0.036 ±0.002	0.806 ±0.008	0.970 ±0.018	0.07	0.10
88JAN27	22.190 ±0.007	0.025 ±0.011	0.807 ±0.010	0.953 ±0.020	0.07	0.10
88JAN28	22.183 ±0.008	0.044 ±0.011	0.829 ±0.013	0.979 ±0.030	0.07	0.10
88JAN29	22.191 ±0.008	0.050 ±0.014	0.830 ±0.006	0.973 ±0.010	0.07	0.10
88FEB11	22.030 ±0.014	0.060 ±0.015	0.731 ±0.010	0.982 ±0.010	0.07	0.10
88FEB12	22.026 ±0.018	0.080 ±0.023	0.731 ±0.008	0.982 ±0.020	0.07	0.10
88FEB13	22.044 ±0.006	0.050 ±0.007	0.793 ±0.014	0.964 ±0.027	0.07	0.10
	Las Campanas / 100 inch telescope / CCD-scale = 0.405″pixel^{-1}					
88FEB08	23.176 ±0.020	0.040 ±0.020	1.137 ±0.020	0.965 ±0.020	0.07	0.10
88FEB09	23.178 ±0.019	0.038 ±0.031	1.141 ±0.017	0.967 ±0.020	0.07	0.10
88FEB10	23.194 ±0.015	0.020 ±0.024	1.162 ±0.021	0.982 ±0.027	0.07	0.10

Figure 2.1

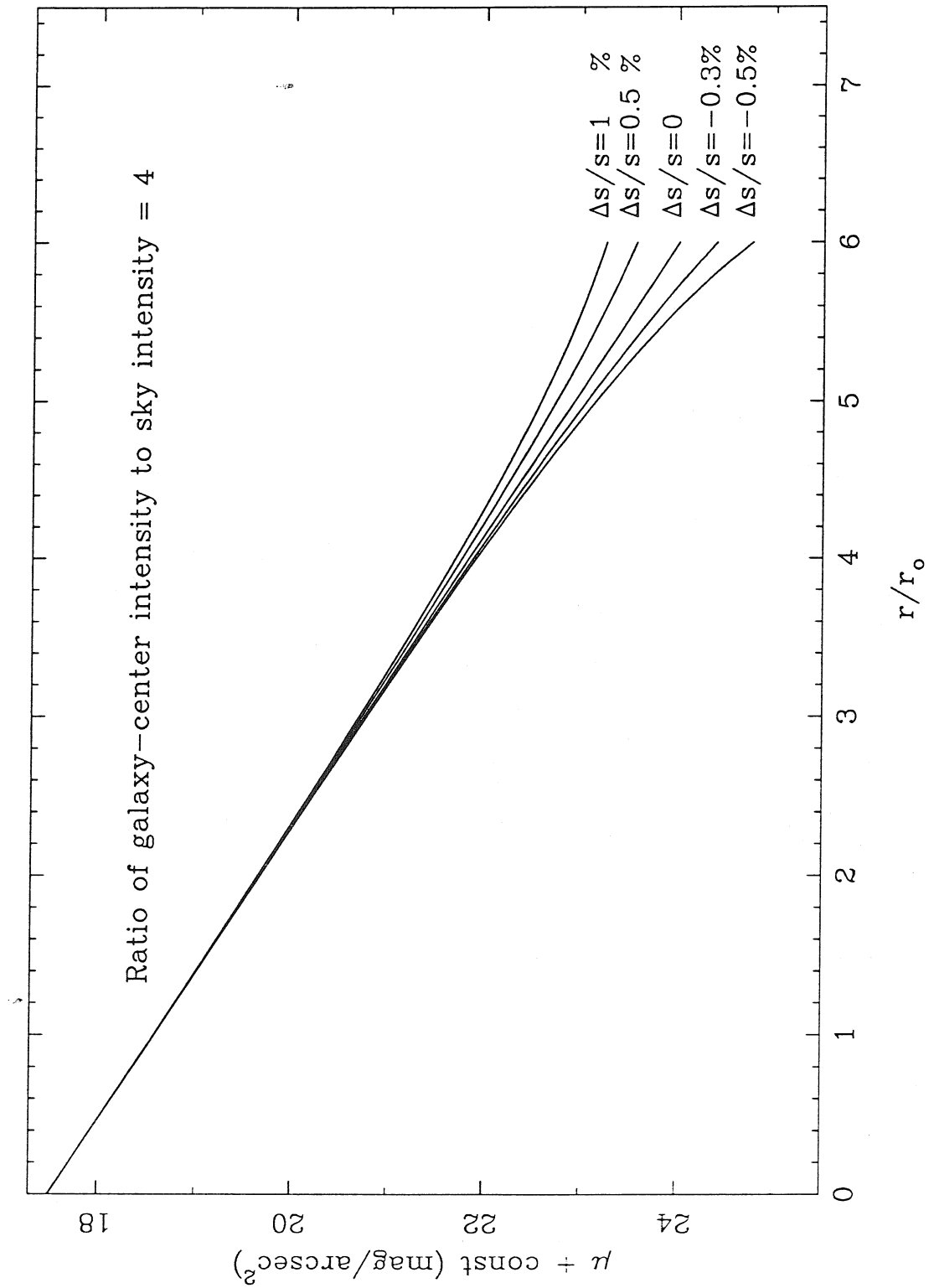
Ratio of galaxy−center intensity to sky intensity = 4
Δs/s=1 %
Δs/s=0.5 %
Δs/s=0
Δs/s=−0.3%
Δs/s=−0.5%
μ + const (mag/arcsec²)
18
20
22
24
0
1
2
3
4
5
6
7
r/r₀

Figure 2.2

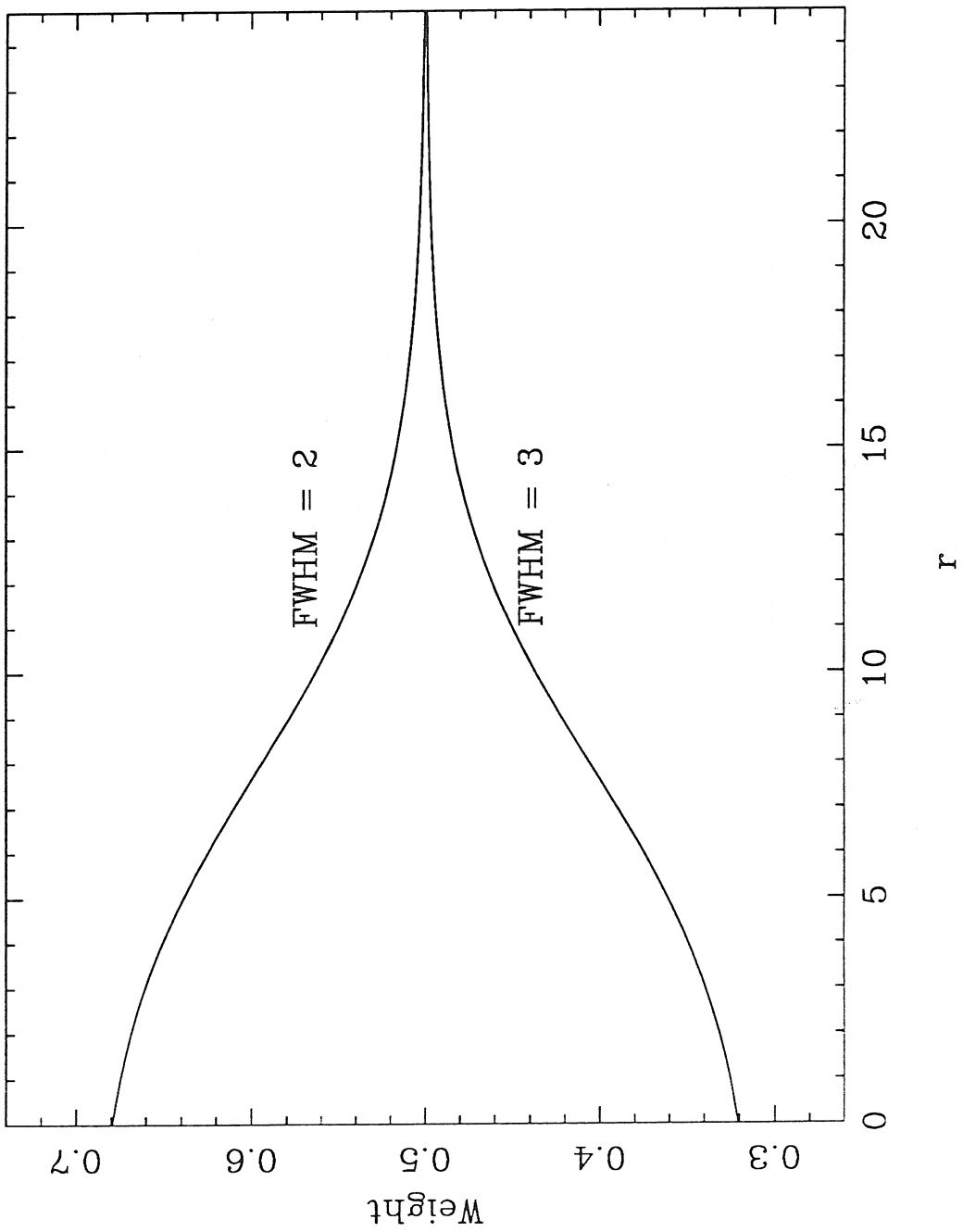

CHAPTER III

VARIOUS EFFECTS ON SURFACE PHOTOMETRY

§3.1 Instruction

What we expect from surface photometry of a galaxy is its *true* or *intrinsic* two dimensional light distribution. Unfortunately, the light of a galaxy has suffered a number of effects (e.g., absorption, scattering and refraction) on its way to an astronomical detector, so that the apparent light distribution, i.e., the surface brightness profile derived in the previous chapter, does not represent the real energy distribution of the galaxy. In order to make use of these distorted profiles for further investigation about galaxies, we either need to "restore" the true profile by correcting the apparent profiles for various effects, or at least to have a good estimate of the errors caused by the effects in the interesting parameters extracted from the distorted profiles.

There are basically two kinds of effects that distort the true light distribution of a galaxy. The first kind of effects are those which the light has suffered after leaving the parent galaxy. These effects are not directly coupled with the properties of the galaxy itself, and can be named as *external effects*, which include, for example, Galactic absorption, cosmological effects (K-correction, cosmological dimming) and seeing effects. The second kind of effects come out of the intrinsic properties of the program galaxy itself, which can be named as *internal effects*. These are basically due to the extinction and scattering of galaxy light by the dust particles within the galaxy. To calculate these effects requires not only the detailed knowledge about the total amount and the 3-dimensional distribution of dust particles and their physical

properties, but also the amount and intrinsic 3-dimensional light distribution of the program galaxy, which is exactly what we are trying to learn. This complication plus the insufficient knowledge about dust in galaxies make it almost impossible to accurately correct for the internal effects. Yet these effects, if not suitably accounted for, may greatly mislead our understanding about galaxies.

Before any specific correction is estimated, it is helpful to outline the formal correction formula for surface brightness profile. Let $J(r)$ = the true surface intensity profile, $I(r)$ = the apparent intensity profile, G = the Galactic absorption factor, C = the cosmological effects, and E = the internal extinction factor. Let $f(r)$ = point spread function (PSF). The apparent intensity profile is expected to be the convolution of the PSF with the *residual* true profile, i.e., J, after going through all other effects:

$$I = [G \cdot C \cdot E \cdot J] * f. \tag{3.1.1}$$

Because of the convolution, the above equation can not be expressed in the form of logarithm addition (i.e., in units of magnitude), unless G, C, and E are constant across the surface of the galaxy. Correction for seeing effects (i.e., deconvolution of equation 3.1.1) is not a trivial problem, and will be discussed in §3.4. At the moment, pretending there is no seeing effect (i.e., set $f(r) = \delta(r)$), equation (3.1.1) can then be expressed in units of magnitude

$$\mu(r) = \eta(r) + A_G + A_C + A_i, \tag{3.1.2}$$

where $\mu(r)$ is the observed surface brightness profile, in the absence of seeing effects; $\eta(r)$ is the intrinsic surface brightness profile that we are intended to recover. A_G, A_C, and A_i are, respectively, the Galactic absorption, the cosmological term, and the internal absorption term. Strictly speaking, the three correction terms all depend on radius r, implying that both the zero point and the shape of the surface brightness profile are changed by these effects.

The Galactic absorption correction term, A_G, and the Cosmological correction, A_C, in equation (3.1.1) will be estimated in §3.2 and §3.3, respectively. The seeing effects will be discussed in §3.4. The internal extinction term, A_i, because of its special importance for the study of this thesis, will be separately discussed at length in Chapter 4.

§3.2 The Galactic Absorption

The light of an external galaxy, before being detected on earth, had to go through the processes of absorption and scattering by the dust particles in our galaxy, namely the Galactic absorption. The Galactic absorption problem has been comprehensively studied by Burstein and Heiles (1978) using the intervening neutral hydrogen density. In this thesis, the predictions of Burstein and Heiles are employed for the galactic absorption correction of our sample galaxies. For the northern-sky galaxies in the sample, absorption values were taken from the extinction list of Burstein and Heiles (1984); and for the southern-sky galaxies, absorption values were kindly provided by Dr. Burstein. There are a number of galaxies in the thesis sample that lie in the "Great Attractor" region (i.e., $230° \leq l \leq 310°$, $-22° \leq b \leq 22°$); for these galaxies, the reddenings were reduced by a factor of 2 from the original Burstein and Heiles predictions, based on the information recently learned during the 7-Samurai survey (Burstein 1990). The extinction given by Burstein and Heiles is expressed as $4\mathrm{E}(B-V)$. Applying the van de Hulst extinction curve No. 15 (Johnson 1968), and the transformation between Johnson and the Cousins systems given by Fernie (1983), we estimated the extinctions at Cousins V and I bands were, respectively 75% and 44% of the extinction value $4\mathrm{E}(B-V)$ as given by Burstein and Heiles.

§3.3 The Cosmological Effects

Surface brightness is simply a measure of the integrated light per unit area on the surface of an object, while, in an expanding universe, both *light* (photons) and *area* (apparent size), as practically measured by astronomers, are subject to cosmological effects. Therefore, surface brightness is expected to be subject to cosmological effects as well.

In an isotropic and homogeneous universe, the general form of the metric is the Robertson-Walker metric

$$dr^2 = c^2dt^2 - R^2(t)\left[\frac{dr^2}{1-kr^2} + r^2d\theta^2 + r^2\sin^2\theta d\phi^2\right]. \tag{3.3.3}$$

Let t and t_o be, respectively, the emission and reception time of an object at comoving radial coordinate r. Then we can write

$$\int_t^{t_o} \frac{c\,dt}{R(t)} = \int_o^r \frac{dr}{\sqrt{1-kr^2}}. \tag{3.3.4}$$

By introducing the Hubble constant $H_o = \frac{\dot{R}_o}{R_o}$, and the parameter $q_o = -\frac{\ddot{R}_o}{R_o}H_o^{-2}$, the above equation yields the relation between comoving coordinate r and the redshift of the object, $z = \frac{R_o}{R} - 1$ (see, e.g., Weinberg 1972)

$$r = \frac{D_L}{(1+z)R_o}, \tag{3.3.5}$$

where D_L is the luminosity distance,

$$D_L = \frac{c}{H_o q_o^2}\left[q_o z + (q_o - 1)(\sqrt{1+2q_o z} - 1)\right]. \tag{3.3.6}$$

The metric distance at the time of emission is given by

$$d = r\,R = \frac{rR_o}{1+z} = \frac{D_L}{(1+z)^2} \tag{3.3.7}$$

If Δx is the physical size of the object at the time of emission, then the apparent size of the object would be

$$\Delta\theta = \frac{\Delta x}{d} = \frac{\Delta x}{D_L}(1+z)^2. \tag{3.3.8}$$

The cosmological effects on luminosity can be estimated as follows (see, e.g., Gunn and Oke 1975; Schneider, Gunn and Hoessel 1983). Define,

$N(\lambda)$ $\equiv$ The number of photons of wavelength λ in the unit interval of $dt\,d\lambda$, emitted by the object at time t.

$n(\lambda)$ $\equiv$ The number of photons of wavelength λ received per unit interval of $dt\,d\lambda$, per unit area, at time t_o.

Because the expansion of the universe will red-shift a λ photon to a $(1+z)\lambda$ photon, and expand a time interval dt to $(1+z)dt$, the relation between $n(\lambda)$ and $N(\lambda)$ is thus,

$$n(\lambda)dtd\lambda = \frac{1}{4\pi d^2} N\Big(\frac{\lambda}{1+z}\Big)\frac{d\lambda}{1+z}\frac{dt}{1+z} = \frac{1}{4\pi D_L^2} N\Big(\frac{\lambda}{1+z}\Big)\,dtd\lambda. \tag{3.3.9}$$

Now, assume the object is observed with a *photon counting device*, through a filter of transmission function $s(\lambda)$. The apparent luminosity will be

$$\begin{aligned} l_s &= \int_o^\infty n(\lambda)\,s(\lambda)\,d\lambda = \frac{1}{4\pi D_L^2}\int_o^\infty N\Big(\frac{\lambda}{1+z}\Big)\,s(\lambda)\,d\lambda \\ &= \left[\frac{1}{4\pi D_L^2}\int_o^\infty N(\lambda)\,s(\lambda)\,d\lambda\right]\left[\frac{\int_o^\infty N(\frac{\lambda}{1+z})\,s(\lambda)\,d\lambda}{\int_o^\infty N(\lambda)\,s(\lambda)\,d\lambda}\right] \qquad (3.3.10a) \\ &\equiv \frac{l_s^o}{K_s}. \qquad (3.3.10b) \end{aligned}$$

where, l_s^o is the apparent luminosity free of cosmological effect (the first bracket of equation 3.3.10a), and K_s is defined as the K-correction (the inverse of the second

bracket of equation 3.3.10a). The subscript s indicates the s filter. If expressed in magnitudes, the above equation becomes

$$m_s = -2.5\log l_s = -2.5\log l_s^o + 2.5\log K_s = m_s^o + k_s. \tag{3.3.11}$$

The k-term now is

$$k_s = 2.5\log\left[\frac{\int_o^\infty N(\lambda)\,s(\lambda)\,d\lambda}{\int_o^\infty N(\frac{\lambda}{1+z})\,s(\lambda)\,d\lambda}\right] = 2.5\log\left[(1+z)\frac{\int_o^\infty F(\lambda)\,s(\lambda)\,\lambda\,d\lambda}{\int_o^\infty F(\frac{\lambda}{1+z})\,s(\lambda)\,\lambda\,d\lambda}\right], \tag{3.3.12}$$

where $F(\lambda) \equiv \frac{hc}{\lambda}N(\lambda)$, is the energy flux of the object.

If the object is observed with a flux-measuring detector instead, the k-term would become

$$k_s = 2.5\log\left[(1+z)\frac{\int_o^\infty F(\lambda)\,s(\lambda)\,d\lambda}{\int_o^\infty F(\frac{\lambda}{1+z})\,s(\lambda)\,d\lambda}\right]. \tag{3.3.13}$$

Equations (3.3.8) and (3.3.10) show, respectively, how the apparent size and the apparent luminosity of a distant object are affected in an expanding universe. Combining these results, one has the apparent surface brightness,

$$B_s = \frac{l_s}{\Delta\theta^2} = \frac{\frac{l_s^o \cdot D_L^2}{\Delta x^2}}{(1+z)^4 K_s} = \frac{B_s^o}{(1+z)^4 K_s}. \tag{3.3.14}$$

where $B_s^o = \frac{l_s^o \cdot D_L^2}{\Delta x^2}$, is obviously the intrinsic surface brightness of the object. Express (3.3.14) in magnitudes, we have

$$\begin{aligned}\mu_s &= -2.5\log B_s = -2.5\log B_s^o + 10\log(1+z) + 2.5\log K_s \\ &= \mu_s^o + 10\log(1+z) + k_s.\end{aligned} \tag{3.3.15}$$

This implies that the surface brightness correction for cosmological effects, that we are seeking for, is given by

$$A_C = 10\log(1+z) + k_s. \tag{3.3.16}$$

The first term in (3.3.16) partly accounts for the cosmological stretching-effect on the angular size of a distant galaxy, as described by equation (3.3.8). The same stretching-effect stretches the coordinate scale (i.e., semi-major axis) of the surface brightness as well, and should be corrected. A stretching factor of $(1+z)^2$ implies a 6 percent stretch for a galaxy at redshift 0.03, the edge of the current sample. Note that the luminosity distance D_L in equation (3.3.8) is also a function of redshift (see equation [3.3.6]); this redshift dependence of D_L should be taken into account, in order to completely remove the redshift dependence of angular diameter (Lynden-Bell *et al.* 1988). To do this, however, one need to know the value of q_0 in equation (3.3.6). In this thesis, a correction for the factor $(1+z)^2$ will be simply applied on the semi-major axes.

Given the energy spectrum of the object $F(\lambda)$, and the filter transmission function $s(\lambda)$, the k-correction can be numerically calculated at any z. We carried out such calculations for different types of galaxies, at both Cousins I and V bands. In these calculations, the energy distributions of different types of galaxies were taken from Pence (1976); and the I and V filter transmission functions were taken from Bessel and Wickramasinghe (1979), and Azusienis and Straizys (1969), respectively. The I-band and V-band k-corrections for different types of galaxies in the redshift range from 0 to 0.05 are plotted in Figure 3.1 and 3.2, respectively. The solid curves represent the k-corrections for a *photon-counting device* [i.e., equation (3.3.12)], and the dashed curves are the k-corrections for a *flux-measuring device* [i.e., equation (3.3.13)]. The I and V bands photon-counting k-corrections, denoted as k_I and k_V respectively, for different types of galaxies in the redshift range from 0 to 0.03, within which all my thesis galaxies lie, can be well approximated by

$$k_I(T,z) = (0.5876 - 0.1658T)\,z \qquad (3.3.17a)$$

$$k_V(T,z) = (1.9728 - 0.4109T)\,z \qquad (3.3.17b)$$

where T is the morphological code of galaxies according to the RC2 catalog.

Strictly speaking, the energy distribution of a galaxy varies with radial coordinates, and the k-correction on surface brightness profile is thus a function of radius. The k-terms calculated above can be regarded as averages of the complete k-correction over the face of a mean galaxy for each type, since the calculation was based on integrated energy distribution (Pence 1976). From the trend of k-correction for different galaxies shown in Figures 3.1 and 3.2, and the fact that a spiral galaxy is usually bluer at outer part than at the center, it is expected that the k effect is not only to change the zero-point of a profile, but also to reduce the slope of the profile. An upper limit of this slope-shallowing effect can be roughly estimated using the difference of k-corrections between an E galaxy and a Sdm galaxy at the same redshift, which is less than 0.03 mag at I-band for galaxies within redshift 0.03 (Figure 3.1). In this thesis, a constant k-correction given by equation (3.3.17) will be applied to all the profiles.

§3.4 The Seeing Effects

Since the discussion of seeing effects on surface photometry by Schweizer (1979, 1981), the problem has been reinvestigated by a number of authors (e.g., Lauer 1985; Djorgovski 1983; Kormendy 1984; Bendinelli, Parmeggiani & Zavatti 1986; Franx, Illingworth & Heckman 1989). The general conclusion is that the luminosity distribution of a galaxy, primarily its central part, can be greatly smeared by seeing. Correction for these effects, however, is not straightforward, and is usually performed using numerical methods, which can be computationally expensive. Techniques for explicitly performing the correction include, for example, 1) the Fast Fourier transform method (see, e.g., Lauer 1985; Djorgovski 1983); 2) the numerical method of Bendinelli, Parmeggiani & Zavatti (1986); or, 3) the iterative technique

developed by Lucy (1974) for general deconvolution problems.

Analytical treatment, by contrast, usually requires a form of the intrinsic luminosity profile, which is not known *a priori*. But the analytical approach is very useful for model analysis, and may help to reveal more about the seeing problem in general. Below, I consider the effects of a circular symmetric PSF on the surface brightness profile, and derive a general analytical expression for the seeing correction on the surface brightness profile and the ellipticity profile.

a) Analytical Analysis

The PSF is assumed to be circularly symmetric, and denoted as $f(r)$. The n^{th} moment of f is defined as

$$F_n = \int_0^{2\pi} d\theta \int_0^{\infty} f(r)\, r^{n+1}\, dr = 2\pi \int_0^{\infty} f(r)\, r^{n+1}\, dr. \tag{3.4.1}$$

The normalization of f requires that $F_0 = 1$.

Let $j(x, y)$ represent the true intensity distribution of a galaxy, and assume that the isophotes are concentric ellipses with constant ellipticity ϵ_0. Denote the major axis intensity profile as $J(a^2)$, where a is the semi-major axis. Then

$$J(a^2) = j(x, y) \tag{3.4.2}$$

and

$$a^2 = x^2 + q_0^2\, y^2, \tag{3.4.3}$$

where $q_0 = (1 - \epsilon_0)^{-1}$ is the major-to-minor axial ratio of the ellipses.

The observed intensity distribution $i(x, y)$ is given by the convolution of $j(x, y)$ with the PSF. Making use of the circular symmetry of the PSF, we have,

$$\begin{aligned} i(x, y) &= \int_0^{2\pi} d\theta \int_0^{\infty} j(x', y') f(r) r\, dr \\ &= \int_0^{2\pi} d\theta \int_0^{\infty} J(a_0^2) f(r) r\, dr, \end{aligned} \tag{3.4.4}$$

with

$$\begin{aligned} x' &= x + r\,\cos\theta \\ y' &= y + r\,\sin\theta \end{aligned} \tag{3.4.5}$$

and

$$a_0^2 = x'^2 + q_0^2\,y'^2 = (x + r\,\cos\theta)^2 + q_0^2\,(y + r\,\sin\theta)^2. \tag{3.4.6}$$

The variation of the observed intensity $i(x,y)$ with eccentric anomaly ϕ along a pre-defined ellipse

$$a^2 = x^2 + q^2y^2 \tag{3.4.7}$$

is obtained by replacing x, y in equations (3.4.4), (3.4.5) and (3.4.6) with the following (i.e., equation (2.3))

$$\begin{aligned} x &= a\,\cos\phi \\ y &= a/q\,\sin\phi \end{aligned} \tag{3.4.8}$$

and we get

$$i(a,\phi) = \int_0^{2\pi} d\theta \int_0^{\infty} J(a_0^2) f(r) r\,dr \tag{3.4.9}$$

with

$$a_0^2 = a^2 + \Delta(a,r,\theta,\phi) \tag{3.4.10}$$

and

$$\Delta(a,r,\theta,\phi) = (\frac{q_0^2}{q^2} - 1)a^2\sin^2\phi + 2a\,r\,(\cos\theta\cos\phi + \frac{q_0^2}{q}\sin\theta\sin\phi) + r^2(\cos^2\theta + q_0^2\sin^2\theta) \tag{3.4.11}$$

Now assume $J(a_0^2)$ can be expanded around a^2 as power series in Δ,

$$J(a_0^2) = J(a^2) + \sum_{n=1}^{\infty} \frac{1}{n!} J^{(n)}(a^2)\,\Delta^n. \tag{3.4.12}$$

Equation (3.4.9) then becomes

$$i(a,\phi) = J(a^2) + \sum_{n=1}^{\infty} \frac{1}{n!} J^{(n)}(a^2) \int_0^{2\pi} d\theta \int_0^{\infty} \Delta^n f(r) r\,dr. \tag{3.4.13}$$

Where the condition for normalization of PSF, i.e., $F_0 = 1$, was used. $J^{(n)}(a^2)$ is the n^{th} derivative of $J(a^2)$ with respect to a^2. If the ellipse defined by equation (3.4.7)

represents a real isophote of the observed intensity distribution $i(x,y)$, then equation (3.4.13) would be independent of ϕ, and would give the observed 1-dimensional intensity profile $I(a^2)$. Operationally, $I(a^2)$, and the isophotal ellipses are found by fitting equation (2.2), so that the harmonic coefficients A_1, A_2, B_1, and B_2 vanish (see the discussion in §2.4). This fitting procedure is equivalent to requiring

$$A_n = \frac{1}{\pi}\int_0^{2\pi} i(a,\phi)\sin n\phi d\phi = 0; \qquad n = 1,2 \qquad (3.4.14a)$$

$$B_n = \frac{1}{\pi}\int_0^{2\pi} i(a,\phi)\cos n\phi d\phi = 0; \qquad n = 1,2 \qquad (3.4.14b)$$

$$I(a^2) = \frac{1}{2\pi}\int_0^{2\pi} i(a,\phi)d\phi. \qquad (3.4.14c)$$

Equations (3.4.14a) and (3.4.14b) define the isophotal ellipse, and (3.4.14c) gives the observed intensity profile. Approximating $i(a,\phi)$ to the second order in Δ in equation (3.4.13), and performing the integration in equations (3.4.14a-c), we found that A_1, A_2, and B_1 are naturally zero as expected, because these coefficients are only sensitive to the center and the position angle of the ellipse, which have been fixed in equation (3.4.7). The requirement of $B_2 = 0$ defines the observed ellipticity, $\epsilon = 1 - 1/q$, as such that,

$$\frac{a^2}{F_2}(\frac{q_0^2}{q^2} - 1)^2 + \left[\frac{2J'}{J''F_2} + (1 + 3q_0^2)\right](\frac{q_0^2}{q^2} - 1) + 2(q_0^2 - 1) = 0. \qquad (3.4.15)$$

Ignoring the first term in the above equation, which is of second order in $(q_0^2/q^2 - 1)$, we then have,

$$q_0^2/q^2 = 1 + \frac{2(1 - q_0^2)}{1 + 3q_0^2 + \frac{2J'}{J''F_2}}. \qquad (3.4.16)$$

Finally, after performing the integration in (3.4.14c), and making use of equation (3.4.16), we have the observed intensity profile, to second order in Δ.

$$I(a^2) = J(a^2) + \left[a^2J'' + \frac{(1 + q_0^2)}{2}J'\right]F_2 + \frac{3}{16}(1 + \frac{2}{3}q_0^2 + q_0^4)J''F_4. \qquad (3.4.17)$$

The above derivation for $I(a^2)$ follows the procedure of practical operation, and illustrates the concept of the ellipse fitting technique discussed in §2.4. As a matter of fact, one can directly integrate equation (3.4.13), and calculate $I(a^2)$ to any order in Δ. It is noted that, by setting $\phi = 0$, equation (3.4.13) just gives the observed intensity distribution along the major axis, i.e.,

$$\begin{aligned} I(a^2) &= i(a,0) \\ &= J(a^2) + \sum_{n=1}^{\infty} \frac{1}{n!} J^{(n)}(a^2) \int_0^{2\pi} d\theta \int_0^{\infty} [2a\,r\,\cos\theta + r^2(\cos^2\theta + q_0^2 \sin^2\theta)]^n f(r) r\, dr \end{aligned} \tag{3.4.18}$$

The integration over θ in the above equation can be done by using the Cauchy Residue Theorem. The final result is,

$$I(a^2) = J(a^2) + \sum_{n=1}^{\infty} \frac{2\pi a^n}{n!} J^{(n)}(a^2) \int_0^{\infty} f(r) r^{n+1} \beta_0^n\, dr, \tag{3.4.19}$$

where the coefficients β_0^n is given by the following iterative relation

$$\beta_m^{n+1} = \sum_{k=-2}^{2} \beta_k^1 \beta_{m-k}^n \tag{3.4.20a}$$

with

$$\begin{aligned} \beta_0^1 &= \frac{r}{2a}(1+q_0^2) \\ \beta_1^1 &= \beta_{-1}^1 = 1 \\ \beta_2^1 &= \beta_{-2}^1 = \frac{r}{4a}(1-q_0^2) \end{aligned} \tag{3.4.20b}$$

It is seen that β_0^n is basically a polynomial function of r, the 1-D integration in equation (3.4.19) is therefore a sum of the moments of the PSF as given in equation (3.4.1). As long as the PSF is known, equation (3.4.19) can be used to estimate $I(a^2)$ to any order. It is not difficult to verify that, if approximated to the second order in β_0, equation (3.4.19) just reduces to (3.4.17).

The above analytical treatment of the seeing effects is useful for model analysis of the effects, but is not appropriate for the purpose of practical correction for

seeing, because we have to invert (3.4.19) to find J, which is not easy to do (see, e.g., Bendinelli, Parmeggiani & Zavatti 1986).

b) Numerical Simulation

Numerical simulation was performed using equation (3.4.9), for a pure exponential disk galaxy, i.e., an intrinsic intensity profile of the form $\exp(-r/r_0)$, and with a Gaussian PSF, $f(r) = (2\pi\sigma^2)^{-1}\exp(-r^2/2\sigma^2)$. It is easy to verify that the FWHM of a Gaussian PSF is equal to 2.36σ. The simulation was done with four different inclination angles of the model galaxy: 0°, 45°, 75° and 90°, and with four values of FWHM: 0.1, 0.3, 0.5 and 0.7, in units of r_0. The change of surface brightness profile of the model galaxy is shown in Figure 3.3 and 3.4, which group the results according to inclination and FWHM, respectively. We can also estimate the seeing effects on ellipticity by performing the simulation along both major and minor axes. Figure 3.5 shows the relative change of ellipticity with semi major axis for different FWHM's and for different inclination angles of the model galaxy.

The major conclusion drawn from Figures 3.3, 3.4 and 3.5 is that seeing can have significant effects on the intensity and ellipticity of the inner region of a disk galaxy, and such effects strongly depend on galaxy inclination. For our sample galaxies, the estimated value of FWHM/r_o peaks around 0.2. and in the worst case it could be as large as 1. However, a large value of FWHM/r_o is always due to small value of r_o, which means that a galaxy with larger FWHM/r_o also has larger apparent radius measured in units of r_o (see Chapter 4) The effect of seeing on the outer part of SB profile (of interest in this thesis, see Chapter 4). for the galaxies of our sample is estimated, in the worst cases, to be around 0.2 mag/arcsec^2, and is expected to be under 0.1 mag/arcsec^2 for most of our galaxies.

It is interesting to compare the simulation results with the prediction given by

the second order approximation of equation (3.4.17). The comparison is made for a disk model galaxy at different inclination angles and using different FWHM values. The seeing corrections on surface brightness profile, given by equation (3.4.17) and the simulation are presented in Figure 3.6a,b. The dashed lines represent the prediction by equation (3.4.17) and the solid lines are the simulation just performed. Figure 3.6a shows how the agreement varies with FWHM/r_o for a disk galaxy at constant inclination 45°, and Figure 3.6b shows the dependence of the agreement on inclination for a constant FWHM/r_o of 0.3. Clearly, the prediction by second order approximation of equation (3.4.17) becomes worse at smaller radii, especially in the case of large inclination angle and large FWHM/r_o value. This is primarily owing to the mathematical properties of an exponential profile — it is not well approximated by a Taylor series of equation (3.4.12) near $r = 0$ (at $r = 0$, the derivatives become infinite).

We did the same experiment using a model galaxy with Hubble profile, i.e. $J(r) \sim (1 + r^2/r_o^2)^{-1}$, which is better behaved than an exponential profile in terms of a Taylor expansion. Figure 3.7 compares the second order approximation (3.4.17) with a simulation for such a model galaxy at inclination = 45°, and using three values for FWHM/r_o. The agreement is much better now.

Again, it should be noted that our discussion above illustrates the importance of seeing effects on surface photometry of disk galaxies of different inclination and size, but does not give any correction formulae directly applicable for real galaxies. In the following discussions in this thesis, I will choose not to make corrections for seeing effects, and will only consider those integrated properties of galaxies which are less affected by seeing and are just what we need for the purpose of this thesis.

REFERENCES FOR CHAPTER 3

Azusienis, A. and Straizys, V. 1969, *Soviet Astronomy AJ*, **13**, 316.

Bendinelli, O. Parmeggiani, G. and Zavatti, F. 1986, *Ap. J.*, **308**, 611.

Bessel, M. S. and Wickramasinghe, D. T. 1979, *Ap. J.*, **227**, 232.

Burstein, D. and Heiles, C. 1978, *Ap. J.*, **225**, 40.

Burstein, D. and Heiles, C. 1984, *Ap. J. Suppl.*, **54**, 33.

Burstein, D. 1990, private communication.

Djorgovski, S. 1983, J. Astr. Ap., **4**, 271.

Fernie, J. D. 1983, *Pub. A. S. P.*, **95**, 782.

Franx,M., Illingworth, G. D. and Heckman, T. M. 1989, *A. J.*, **98**, 538.

Gunn, J. E. and Oke, J. B. 1975, *Ap. J.*, **195**, 255.

Johnson, H. L. 1968, in *Nebulae and Interstellar Matter*, ed. B. Middlehurst and L. Aller (Chicago: University of Chicago Press), p.167.

Kormendy, J. 1984, *Ap. J.*, **295**, 73.

Lauer, T. R. 1985, *Ap. J. Suppl.*, **57**, 473.

Lucy, L. B. 1974, *Ap. J.*, **79**, 745.

Lynden-Bell, D. *et al.* 1988, *Ap. J.*, **326**, 19.

Pence, 1976, *Ap. J.*, **203**, 39.

Sandage, A. 1973, *Ap. J.*, **183**, 711.

Schneider, D. P., Gunn, J. E. and Hoessel, J. G. 1983, *Ap. J.*, **264**, 337.

Weinberg, S. 1972, *Gravitation and Cosmology*, (New York).

Figure Captions for Chapter 3

Figure 3.1: I-band k-corrections, for different types of galaxies and different detectors, as a function of radial velocity.

Figure 3.2: V-band k-corrections, for different types of galaxies and different detectors, as a function of radial velocity.

Figure 3.3: Simulation of seeing effects on the surface brightness profiles of e-disk galaxies: each panel shows the effects of different seeing (FWHM) on a galaxy viewed at a given inclination angle.

Figure 3.4: Simulation of seeing effects on the surface brightness profiles of e-disk galaxies: each panel shows the effects of a constant FWHM on a galaxy of different inclination angles.

Figure 3.5: Simulation of seeing effects on the ellipticity profile of e-disk galaxies: relative ellipticity change is plotted against semi-major axis (in units of disk-scale length), for galaxies of different (true) inclinations, and for different seeing values.

Figure 3.6a: Effects of seeing on surface brightness profile — compare the results of simulation (solid line) and the second order approximation (dashed line) given by eq. (3.4.17), for an e-disk galaxy at inclination 45°, and with four different values of seeing.

Figure 3.6b: Effects of seeing on surface brightness profile — compare the results of simulation (solid line) and the second order approximation (dashed line) given by eq. (3.4.17), for an e-disk galaxy at four different inclinations, and with a constant value of seeing.

Figure 3.7: Effects of seeing on surface brightness profile — compare the results of simulation (solid line) and the second order approximation (dashed line) given by eq. (3.4.17) for a galaxy with Hubble-profile, and at inclination of 45°.

Figure 3.1

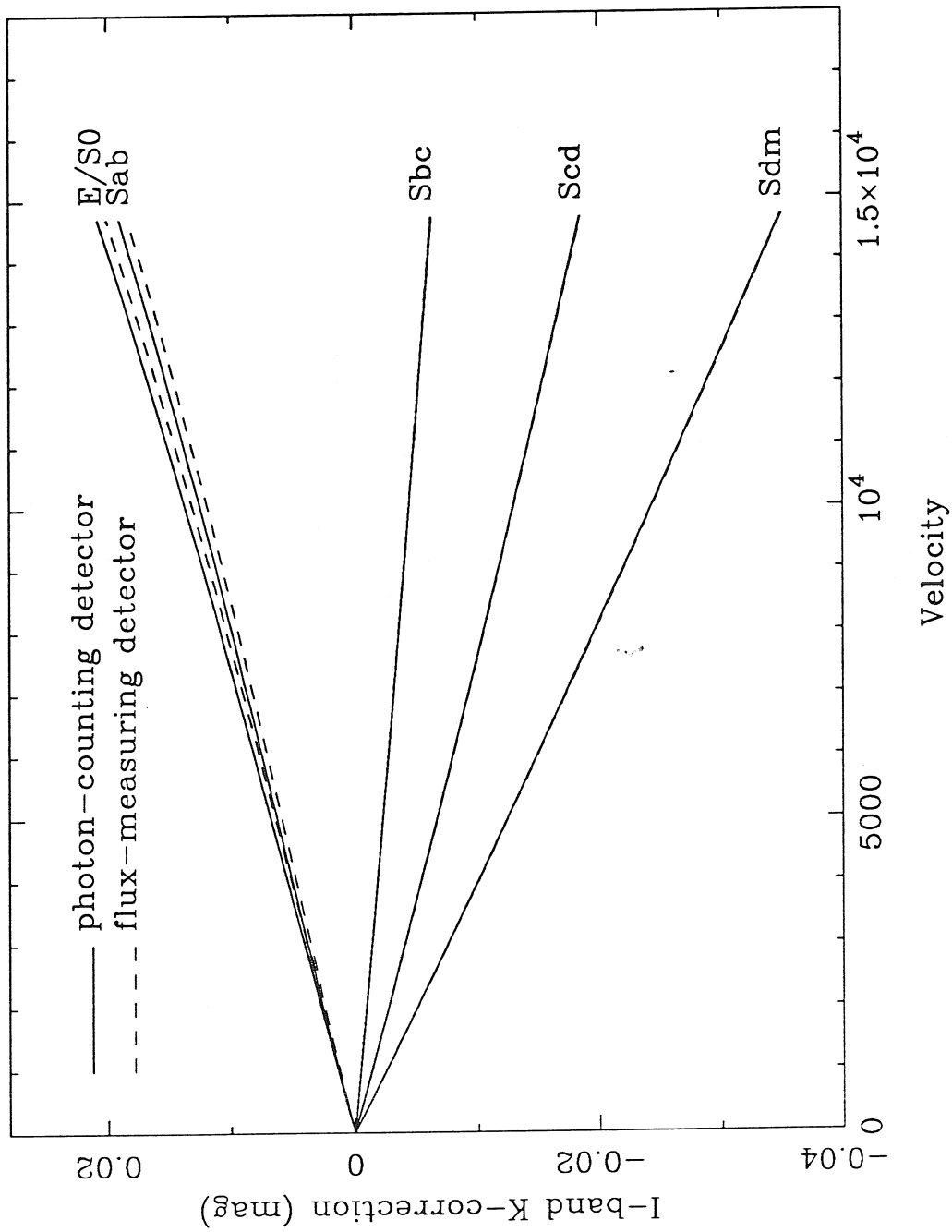
E/S0
Sab
Sbc
Scd
Sdm
photon−counting detector
flux−measuring detector
I−band K−correction (mag)
0.02
0
−0.02
−0.04
0
5000
10^4
1.5×10^4
Velocity

Figure 3.2

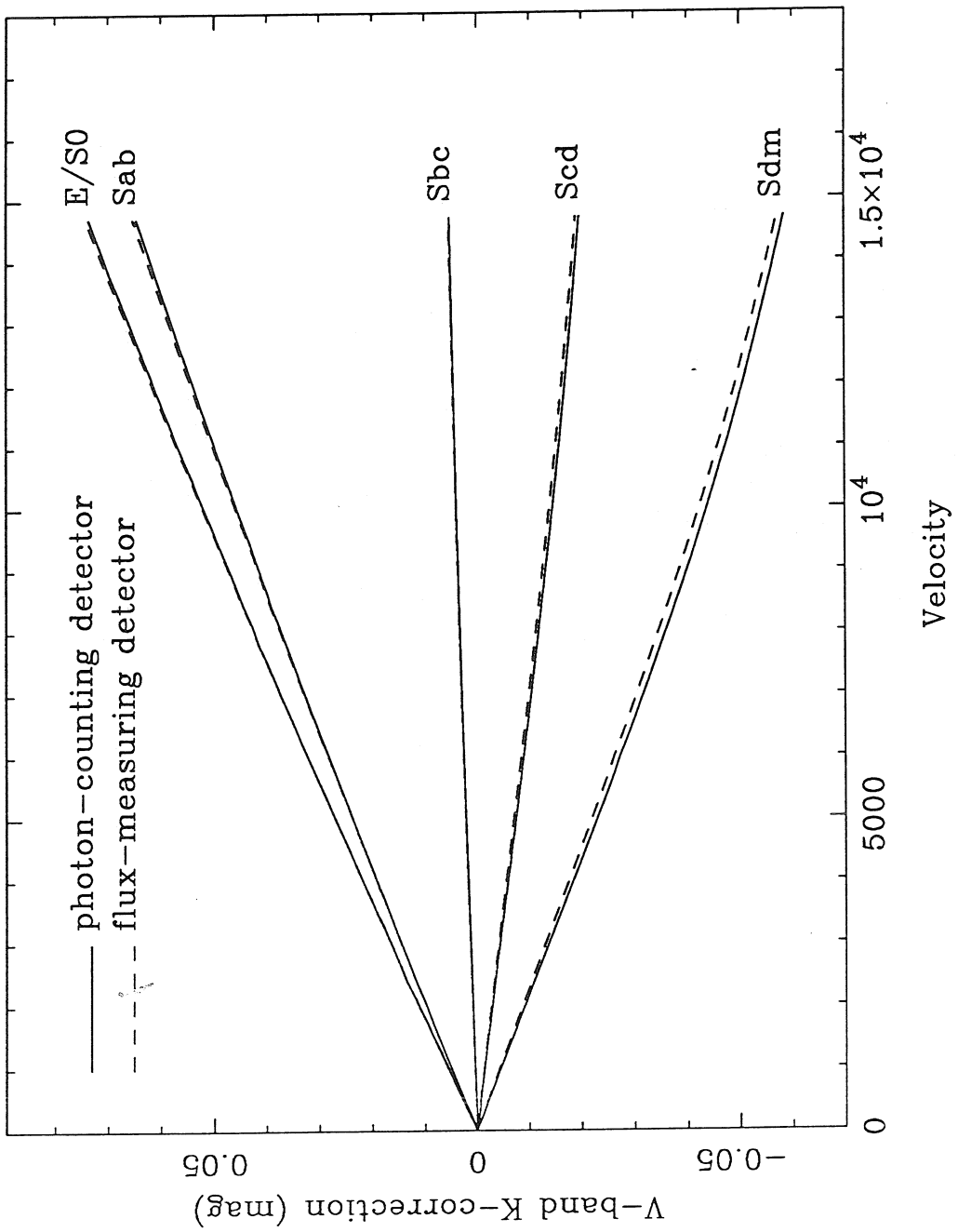
E/S0
Sab
Sbc
Scd
Sdm
photon–counting detector
flux–measuring detector
V–band K–correction (mag)
0.05
0
–0.05
0
5000
10^4
1.5×10^4
Velocity

Figure 3.3

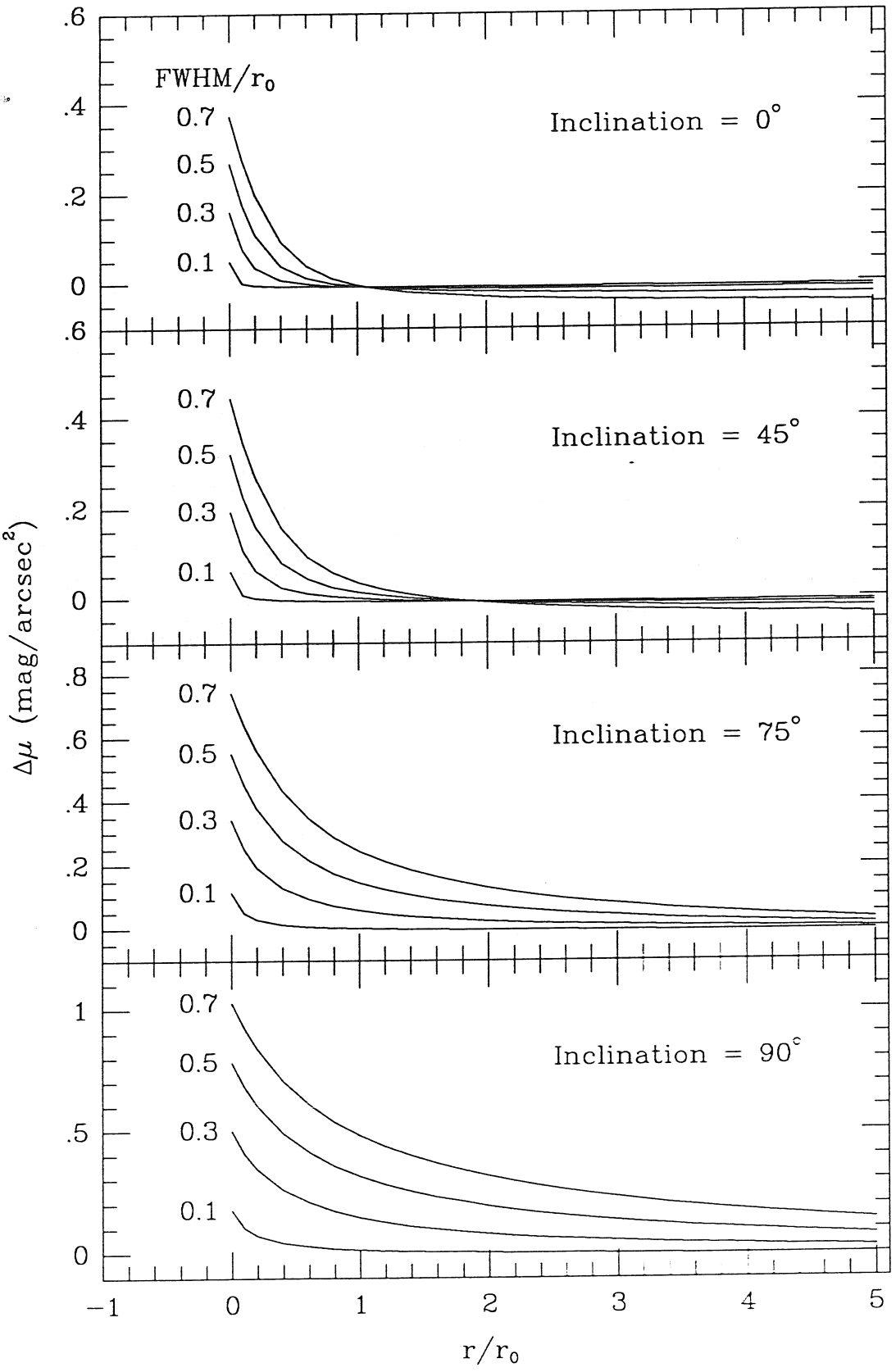
FWHM/r0
0.7
0.5
0.3
0.1
Inclination = 0°
Inclination = 45°
Inclination = 75°
Inclination = 90°
Δμ (mag/arcsec²)
r/r0
.6
.4
.2
0
.8
1
.5
−1
2
3
4
5

Figure 3.4

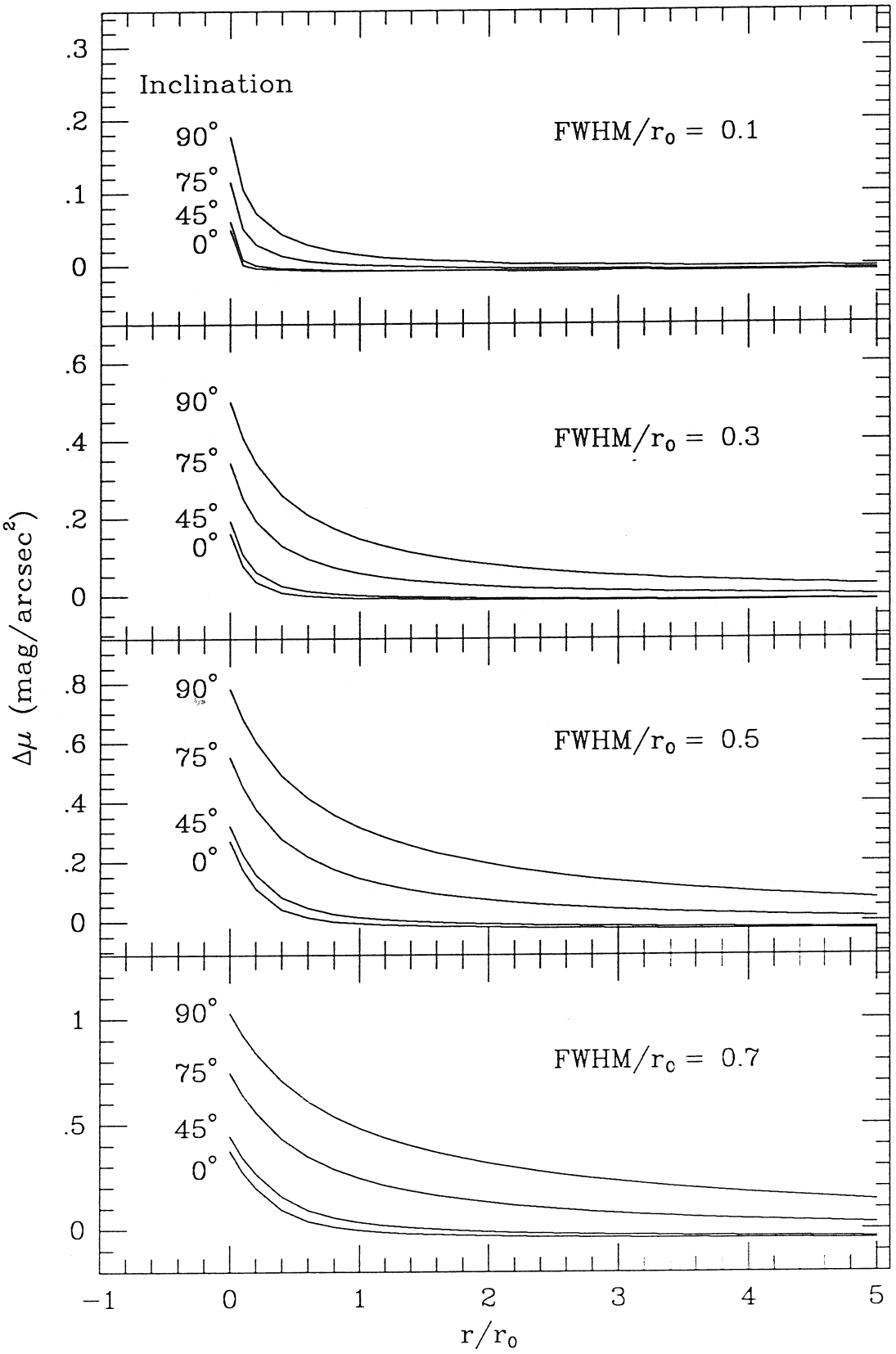
Inclination
90°
75°
45°
0°
FWHM/r0 = 0.1
FWHM/r0 = 0.3
FWHM/r0 = 0.5
FWHM/r0 = 0.7
Δμ (mag/arcsec²)
r/r0
.3
.2
.1
0
.6
.4
.2
0
.8
.6
.4
.2
0
1
.5
0
−1
0
1
2
3
4
5

Figure 3.5

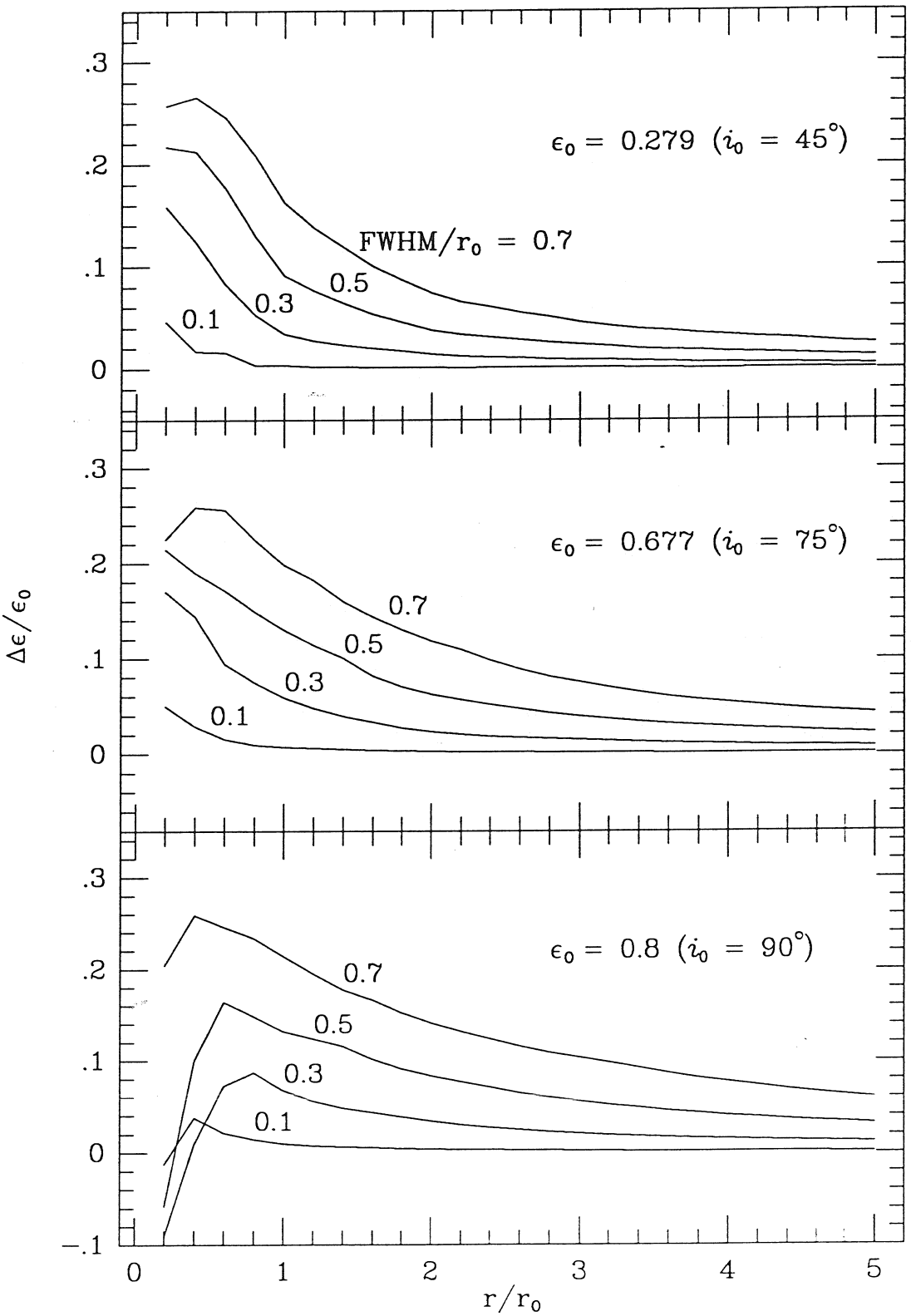
ϵ_0 = 0.279 (i_0 = 45°)
FWHM/r_0 = 0.7
0.5
0.3
0.1
ϵ_0 = 0.677 (i_0 = 75°)
0.7
0.5
0.3
0.1
ϵ_0 = 0.8 (i_0 = 90°)
0.7
0.5
0.3
0.1
$\Delta\epsilon/\epsilon_0$
r/r_0
.3
.2
.1
0
−.1
0
1
2
3
4
5

Figure 3.6

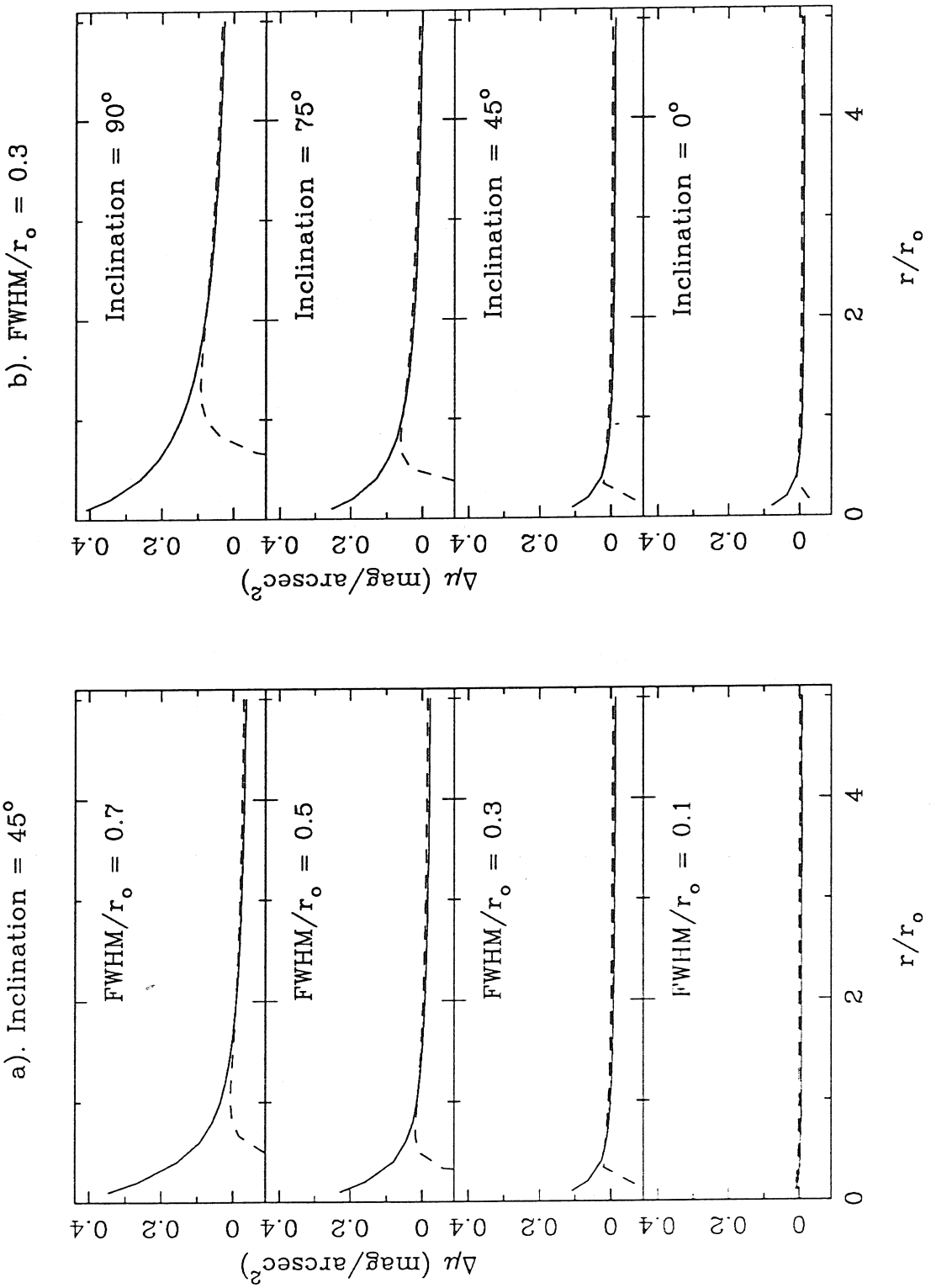
a). Inclination = 45°
FWHM/r$_o$ = 0.7
FWHM/r$_o$ = 0.5
FWHM/r$_o$ = 0.3
FWHM/r$_o$ = 0.1
Δμ (mag/arcsec^2)
r/r$_o$
b). FWHM/r$_o$ = 0.3
Inclination = 90°
Inclination = 75°
Inclination = 45°
Inclination = 0°
Δμ (mag/arcsec^2)
r/r$_o$

Figure 3.7

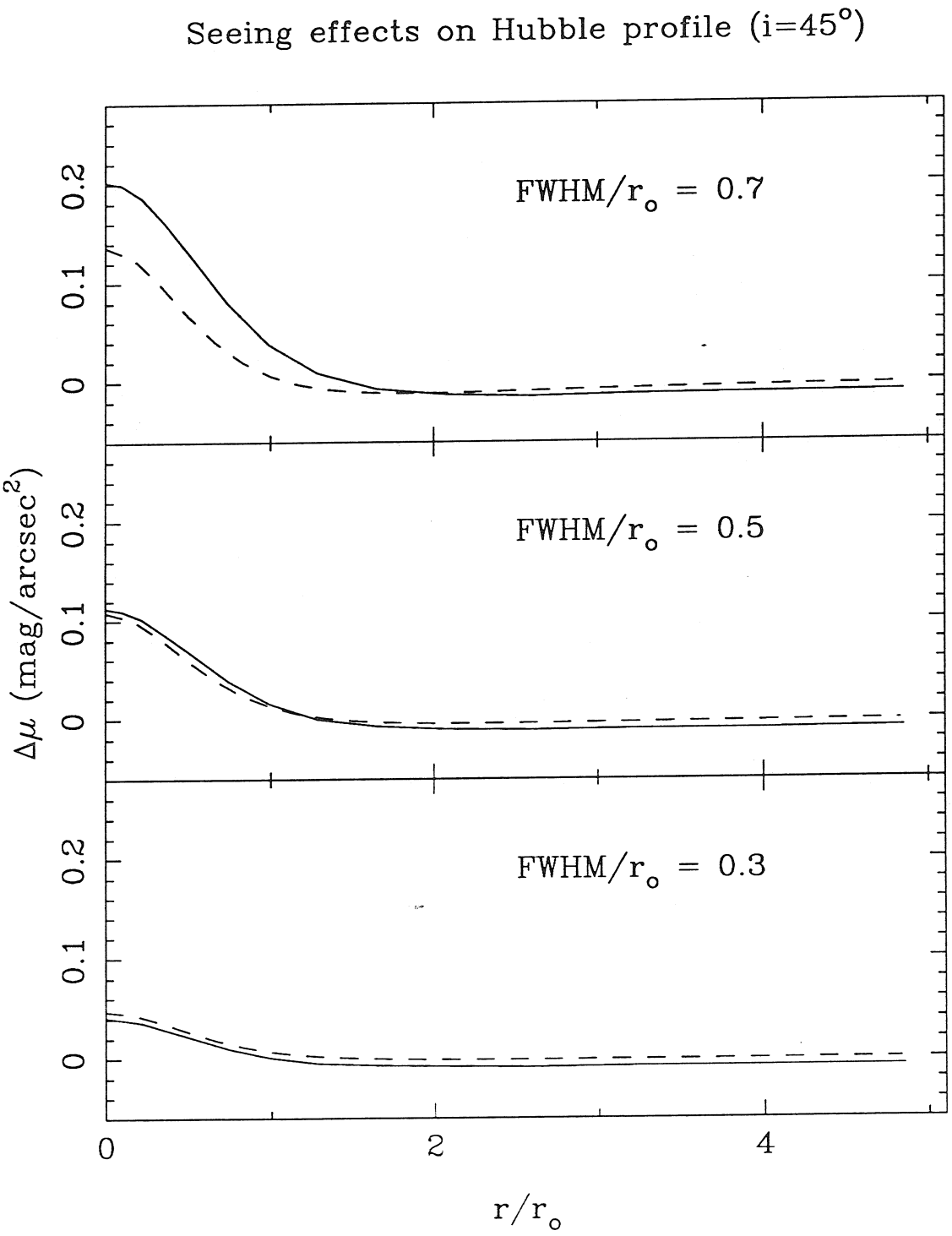
Seeing effects on Hubble profile (i=45°)
FWHM/r$_o$ = 0.7
FWHM/r$_o$ = 0.5
FWHM/r$_o$ = 0.3
Δμ (mag/arcsec^2)
r/r$_o$
0
0.1
0.2
2
4

CHAPTER IV

THE INTERNAL EXTINCTION IN SPIRAL GALAXIES

§4.1 Introduction

From the optical point of view, a galaxy can be regarded as being composed of two kinds of matter: stars, which emit optical light; and dust, which absorbs and scatters the optical light. To study the photometric properties of galaxies in the optical range, it is essential to remove the effects of dust. The direct observational information we obtain from surface photometry of a galaxy is its *apparent* light distribution (i.e., surface brightness profile), and also the *apparent* magnitude and *apparent* size. We need to know how these properties are changed by the dust in the galaxy.

Since the studies of Holmberg (1958, 1975), it has been generally accepted that spiral galaxies are optically rather thin. However, this conventional view has recently been challenged by a number of investigators. Disney, Davies and Phillipps (1989) first showed that the data used by Holmberg could be equally well explained by optically thick models, and there were no good observational data against the hypothesis that spirals are optically thick. Valentijn (1990), using a very large sample of about 16000 galaxies, provides evidence for optically thick spiral disks. If the discs of galaxies are indeed optically thick, much of our understanding about spiral galaxies will have to be reviewed (Davies 1990; Disney, Davies and Phillipps 1989). It is interesting to note that our own Galaxy is not optically very thick, at least at the position of the solar system.

The optical light absorbed by dust ought to be reemitted in the far infrared region; therefore, a detailed investigation of the effects of dust on the photometric

properties of galaxies has to involve the study of far infrared properties of galaxies. However, we do not yet have a complete picture of galaxies in the FIR, although the IRAS data, which is sensitive only to the warmer component of dust, provides part of the information. A complete study is thus awaiting for further extensive observations in the sub-millimeter region, which best measures the radiation of cooler dust. The infrared perspective on dust in galaxies has been reviewed by Joseph (1988), based on the IRAS data.

Studies of the extinction problem from optical bases have also been conducted. van Houten (1961) considered the dust influence on the observed light distribution of galaxies using simple models and derived expressions for the intensity of scattered light in optically thin layers. Elmegreen (1980) studied individual dust complexes in face-on spiral galaxies. Kylafis & Bahcall (1987) and Byun & Freeman (1990) have investigated the extinction problem for simple models of the dust and stellar distributions, by explicitly solving the radiative transfer problem including both scattering and pure absorption. A less model-dependent approach to the galactic extinction problem is to statistically study the dependence of the apparent optical properties of galaxies on inclination for a large galaxy sample, because dust extinction is supposed to make a galaxy look different when viewed at different inclination angles. This is a cheaper way to investigate the dust effects. However, as pointed out by Disney, Davies and Phillipps (1989), this method is not sensitive to the total absorption, but it is suitable for studying the absorption relative to a face-on view. A number of authors have utilized this method to study the extinction problem and derived magnitude corrections relative to the face-on case (Holmberg 1958; Holmberg 1975; Heidmann, Heidmann and de Vaucouleurs 1972; Tully and Fouque 1985; Kodaira & Watanabe 1988).

Although a great deal of effort has been made in understanding the dust effects on optical properties of galaxies, the subject still remains very controversial, and does not seem to get enough attention in general. For example, the commonly

adopted magnitude correction for internal absorption in the literature largely relies on the RC2 catalogue and the *Revised Shapley-Ames Catalogue of Bright Galaxies* (Sandage & Tammann 1981), which in turn lean heavily on the study of Holmberg (1958) and Heidmann, Heidmann & de Vaucouleurs (1972). The amplitude of such corrections as employed by different investigators can differ by a factor of 2 or more, and there is even an obvious mistake often seen in literature in the case of applying the magnitude corrections for internal absorption (see discussion in §4.4). Below, I re-examine the dust effects on optical properties of spiral galaxies using the surface photometry data of the galaxies in the sample of this thesis. An empirical correction for diameter is derived using a new statistical method; corrections for magnitude and color (to the face-on case) are also derived, and relevant problems are discussed.

§4.2 Effects of Dust on Surface Brightness Profile and Isophotal Diameter

It is expected that a spiral galaxy, observed at different inclination angles, would show different apparent surface brightness profiles, owing to the effects of projection, i.e., pure geometrical brightening, and to internal dust extinction. Let $\mu^i(r)$ be the apparent major surface brightness profile of a galaxy at inclination i, and $\mu^0(r)$ be its face-on surface brightness profile. In general, $\Delta\mu(i,r) = \mu^i(r) - \mu^0(r)$ is a function of both i and r. For a dust free disk galaxy,

$$\Delta\mu = -2.5 \log R \tag{4.1}$$

where R is the (major to minor) axis ratio. It is interesting to see what $\Delta\mu(i,r)$ would be for real spiral galaxies.

In order to study the dust effect on SB profiles, one certainly needs to filter away all other possible effects, which distort the profile. As we learned in Chapter 3, the seeing smearing effect could significantly distort the SB profile, especially in the inner part of the profile, and it strongly depends on inclination. This suggests that the seeing effects have to be properly handled in our analysis using the inclination approach. In principle, seeing effects could be well corrected (see section

§3.3 for more discussion), and the study of dust effects on the SB profiles should be performed after the seeing effects have been corrected for. In this thesis, however, I bypass this approach, and perform some simple tests on the outer part of SB profiles, where the seeing effects are small.

To study of the systematic behavior of the outer part of the SB profile with inclination, one needs to quantify the (outer part) profile in some uniform manner. The fact that most of the profiles show extended "flat tails" in their outer part suggests an analytical function of the e-disk form, i.e.,

$$\mu^i(r) = \mu_0^i + \alpha^i r \tag{4.2}$$

for the flat part of the profiles. It should be pointed out that this form is just for a convenient mathematical representation of the shape of the SB profile at the outer part, and it is not the concern here as to whether or not it coincides with the physical disk component. All we need is a reasonable assumption that the form of this representation is invariant with inclination; in other words, the outer flat part of the SB profile of a galaxy remains flat when viewed at different inclination angle, but with different zero-point and slope (μ_0^i and α^i), due to dust extinction and geometrical projection.

The flat part of a profile can be easily defined by visually inspecting the profile for each galaxy (see Figure 5.1). Most of the sample galaxies show very well behaved flat tails. Equation (4.2) is fitted to the identified flat part, which gives the parameters α^i and μ_0^i for each galaxy. The variation of these two parameters tells us how the SB profile in the outer part is affected by dust.

Because α^i is a distance-dependent parameter, its dependence on inclination is subject to large noise from distance variation in the sample galaxies. Ideally, one could scale α^i using a suitably defined metric scale (which must be independent of inclination), and then study the dependence of such scaled α on inclination. This will remove the scatter introduced by distance, and may also reduce the intrinsic

galaxy-to-galaxy variation of α due to different luminosity distributions in galaxies. However, it is almost impossible to define such a (inclination-independent) metric scale from the photometric data (e.g., the SB profile itself) which is subject to inclination effects. To see how α^i varies with inclination, I simply scaled the α^i values of cluster member galaxies using mean cluster distances adopted from Aaronson (1986, 1989). Figure 4.1 shows the plot of such scaled α against inclination; no clear correlation is seen in the plot. The preliminary conclusion is thus: the dust effects on the slope of outer part SB profile of a galaxy is not sensitive to the inclination angle of the galaxy.

In contrast, the parameter μ_0^i, which is distance independent, shows strong dependence on inclination. In Figure 4.2, μ_0^i is plotted against the logarithm of axial ratio (those galaxies with $\log R > 0.7$ are plotted at $\log R = 0.7$, same below), The best linear fit to the data is given by,

$$\mu_0^i = 20.03(\pm 0.24) - 1.90(\pm 0.22)\ \log R. \tag{4.3}$$

This equation implies that the outer flat part of the SB profile of a galaxy becomes brighter with increasing inclination. However, comparing equation (4.3) with (4.1), we find that the rate of this brightening (i.e., the slope of the equation) is about 75% of that expected for a sample of dust-free galaxies, and the difference is significant at 3 σ level. This is explained by the effect of dust absorption; that is, at least in the outer part of a disk galaxy, the amount of absorption relative to its face-on value is, on average,

$$\Delta\mu_d(i, r) = 0.6 \log R. \tag{4.4}$$

It should be noted that this equation is based on the outer part of the SB profiles, typically beyond two thirds of the apparent size of a galaxy, and thus may not apply in the inner part of disk. It would be interesting to further study the behavior of $\Delta\mu_d$ at the inner disk, which, as pointed out above, requires the seeing effects being well removed. A complete knowledge of $\Delta\mu_d(i, r)$ at all radii r, would allow us to calculate the total light absorption relative to face-on, $\Delta m(i)$. For example,

if equation (4.4) applies at the inner part of a galaxy as well, then the internal absorption to the total light (at I band), relative to the face-on case, would also be $\Delta m(i) = 0.6 \log R$.

It is naturally expected that the $\Delta\mu_d - \log R$ (or $\mu_0^i - \log R$) relation should also have some dependence on galaxy type. The galaxies in the current sample are mostly of type 3 to 5; type dependence of the $\mu_0^i - \log R$ relation is indeed noticeable, though with large uncertainty. This is demonstrated in Figure 4.3, where the best fitting slope for galaxies in a range of different types is plotted against the number weighted mean type value. The trend of this variation indicates that early type galaxies are more affected by dust than late type galaxies *in the outer part of the disk*. Based on Figure 4.3, I will adopt the following formula for inclination corrections of the (outer part) SB profiles of spiral galaxies,

$$\Delta\mu(i,r) = C(T) \log R \tag{4.5a}$$

with

$$C(T) = \begin{cases} -1.8, & 0 \le T \le 3 \\ -2.0, & 4 \le T \le 5 \\ -2.3, & T \ge 6 \end{cases} \tag{4.5b}$$

Once we know how the surface brightness of a galaxy changes with inclination, we can then use it to predict the change of isophotal radius of a galaxy with inclination. If A^i is the radius, corresponding to a constant SB level. of a galaxy observed at inclination i, and A^0 is its face-on value, then equation (4.5) implies,

$$\frac{A^0 - A^i}{r_o} = 0.92\, C(T) \log R = \begin{cases} -1.65 \log R, & 0 \le T \le 3 \\ -1.93 \log R, & 4 \le T \le 5 \\ -2.12 \log R, & T \ge 6 \end{cases} \tag{4.6a}$$

where r_o is an equivalent disk scale-length, calculated using the slope (α^i) of the surface brightness profile at a given radius, i.e., $r_o = 1.086/\alpha^i$. Similarly, for a

dust-free galaxy, i.e., $C(T) = -2.5$, we have

$$\frac{A^0 - A^i}{r_o} = -2.3 \log R \tag{4.6b}$$

Note that the right-hand-side of equation (4.6a) represents the SB variation with inclination *averaged within a given galaxy type range*, while the left-hand-side is a similar quantity for an individual galaxy. Direct application of this formula to individual galaxies may yield large accidental errors, especially for those galaxies which have extreme apparent r_o's, or for very small galaxies whose r_o's may suffer large seeing bias. A further "polishing" is thus made by replacing A^i/r_o in the equation with the median value of the corresponding galaxies in each type range. Figure 4.4 shows the distribution of $A^i_{23.5}/r_o$ for the sample galaxies in each of the three type ranges ($A_{23.5}$ refers to isophotal level of 23.5 mag/arcsec^2). The median value of $A^i_{23.5}/r_o$ is found to be 4.58 for galaxies of type 0-3, 4.45 for galaxies of type 4-5, and 3.76 for galaxies of type 6 and later. Substituting these median values for $A^i_{23.5}/r_o$ in equation (4.6a), we then have,

$$\frac{A^0}{A^i} = \begin{cases} 1 - 0.36 \log R, & 0 \le T \le 3 \\ 1 - 0.43 \log R, & 4 \le T \le 5 \\ 1 - 0.55 \log R, & T \ge 6 \end{cases} \tag{4.7}$$

This equation gives a simple correction of isophotal radius at $\mu_I = 23.5$ mag/arcsec^2. In Figure 4.5, equation (4.7) is compared with the RC2 formula,

$$\log A^0 = \log A^i - 0.235 \log R \tag{4.8}$$

which refers to the isophote of $\mu_B = 25.0$ mag/arcsec^2, and crudely corresponds to $\mu_I \lesssim 23.5$ mag/arcsec^2 (note that the coefficient in the RC2 formula above may depends on wavelength band). The dotted line represents the RC2 formula, and the solid lines show the predictions of equation (4.7).

The general agreement between equation (4.7) and the RC2 formula is not bad. The most significant difference between the RC2 formula and equation (4.7)

might be the conceptual fact that equation (4.7) (or equation [4.6a]) depends on galaxy type, i.e., the luminosity distribution, while the RC2 formula just predicts the same correction for any galaxies of same inclination. It is easy to imagine that a realistic diameter correction for inclination should be dependent on the luminosity distribution of the galaxy. In fact, the form of the RC2 formula was based on a theoretical formula derived for dust-free galaxies by Heidmann, Heidmann and de Vaucouleurs (1972), in which they assumed the 3-D luminosity distribution had a power law form r^n. The coefficient of $\log R$ in the correction formula is just given by $(n-1)^{-1}$, which is generally not a constant, unless all galaxies have same luminosity distribution. If, instead of making any specific assumption about the 3-D luminosity distribution, one simply uses the empirical 2-D luminosity distribution, i.e., e^{-r/r_o}, for disk galaxies, then from the model of Heidmann, Heidmann and de Vaucouleurs (1972), one directly gets equation (4.6b) for the diameter correction of dust-free galaxies.

A more direct comparison between RC2 and equation (4.7) is presented in Figure 4.6, where the predicted face-on radii $A^0_{2.35}$ for our sample galaxies using the two formulae are plotted one against another.

§4.3 Magnitude Correction for Internal Absorption

We define mean surface brightness as follows:

$$\Sigma^i_{23.5} = I^i_{23.5} + 5 \log A^0_{23.5} \tag{4.9}$$

where $I^i_{23.5}$ and $A^0_{23.5}$ are, respectively, the *apparent* I isophotal magnitude and the face-on isophotal radius at $\mu_I = 23.5$ mag/arcsec based on equation (4.7). $I^i_{23.5}$ is corrected for Galactic absorption and k-term as explained in §3.3. In Figure 4.7, $\Sigma^i_{23.5}$ is plotted against $\log R$ for the sample galaxies. Galaxies in the type ranges 0 - 3, 4 - 5, and 6 - 10 are represented with different symbols (solid circle, star, and

open circle). A straight line fit to the data in each type range yields,

$$\Sigma^i_{23.5} = \begin{cases} 20.15(\pm 0.07) + 0.73(\pm 0.16)\log R, & 0 \leq T \leq 3 \\ 20.32(\pm 0.09) + 0.90(\pm 0.18)\log R, & 4 \leq T \leq 5 \\ 20.79(\pm 0.14) + 0.51(\pm 0.23)\log R, & T \geq 6 \end{cases} \tag{4.10}$$

The decrease of the mean surface brightness with inclination shown in Figure 4.7 and equation (4.10) is believed to be caused by the internal absorption of galaxies. Equation (4.10) thus implies a correction to the isophotal magnitude $I_{23.5}$, for internal absorption, of the same amount:

$$\Delta I = \begin{cases} 0.73(\pm 0.16)\log R, & 0 \leq T \leq 3 \\ 0.90(\pm 0.18)\log R, & 4 \leq T \leq 5 \\ 0.51(\pm 0.23)\log R, & T \geq 6 \end{cases} \tag{4.11}$$

A number of points should be noted regarding our analysis above and the results expressed in equations (4.7) and (4.11).

1) Clearly, the basic idea in our derivation of the two equations is to construct a photometric quantity, and then see how it varies with inclination. The systematic change with inclination is interpreted as a dust effect. In deriving the radius correction (equation [4.7]), we defined μ^i_o as such a diagnostic quantity (§4.2); while for deriving the magnitude correction (equation [4.11]), we chose the mean surface brightness as such a quantity, as Holmberg (1958) and others did. Burstein (1982) and Tully & Fouque (1985) defined a diagnostic quantity as the surface brightness residual from the mean relation between surface brightness and velocity-width. Such a quantity might be sensitive to the slope of the relation, and also, to the errors in velocity width, which in turn depends on inclination.

2) The underlying assumption that *the apparent variation of a diagnostic quantity with inclination is due to the effect of dust only* may not be true, if the diagnostic quantity is not properly constructed; because there are other effects (like

seeing, as discussed in Chapter 3) which could make the apparent photometric properties of galaxies a strong function of inclination. To ensure equations (4.7) and (4.11) are not biased by seeing effects, we repeated the above analyses with the 100 smallest galaxies excluded from the sample, and derived nearly the same (diameter and magnitude correction) equations for galaxies of the two early type ranges; the result for the late type galaxies ($T \geq 6$) however showed a large deviation, which is believed to reflect statistical fluctuation due to the small number of galaxies in the type range.

3) Because the relative distribution of stars and dust varies with radius within galaxies, the amount of internal absorption should be a function of radius too. To study the differential extinction effect of galaxies using a large surface photometry dataset, it is important to have a well defined scale length, such that it is independent of inclination and best characterizes the relative distribution of dust and stars within the galaxy. It is also helpful with such a scale length to reduce the uncertainties in the above analyses, and to yield a better estimate of the diameter correction (equation [4.7]) and the integrated absorption (equation [4.11]). Unfortunately, it is difficult to define such a scale using the photometric data alone, both because of a lack of the knowledge about the dust distribution in galaxies, and because of other effects on the surface brightness profiles, especially those which are sensitive to inclination, like the seeing effects.

4) Equation (4.11) is our estimate of the correction for internal absorption in spiral galaxies in the I bandpass. Although there is not a critical way of checking its reliability, we do believe it provides a reasonable correction based on two simple straightforward tests. First, the apparent trend of magnitude variation with inclination is well removed by equation (4.11); second, applying this correction reduces the scatter in the Tully-Fisher relation. Comparing our results with other works might provide a good external check. Unfortunately, as far as is known to the author, there is no similar work *in the I bandpass* available in the

literature, and, as discussed below, one should not simply apply an *extinction curve* to scale the internal absorptions at different bandpasses. Equation (4.11) implies that the internal extinction peaks for galaxies of type $4 \sim 5$, which is qualitatively in agreement with the result of IRAS data (Jone & Brink 1987).

5) The correction given by equation (4.11) was derived for isophotal magnitude at the level of $\mu_I = 23.5$. Corrections to magnitudes at other isophotal levels are expected to be different, due to differential dust absorption across a galaxy disk. We will, however, extend the use of (4.11) to the total magnitude. This is not expected to introduce errors of more than the uncertainty in the correction itself, because the mag increment $I_{23.5} - I_{tot}$ for a typical galaxy is only 0.10 mag (see Chapter 5).

6) As discussed in §4.2, if the surface brightness correction (4.5) applies in the inner disk as well, we would predict the magnitude correction to be $(C[T] - 2.5) \log R$, i.e., $0.7 \log R$ for $0 \leq T \leq 3$, $0.5 \log R$ for $4 \leq T \leq 5$, and $0.2 \log R$ for $T \geq 6$. Comparing these with equation (4.11), we may get an idea that early type galaxies ($T \geq 3$), on average, suffer almost equal dust extinction in both inner and outer regions, while late type galaxies seem to be absorbed more in the inner part than in the outer part.

7) In our study, we simply assumed the magnitude correction to face-on value linearly depends on $\log R$, which is the format used in RC2. There are other simple forms seen in the literature, for example, $(\sec i - 1)$ and $\log(\sec i)$, which need a inclination cutoff (usually at $70° \sim 80°$). Tully and Fouque (1985) used a more complicated form based on a simple dust distribution model. Because of the large intrinsic scatter in the photometric parameters, the actual form of the correction formula is usually not very important, at least from a practical point of view.

§4.4 Color Correction for Internal Absorption

The apparent $(V-I)$ integrated color within the isophotal radius of $A_{23.5}$ is plotted against $\log R$ in Figure 4.8 for the sample galaxies. A trend of reddening with inclination is seen, though with large scatter. The best fit to the data yields a color correction to face-on value of

$$\Delta(V-I) = 0.22(\pm 0.09)\,\log R. \tag{4.12}$$

No clear type dependence was found, probably due to large scatter in the data. The plot in Figure 4.8 seems to plateau, or begin to drop beyond $\log R = 0.5$. Applying a straight line fit with maximum cut off at $\log R = 0.5$, will slightly increase the slope to 0.25.

Equation (4.11) and (4.12) imply a relative extinction relation of $\Delta I/\Delta(V-I) = 2.3 \sim 4.1$. This is compared with a value of 1.4 for the ratio as calculated using the theoretical extinction curve of van de Hulst (Johnson 1968). The difference reflects, apart from statistical errors, the relative distribution of dust and stars within galaxies, as demonstrated below.

In general, the face-on correction of magnitude, at a given bandpass X, for internal absorption within a galaxy, is a function of inclination and a typical optical depth τ_X of the absorbing material, i.e.,

$$\Delta X = g(\tau_X, i). \tag{4.13}$$

where the function g depends on the detailed distribution of dust and stars within the galaxy. For a simple *screen dust model*, in which a dust layer with optical depth τ_X lies above all the stars (see, e.g., Disney, Davies & Phillips 1989), g is simply given by,

$$g(\tau_X, i) = 1.086\,\tau_X\,(\sec i - 1). \tag{4.14}$$

For a *Sandwich dust model*, i.e., a slab of stars of thickness 1, has a dust layer of thickness q $(0 \le q \le 1)$ and optical depth τ_X embedded in its center (see, Tully

& Fouque 1985; Disney, Davies & Phillips 1989),

$$g(\tau_X, i) = -2.5 \log\left[\frac{0.5(1-q)(1+e^{-\tau_X \sec i}) + q(1-e^{-\tau_X \sec i})(\tau_X \sec i)^{-1}}{0.5(1-q)(1+e^{-\tau_X}) + q(1-e^{-\tau_X})\tau_X^{-1}}\right]. \tag{4.15}$$

If $\chi(\lambda)$ is the extinction law of dust in the galaxy, i.e.,

$$\tau_\lambda \sim \chi(\lambda), \tag{4.16}$$

an individual star in the galaxy should obey this law (i.e., the extinction of its light is proportional to $\chi[\lambda]$). Equation (4.14) implies that the integrated absorption of a screen dust model also obeys this law, but that of a sandwich model does not, as seen from equation (4.15). Actually, it is easy to prove that the only case for the integrated absorption to satisfy the extinction law of individual stars is that all the stars in the galaxy suffer the same amount of extinction, that is just a screen dust model. The extinction of galaxy light by our own Galaxy, for example, can be well scaled by the extinction law of individual stars, because dust in our Galaxy is just like a screen for other galaxies. As for the internal absorption of galaxies, our data just showed, however, that the integrated absorptions at V and I bands do not follow the general extinction curve of van de Hulst; this indicates that a screen model is not appropriate for disk galaxies, as expected, since not all the stars in a galaxy suffer same amount of extinction as seen by an outside observer. On the other hand, the sandwich model is able to account for the empirical relations of both (4.11) and (4.12) reasonably well, with the two parameters $q \sim 0.5$, and $\tau_B \sim 1.0$ (the optical depth at B band).

A general conclusion is: the integrated absorption in a galaxy does not follow the extinction law that applies to individual stars in the galaxy: instead, the scaling law for the former is largely determined by the relative amount and distribution of stars and dust within the galaxy (i.e., the functional form of g). rather than the extinction law for individual stars which scales τ_X, a variable of g. This is in fact a

quite trivial statement. Unfortunately, most investigators working on the relevant subject have overlooked this fact, and incorrectly employed the extinction law for individual stars to scale the integrated absorptions from one band to another. For example, Aaronson and collaborators, in a series of papers about IR Tully-Fisher relation, have chosen not to make any correction for the internal absorption at H band, believing that the correction at H band is only 10 percent of that at B band according to the extinction curve of van de Hulst (e.g., Aaronson, Huchra & Mould 1979). This could introduce systematic errors in their data. In fact, it is easy to show, using the Sandwich dust model, that the face-on correction for internal absorptions at the H band can be as large as, or even larger than that at B band. For example, for a sandwich model with $q = 0.5$, the ratio of H magnitude correction from 75° to 0° to the corresponding B magnitude correction varies from 0.24 to 1.37 when τ_B increases from 1 to 4! It is worth noticing that the negative detection of strong dependence of $H_{-0.5}$ (as defined by Aaronson *et al.* 1980) on inclination may not be taken as evidence for a negligible internal absorption at H band; this is because the magnitude $H_{-0.5}$ suffers another simple inclination effect due to the use of a finite aperture as discussed by Christensen (1990), which, in contrast to the absorption effect, makes an edge-on galaxy brighter than its face-on identity.

The fact that the integrated light absorption of a galaxy depends on both inclination and the relative distribution of stars and dust within the galaxy may be used to put interesting constraints on the dust distribution in galaxies. For example, as demonstrated above, the integrated absorption at V and I bands as implied by our data simply ruled out the possibility of a screen dust model. In general, for such purposes, one may need to compare and analyze the inclination variations of some carefully defined (extinction-sensitive) photometric parameters *at different bandpasses.*

REFERENCES FOR CHAPTER 4

Aaronson, M., Huchra, J. and Mould, J. 1979, *Ap. J.*, **229**, 1.

Aaronson, M. *et al.* 1986, *Ap. J.*, **302**, 563.

Aaronson, M. *et al.* 1989, *Ap. J.*, **338**, 654.

Burstein, D. 1982, *Ap. J.*, **253**, 539.

Byun,Y. I. and Freeman, K. C. 1990, preprint.

Christensen, J. H. 1990, *M. N. R. A. S.*, **246**, 535.

Davies, J. I. 1990, *M. N. R. A. S.*, **245**, 350.

Disney, M., Davies, J. and Phillips, S. 1989, *M. N. R. A. S.*, **239**, 939.

Elmegreen, D. M. 1980, *Ap. J. Suppl.*, **43**, 37.

Heidmann, J., Heidmann, N. and de Vaucouleurs, G. 1972, *Mem, R. astr. Soc.*, **76**, 121.

Holmberg, E. 1958, *Med. Lunds Astr. Obs.*, Ser. II. No. 136.

Holmberg, E. 1975, *Stars and Stellar Systems*, Vol. IX, eds. Sandage, A. and Kristian, J., University of Chicago.

Johnson, H., J. 1968, in *Star and Stellar Systems.*, Vol. 7, ed. B. M. Middlehurst and L. H. Aller (Chicago: University of Chicago Press), p. 167.

Jone, T. and Brink, K. 1987, in *Star Formation in Galaxies*, ed. C. J. Lansdale Persson (Washington D.C.: NASA), p. 323.

Joseph, R. D. 1988, in *Dust in the Universe*. eds. M. E. Bailey and D. A. Williams. (Cambridge: Cambridge University Press). p. 467.

Kodaira, K. and Watanabe, M. 1988, *A. J.*, **96**, 1593.

Kylafis, N. D. and Bahcall, J. N. 1987, *Ap. J.*, **317**, 637.

Sandage, A. and Tammann, G. A. 1981, *Revised Shapley-Ames Catalogue of Bright Galaxies*, Carnegie Institute, Washington.

Tully, R. B. and Fouque, P. 1985, *Ap. J. Suppl.*, **58**, 67.

Valentijn, E. A. 1990, *Nature*, **346**, 153.

van Houten, C. J. 1961, *Bull. Astr. inst. Netherlands*, **16**, 1.

Figure Captions for Chapter 4

Figure 4.1: Slope of the outer flat part of surface-brightness profile, scaled by cluster distance, is plotted against logarithm of axial ratio (for cluster member galaxies only). The axial ratio is chopped at a minimum value of 0.2 (same below).

Figure 4.2: Zero-point of the outer flat part of surface-brightness profile plotted against logarithm of axial ratio.

Figure 4.3: slope of a linear fit to Figure 4.2 in different type range is plotted against the number-weighted mean type value.

Figure 4.4: Histogram of the ratio $A_{23.5}/r_o$ for galaxies in three type ranges, a) $T \leq 3$, b) $4 \leq T \leq 5$, and c) $T \geq 6$. Where r_o is an equivalent scale-length measured from the outer flat part of surface brightness profile.

Figure 4.5: Comparison between the inclination-correction formula for isophotal radius given by equation (4.7) and that of RC2.

Figure 4.6: Face-on isophotal radii of the sample galaxies as corrected by equation (4.7) vs the corresponding values corrected by RC2 formula.

Figure 4.7: Mean surface brightness defined by equation (4.9) is plotted against logarithm of axial ratio. Galaxies in three different type ranges ($T \leq 3$, $4 \leq T \leq 5$, and $T \geq 6$) are plotted in different symbols.

Figure 4.8: $(V - I)$ color is plotted against logarithm of axial ratio for galaxies of different types.

Figure 4.1

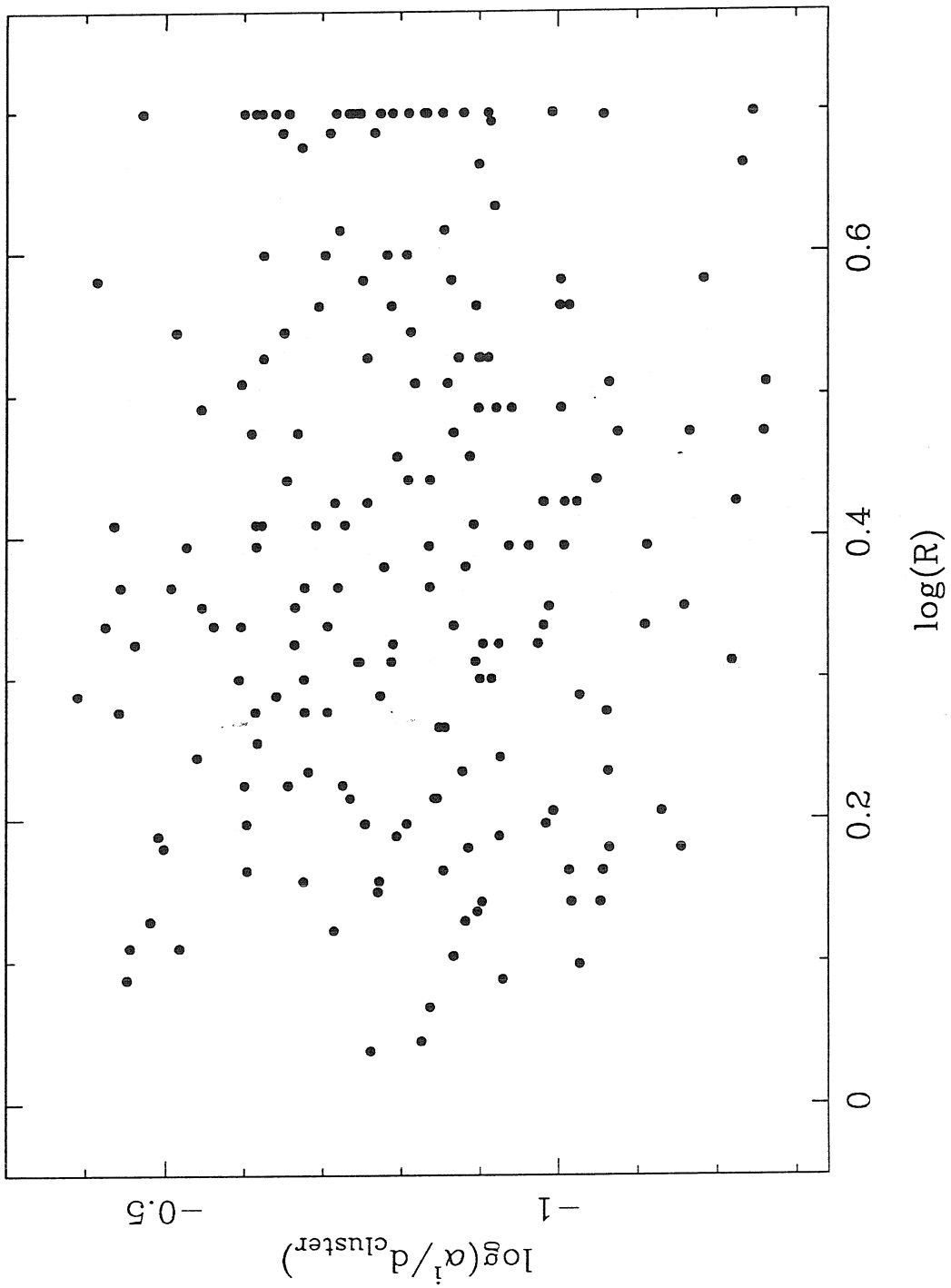

Figure 4.2

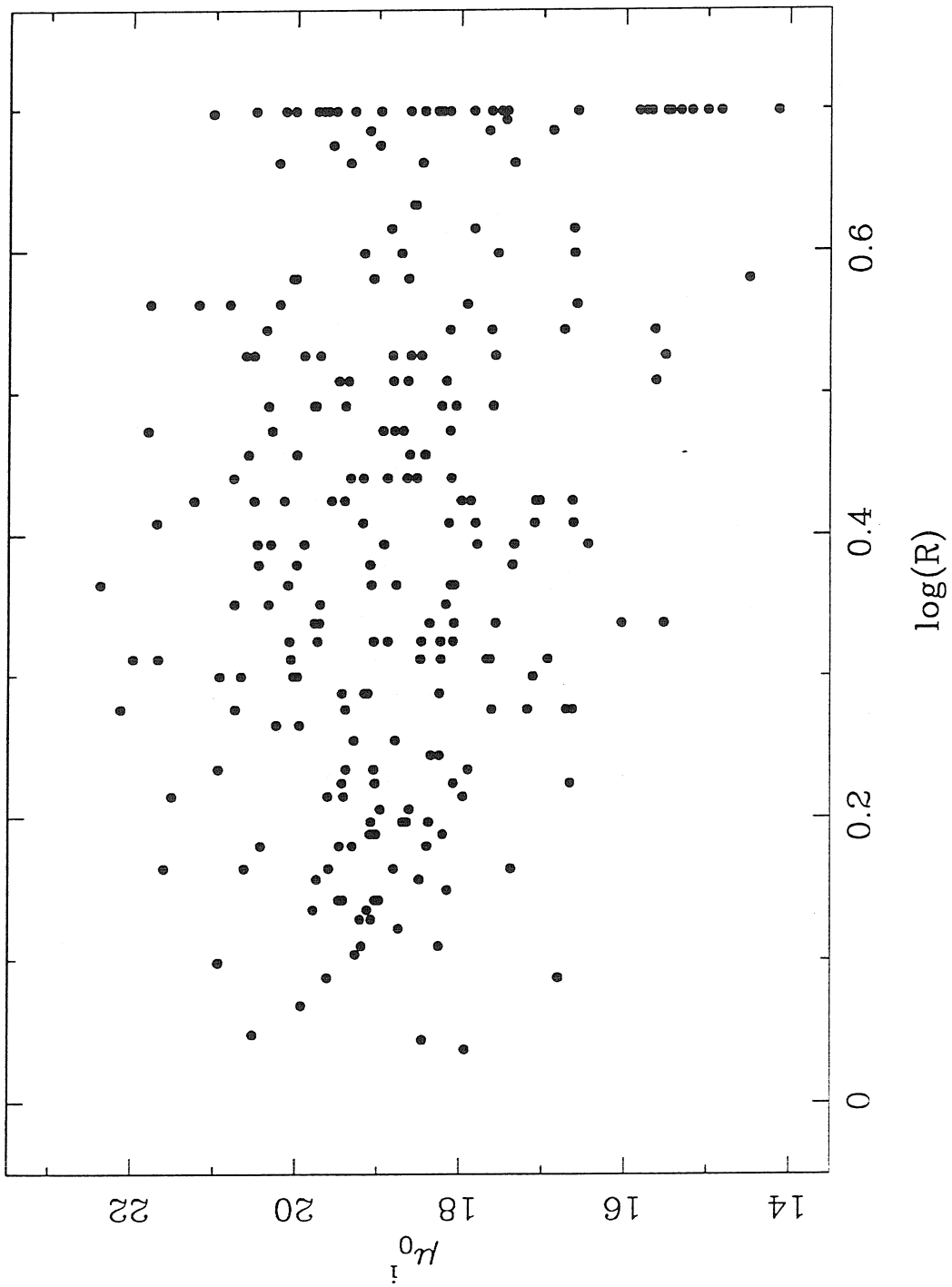

Figure 4.3

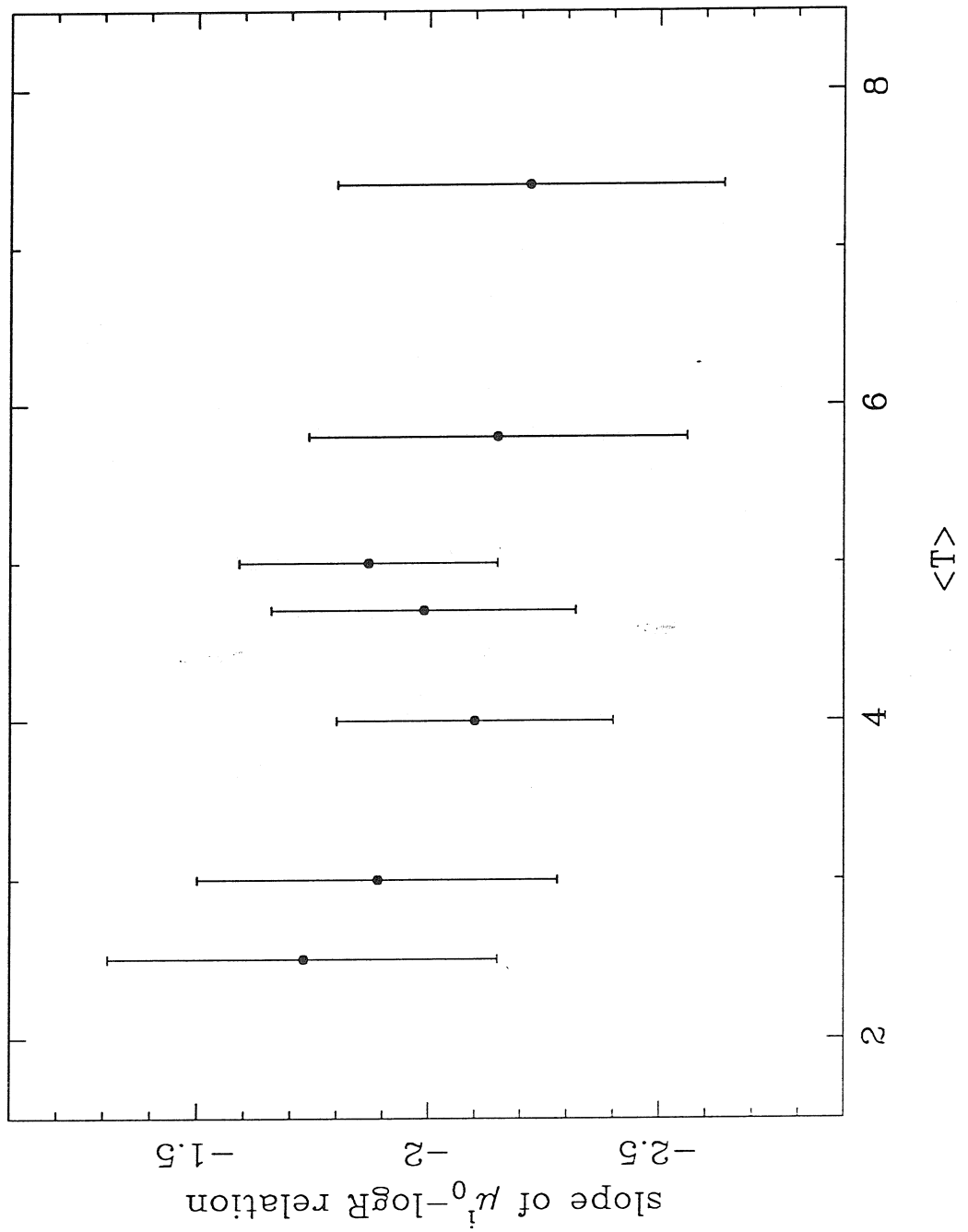

Figure 4.4

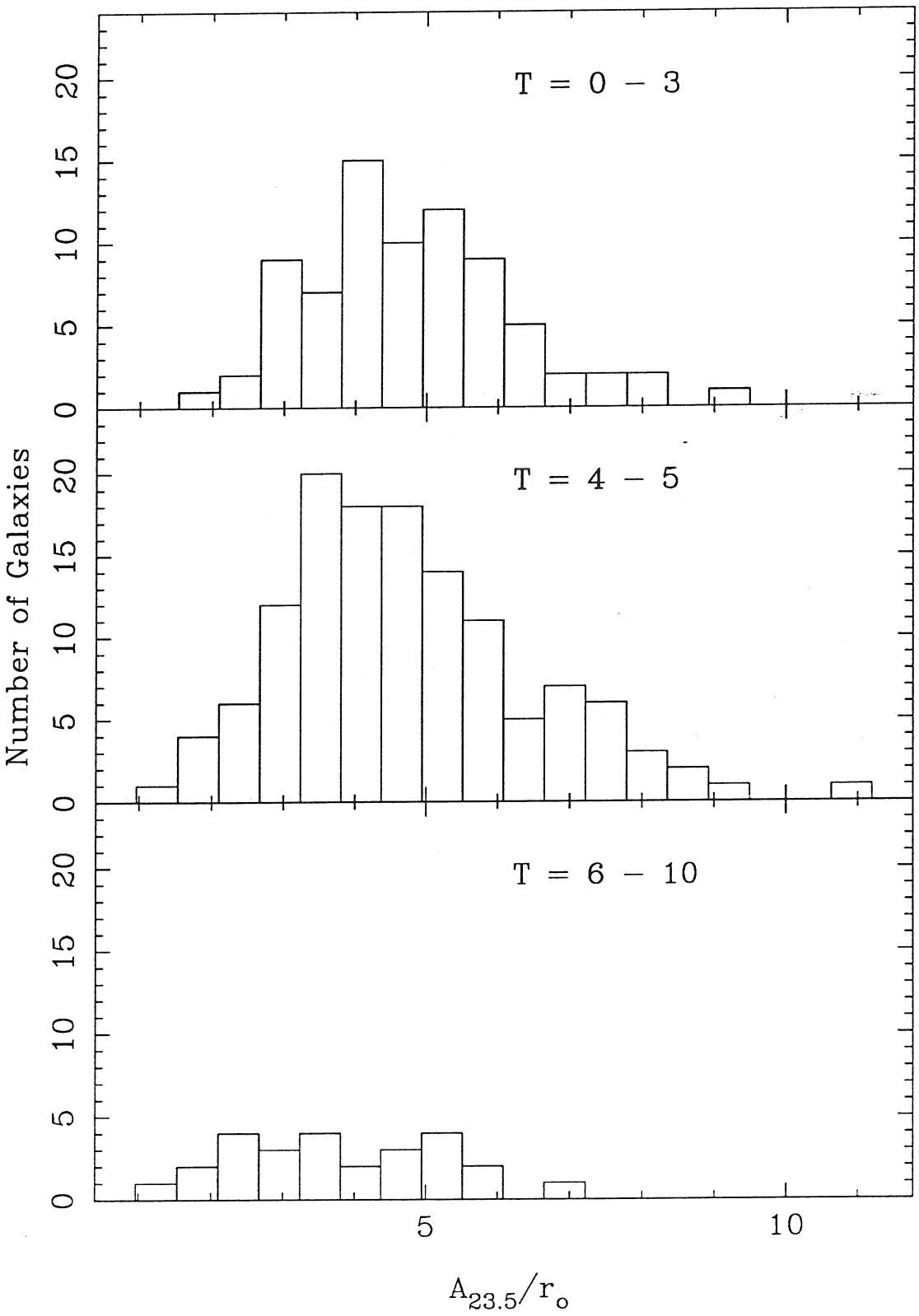

Figure 4.5

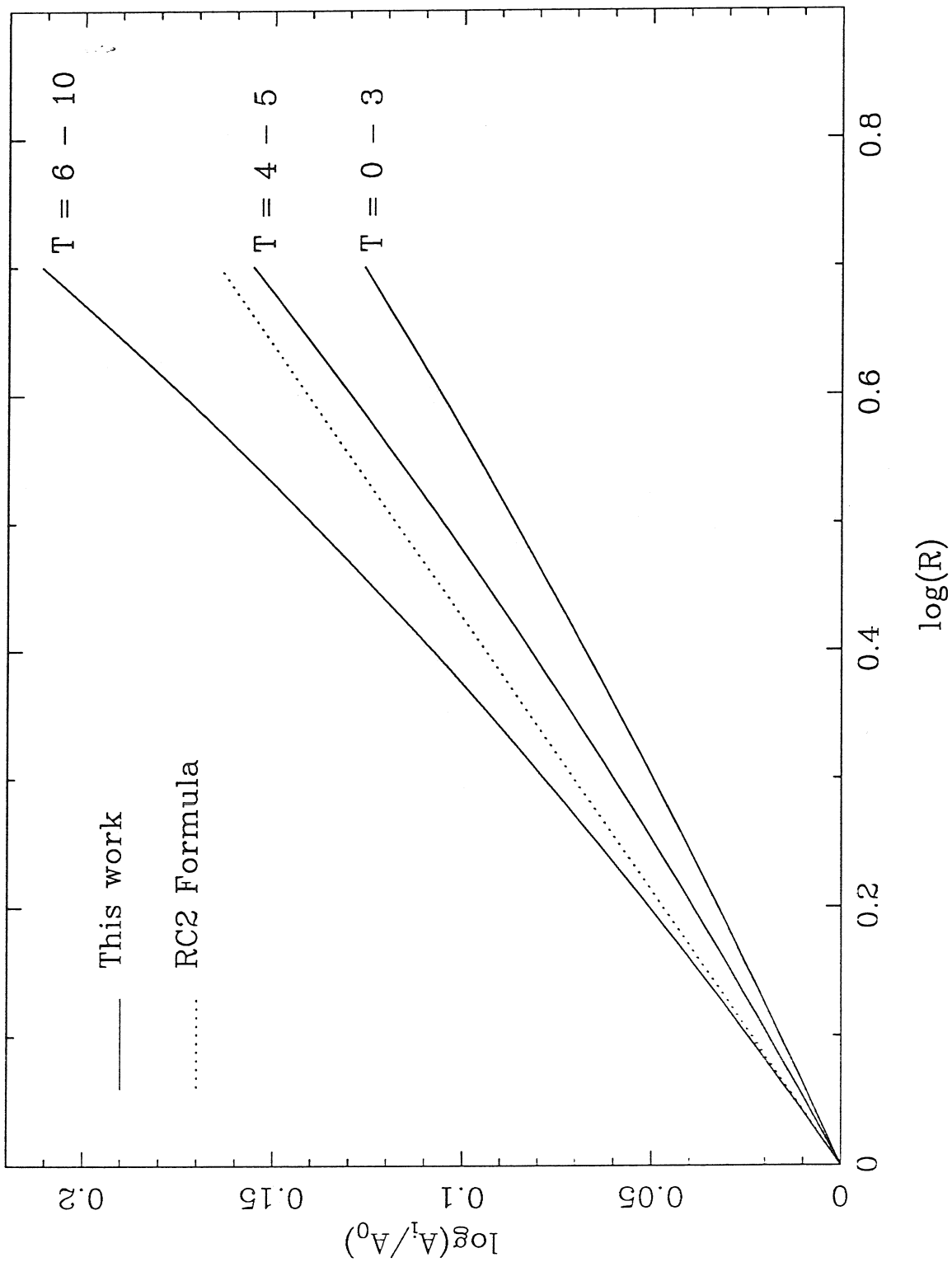
T = 6 – 10
T = 4 – 5
T = 0 – 3
This work
RC2 Formula
log(A_i/A_0)
log(R)
0
0.05
0.1
0.15
0.2
0.2
0.4
0.6
0.8

Figure 4.6

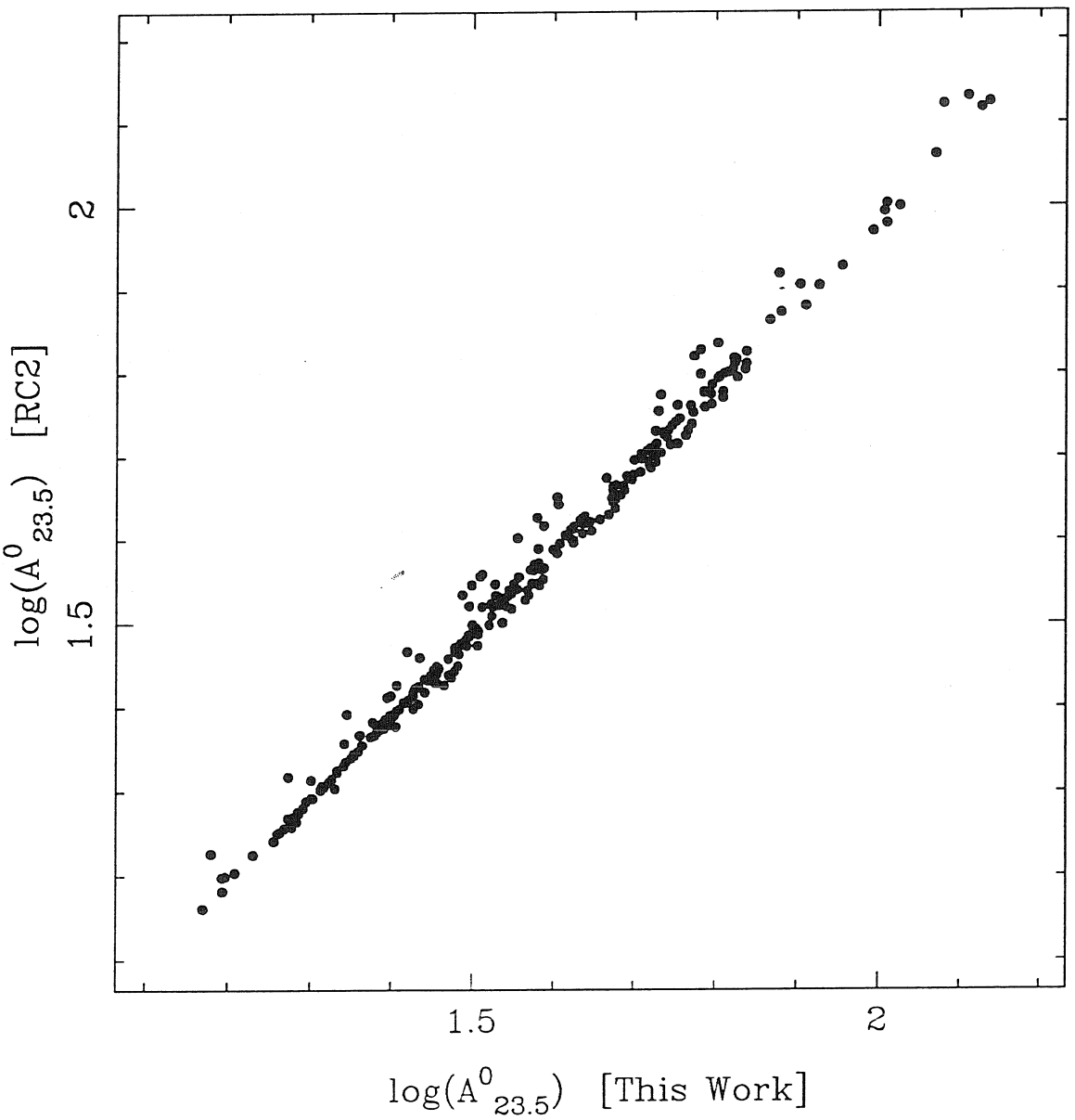

Figure 4.7

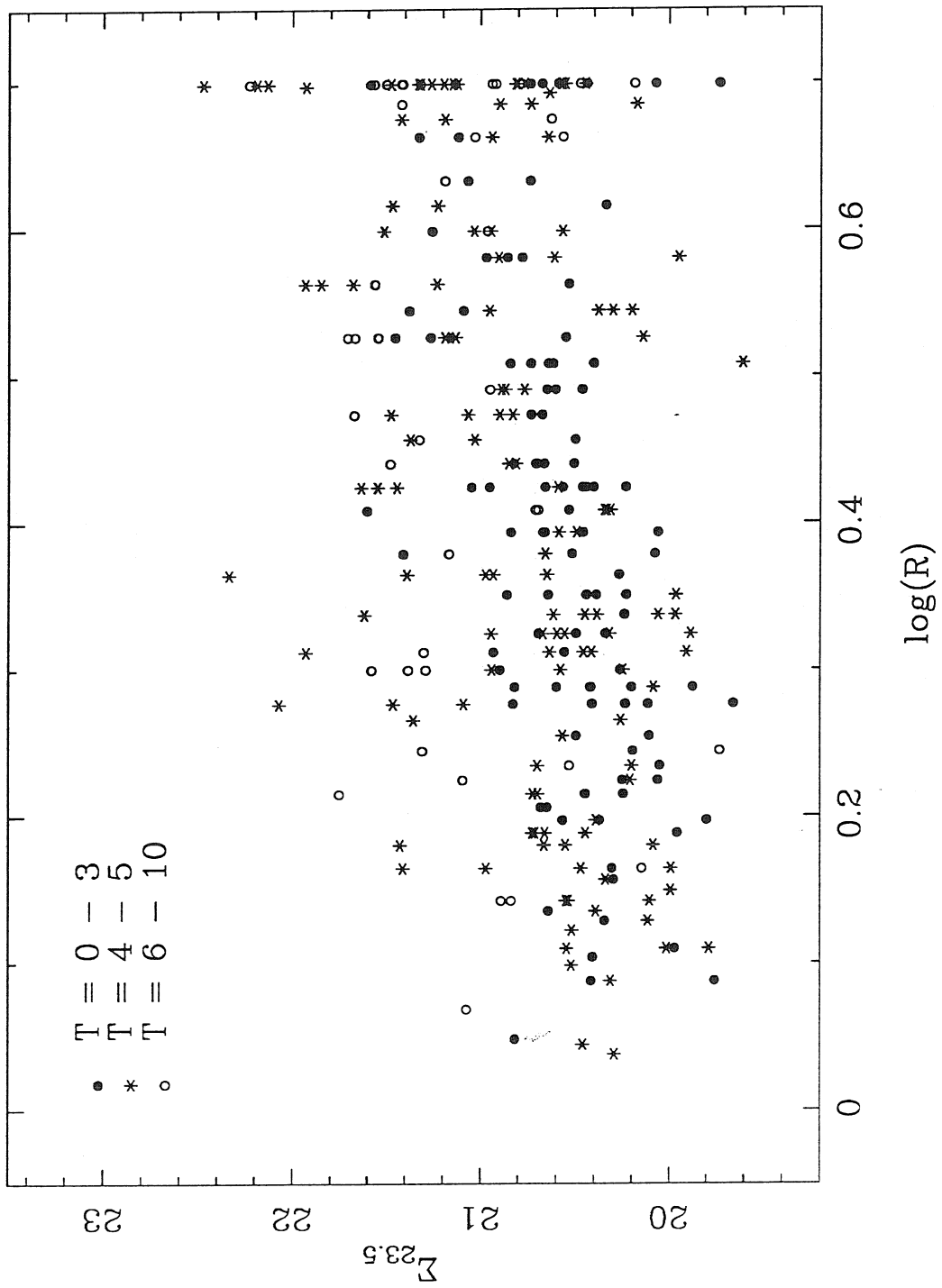

Figure 4.8

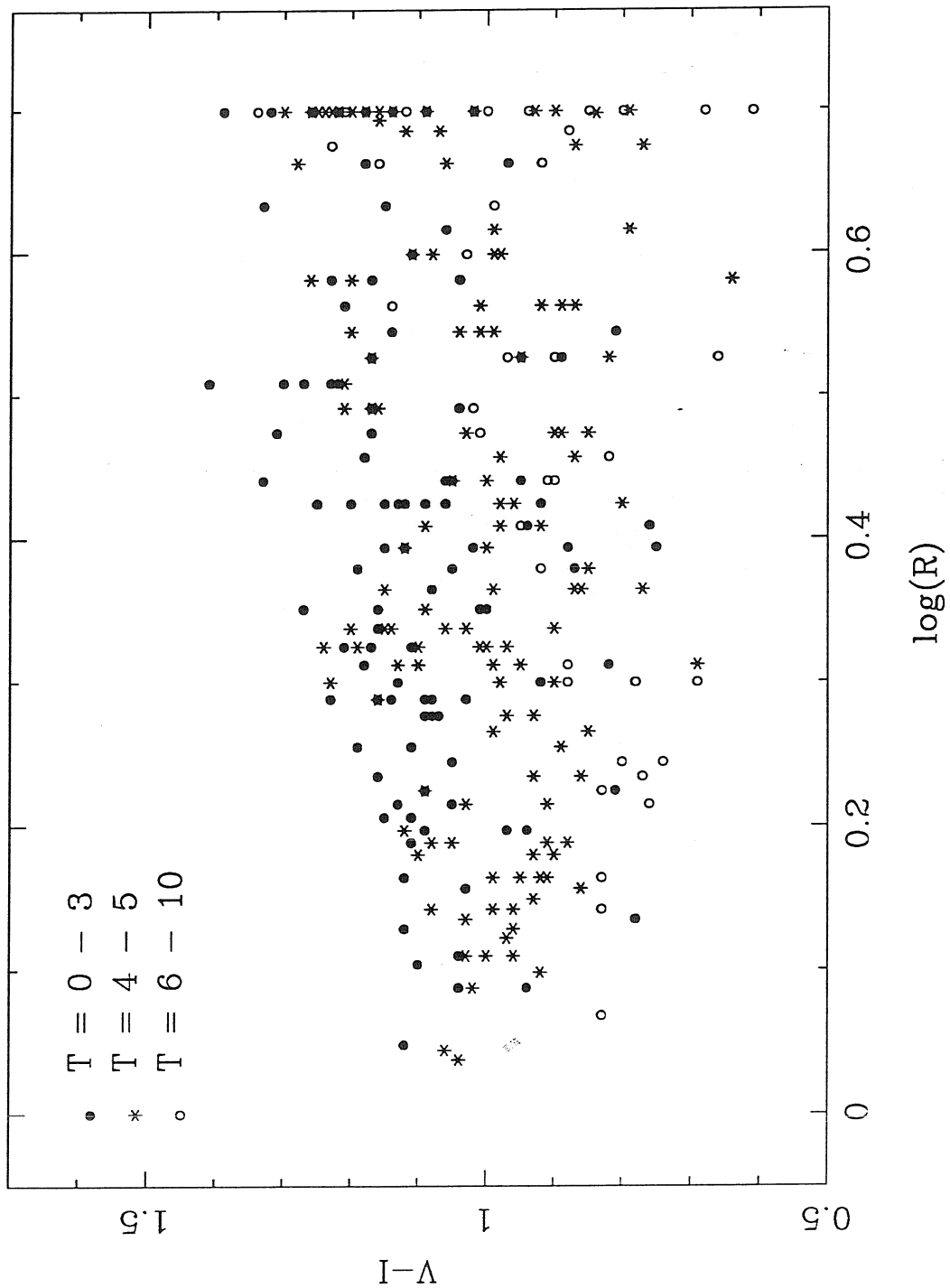

CHAPTER V

DATA PRESENTATION

Various effects on surface photometry and the corresponding corrections have been discussed in Chapter 4. After correcting for these effects, the surface photometry results of all the sample galaxies are graphically presented in Figure 5.1. Each galaxy takes four panels in Fig 5.1 with the following contents:

Panel 1: the I band surface brightness profile, corrected for Galactic absorption, cosmological dimming, and k-term, but not for seeing and inclination effects.

Panel 2: the I isophotal magnitude as a function of semi-major axis. The magnitudes were corrected for Galactic absorption, and k-term, but not for internal absorption.

Panel 3: the integrated $V - I$ color as a function of semi-major axis. Corrections were made for Galactic absorption and k-term. (Note that the two galaxies 383-44 and 323-39 do not have reliable V images, and thus have no color information. In panel 3 of these two galaxies, a different photometric quantity irrelevant to this thesis is presented).

Panel 4: ellipticity as a function of semi-major axis. Seeing effects were not corrected.

Table 5.1 summaries the integrated photometric parameters extracted from the profiles of Figure 5.1, which forms the fundamental data base for the discussions in next three chapters.

Col. 1: Galaxy name.

Col. 2: Morphological type.

Col. 3: Inclination of the galaxy, calculated assuming an intrinsic flattening of 0.2.

Col. 4: W, HI velocity width at the 20% level in units of kms^{-1}, adopted from Aaronson *et al.* (1986, 1989), and corrected for redshift and inclination. The inclination listed in Col. 3 was used in the correction. No attempts were made to correct for a possible non-rotational component in the velocity width (Bottinelli *et al.* 1983).

Col. 5: $I_{23.5}$, magnitude within isophote $\mu_I = 23.5$ mag/arcsec^2, corrected for Galactic absorption, k-term, and internal absorption. In the case that the outermost aperture does not reach this isophotal level, extrapolation is made from the outermost aperture to the desired isophote, assuming the light distribution beyond the outermost aperture has an exponential form of that defined by the outer part of the surface brightness profile. If b/a is the minor-to-major axial ratio, r is the semi-major axis of the outermost aperture, $I(r)$ is the magnitude within this aperture, and μ_o and r_o are the two parameters characterizing the exponential form of the outer part surface brightness profile (i.e., "central surface brightness" and "disk-scale length", respectively), the extrapolated isophotal magnitude is then given by,

$$I_{23.5} = I(r) - 2.5 \log\left\{1 + \frac{b}{a}\left[q(r/r_o) - q(r'/r_o)\right] 10^{-0.4[I_t - I(r)]}\right\}, \qquad (5.1)$$

where

$$I_t = \mu_o - 5 \log r_o - 1.995 \qquad (5.2)$$

is the total magnitude of a pure e-disk galaxy characterized by μ_o and r_o; and the function $q(r)$ reflects the luminosity–radius relation of such an e-disk galaxy,

$$q(x) = (1 + x)e^{-x}, \qquad (5.3)$$

r' is the extrapolated isophotal radius at $\mu_I = 23.5$ mag/arcsec^2, and is given by

$$r' = (23.5 - \mu_o)\frac{r_o}{1.086}. \qquad (5.4)$$

Col. 6: I_{tot}, the total I magnitude, extrapolated from the outermost aperture, and corrected for Galactic absorption, k-term, and internal absorption. To extrapolate the total magnitude, we make the same basic assumption as we just did for extrapolating the isophotal magnitude above, i.e., the light distribution beyond the outermost aperture has an e-disk form specified by μ_o and r_o, which are estimated from the outer part of the surface brightness profile. Again, let r be the semi-major axis of the outermost aperture, $I(r)$ be the magnitude within this aperture, and b/a be the minor-to-major axial ratio, then the extrapolated total magnitude is given by

$$I_{tot} = I(r) - 2.5 \log\left\{1 + \frac{b}{a} q(r/r_o)\, 10^{-0.4[I_t - I(r)]}\right\}. \tag{5.5}$$

Col. 7: ΔI_i, the amount of magnitude correction for internal absorption given by equation (4.11).

Col. 8: $V - I$, integrated $(V - I)$ color within isophote $\mu_I = 23.5$ mag/arcsec^2, corrected for Galactic absorption, k-term, and inclination effects.

Col. 9: $A_{23.5}$, face-on isophotal radius at level $\mu_I = 23.5$ mag/arcsec^2, in units of arcseconds, derived using equation (4.7).

Col. 10: C_{20}, semi-major radius of the isophote which encloses 20% of the total light of the galaxy (in units of arcseconds).

Col. 11: C_{50}, semi-major radius of the isophote which encloses 50% of the total light of the galaxy (in units of arcseconds).

Col. 12: C_{80}, semi-major radius of the isophote which encloses 80% of the total light of the galaxy (in units of arcseconds).

Col. 13: $H_{-0.5}$, the H magnitude adopted from Aaronson *et al.*

Col. 14: Velocity of the galaxy corrected to the centroid of the LG, in units

of kms^{-1}. A star (*) is marked after the velocity value, if the galaxy was not classified as a cluster member in Bothun *et al.* (1985) or Aaronson *et al.* (1989). These non-members will not be used in the study of TF relation in next chapter.

REFERENCES FOR CHAPTER 5

Aaronson, M. *et al.* 1986, *Ap. J.*, **302**, 536.

Aaronson, M. *et al.* 1989, *Ap. J.*, **338**, 654.

Bothun, G. D. *et al.* 1985, *Ap. J. Suppl.* , **57**, 437.

Bottinelli *et al.* 1983, *Astr. Ap.*, **118**, 4.

Figure Captions for Chapter 5

Figure 5.1: The results of surface photometry for the galaxies studied in this thesis are graphically presented: Each page contains 4 galaxies, for each galaxy, displayed in 4 panels from top to bottom are,

1) the profile of I-band surface brightness. μ_I is corrected for Galactic absorption, k-term, and cosmological dimming effects.

2) the profile of I-band isophotal magnitude. Correction is made for Galactic absorption, and k-term.

3) the profile of $(V-I)$ color within the isophote of $\mu_I = 23.5$ mag/arcsec^2. $(V-I)$ is corrected for Galactic absorption, and k-term.

4) the profile of ellipticity.

The x-axes of these profiles (i.e., semi-major axes r) are also corrected for cosmological stretching effect (see Chapter 4 for details).

Table 5.1

Derived Properties of The Sample Galaxies

Name (1)	T (2)	i (3)	W (4)	$I_{23.5}$ (5)	I_{tot} (6)	ΔI_i (7)	$V-I$ (8)	$A^0_{23.5}$ (9)	C_{20} (10)	C_{50} (11)	C_{80} (12)	$H_{-0.5}$ (13)	V (14)
PISCES													
N295	3	69	498	10.98	10.94	0.29	1.07	68.8	7.5	29.5	48.9	10.05	5666
N296	5	78	278	13.24	13.15	0.49	0.88	27.8	6.6	17.3	27.8	13.14	5861
N444	5	79	296	12.72	12.48	0.51	0.90	39.8	11.8	29.0	52.8	12.45	5034
N452	2	76	530	11.23	11.12	0.37	1.13	67.1	5.0	18.0	61.8	9.98	5156
N536	3	74	588	10.77	10.63	0.35	1.08	81.4	7.8	29.7	82.7	9.75	5383
N582	3	80	465	11.53	11.37	0.42	1.05	58.3	9.2	24.1	57.5	10.56	4542
U525	5	60	287	13.30	13.05	0.25	0.91	38.2	18.6	35.5	43.6	12.76	5146
U540	15	57	329	12.80	12.72	0.12	0.75	23.0	4.5	11.4	17.8	12.56	5192
U556	3	61	465	12.79	12.66	0.21	1.17	30.5	4.6	10.5	25.8	11.01	4836
U557	5	67	295	13.35	13.16	0.33	0.79	28.7	8.3	16.5	30.6	13.16	4708
U575	4	90	315	13.10	13.02	0.63	1.00	23.1	5.8	14.5	24.4	12.91	4876
U633	3	80	418	12.50	12.39	0.42	0.92	38.7	4.0	14.5	34.9	11.62	5783
U673	5	71	334	13.71	13.35	0.38	0.90	29.5	7.1	20.1	44.1	12.95	6457
U679	15	87	204	14.71	14.50	0.34	0.74	18.8	9.6	19.9	29.2	14.78	5286
U732	5	54	368	12.65	12.50	0.19	0.99	37.7	8.3	18.4	36.2	11.83	5645
U841	4	81	305	13.02	12.91	0.54	0.96	31.3	8.1	18.3	33.5	12.43	5773
U987	1	73	450	11.75	11.68	0.33	1.09	48.2	3.2	12.6	34.6	10.42	4856
U1033	5	87	353	12.10	12.02	0.62	0.93	43.2	6.9	22.7	45.4	11.17	4228 *
U1066	5	79	179	15.37	14.70	0.51	0.78	15.6	5.7	18.2	32.4	14.74	5268
Z501021	5	90	408	12.42	12.31	0.63	1.11	41.2	10.8	27.0	47.3	11.90	5299

Table 5.1 —— continued

Name (1)	T (2)	i (3)	W (4)	$I_{23.5}$ (5)	I_{tot} (6)	ΔI_i (7)	$V-I$ (8)	$A^0_{23.5}$ (9)	C_{20} (10)	C_{50} (11)	C_{80} (12)	$H_{-0.5}$ (13)	V (14)
A400													
U2285	9	72	332	13.51	13.42	0.22	0.82	24.9	6.5	16.4	24.8	12.64	8393
U2364	2	72	382	13.18	13.11	0.32	1.24	27.1	2.1	9.3	23.7	11.92	5471 *
U2367	-2	76	624	11.62	11.49	0.37	1.31	58.9	6.7	24.3	61.1	10.54	7426
U2375	1	76	465	12.68	12.39	0.37	1.20	29.5	3.0	15.1	39.4	11.64	7647
U2405	5	72	477	12.57	12.38	0.40	0.96	37.7	6.5	20.9	42.1	11.59	7748
U2414	5	87	428	13.24	13.20	0.62	0.98	23.7	5.6	13.9	24.3	12.63	8298
U2415	4	75	378	13.45	13.30	0.44	1.07	25.1	4.8	11.3	27.1	12.33	7809
U2454	5	85	386	13.10	13.04	0.60	1.15	28.0	5.7	14.6	26.8	12.37	7667
U2509	4	77	371	12.65	12.55	0.47	1.06	25.3	6.1	16.5	26.2	12.08	5877 *
Z415055	5	40	—	13.87	13.82	0.10	0.94	16.2	4.3	6.9	10.8	——	6956
Z415058	5	51	—	13.55	13.43	0.17	1.04	25.0	5.2	12.9	21.7	——	8437
A539													
U3219	5	65	348	13.60	13.42	0.30	0.99	35.0	7.2	20.1	34.6	13.03	8419
U3220	5	50	367	14.06	13.83	0.16	0.89	27.6	5.4	16.2	29.7	13.55	8446
U3236	4	64	470	13.02	12.94	0.29	1.13	28.1	4.2	11.1	23.2	12.51	8440
U3248	3	71	480	12.37	12.23	0.31	0.98	47.2	4.3	18.0	45.7	11.35	8860
U3269	4	46	444	12.90	12.83	0.13	0.90	24.7	4.8	10.3	17.6	12.20	8871
U3270	5	63	417	13.42	13.35	0.28	0.89	22.4	4.0	10.2	19.8	12.58	8563
U3275	2	85	566	12.81	12.53	0.48	1.05	36.8	5.7	23.6	50.7	11.56	7901
U3282	5	45	465	12.79	12.66	0.13	0.96	33.5	9.2	15.2	28.9	——	8188

Table 5.1 —— continued

Name (1)	T (2)	i (3)	W (4)	$I_{23.5}$ (5)	I_{tot} (6)	ΔI_i (7)	$V-I$ (8)	$A^0_{23.5}$ (9)	C_{20} (10)	C_{50} (11)	C_{80} (12)	$H_{-0.5}$ (13)	V (14)	
U3291	5	71	—	13.20	13.15	0.38	0.72	25.2	9.2	14.3	23.9	——	8831	
Z421011	4	65	428	13.06	12.96	0.30	0.96	25.4	4.5	10.0	21.2	12.21	8841	
Z421012	5	40	—	13.32	13.24	0.10	0.98	18.8	4.9	8.5	15.8	——	8849	
Z421030	4	65	514	13.05	13.01	0.30	1.13	21.0	3.4	8.7	18.4	12.05	8487	
CANCER														
I2288	6	56	287	14.44	14.10	0.12	0.72	15.6	3.2	8.5	20.5	13.97	4514	
I2348	2	61	408	13.60	13.36	0.21	1.03	19.0	1.7	7.4	20.7	12.52	5869	*
N2535	5	56	—	11.64	11.52	0.21	0.81	58.8	12.2	25.4	50.3	——	4022	
N2545	0	60	527	11.05	10.99	0.20	1.03	59.2	4.1	20.4	39.5	——	3296	*
N2570	2	54	379	13.33	13.15	0.16	1.01	24.6	3.5	10.0	24.1	12.23	6439	*
N2575	5	40	—	11.94	11.81	0.10	1.01	50.2	12.6	24.0	43.9	11.07	3785	*
N2582	3	52	—	11.88	11.80	0.14	1.05	35.9	8.6	19.6	27.3	11.41	4314	
N2595	4	50	—	11.10	10.98	0.16	1.06	76.0	11.1	36.3	64.4	——	4231	
N2596	3	71	468	11.97	11.86	0.31	1.07	43.2	7.6	21.0	37.3	11.33	5808	*
U4299	4	90	411	11.84	11.73	0.63	1.12	41.8	6.0	23.4	48.3	10.94	4195	
U4329	5	70	302	13.51	13.41	0.37	0.90	19.3	4.9	10.5	18.5	11.49	3714	
U4344	15	32	—	13.43	13.11	0.03	0.82	33.3	12.6	21.0	36.4	12.50	4928	
U4361	5	74	216	13.62	13.44	0.43	0.80	25.3	7.3	20.0	29.6	13.70	3645	*
U4386	3	90	498	11.22	11.18	0.51	1.25	46.6	7.1	31.6	52.0	10.61	4547	
U4399	9	70	266	13.51	13.33	0.20	0.87	25.1	5.7	14.2	29.6	13 00	4396	
U4400	5	89	250	14.13	13.83	0.63	0.70	27.2	5.4	18.4	45.4	13.93	4293	
U4405	0	71	527	12.08	12.03	0.31	1.05	37.0	2.6	11.2	30.1	10.91	5559	*
U4424	5	79	248	14.32	13.87	0.51	0.76	26.3	6.4	20.8	46.0	14.03	4336	

Table 5.1 —— continued

Name (1)	T (2)	i (3)	W (4)	$I_{23.5}$ (5)	I_{tot} (6)	ΔI_i (7)	$V-I$ (8)	$A^0_{23.5}$ (9)	C_{20} (10)	C_{50} (11)	C_{80} (12)	$H_{-0.5}$ (13)	V (14)
U4444	5	70	216	11.97	11.93	0.37	1.01	39.9	7.2	20.2	33.0	——	1955 *
U4446	5	90	348	13.37	13.30	0.63	0.95	22.6	9.3	16.6	27.4	12.84	5897 *
Z89001	8	48	—	14.08	14.01	0.08	0.80	15.7	4.5	7.7	12.8	——	5591 *
Z119019	5	90	—	13.49	13.34	0.63	1.09	26.0	6.5	21.8	33.9	——	4178
Z119044	7	57	193	14.30	13.88	0.12	0.69	23.8	8.5	21.9	31.0	14.46	3405 *
Z119047	4	38	464	12.67	12.42	0.09	0.90	35.6	4.7	14.8	37.7	——	4424
Z119051	5	51	320	13.98	13.80	0.17	0.84	20.7	5.4	13.4	21.1	13.53	4928
Z119053	5	43	313	13.84	13.71	0.12	0.93	17.0	2.4	7.2	15.0	12.93	4749
Z119066	5	47	319	12.92	12.81	0.14	0.83	28.5	4.9	10.4	22.8	12.55	4045
Z119095	4	85	429	13.74	13.65	0.60	0.93	18.2	2.3	7.4	17.9	12.81	5286 *
Z119107	5	81	371	13.51	13.44	0.54	0.99	20.1	4.1	10.7	19.9	13.02	5193 *
A1367													
I742	2	43	—	12.50	12.38	0.09	1.09	35.5	8.5	20.9	30.5	12.09	6349
N3697	3	75	558	11.68	11.62	0.36	0.94	52.7	6.3	27.1	47.8	10.80	6187
N3701	4	62	344	12.11	12.00	0.27	0.84	43.5	7.9	20.1	37.7	11.45	2748 *
N3832	5	45	—	11.86	11.76	0.13	0.93	51.1	16.3	28.4	46.5	——	6841
N3840	1	36	493	12.67	12.43	0.06	0.92	34.4	4.0	16.5	35.2	11.62	7298
N3861	3	53	608	11.42	11.31	0.15	1.07	65.4	5.8	23.1	59.3	10.47	5024
N3883	3	27	—	11.45	11.20	0.03	1.11	73.7	14.7	44.0	75.3	10.72	6955
N3933	4	64	396	12.13	12.06	0.29	1.04	31.1	6.5	18.0	26.2	11.42	3656 *
N3947	3	57	—	11.83	11.76	0.18	1.00	43.3	7.3	21.6	38.5	11.08	6127
N3951	4	63	472	12.21	12.15	0.28	1.07	30.4	5.6	12.4	25.3	11.31	6408
U6509	5	90	204	13.72	13.24	0.63	0.76	42.1	18.2	49.3	77.3	13.64	2841 *

Table 5.1 —– continued

Name (1)	T (2)	i (3)	W (4)	$I_{23.5}$ (5)	I_{tot} (6)	ΔI_i (7)	$V-I$ (8)	$A^0_{23.5}$ (9)	C_{20} (10)	C_{50} (11)	C_{80} (12)	$H_{-0.5}$ (13)	V (14)
U6586	4	51	400	12.63	12.55	0.17	1.01	37.3	7.9	22.5	30.6	11.79	3871 *
U6686	3	90	419	12.31	12.16	0.51	1.12	56.7	5.7	21.3	63.4	11.16	6458
U6743	4	26	—	12.63	12.52	0.04	1.05	36.1	8.8	18.1	31.3	—–	6679
U6821	4	44	—	12.54	12.40	0.12	1.00	35.2	8.5	18.4	32.7	11.85	6372
U6837	5	90	368	14.01	13.88	0.63	1.02	20.0	6.0	14.8	26.1	13.21	5901
U6876	2	55	—	12.62	12.57	0.16	1.05	28.6	4.1	13.5	22.0	11.97	6777
U6891	2	83	399	12.92	12.78	0.46	1.02	34.5	3.5	13.9	38.3	11.88	6703
Z97005	5	54	343	13.84	13.66	0.19	0.87	21.5	4.3	10.4	20.8	13.28	6045
Z97033	4	65	444	13.30	13.23	0.30	1.07	19.6	2.8	7.4	15.9	12.40	7663
Z97058	7	70	304	13.78	13.70	0.20	0.86	22.0	5.7	12.5	22.7	13.28	6653
Z97062	5	65	317	14.00	13.89	0.30	0.83	18.3	3.3	7.7	16.9	13.31	7708
Z97068	4	55	418	12.87	12.78	0.20	1.05	26.8	3.8	9.0	23.1	11.52	5889
Z97152	3	71	464	12.96	12.91	0.31	1.12	26.7	2.5	9.4	21.9	12.12	6118
Z97180	8	74	318	14.40	13.74	0.24	0.92	25.5	15.9	31.6	53.8	14.01	6121
Z97185	5	72	360	13.48	13.38	0.40	0.91	24.3	5.4	12.8	24.2	13.04	6271
Z126083	3	39	—	12.82	12.68	0.08	1.08	31.7	7.5	18.3	29.4	—–	5975
Z126104	5	58	366	13.96	13.87	0.23	0.84	18.8	3.3	7.3	15.2	—–	6616
Z127005	5	64	333	13.67	13.49	0.29	0.91	22.0	5.3	12.5	23.4	13.05	6800
Z127049	4	69	327	13.30	13.08	0.35	1.04	24.4	4.3	12.1	28.3	12.52	6994
Z127056	4	80	431	13.05	12.98	0.52	1.14	18.9	3.7	10.2	19.1	12.17	6771
Z127082	5	48	355	12.90	12.80	0.15	0.92	24.4	4.5	14.1	21.4	12.59	6595
Z127083	3	36	—	13.22	13.17	0.06	1.02	19.7	1.7	6.1	12.0	—–	6680

Table 5.1 —— continued

Name (1)	T (2)	i (3)	W (4)	$I_{23.5}$ (5)	I_{tot} (6)	ΔI_i (7)	$V-I$ (8)	$A^0_{23.5}$ (9)	C_{20} (10)	C_{50} (11)	C_{80} (12)	$H_{-0.5}$ (13)	V (14)	
COMA														
I821	4	24	—	12.76	12.68	0.03	1.03	31.6	8.3	18.0	25.9	12.32	6751	
I842	5	63	445	12.62	12.53	0.28	1.04	31.8	7.0	19.6	28.2	11.99	7285	
I3949	4	87	—	12.63	12.60	0.62	0.98	24.2	4.2	10.4	20.1	11.95	7469	
I4040	4	70	—	13.62	13.52	0.37	0.84	18.5	3.4	7.3	16.1	12.70	7633	
I4088	2	75	499	12.50	12.44	0.36	1.07	35.4	4.1	13.7	31.7	11.47	7114	
N4966	3	60	514	11.99	11.96	0.20	1.01	31.1	3.0	11.8	22.2	11.19	7057	
N5065	5	51	400	12.59	12.48	0.17	0.87	34.4	8.1	15.7	28.6	11.91	5555	
N5081	3	74	577	11.66	11.59	0.35	1.22	55.5	8.7	28.6	44.4	11.10	6680	
U7754	5	68	325	13.34	13.23	0.34	0.77	24.9	5.6	12.3	22.2	12.81	4574	*
U7978	5	50	434	13.13	12.96	0.16	0.89	28.3	6.5	13.6	25.8	12.33	8106	
U8013	3	77	396	13.54	13.34	0.38	0.84	32.1	4.4	18.3	37.1	12.87	7884	
U8017	5	76	564	12.20	12.16	0.46	1.11	24.5	4.5	12.9	21.0	11.30	7062	
U8161	3	64	430	13.05	12.97	0.24	1.15	27.6	3.2	8.6	23.8	11.48	6682	
U8195	15	90	260	14.24	14.13	0.35	0.86	22.2	10.7	21.4	31.7	13.77	7064	
U8229	3	65	422	12.38	12.34	0.25	1.09	33.2	3.9	17.8	29.0	11.38	5990	
U8244	5	71	322	13.92	13.66	0.38	0.88	28.1	8.8	21.4	35.0	13.56	7123	
Z160058	5	75	380	13.19	13.03	0.44	1.06	26.8	6.3	16.3	30.8	12.57	7657	
Z74-23														
N5409	3	53	444	12.16	12.04	0.15	1.11	47.2	4.1	25.5	40.8	11.24	6237	
N5416	5	45	531	12.09	12.01	0.13	1.05	37.7	6.3	12.7	26.4	11.15	6208	

Table 5.1 —— continued

Name (1)	T (2)	i (3)	W (4)	$I_{23.5}$ (5)	I_{tot} (6)	ΔI_i (7)	$V-I$ (8)	$A^0_{23.5}$ (9)	C_{20} (10)	C_{50} (11)	C_{80} (12)	$H_{-0.5}$ (13)	V (14)
U8918	4	80	339	12.64	12.47	0.52	1.08	30.9	6.9	18.8	36.3	11.77	4070 *
U8927	4	73	331	13.33	13.24	0.41	0.89	28.7	8.8	18.7	29.5	13.30	7081
U8948	3	70	383	12.95	12.83	0.30	0.86	28.6	5.5	13.3	28.9	11.85	5969
U8950	5	90	219	14.78	14.47	0.63	0.65	22.1	5.5	18.0	33.7	14.45	5843
U8951	5	81	310	14.06	13.85	0.54	0.86	24.1	7.0	17.5	31.6	13.87	5857
U8967	4	82	388	13.01	12.86	0.55	0.67	34.1	5.0	16.7	38.3	11.67	5611
U9023	5	67	290	14.26	14.01	0.33	0.92	22.9	5.8	15.9	27.3	13.80	7185
U9027	5	82	299	14.35	14.21	0.55	0.87	20.6	3.4	14.6	23.8	13.90	6853
Z74012	7	68	320	14.47	14.24	0.19	0.84	20.0	6.4	14.7	24.8	13.82	6854
Z74035	8	90	244	15.16	14.97	0.35	0.66	15.1	5.7	14.4	23.1	14.49	4558 *
A2151													
I1155	4	36	406	13.32	13.25	0.08	1.00	24.1	3.3	11.1	17.1	12.55	10730
I1173	4	64	489	13.22	13.12	0.29	1.18	26.1	3.3	11.8	24.3	12.26	10542
N6050	2	60	442	13.79	13.70	0.20	1.02	19.2	2.4	7.8	16.4	12.72	9700
U10085	5	48	419	13.17	13.04	0.15	0.96	26.9	4.4	11.1	22.1	12.16	9832
U10190	5	90	318	14.78	14.51	0.63	0.88	14.8	3.5	9.7	22.6	14.10	11182
U10195	3	80	567	13.16	13.01	0.42	1.11	30.1	3.1	10.8	29.4	11.91	10840
Z108108	3	52	379	13.95	13.86	0.14	0.90	18.0	1.6	5.6	13.5	12.73	10741
Z108140	1	66	561	12.86	12.76	0.26	1.74	28.4	3.1	14.1	26.0	12.27	11716
Z108158	4	78	518	12.99	12.95	0.49	1.09	23.9	3.6	10.4	21.7	12.26	10706

Table 5.1 —– continued

Name (1)	T (2)	i (3)	W (4)	$I_{23.5}$ (5)	I_{tot} (6)	ΔI_i (7)	$V-I$ (8)	$A^0_{23.5}$ (9)	C_{20} (10)	C_{50} (11)	C_{80} (12)	$H_{-0.5}$ (13)	V (14)
PEGASUS													
I1474	5	67	305	13.73	13.56	0.33	1.08	20.8	1.8	9.2	21.2	11.80	3665
I5309	3	62	360	12.18	12.03	0.22	1.07	50.0	8.2	22.7	45.6	11.61	4386
N7536	3	66	382	11.95	11.87	0.26	0.93	44.2	12.2	22.6	38.6	11.09	4927
N7591	3	61	490	11.64	11.50	0.21	1.02	40.2	4.9	15.8	39.7	10.32	5146
N7593	4	50	358	12.53	12.47	0.16	0.86	30.1	6.7	12.9	21.0	12 00	4319
N7631	3	67	408	11.51	11.44	0.27	1.01	49.8	8.6	20.4	43.3	10.71	3941
U12382	5	90	302	13.76	13.68	0.63	1.09	19.3	4.0	9.4	19.9	12.72	3716
U12423	5	90	526	11.77	11.62	0.63	1.16	61.1	8.8	31.1	75.9	10.82	5046
U12451	10	90	209	13.71	13.45	0.35	0.80	30.8	18.2	37.0	50.9	13.65	3825
U12467	15	79	249	13.34	12.99	0.28	1.03	38.8	16.1	38.9	63.8	13.35	3696
U12494	5	74	260	13.30	13.13	0.43	0.81	35.4	11.5	23.7	41.5	13.42	4376
U12547	5	67	256	13.21	13.06	0.33	0.80	30.1	5.7	14.9	32.1	12.97	5299
U12555	5	79	256	14.12	13.82	0.51	0.81	25.7	8.1	19.8	35.7	14.11	5101
U12561	15	77	232	13.93	13.57	0.26	0.86	31.3	12.5	31.9	49.4	13.88	3944
U12571	3	61	363	12.85	12.71	0.21	1.08	32.2	8.7	17.3	29.9	11.66	4129
A2634													
N7747	3	71	618	11.97	11.92	0.31	1.17	42.1	3.3	15.8	29.8	10.78	7933
U12631	3	77	489	12.76	12.68	0.38	1.06	30.3	2.1	10.3	24.9	11.72	9430
U12678	3	90	545	12.84	12.76	0.51	1.18	29.2	3.2	12.3	26.8	11.95	9198
U12701	5	90	375	13.78	13.68	0.63	1.06	19.0	3.1	9.8	19.6	12.81	9104

Table 5.1 —— continued

Name (1)	T (2)	i (3)	W (4)	$I_{23.5}$ (5)	I_{tot} (6)	ΔI_i (7)	$V-I$ (8)	$A^0_{23.5}$ (9)	C_{20} (10)	C_{50} (11)	C_{80} (12)	$H_{-0.5}$ (13)	V (14)
U12721	3	63	472	12.76	12.66	0.23	1.12	38.7	3.8	12.7	33.0	11.49	7849
U12746	5	90	486	12.46	12.38	0.63	1.10	31.3	5.5	22.7	38.2	11.62	7678
U12755	3	61	595	12.28	12.19	0.21	1.10	38.5	6.1	13.9	29.0	11.07	9033
Z476112	5	61	572	12.79	12.72	0.26	1.10	25.5	5.8	11.5	18.7	11.52	9645
Z477024	4	62	364	13.41	13.32	0.27	1.17	20.6	2.8	10.7	19.5	12.62	8369
Z477033	0	54	580	12.46	12.37	0.16	1.09	33.5	4.1	12.4	26.6	11.45	8109
Z498012	4	66	432	12.87	12.79	0.32	1.02	22.6	4.3	13.2	21.0	12.19	9281
ANTLIA													
318-4	5	90	386	10.79	10.75	0.63	1.04	63.8	18.5	42.0	67.6	10.39	2666
437-14	3	90	399	10.84	10.81	0.51	0.95	47.5	7.2	21.7	41.1	9.99	2604
437-18	3	81	352	12.97	12.69	0.44	0.99	37.1	8.0	20.8	50.3	——	3118
437-56	3	52	331	11.97	11.86	0.14	0.93	49.1	10.3	22.7	41.5	11.20	2665
I2531	5	90	531	10.21	10.10	0.63	1.08	134.0	28.2	72.6	148.4	9.30	2190 *
I2556	5	59	277	12.38	12.11	0.24	0.80	55.8	16.6	38.8	65.4	12.28	2237
I2559	3	69	304	12.15	11.99	0.29	0.94	47.8	9.1	19.6	45.6	11.20	2716
I2560	3	69	442	10.24	10.12	0.29	1.04	106.2	16.5	51.6	98.9	9.44	2632
N3223	3	48	602	9.50	9.42	0.12	1.09	136.9	18.0	49.5	92.3	8.55	2629
N3347A	5	78	370	11.07	11.05	0.49	0.93	53.4	16.6	35.1	52.6	10.57	2519
N3347B	7	81	362	11.65	11.57	0.30	0.91	63.5	19.6	45.6	77.0	11.05	2922
N3449	3	71	581	10.35	10.28	0.31	1.01	90.3	6.3	24.4	64.2	9.32	3032

Table 5.1 —– continued

Name (1)	T (2)	i (3)	W (4)	$I_{23.5}$ (5)	I_{tot} (6)	ΔI_i (7)	$V-I$ (8)	$A^0_{23.5}$ (9)	C_{20} (10)	C_{50} (11)	C_{80} (12)	$H_{-0.5}$ (13)	V (14)
CEN30													
268-44	5	64	333	12.30	12.18	0.29	0.95	35.1	5.9	15.1	28.9	11.28	3269
268-46	10	77	211	12.80	12.53	0.26	0.79	53.7	21.2	48.3	78.9	12.61	2056
269-28	5	74	263	13.42	13.14	0.43	0.76	24.9	6.7	15.9	33.4	13.05	3059
269-52	5	90	241	14.04	13.70	0.63	0.79	31.9	7.1	27.0	52.5	13.69	2983 *
322-42	4	77	293	12.09	11.90	0.47	0.84	53.2	18.3	35.0	65.7	12.08	3714
322-85	5	77	218	13.18	12.98	0.47	0.71	31.4	7.8	20.7	37.4	13.01	3764
323-27	5	59	424	11.26	11.10	0.24	0.94	56.4	12.3	27.5	52.2	10.81	3655
323-72	5	75	190	13.30	13.16	0.44	1.11	26.7	6.4	15.4	28.9	12.82	3085
381-14	4	86	244	13.15	12.96	0.61	0.74	30.6	9.2	17.9	39.8	12.86	3102
N4603	5	52	517	9.86	9.79	0.18	1.08	117.4	26.6	56.8	90.6	9.32	2369
N4603A	3	72	314	11.80	11.57	0.32	0.86	47.5	6.5	19.0	54.5	10.72	3535
N4672	3	58	470	11.69	11.54	0.19	1.06	52.8	7.9	19.8	45.9	10.32	3052
CEN45													
268-37	4	60	379	12.47	12.20	0.25	0.87	47.2	8.6	21.6	56.1	11.86	4686
322-48	5	81	292	12.88	12.76	0.54	0.87	32.0	8.8	19.3	33.6	12.38	4083
323-25	5	56	482	11.41	11.33	0.21	0.88	52.0	11.6	18.7	34.2	10.39	4043
323-39	3	60	332	13.63	13.45	0.20	—–	25.1	5.0	11.9	25.7	13.31	4811
323-73	3	55	389	12.55	12.47	0.16	0.77	32.2	4.3	10.0	21.1	11.58	4777
N4679	4	69	470	11.02	10.94	0.35	0.92	66.7	10.8	26.1	50.6	10.22	4469

Table 5.1 —— continued

Name (1)	T (2)	i (3)	W (4)	$I_{23.5}$ (5)	I_{tot} (6)	ΔI_i (7)	$V-I$ (8)	$A^0_{23.5}$ (9)	C_{20} (10)	C_{50} (11)	C_{80} (12)	$H_{-0.5}$ (13)	V (14)
E508													
443-79	7	77	150	14.11	13.65	0.26	0.55	27.2	12.1	29.1	50.0	13.94	1935 *
507-41	7	45	229	13.11	12.87	0.07	0.80	34.0	8.3	15.5	37.2	12.96	2988 *
507-42	3	62	320	12.33	12.24	0.22	0.86	34.8	3.8	10.4	26.0	11.42	3028 *
507-67	5	48	273	12.14	11.85	0.15	0.89	54.4	12.3	31.5	63.0	11.54	2871
508-11	6	90	262	12.20	12.07	0.35	0.71	59.4	29.1	44.1	83.7	11.77	2424
508-19	5	80	287	12.26	12.11	0.52	0.52	42.2	16.5	24.5	47.2	12.22	2777
508-51	7	62	155	13.23	12.95	0.15	0.72	38.2	12.7	26.1	47.7	13.13	1997 *
508-7	8	62	190	13.67	13.22	0.15	0.82	32.5	14.2	30.5	47.5	13.16	2803
576-11	5	90	328	11.56	11.42	0.63	0.88	66.9	16.8	36.8	79.6	10.91	2606
576-32	5	42	405	11.29	11.20	0.11	0.95	66.5	20.6	34.1	58.5	10.90	2884
576-40	6	83	185	12.84	12.68	0.32	0.86	40.4	9.8	25.5	53.0	12.39	1928 *
I4237	3	47	418	11.13	11.04	0.11	1.00	64.7	17.2	29.3	47.6	10.47	2507
N5022	3	90	386	11.11	11.07	0.51	1.04	58.0	4.8	18.0	45.6	10.26	2847
HYDRA													
437-30	5	88	435	11.00	10.88	0.62	1.02	63.6	9.3	30.4	67.6	10.06	3515
437-34	3	70	210	14.65	14.07	0.30	0.68	21.4	10.6	21.1	39.3	13.65	3530
437-4	3	69	350	11.90	11.84	0.29	0.67	37.4	9.4	20.5	35.2	11.25	3056
437-54	6	90	294	13.49	13.29	0.35	1.07	26.3	7.8	19.5	39.3	12.23	3227
501-1	6	63	296	12.81	12.30	0.16	0.82	46.3	19.2	43.1	86.2	12.49	3576
501-2	3	90	402	12.71	12.55	0.51	1.12	29.8	5.4	17.6	35.3	11.92	3292

Table 5.1 —— continued

Name (1)	T (2)	i (3)	W (4)	$I_{23.5}$ (5)	I_{tot} (6)	ΔI_i (7)	$V-I$ (8)	$A^0_{23.5}$ (9)	C_{20} (10)	C_{50} (11)	C_{80} (12)	$H_{-0.5}$ (13)	V (14)	
501-68	4	74	362	11.92	11.79	0.43	0.94	51.3	7.9	24.3	54.3	11.47	2843	
501-82	3	68	440	12.11	11.99	0.28	0.97	42.2	4.5	17.5	37.2	11.22	4321	
501-86	5	65	415	11.76	11.65	0.30	1.08	47.6	16.8	32.8	46.4	11.57	3492	
N3463	3	66	461	11.74	11.50	0.26	0.94	44.2	5.8	18.5	50.0	10.83	3723	
N3557														
319-11	5	48	415	11.21	10.66	0.15	0.88	102.3	25.8	86.4	173.1	11.09	2852	
377-21	3	69	352	11.84	11.78	0.29	0.80	51.0	10.2	26.4	46.7	11.32	2507	
377-31	5	64	362	11.94	11.71	0.29	0.94	55.3	16.5	31.4	62.3	11.55	2770	
377-34	4	86	240	11.83	11.69	0.61	0.64	62.5	18.8	39.8	72.3	11.79	2329	*
377-40	4	71	237	14.62	14.24	0.38	0.72	21.2	5.8	14.8	31.7	14.26	3764	*
378-11	3	85	326	12.93	12.78	0.48	0.84	38.3	7.1	19.1	39.6	12.30	2988	*
378-3	5	62	310	11.89	11.67	0.27	0.92	57.0	14.1	25.8	61.7	11.52	2775	
N3533	3	76	424	11.09	11.01	0.37	1.12	68.6	8.2	26.3	55.6	9.93	2861	
N3568	5	78	311	10.62	10.58	0.49	0.90	68.8	14.5	38.5	59.3	10.27	2153	*
N3573	0	66	554	10.63	10.46	0.26	1.20	98.6	7.6	32.8	94.9	9.51	2143	*
Southern sky galaxies without HI measurements														
263-51	3	64	—	11.89	11.83	0.24	1.11	47.0	14.4	22.6	34.4	——	——	
321-10	4	90	—	11.78	11.72	0.63	1.11	42.9	8.7	21.9	45.3	——	——	
321-16	3	77	—	11.91	11.81	0.38	0.78	62.4	11.9	35.5	62.8	——	——	
321-18	10	62	—	12.66	12.25	0.15	0.63	56.7	19.7	48.0	85.7	——	——	
322-9	1	71	—	11.98	11.82	0.31	0.84	54.0	12.0	20.0	51.3	——	3717	

Table 5.1 —— continued

Name (1)	T (2)	i (3)	W (4)	$I_{23.5}$ (5)	I_{tot} (6)	ΔI_i (7)	$V-I$ (8)	$A^0_{23.5}$ (9)	C_{20} (10)	C_{50} (11)	C_{80} (12)	$H_{-0.5}$ (13)	V (14)
323-42	3	72	—	11.91	11.77	0.32	0.97	52.3	11.4	26.2	50.6	——	——
324-23	8	90	—	11.88	11.76	0.35	0.47	60.5	25.5	56.2	87.4	——	1443
377-17	5	67	—	15.37	14.03	0.33	0.70	21.2	19.2	39.8	71.6	——	——
380-14	3	66	—	11.79	11.54	0.26	1.09	52.3	10.8	29.6	61.0	——	——
380-29	5	73	—	12.92	12.65	0.41	0.78	40.6	19.6	31.1	51.5	——	——
380-34	10	90	—	14.33	13.86	0.35	0.54	32.4	28.9	43.8	59.2	——	——
380-8	6	73	—	13.45	13.15	0.23	0.73	33.8	15.7	31.0	47.1	——	——
382-32	6	90	—	12.87	12.77	0.35	1.20	32.5	5.3	23.8	43.5	——	——
382-4	3	68	—	13.26	12.91	0.28	0.79	37.5	13.3	30.3	49.7	——	——
382-41	8	90	—	13.72	13.51	0.35	0.71	31.6	12.4	24.9	49.9	——	——
382-45	8	72	—	12.35	11.98	0.22	0.81	60.5	36.7	62.1	90.3	——	1455
382-58	6	85	—	11.57	11.47	0.33	1.03	54.0	7.7	27.3	67.9	——	——
383-2	3	61	—	12.50	12.37	0.21	0.97	41.8	5.9	19.6	38.1	——	——
383-27	1	83	—	12.04	11.98	0.46	1.20	44.4	10.9	20.7	39.5	——	——
383-44	3	64	—	12.51	12.40	0.24	——	38.8	5.1	14.7	32.5	——	3987
383-48	1	78	—	12.06	11.92	0.40	1.03	53.3	5.3	17.6	50.2	——	——
383-60	3	44	—	12.17	11.96	0.10	0.75	47.2	13.2	28.1	47.9	——	——
383-72	3	71	—	13.32	12.98	0.31	1.04	25.4	6.6	20.6	36.4	——	——
383-88	3	72	—	11.94	11.84	0.32	0.96	48.8	12.2	26.8	45.5	——	——
384-2	8	54	—	13.01	12.32	0.11	0.72	53.3	26.7	57.8	93.0	——	——
437-31	6	55	—	13.34	12.97	0.11	0.79	33.8	10.9	23.7	45.9	——	——
442-28	5	60	—	13.22	12.17	0.25	0.87	52.5	38.6	77.1	139.6	——	——
443-21	6	90		12.22	12.17	0.35	0.98	38.0	14.5	33.6	47.5	——	——
443-42	3	90	—	11.18	11.10	0.51	1.08	64.4	15.4	42.0	65.3	——	——
443-59	3	78	—	12.69	12.57	0.40	0.70	45.5	11.8	31.2	48.5	——	——

Table 5.1 —— continued

Name (1)	T (2)	i (3)	W (4)	$I_{23.5}$ (5)	I_{tot} (6)	ΔI_i (7)	$V-I$ (8)	$A^0_{23.5}$ (9)	C_{20} (10)	C_{50} (11)	C_{80} (12)	$H_{-0.5}$ (13)	V (14)
443-83	6	85	—	11.31	11.18	0.33	0.79	75.5	24.3	54.5	99.0	——	2382
444-47	3	77	—	12.88	12.69	0.38	0.84	38.1	8.7	20.5	41.2	——	——
445-14	1	58	—	11.21	11.15	0.19	1.14	55.1	3.9	14.3	36.2	——	——
445-26	6	90	—	12.79	12.72	0.35	0.88	36.0	2.1	11.2	42.2	——	——
445-58	4	63	—	11.67	11.52	0.28	0.93	54.6	12.5	26.2	54.2	——	——
445-81	6	90	—	11.81	11.73	0.35	1.00	40.3	11.1	22.9	43.4	——	——
507-62	3	76	—	11.20	11.12	0.37	1.17	64.5	14.6	26.4	54.8	——	——
510-7	1	79	—	11.52	11.45	0.41	1.10	52.5	8.5	23.8	45.9	——	——
I1657	3	82	—	11.13	11.08	0.45	0.94	56.4	9.9	21.5	45.1	——	3564
I3290	3	40	—	10.96	10.89	0.08	1.02	61.1	6.0	22.4	44.5	——	3342
I4214	-2	51	—	9.78	9.73	0.14	1.07	101.7	7.3	32.5	70.9	——	2297
I4299	1	68	—	11.16	11.08	0.28	1.11	53.3	3.1	12.3	36.5	——	4028
I4351	6	86	—	9.89	9.81	0.34	1.10	120.0	13.8	52.1	128.9	——	2661
N4112	1	60	—	11.06	10.98	0.20	1.03	62.3	5.7	19.6	42.0	——	——
N4219	3	75	—	10.05	9.99	0.36	1.07	102.4	15.0	39.3	80.6	——	1980
N424	1	71	—	11.32	11.27	0.31	1.01	61.2	5.4	14.7	38.6	——	3496
N4980	1	63	—	11.89	11.79	0.23	0.76	48.6	9.9	25.9	46.0	——	1456
N5121A	5	63	—	14.98	14.01	0.28	0.63	21.6	12.8	28.9	49.1	——	——
N5161	6	75	—	10.15	9.98	0.25	0.92	128.8	21.4	57.4	155.0	——	2370
N5188	2	64	—	10.46	10.40	0.24	1.05	84.6	12.7	29.1	64.3	——	2366
N5302	1	56	—	10.77	10.70	0.17	1.11	66.3	6.7	23.4	48.4	——	3289
N5398	8	45	—	11.30	11.12	0.07	0.80	80.2	19.9	38.0	79.4	——	1225

Figure 5.1

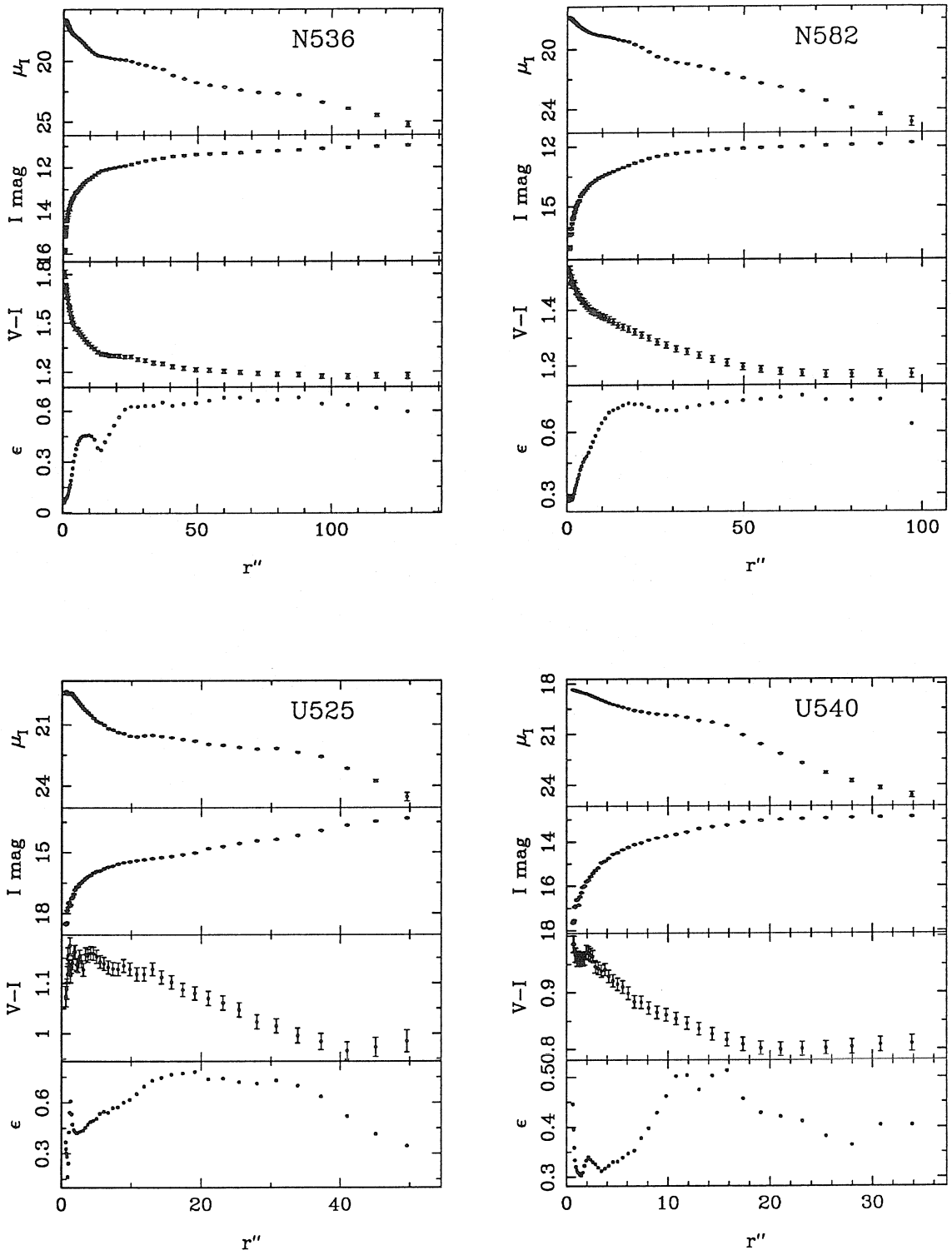

Figure 5.1 —- continued

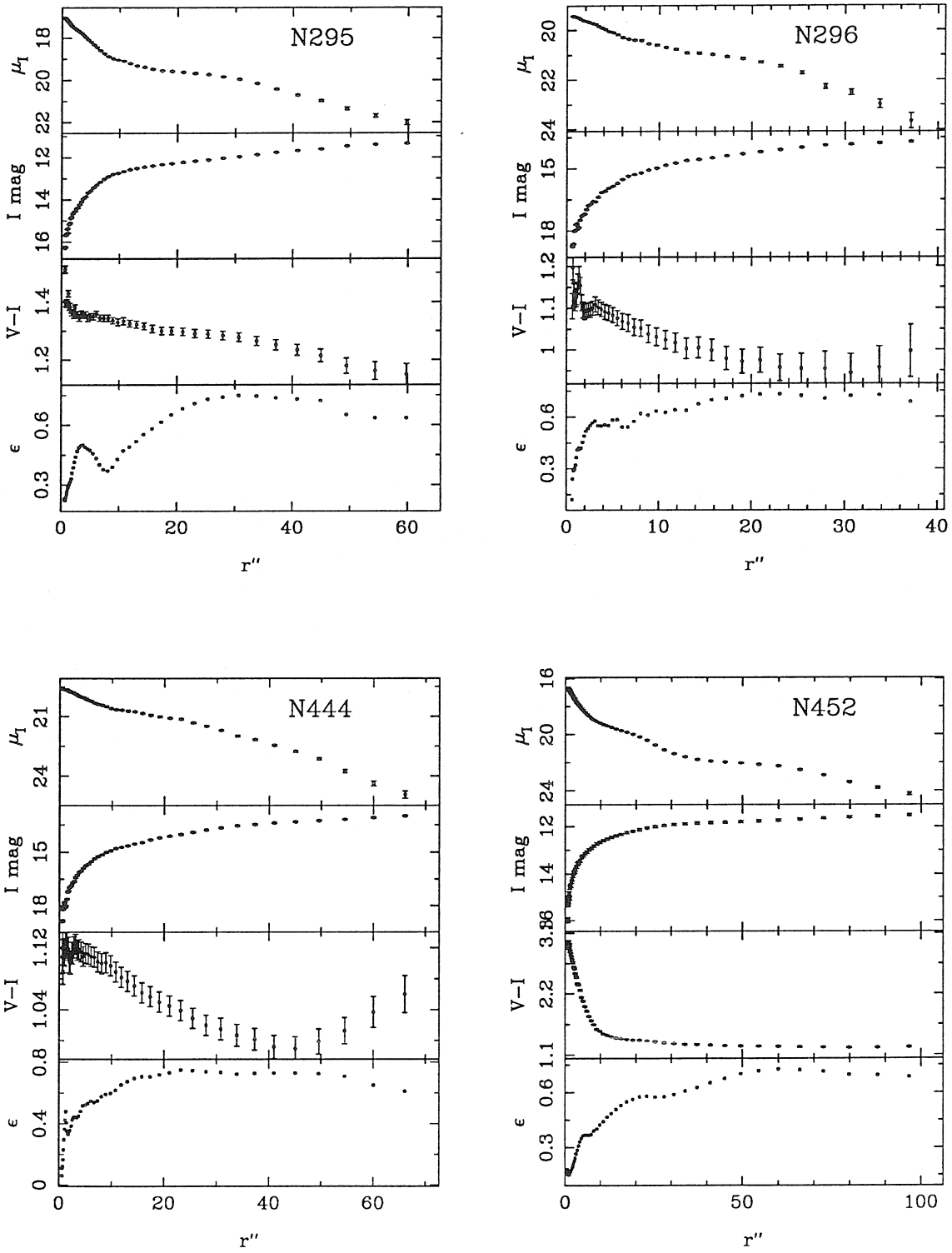

Figure 5.1 —- continued

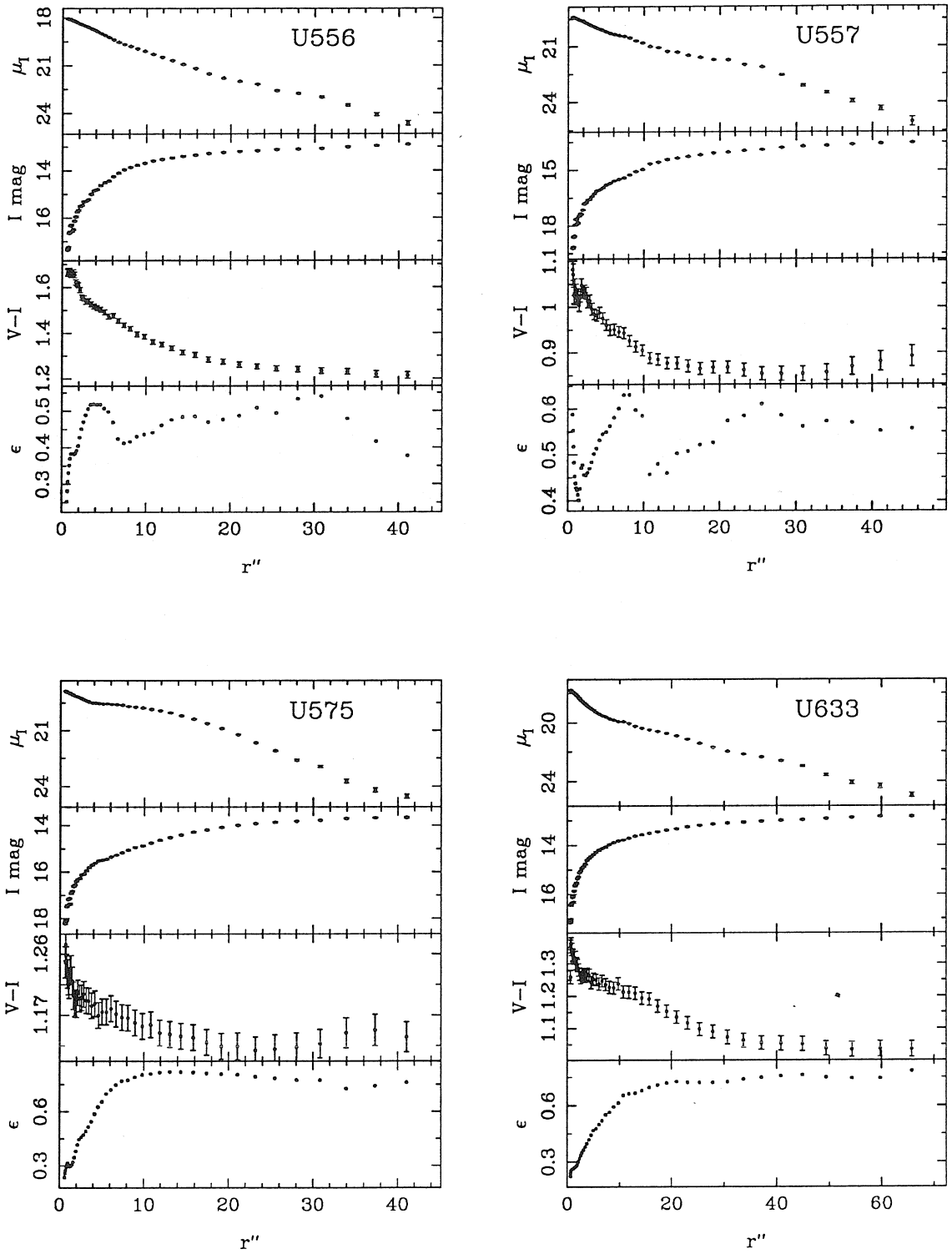

Figure 5.1 —- continued

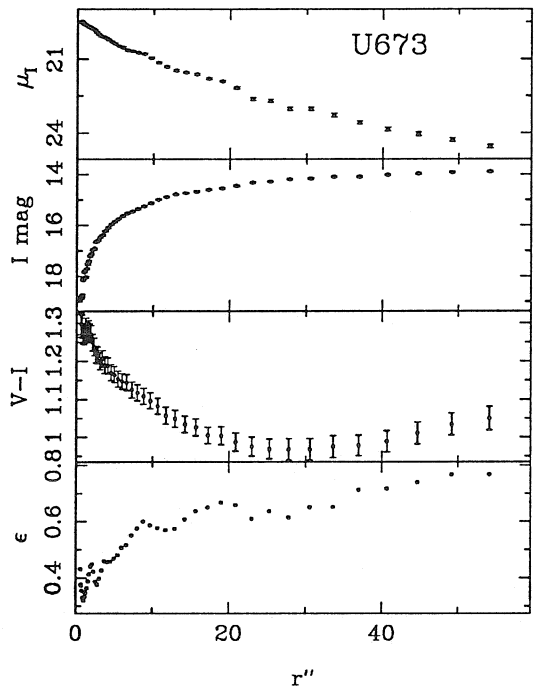

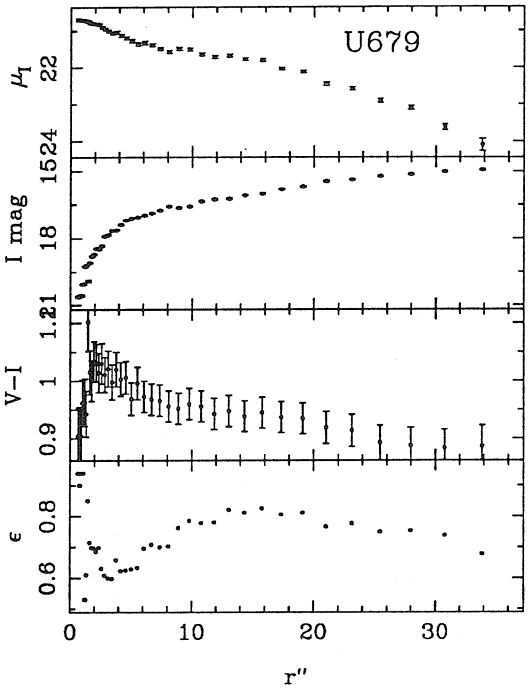

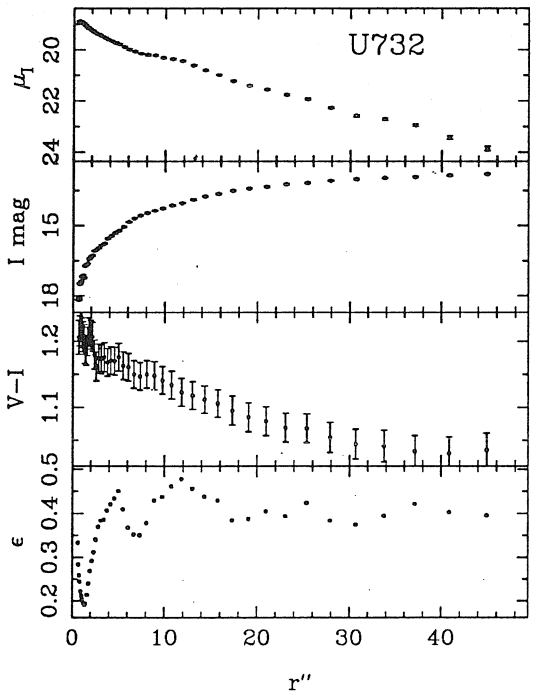

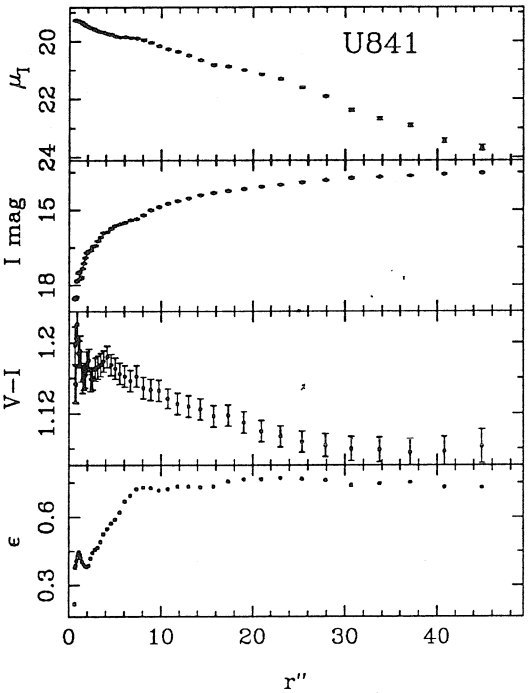

Figure 5.1 —- continued

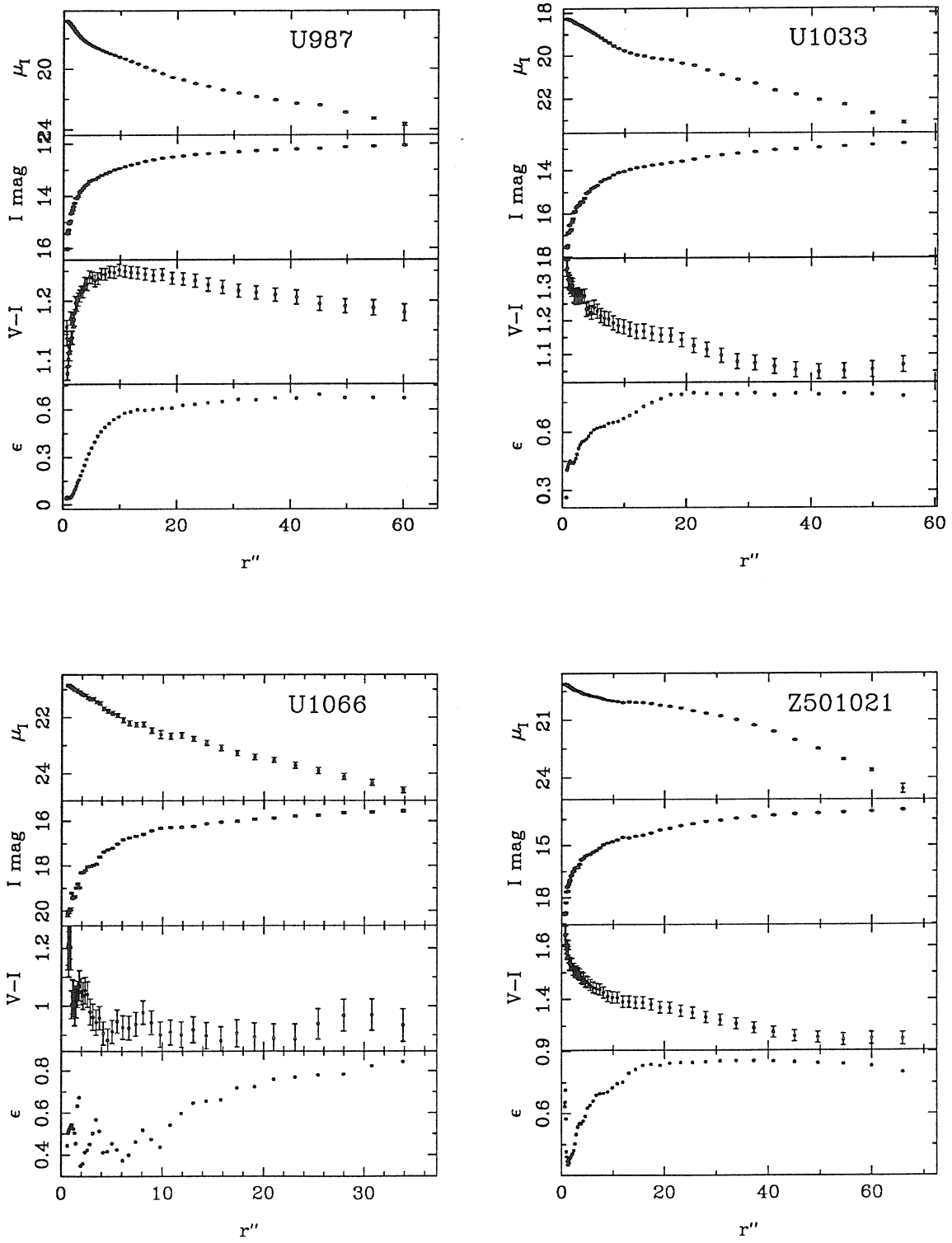

Figure 5.1 —- continued

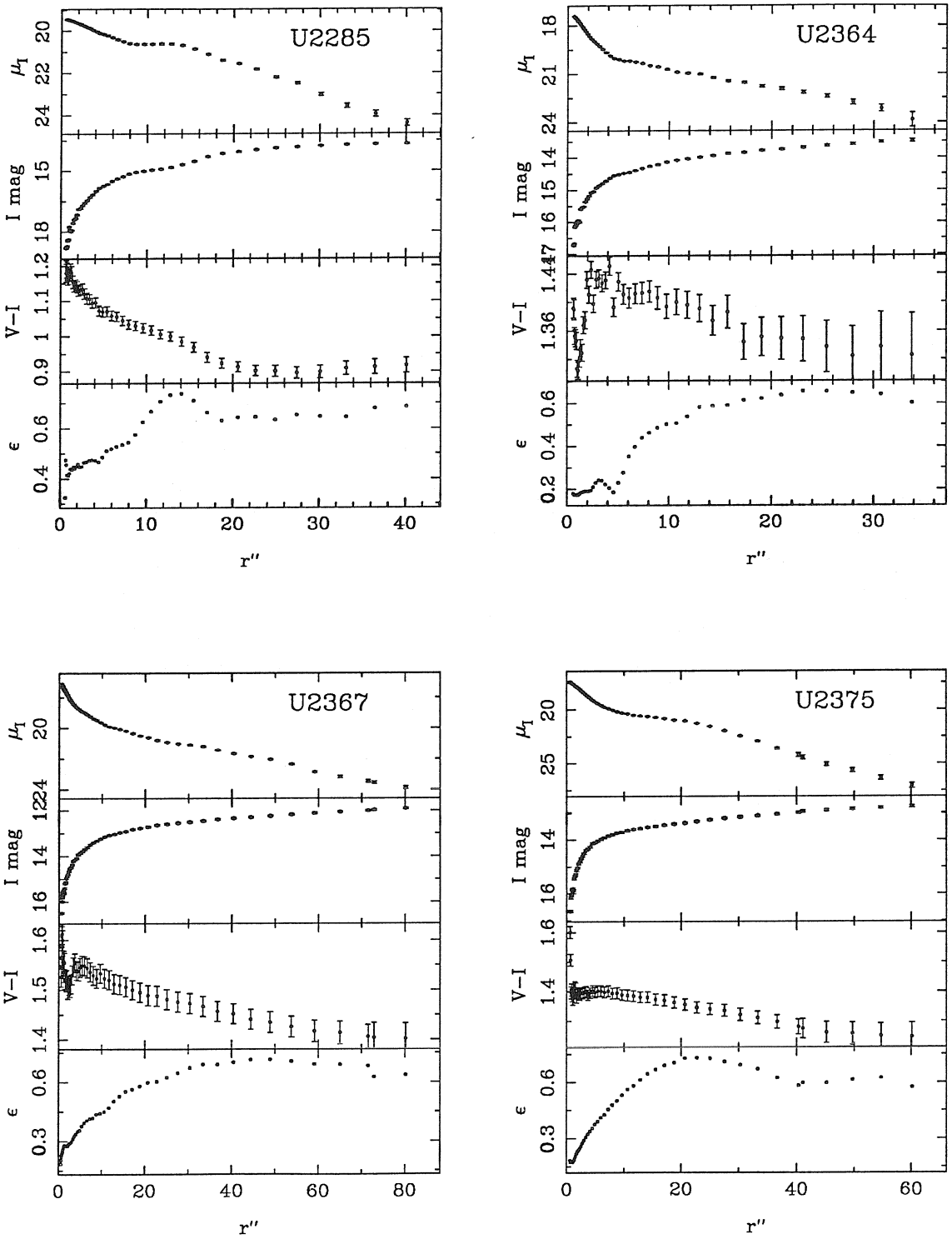

Figure 5.1 —- continued

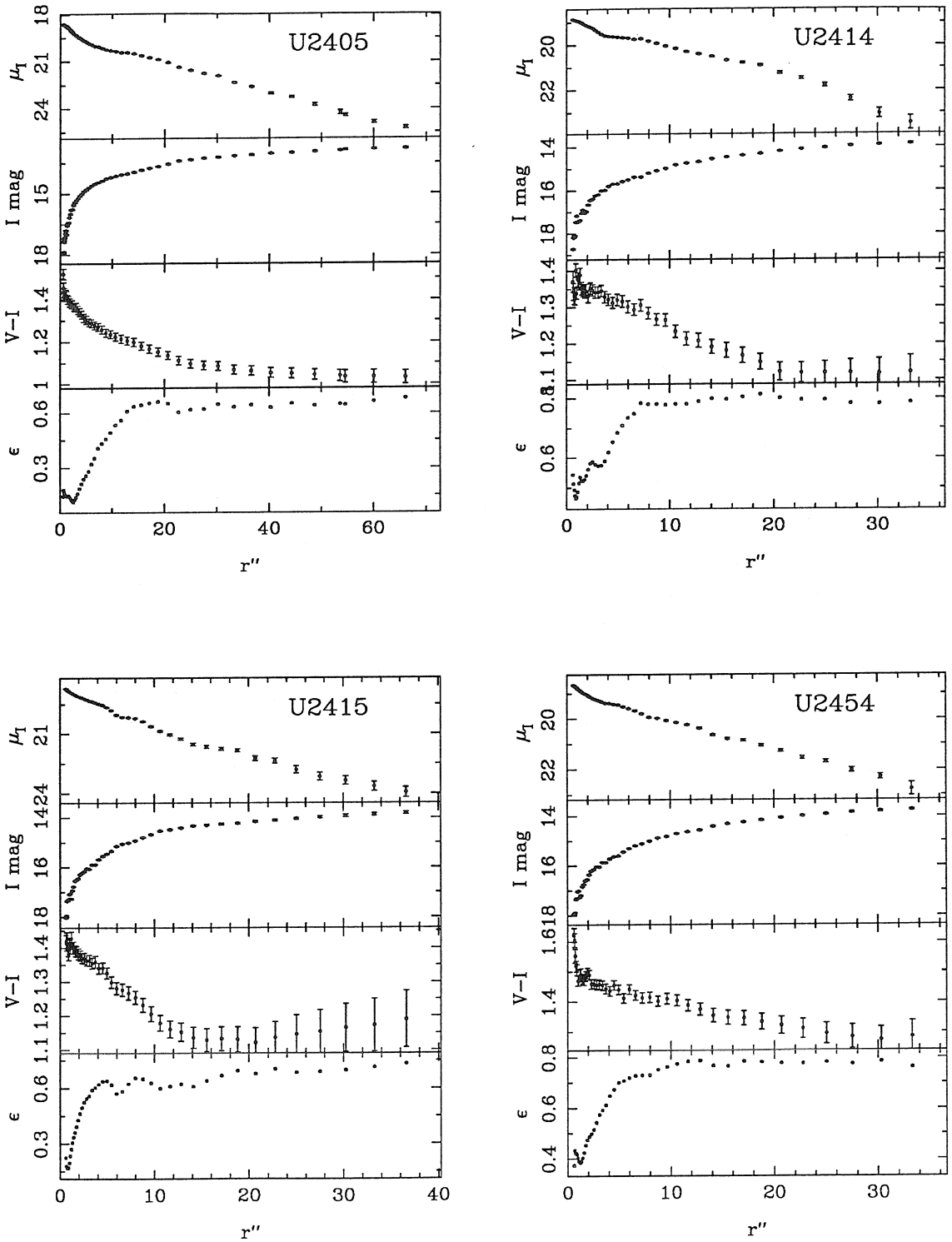

Figure 5.1 —- continued

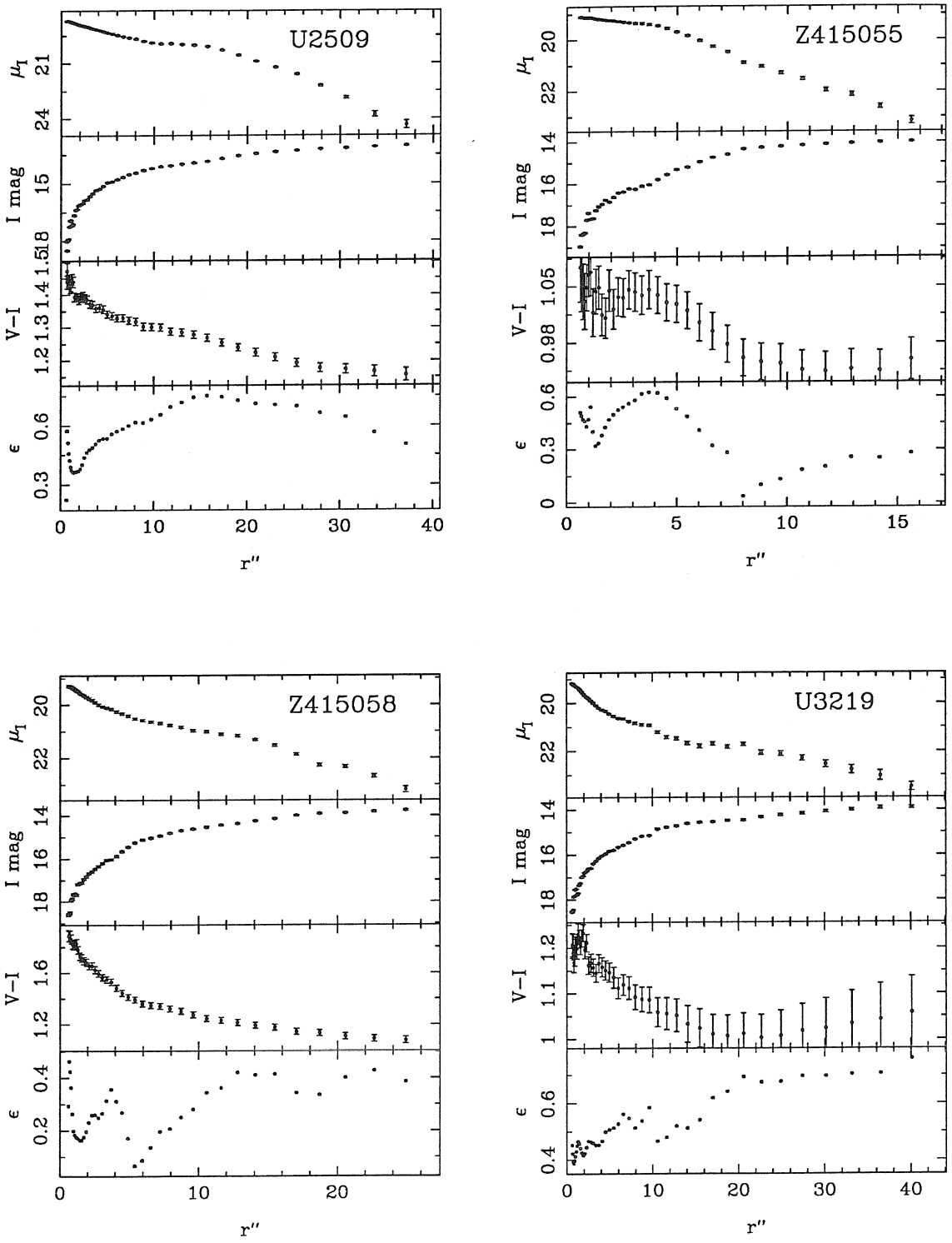

Figure 5.1 —- continued

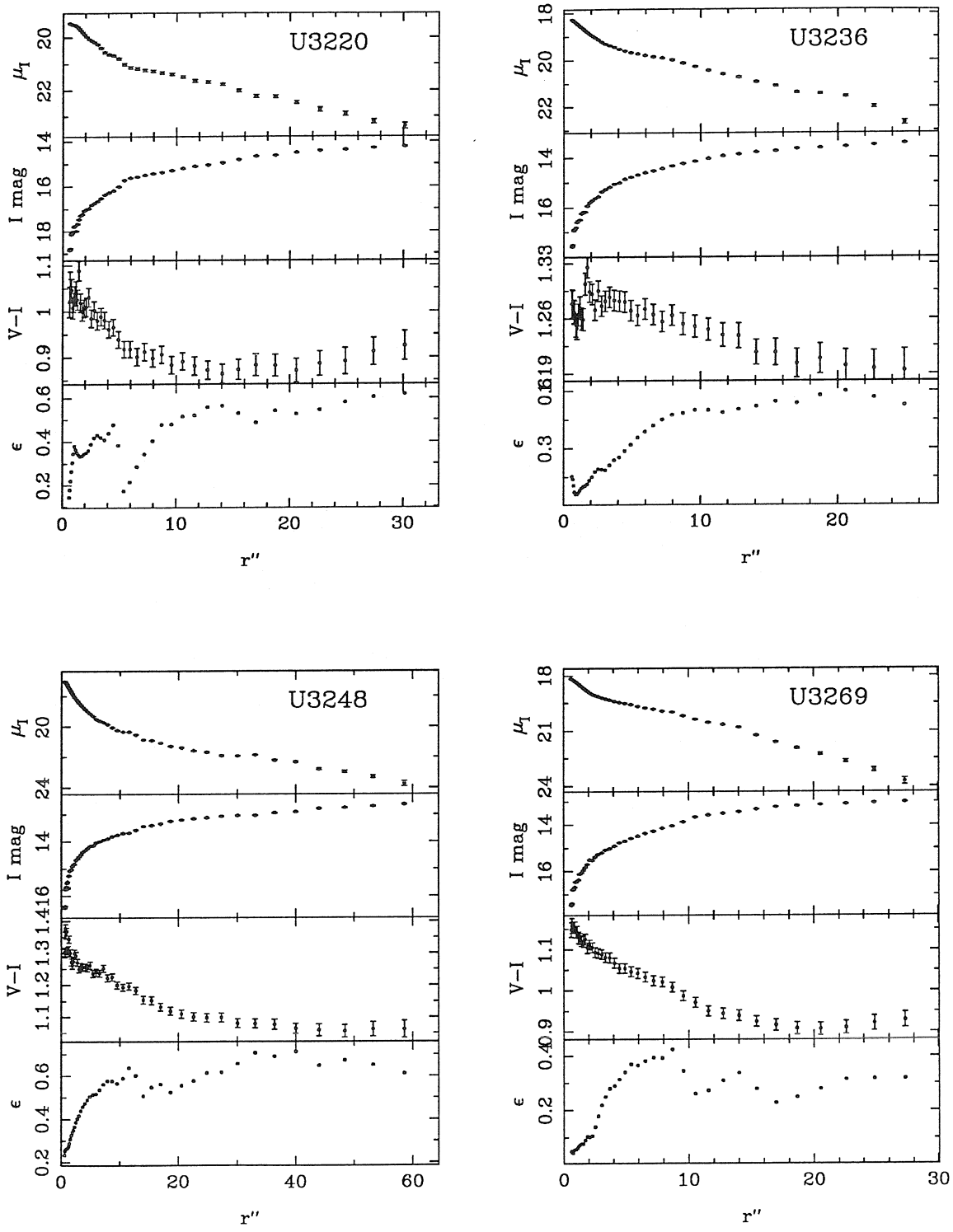

Figure 5.1 —- continued

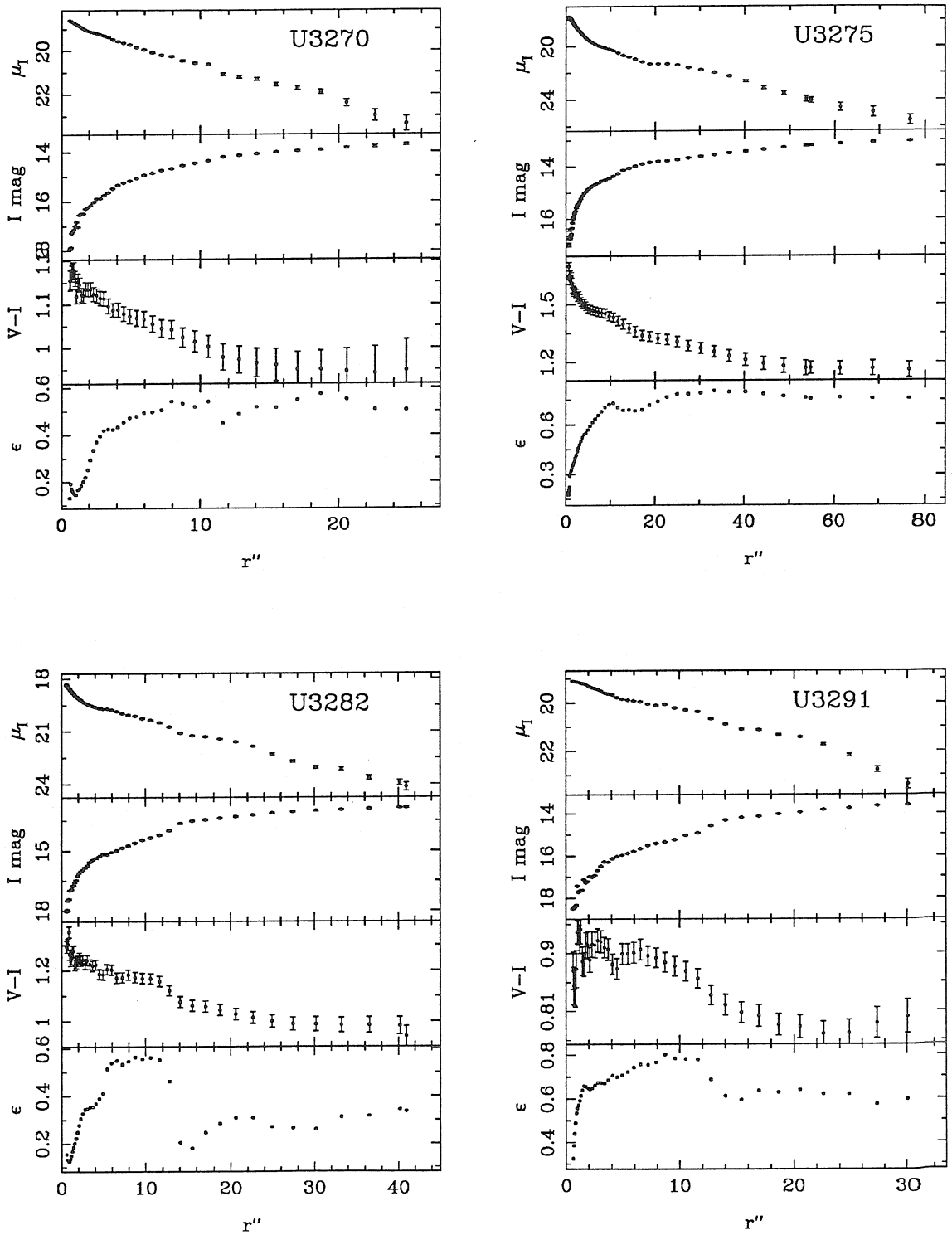

Figure 5.1 — continued

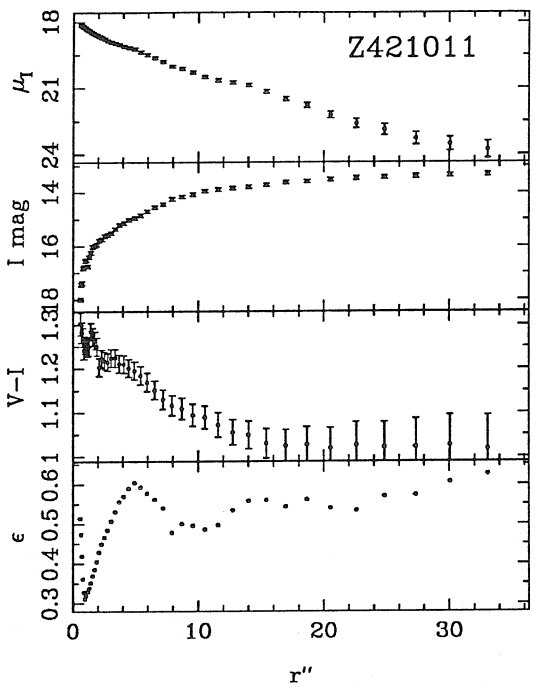

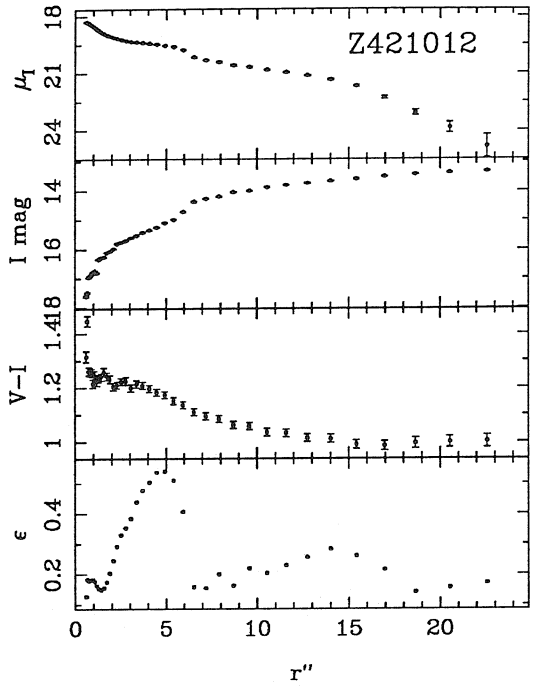

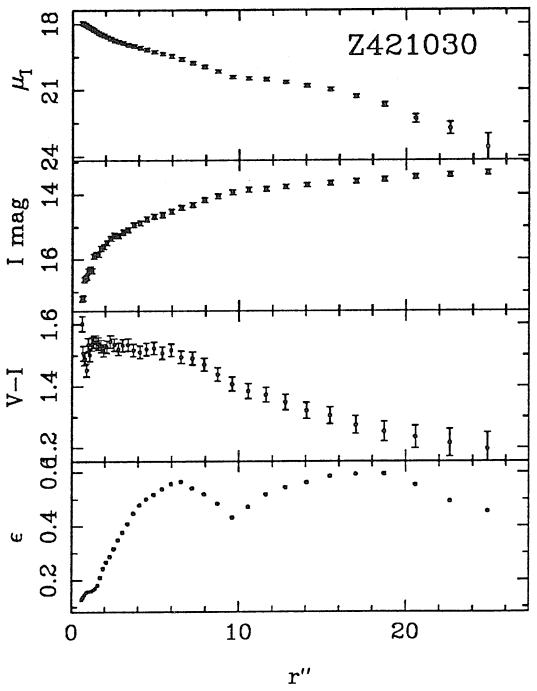

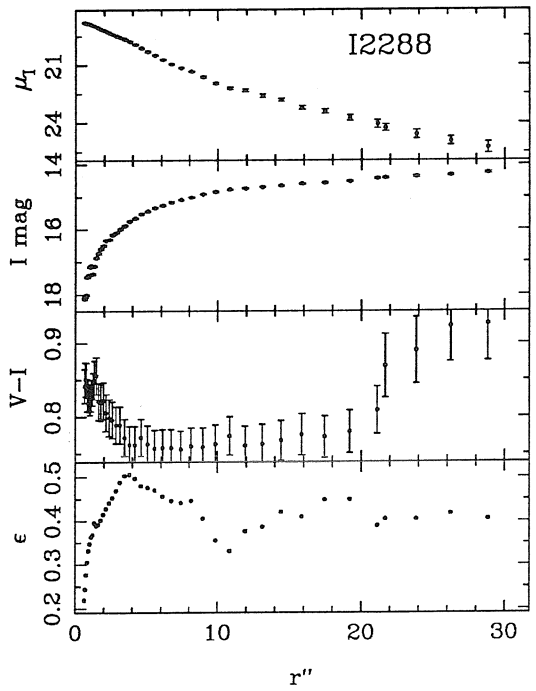

Figure 5.1 — continued

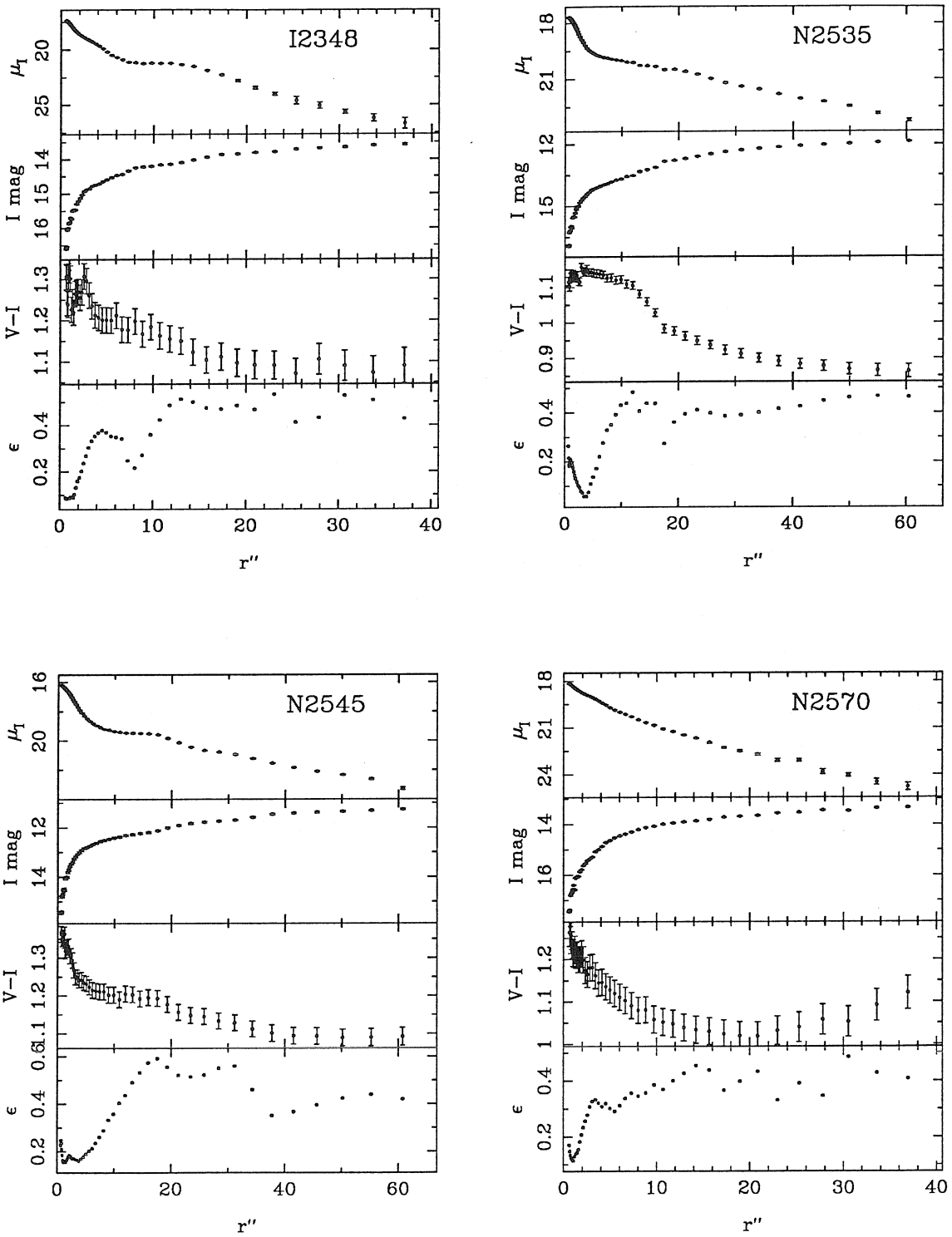

Figure 5.1 — continued

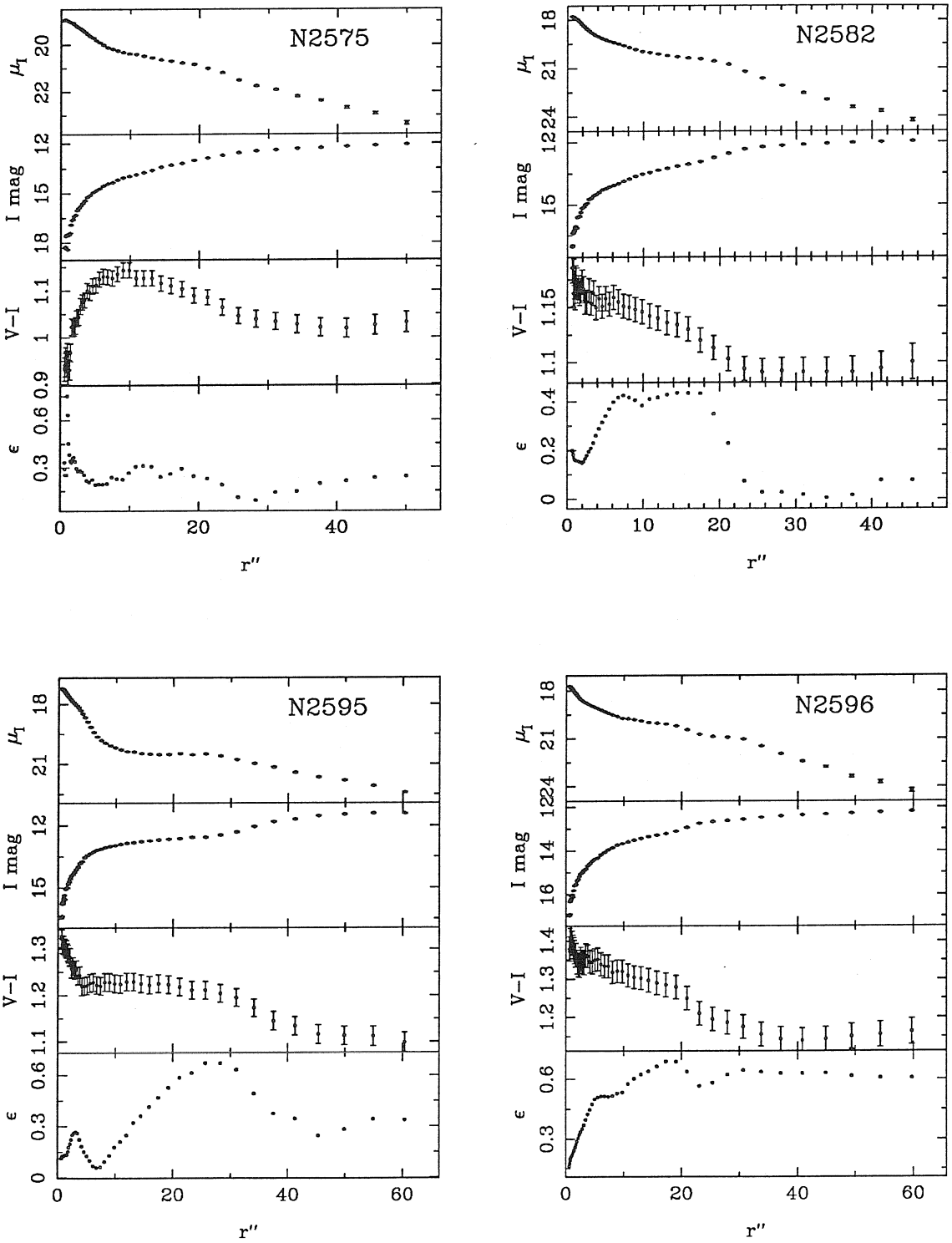

Figure 5.1 — continued

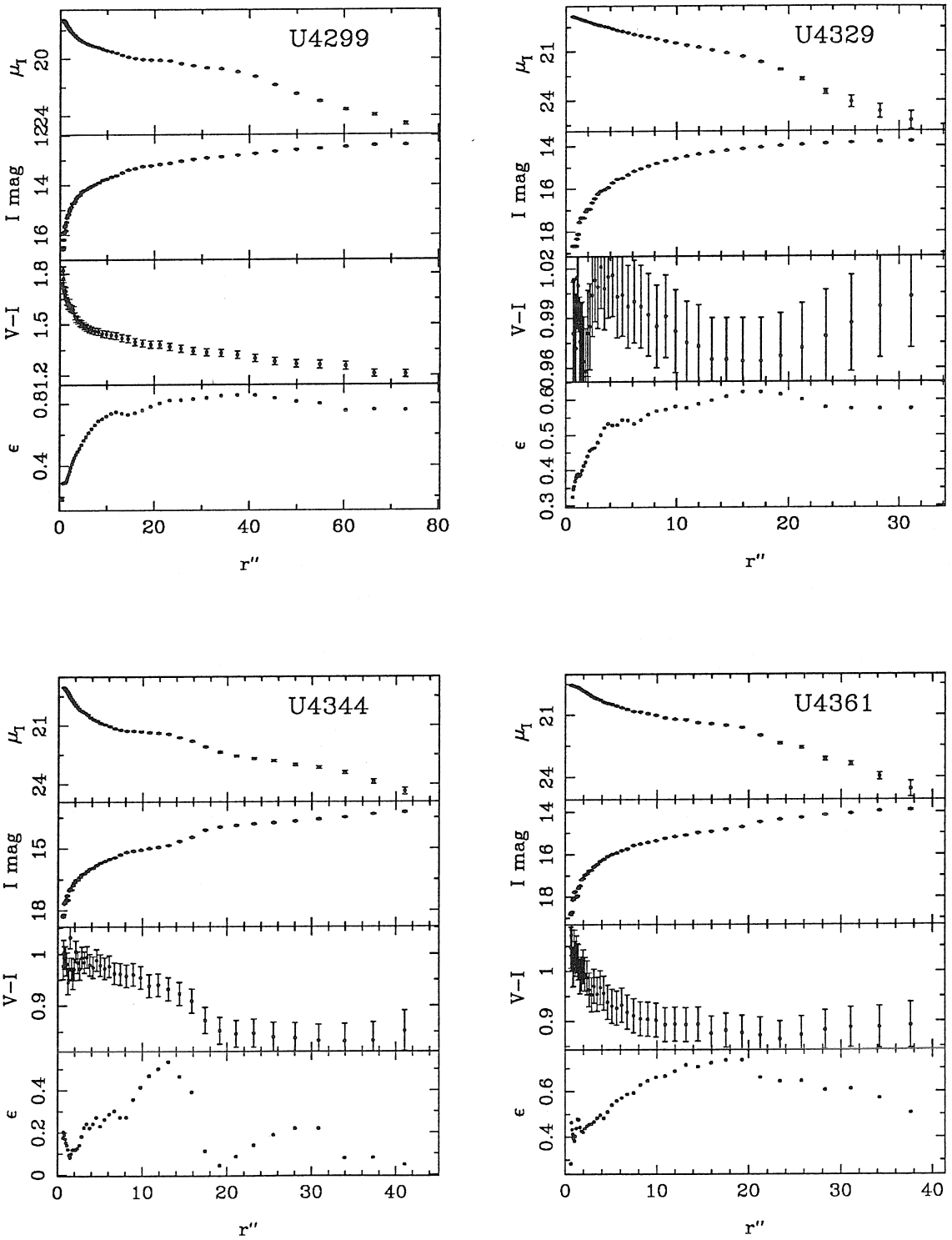

Figure 5.1 — continued

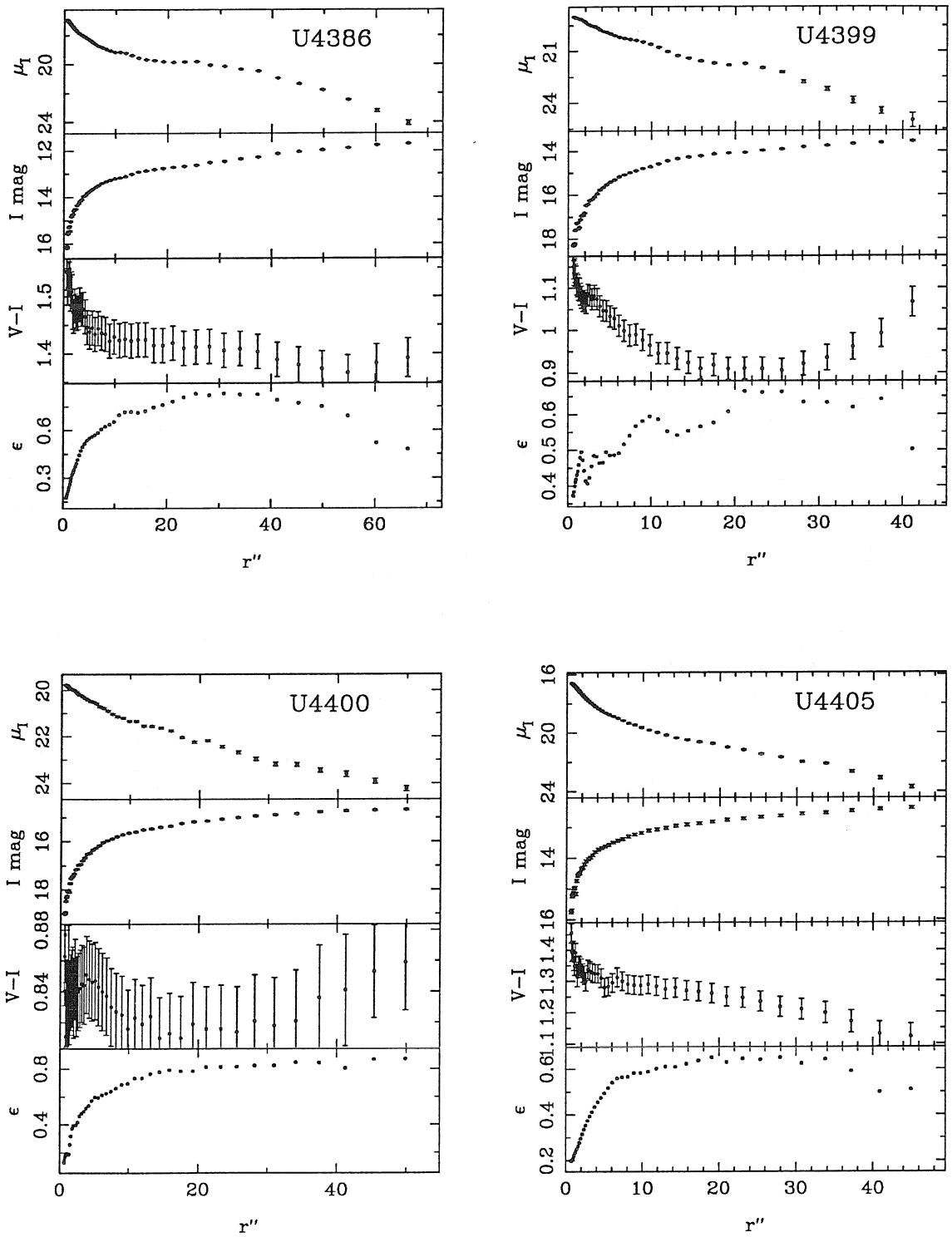

Figure 5.1 — continued

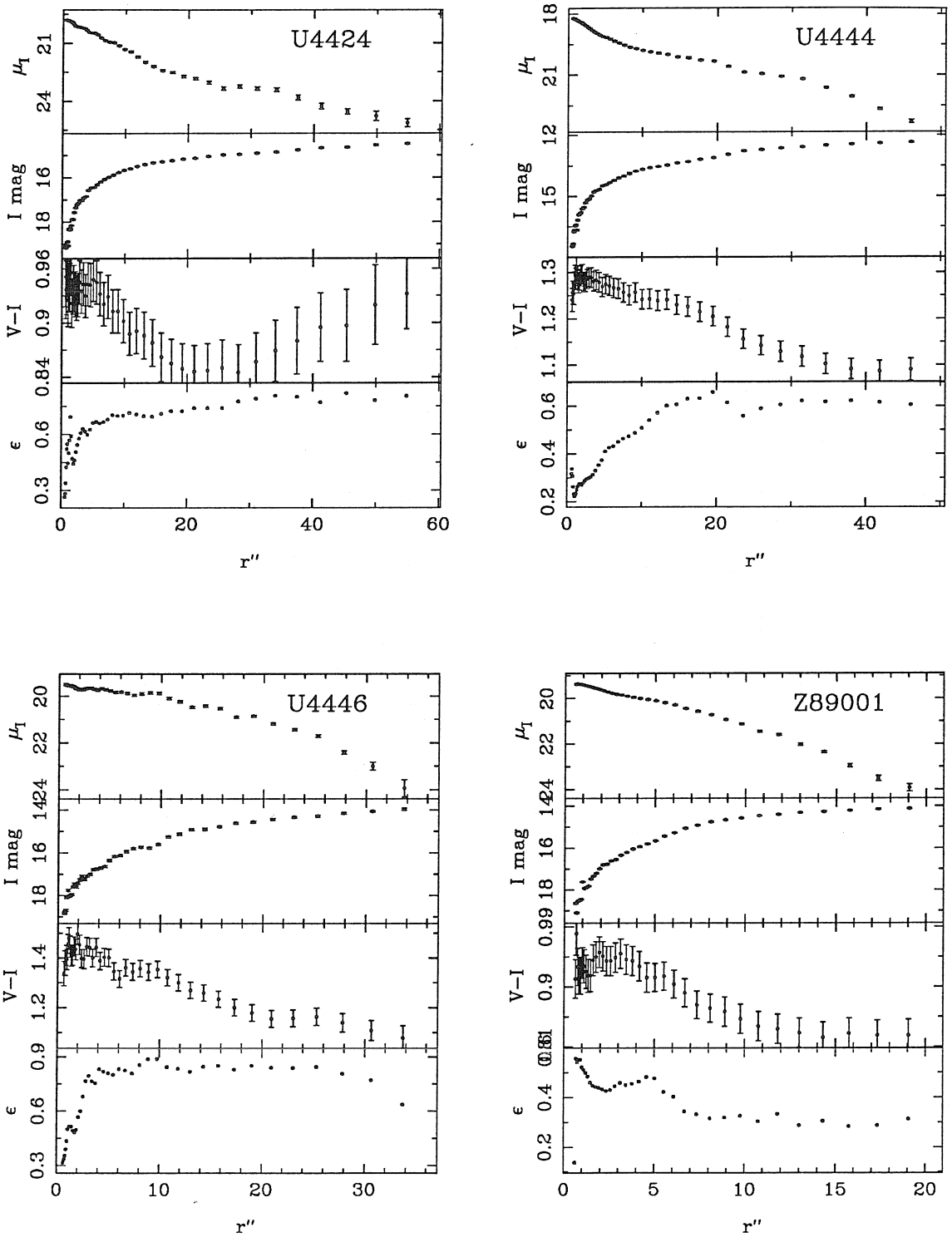

Figure 5.1 — continued

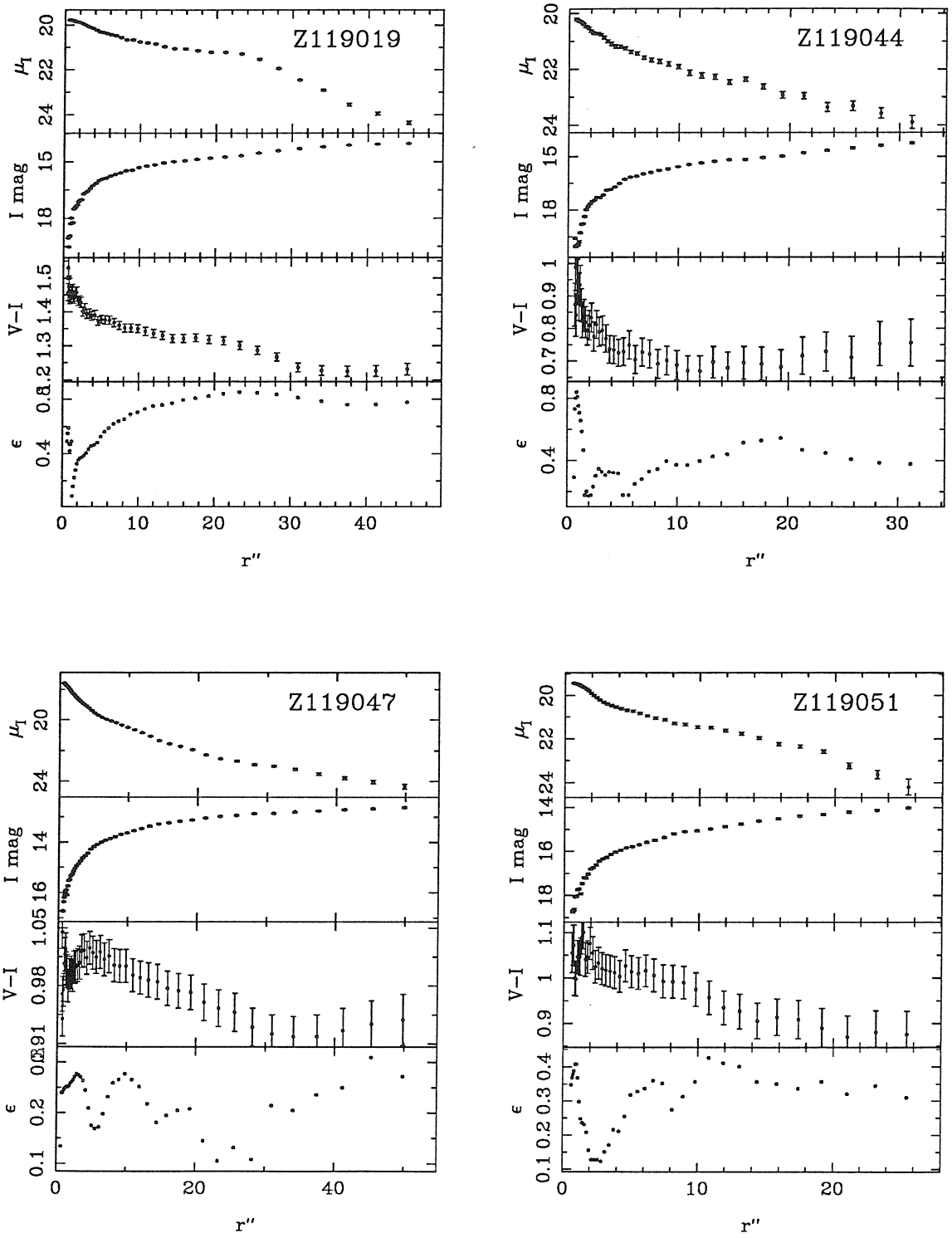

Figure 5.1 — continued

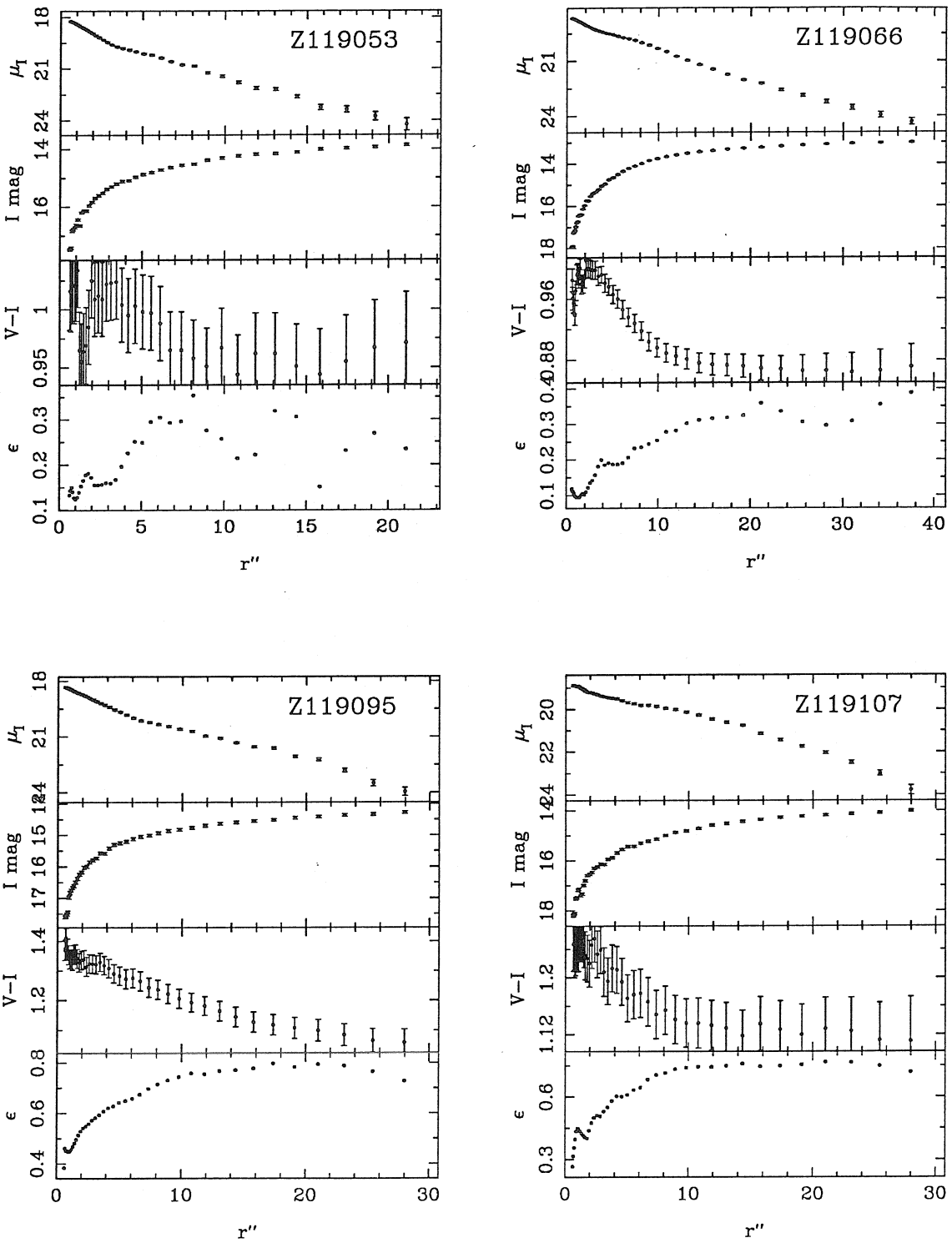

Figure 5.1 — continued

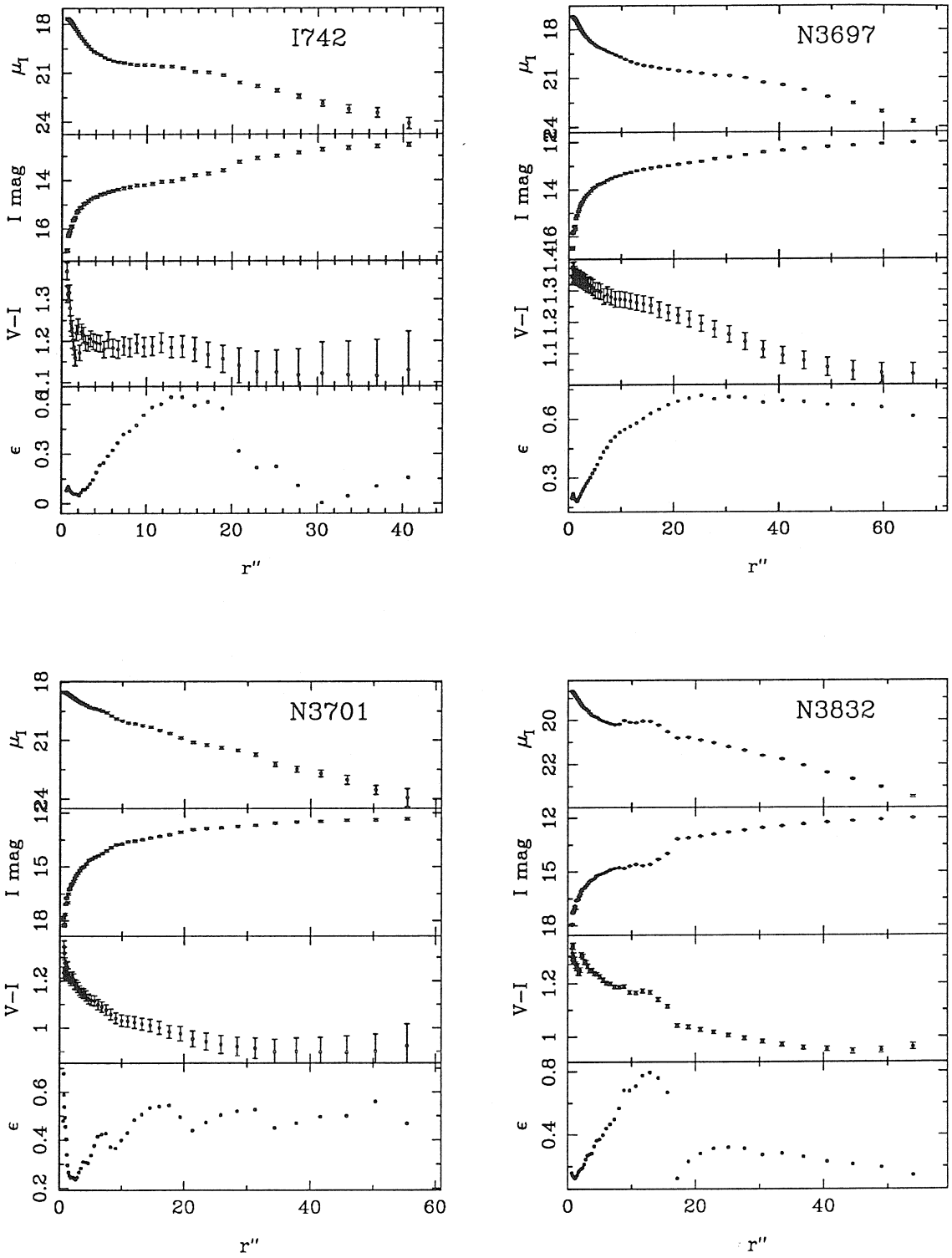

Figure 5.1 — continued

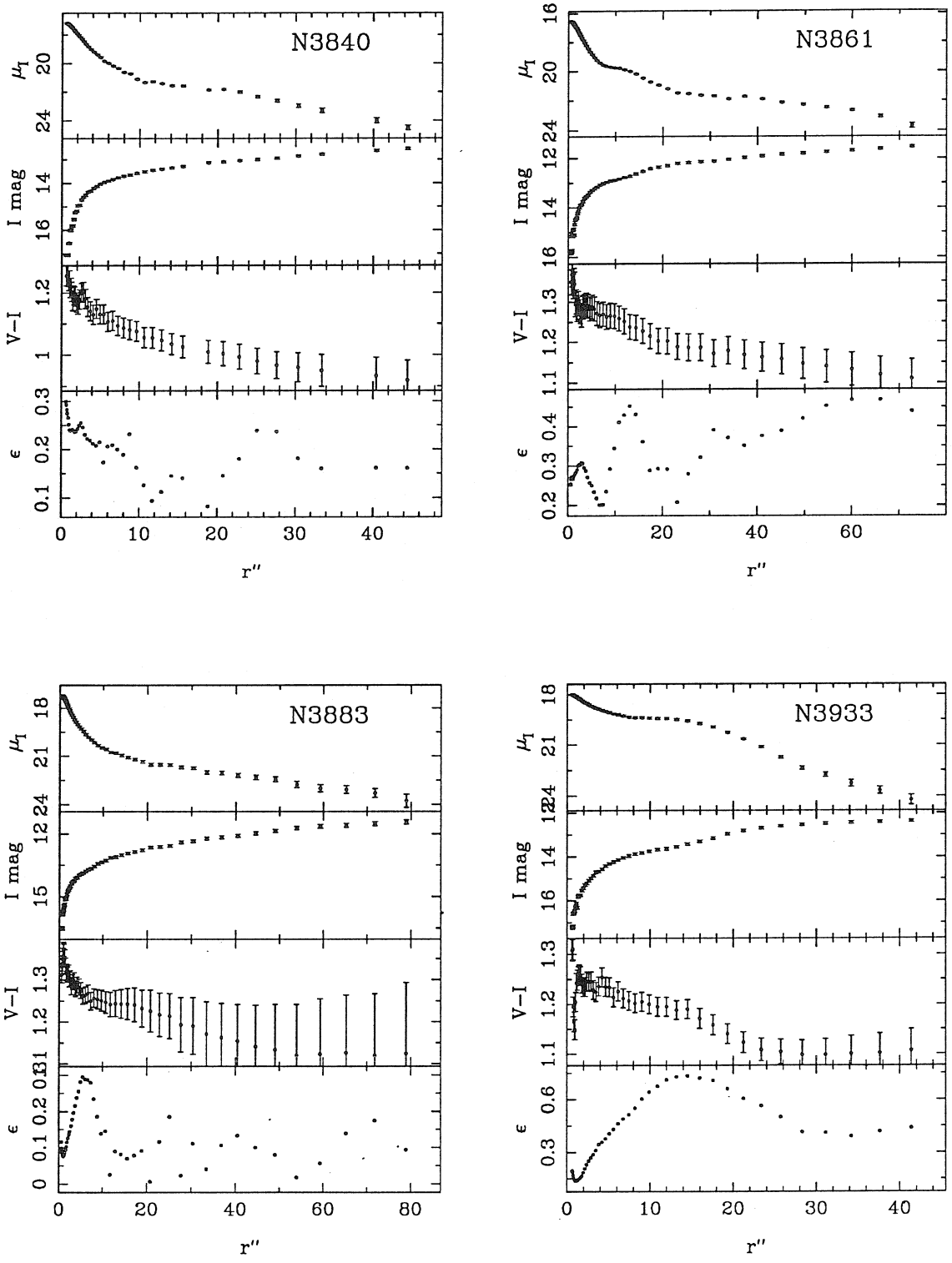

Figure 5.1 — continued

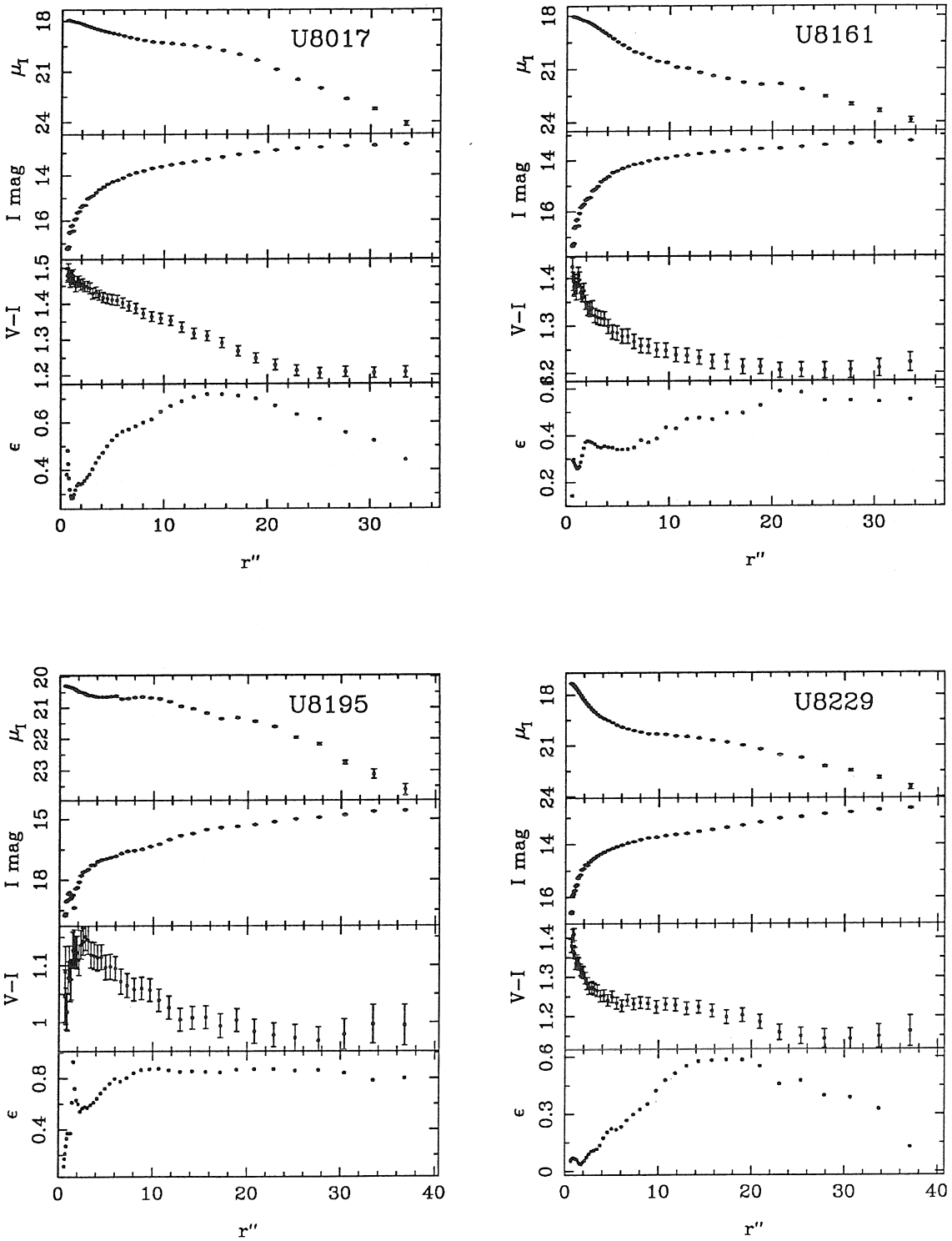

Figure 5.1 — continued

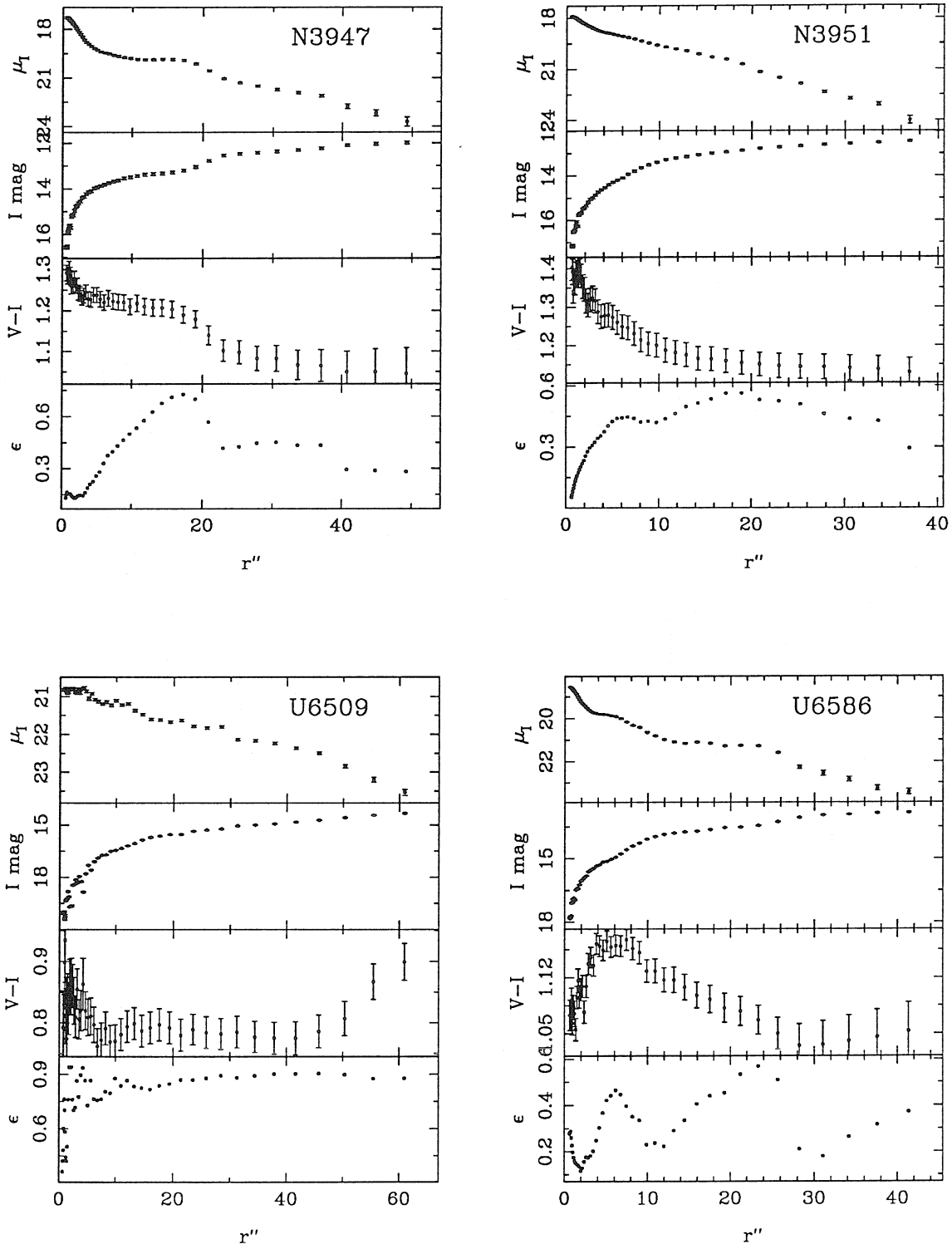

Figure 5.1 — continued

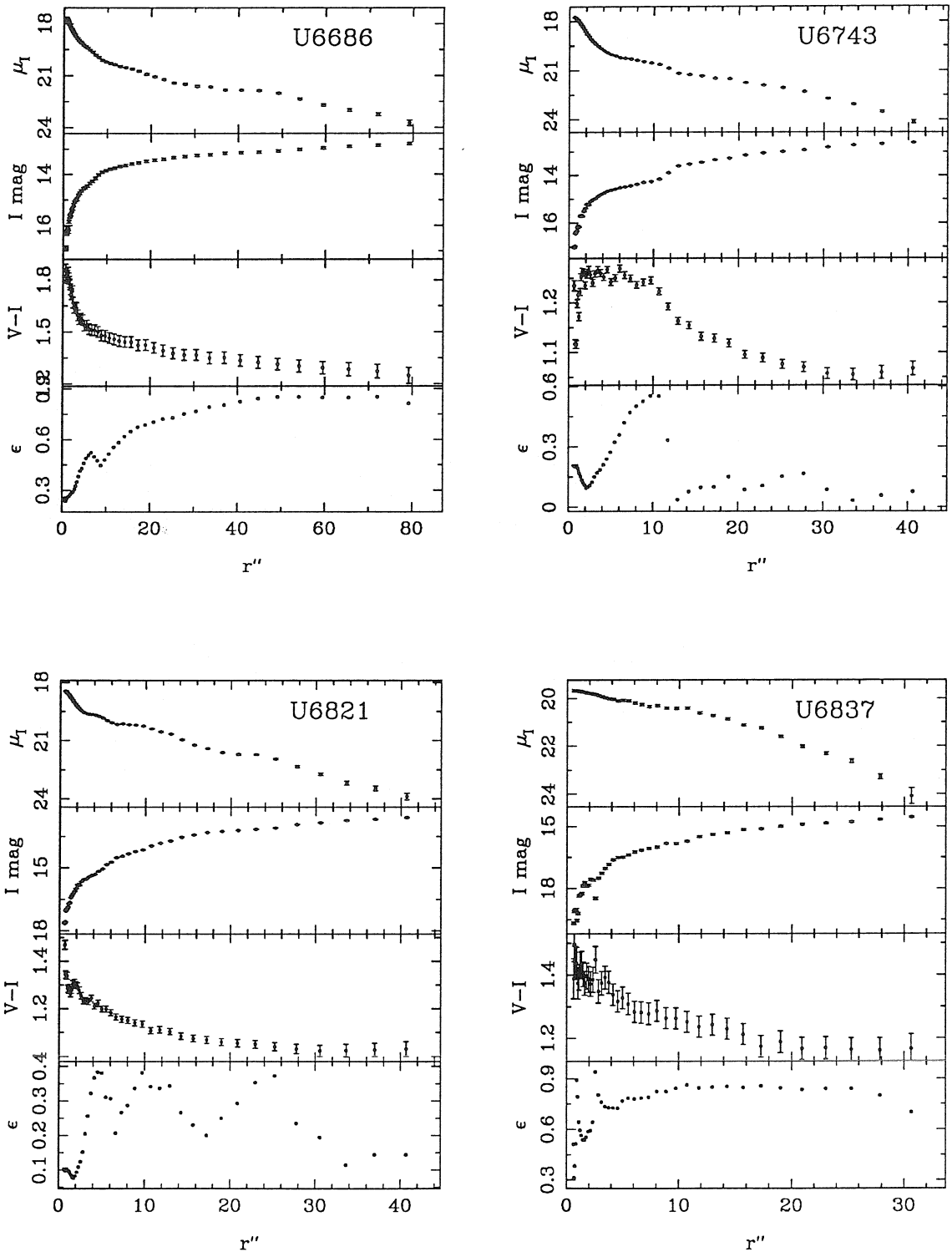

Figure 5.1 — continued

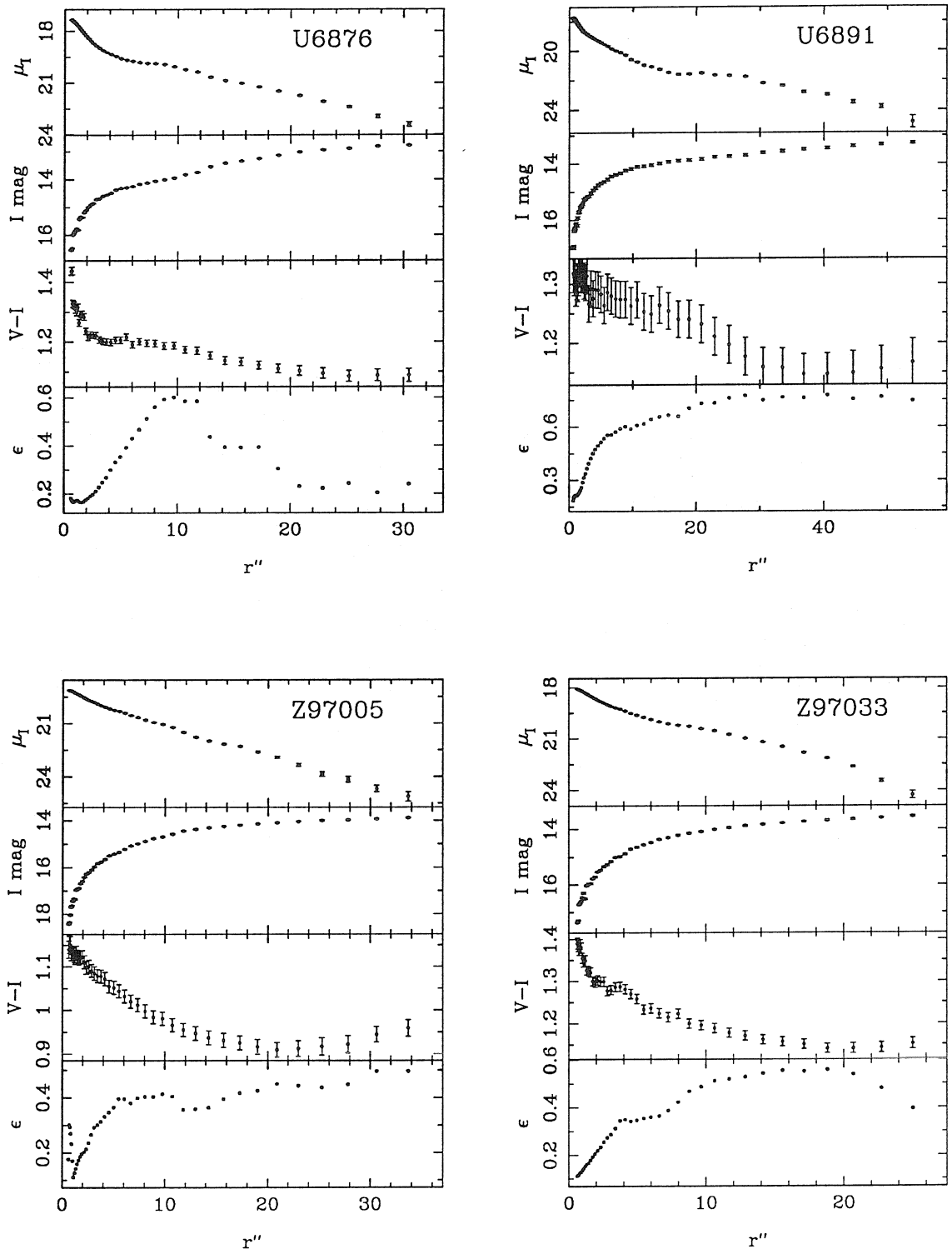

Figure 5.1 — continued

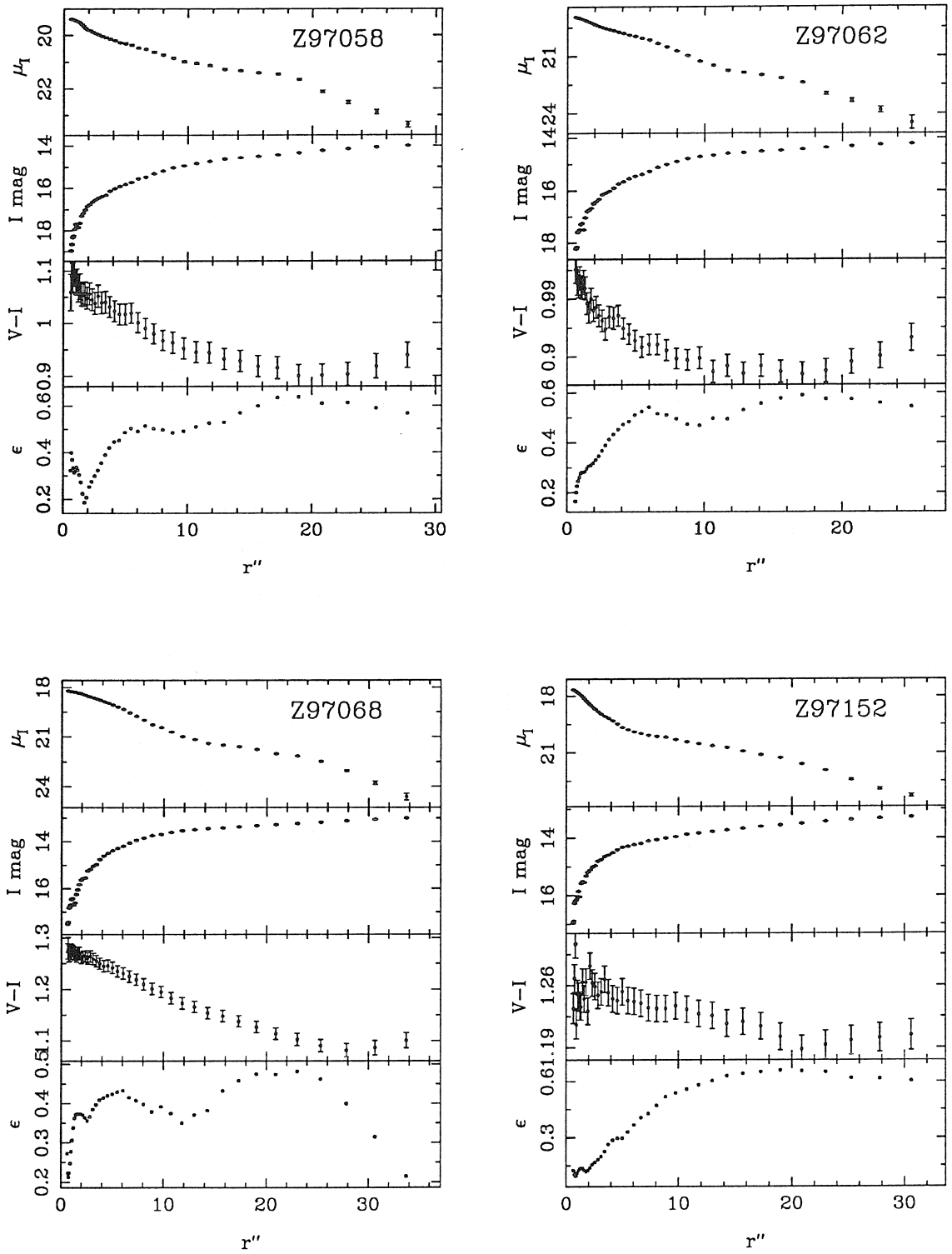

Figure 5.1 — continued

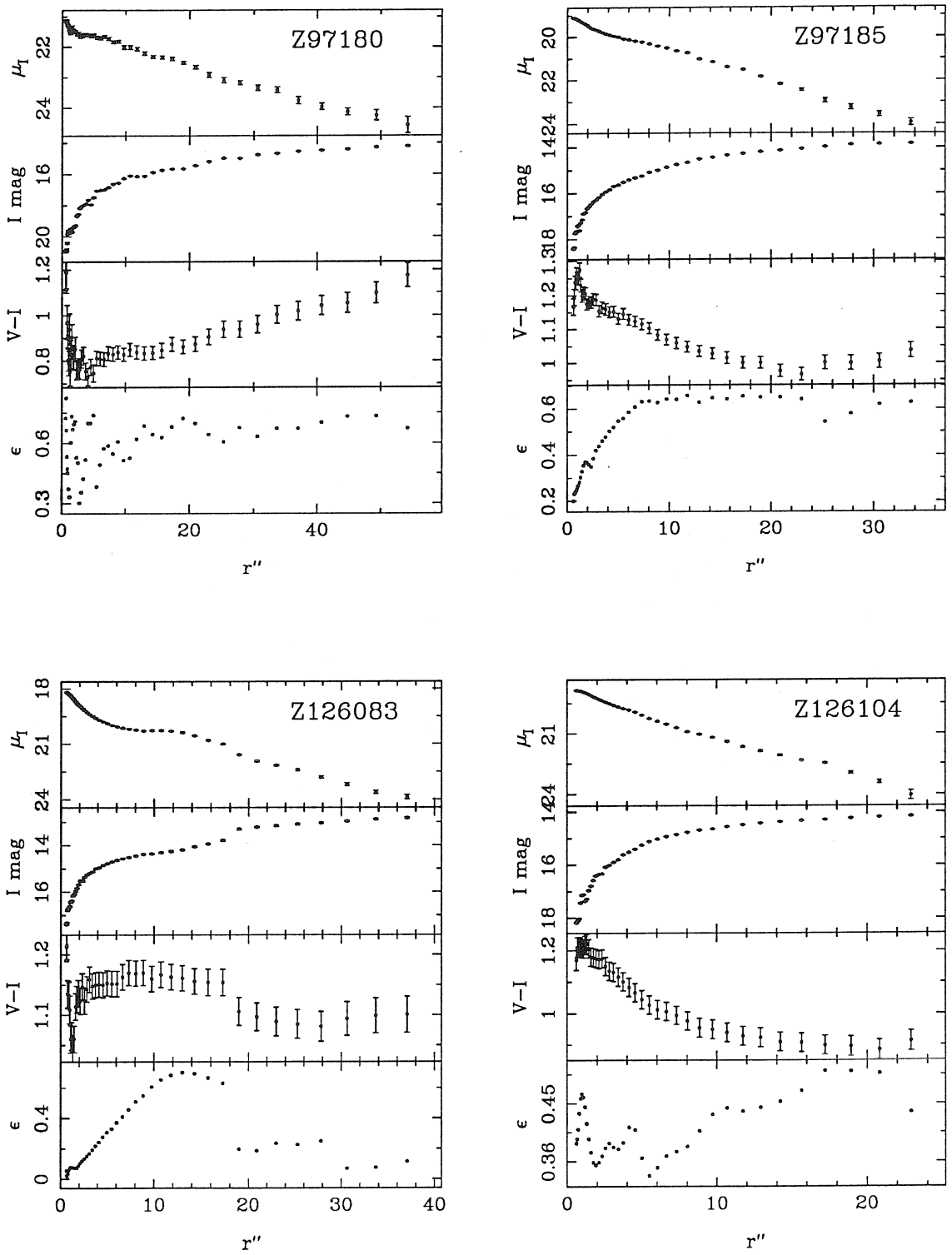

Figure 5.1 — continued

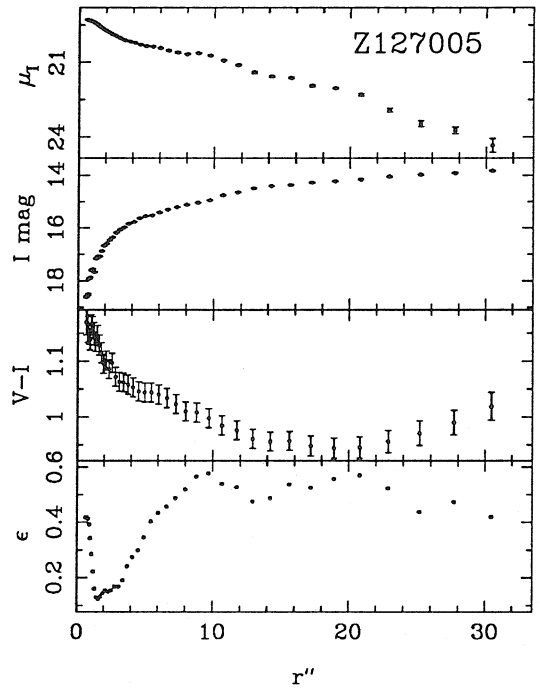

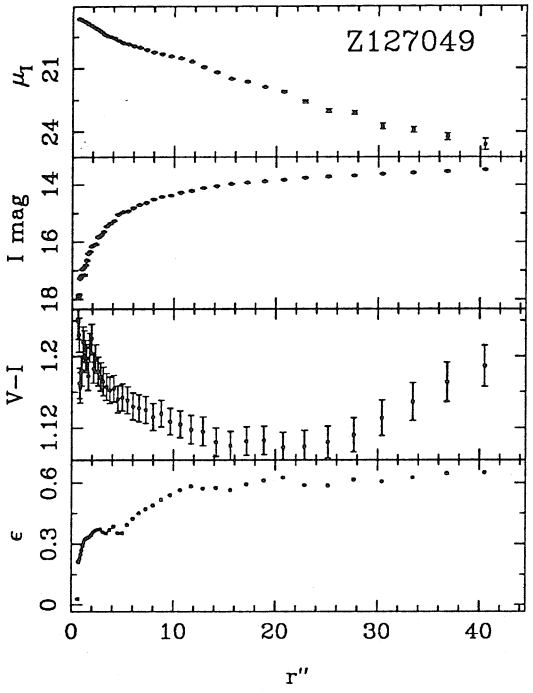

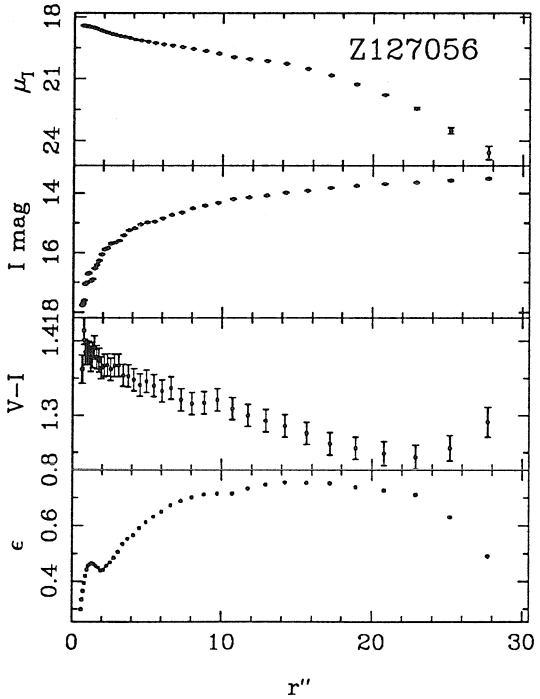

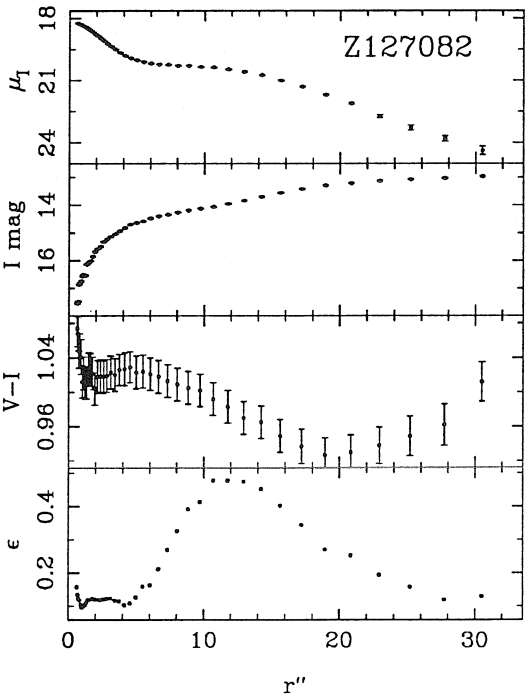

Figure 5.1 — continued

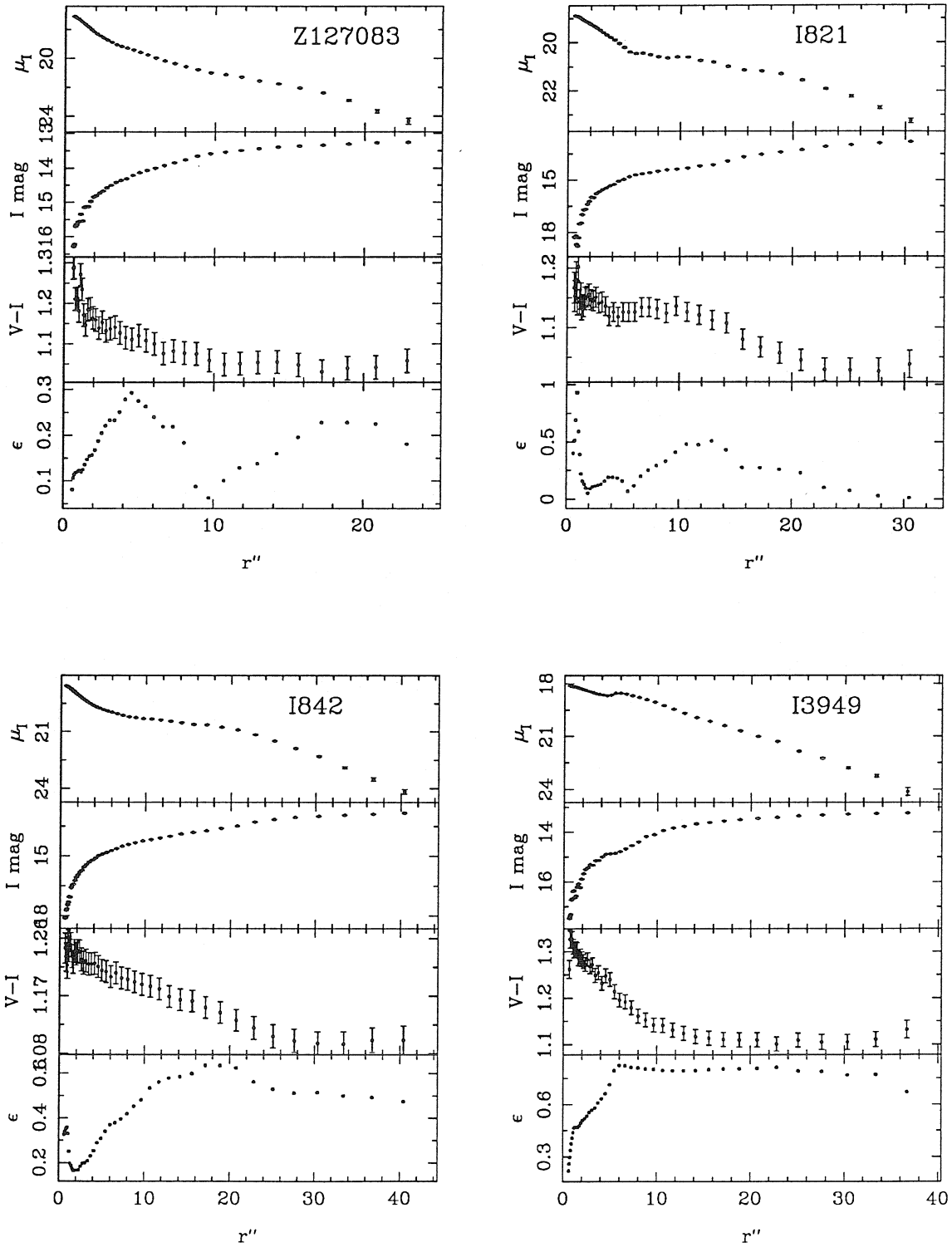

Figure 5.1 — continued

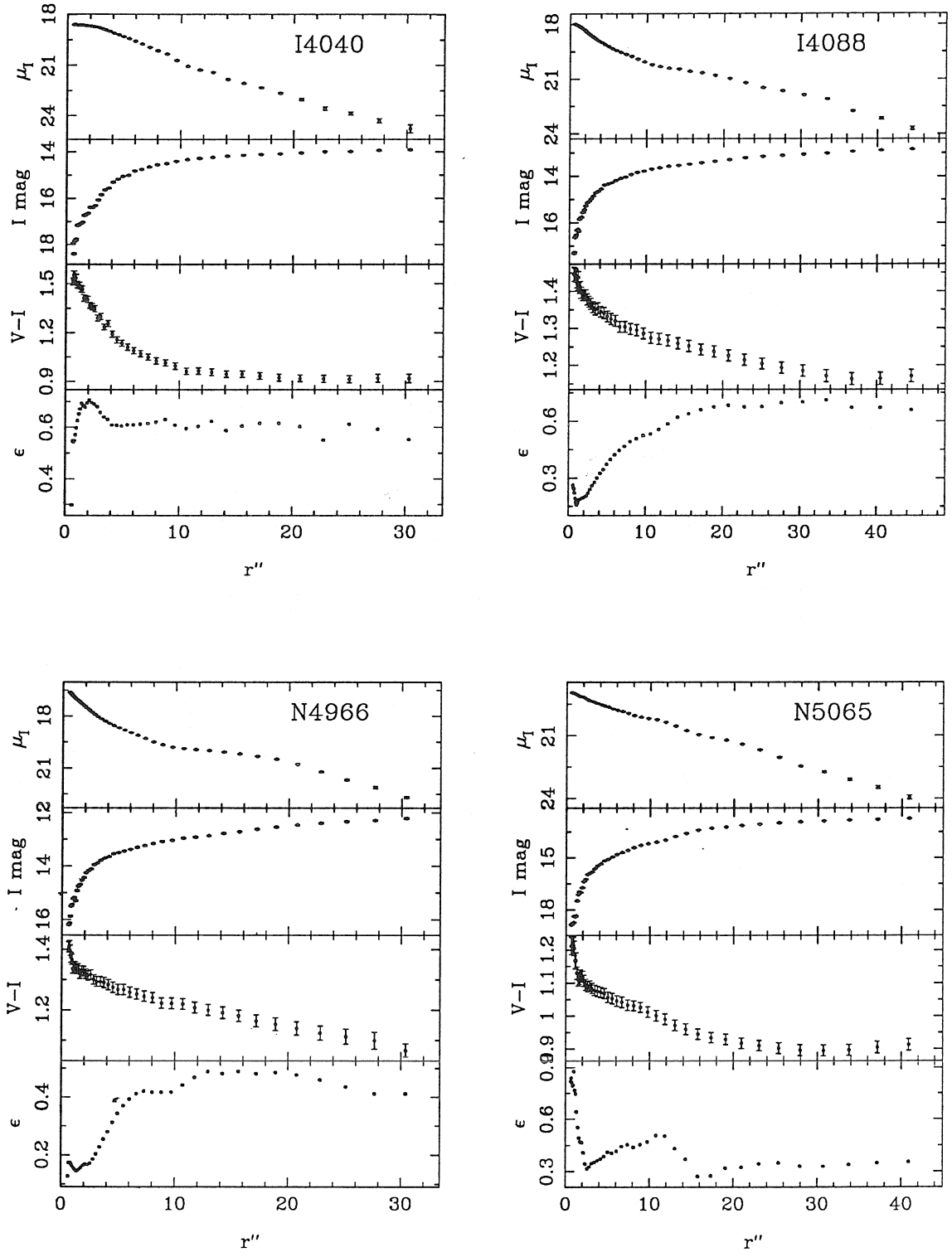

Figure 5.1 — continued

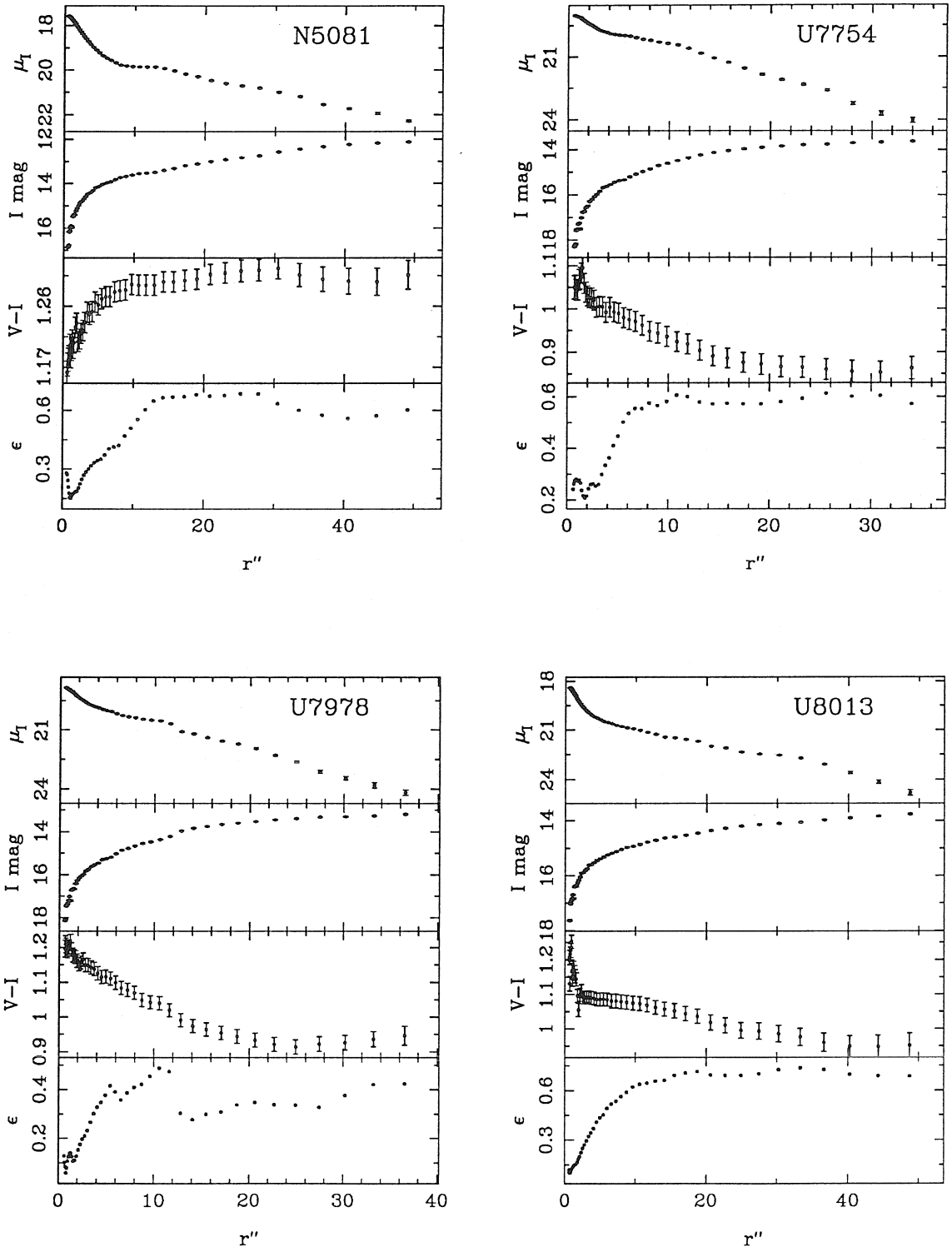

Figure 5.1 — continued

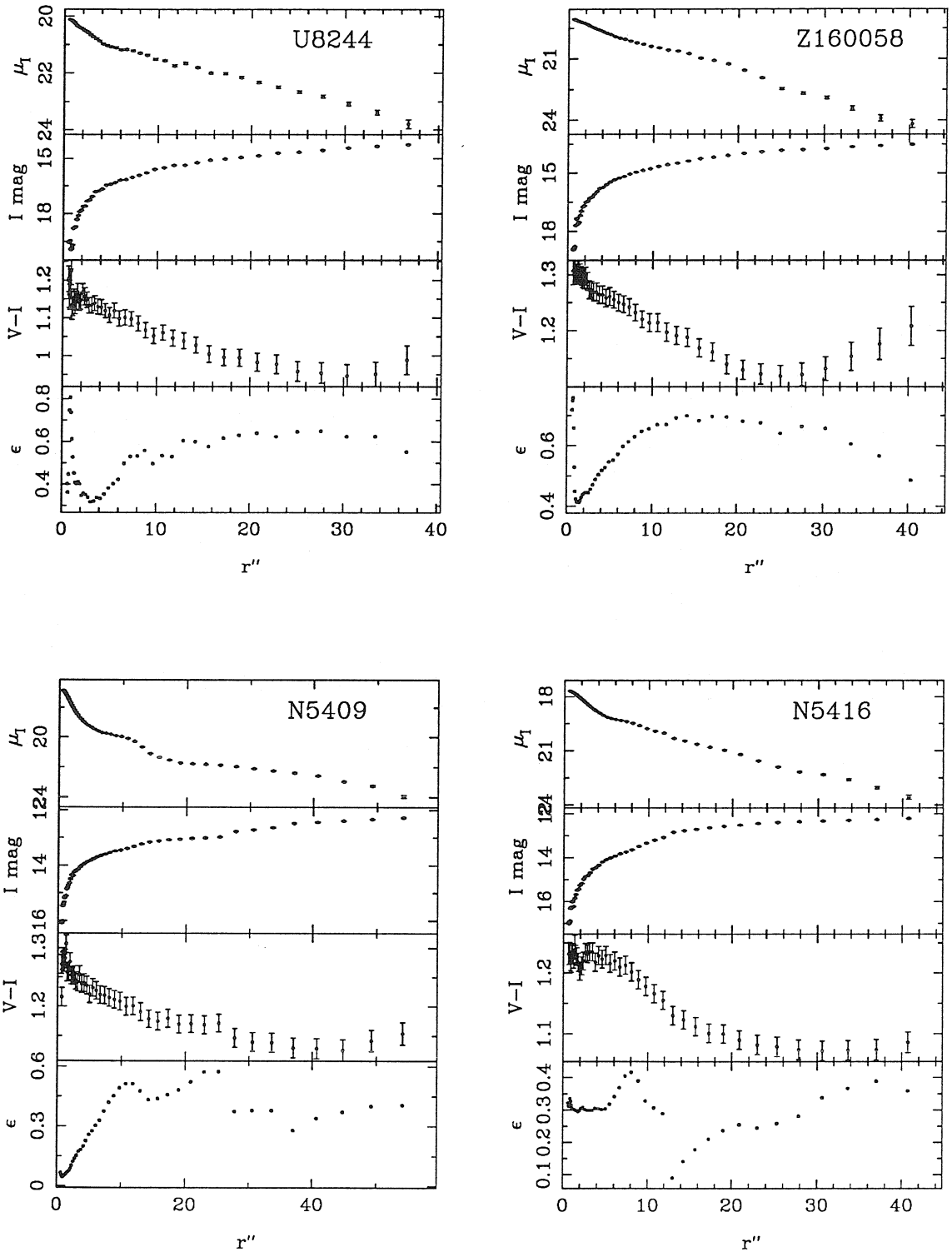

Figure 5.1 — continued

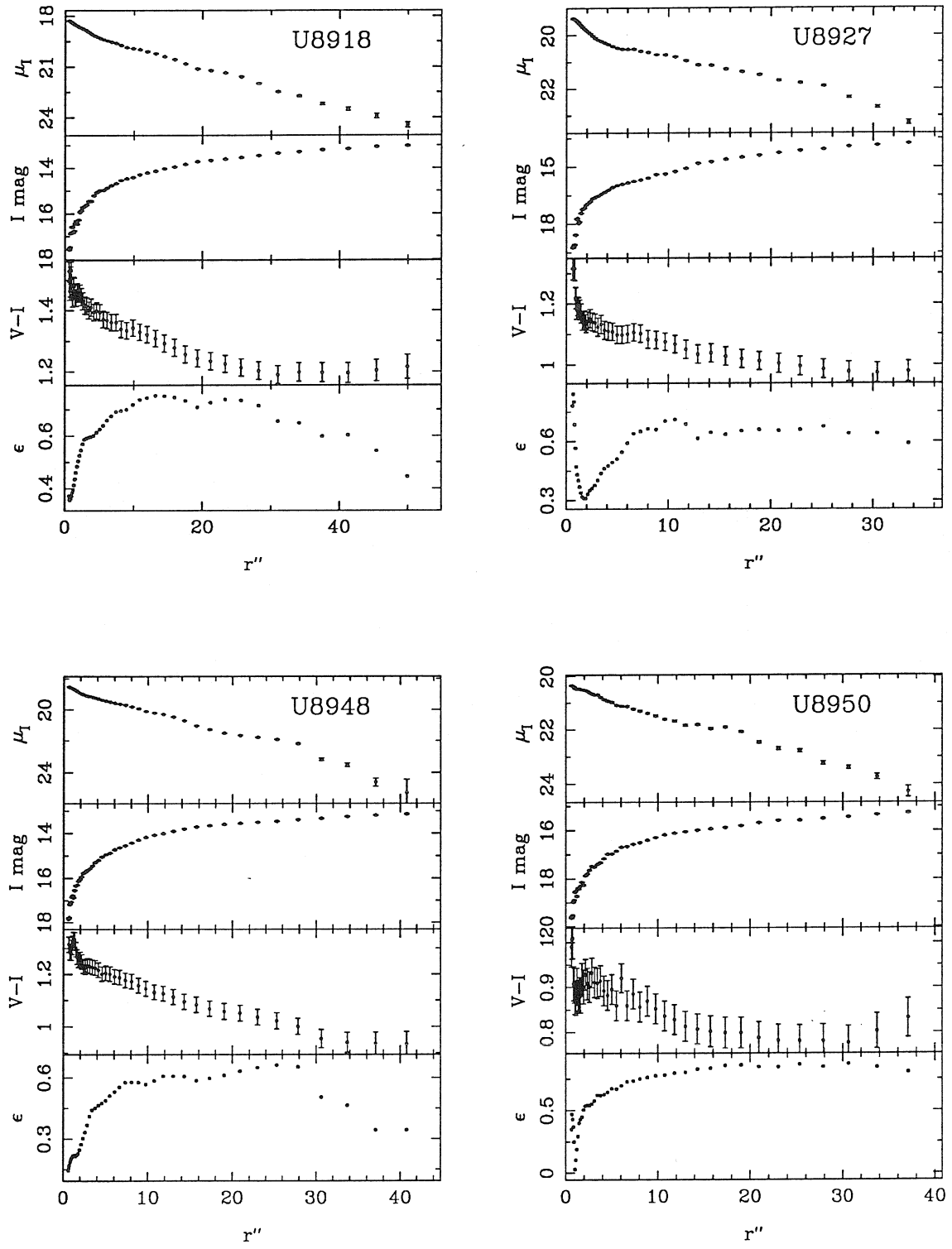

Figure 5.1 — continued

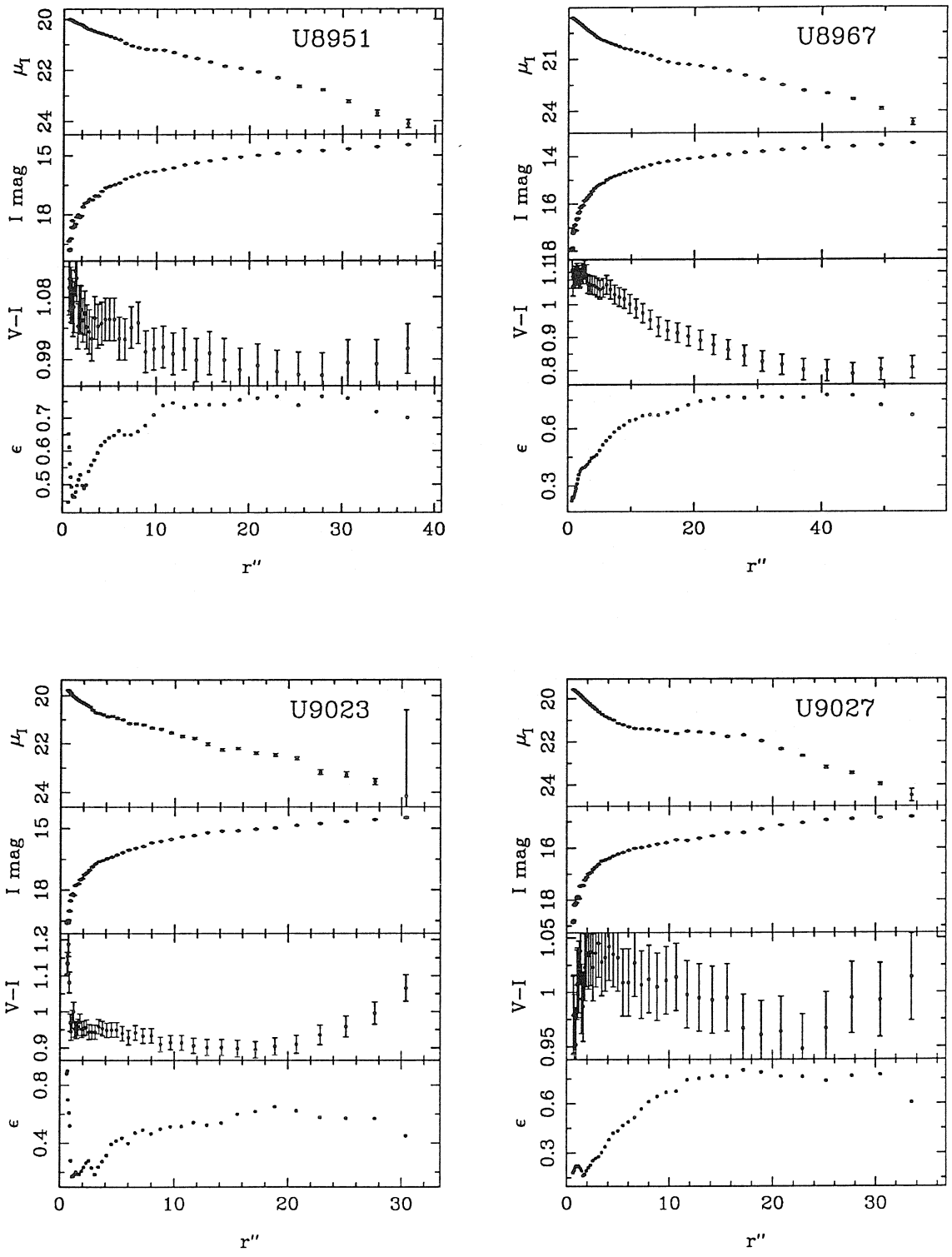

Figure 5.1 — continued

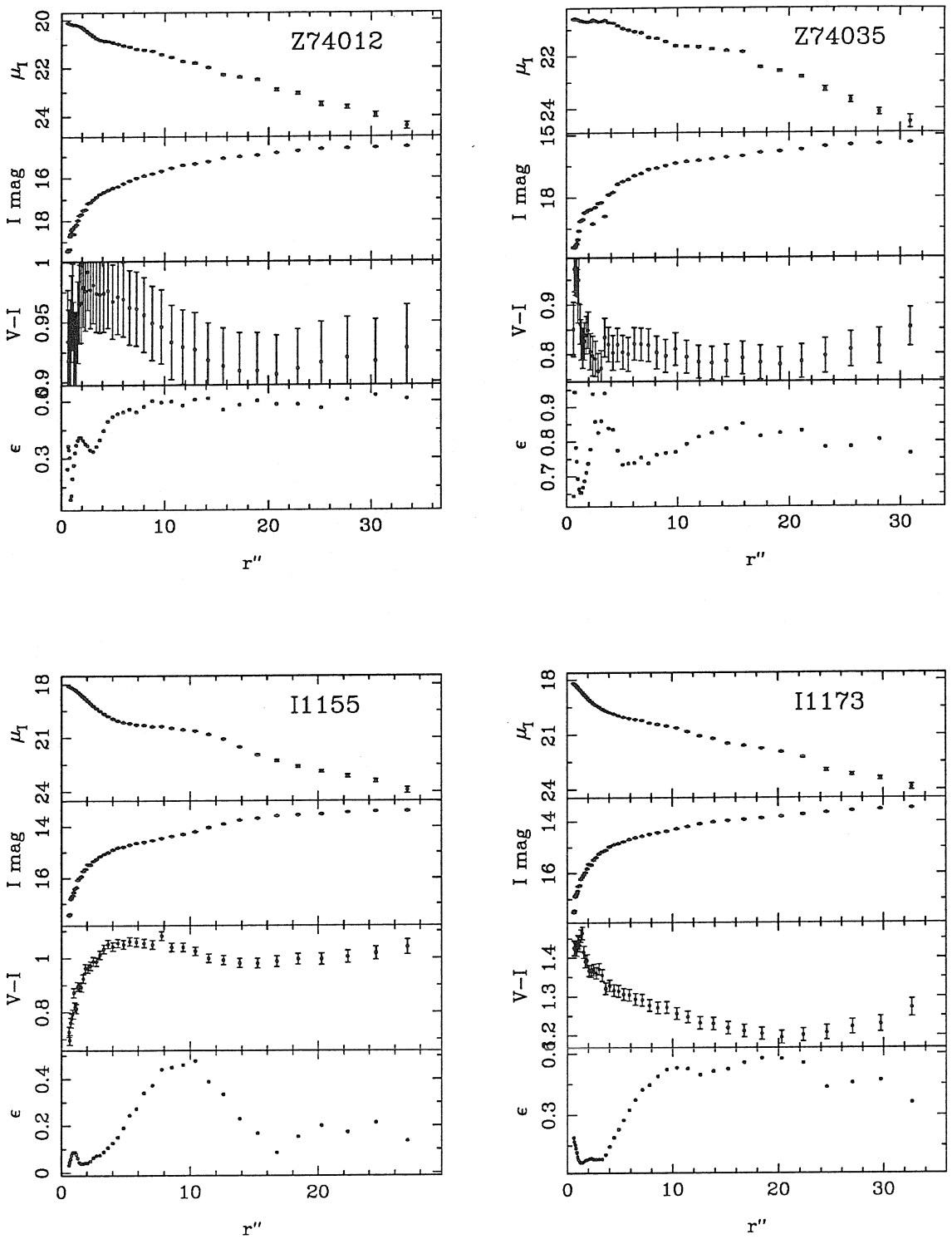

Figure 5.1 — continued

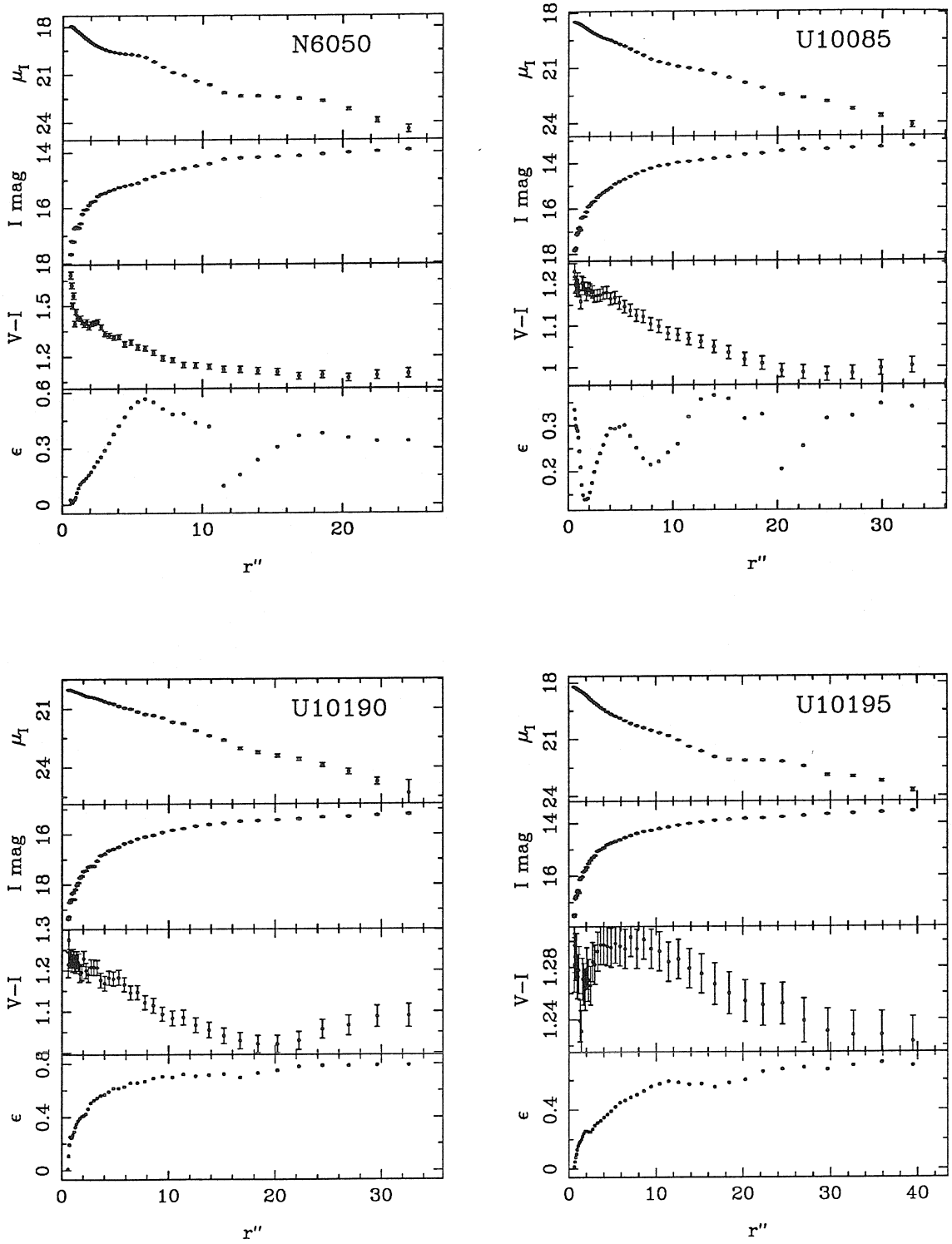

Figure 5.1 — continued

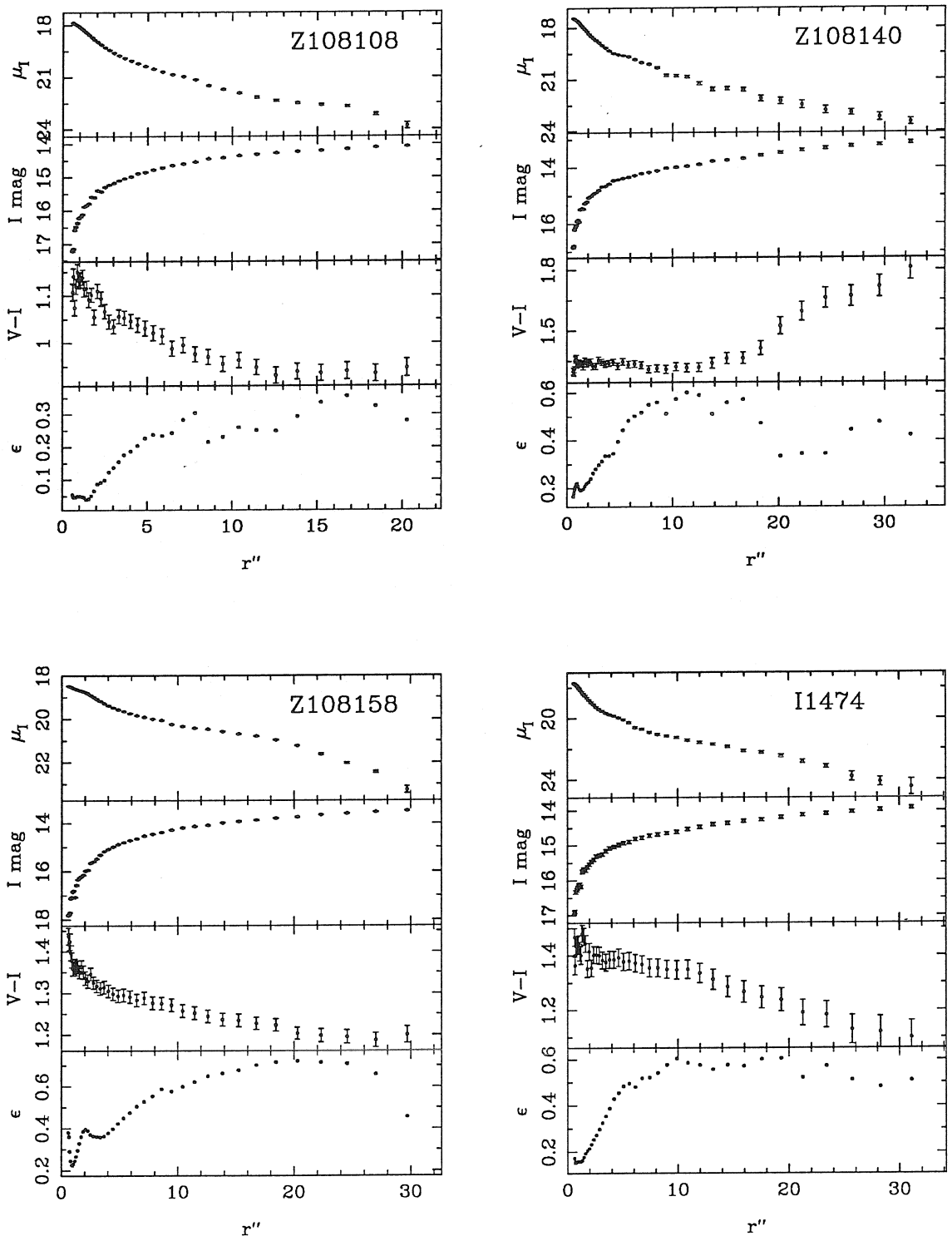

Figure 5.1 — continued

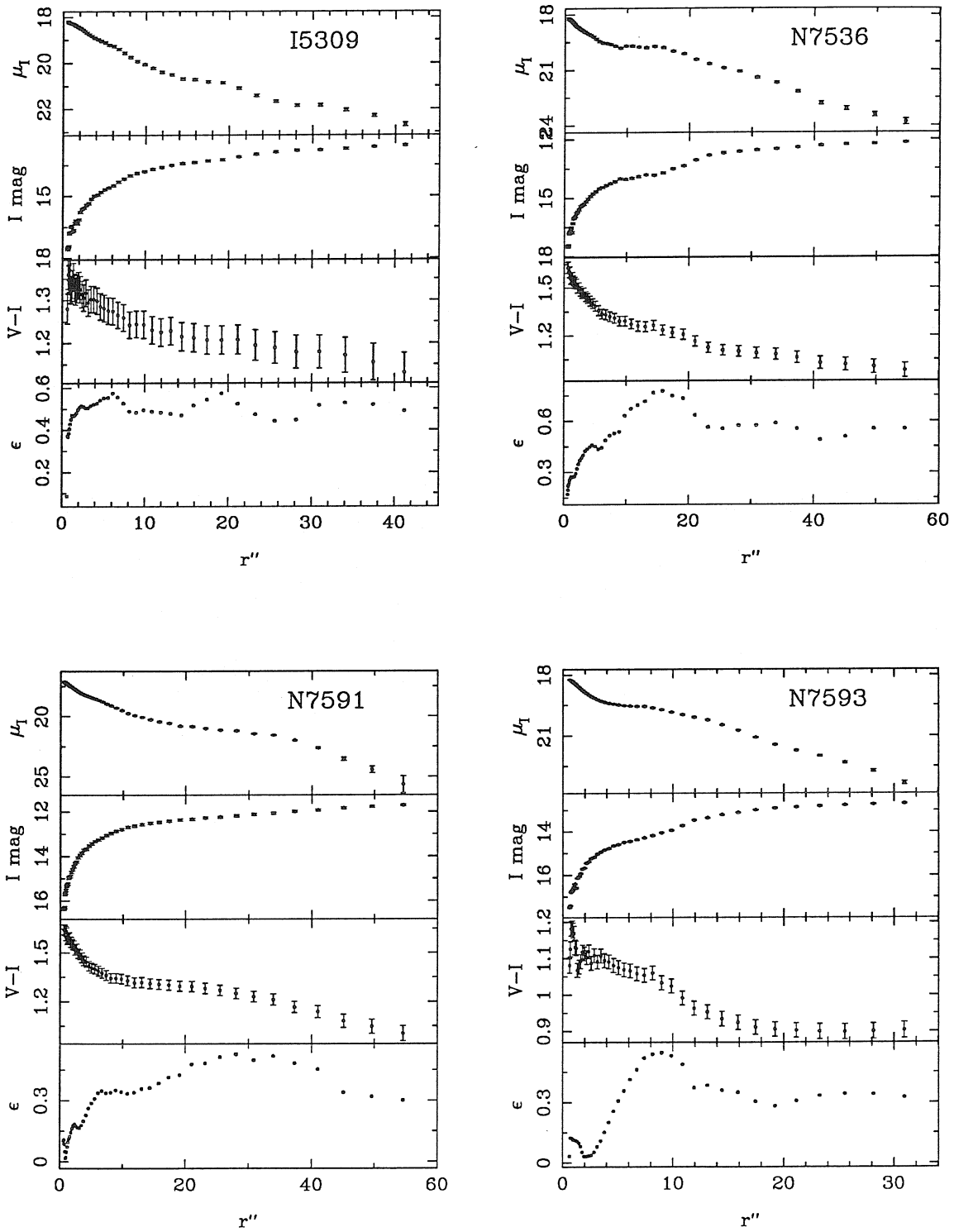

Figure 5.1 — continued

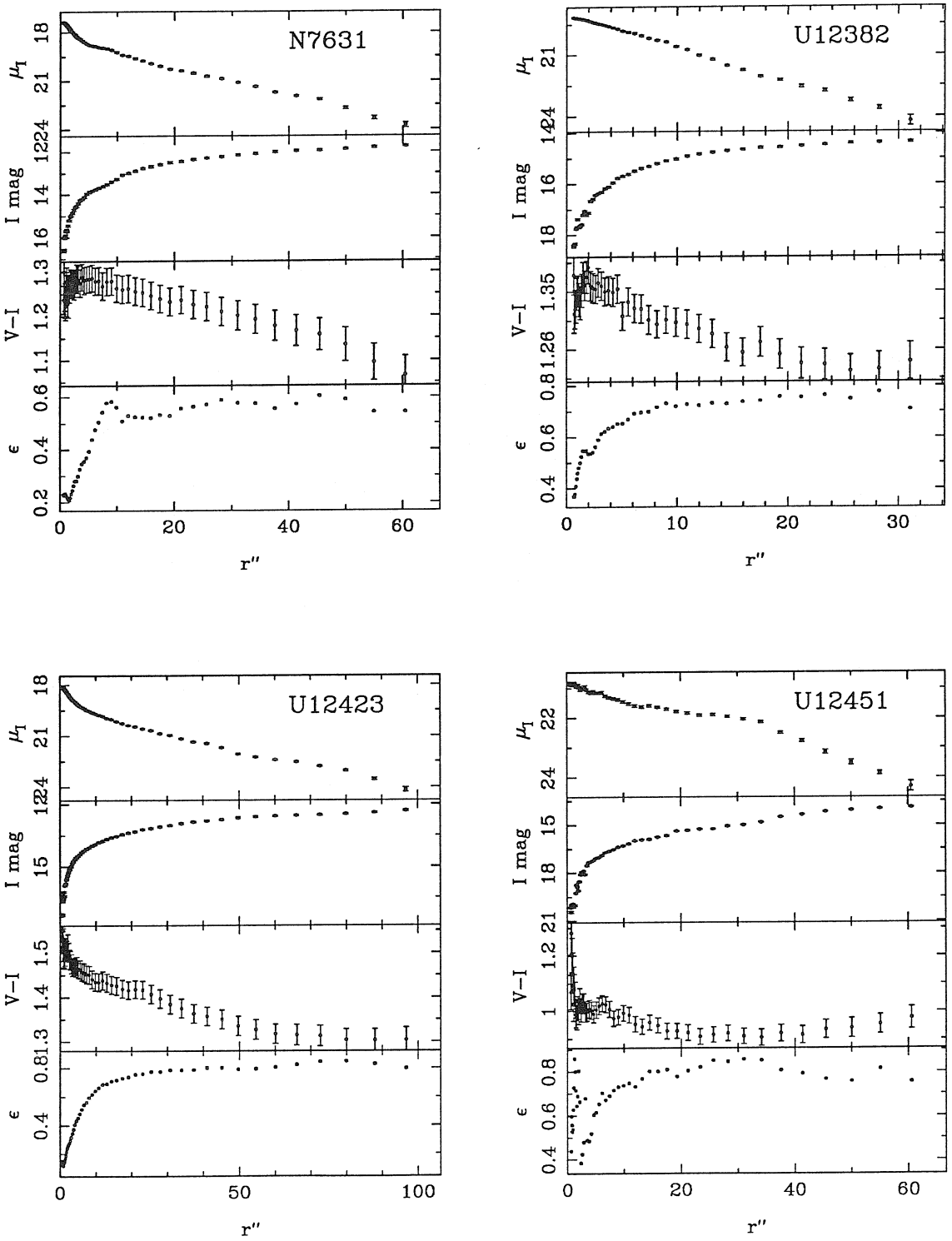

Figure 5.1 — continued

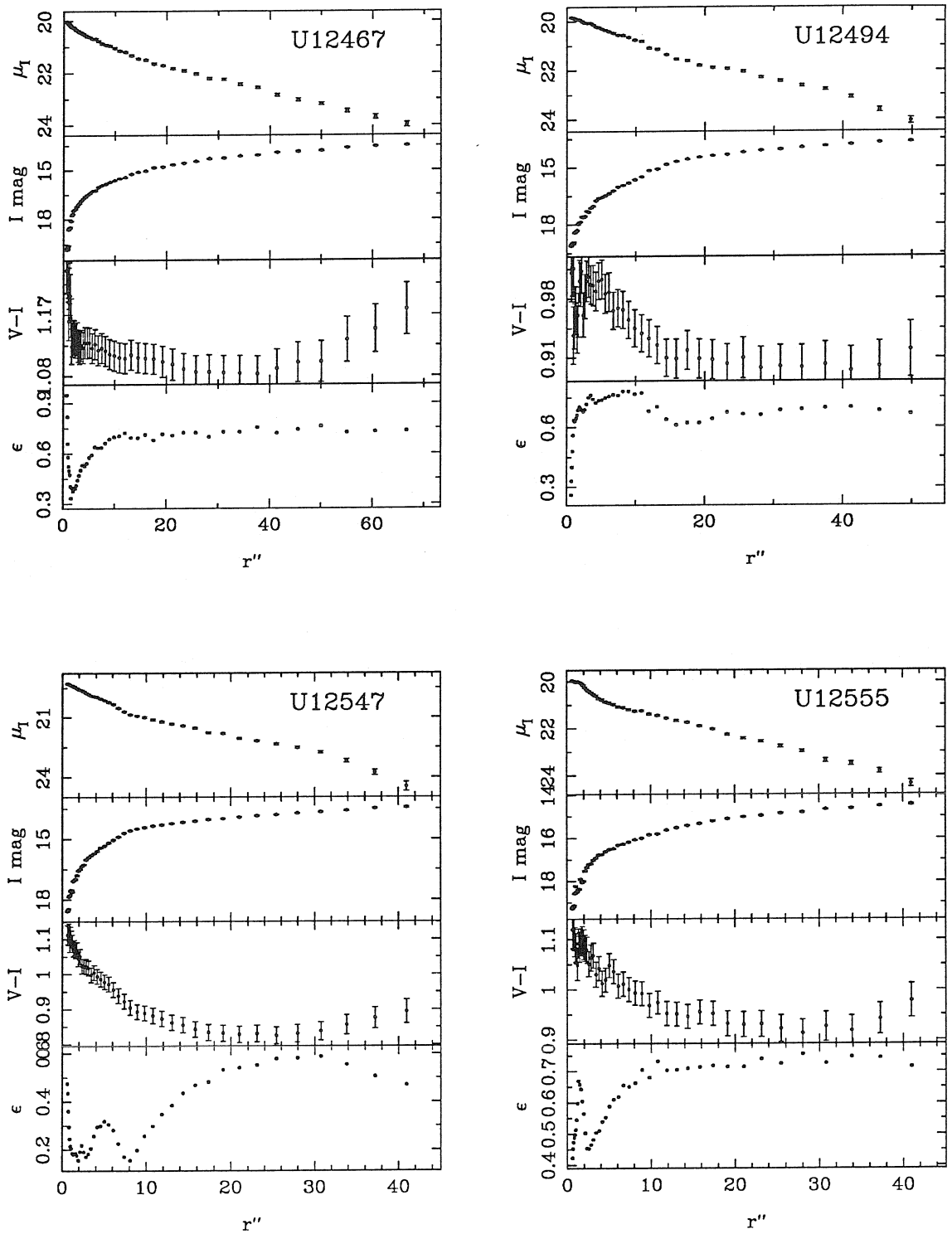

Figure 5.1 — continued

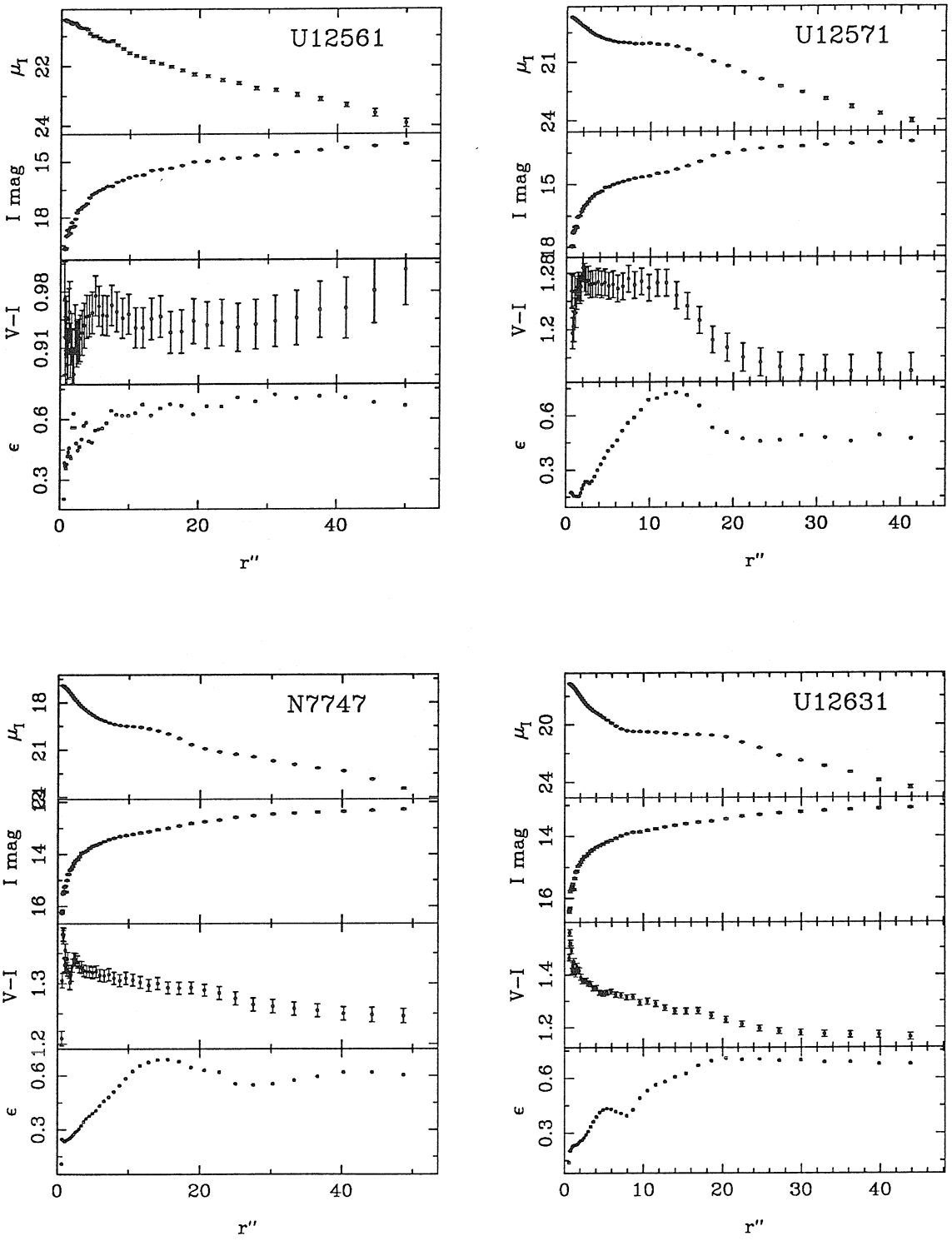

Figure 5.1 — continued

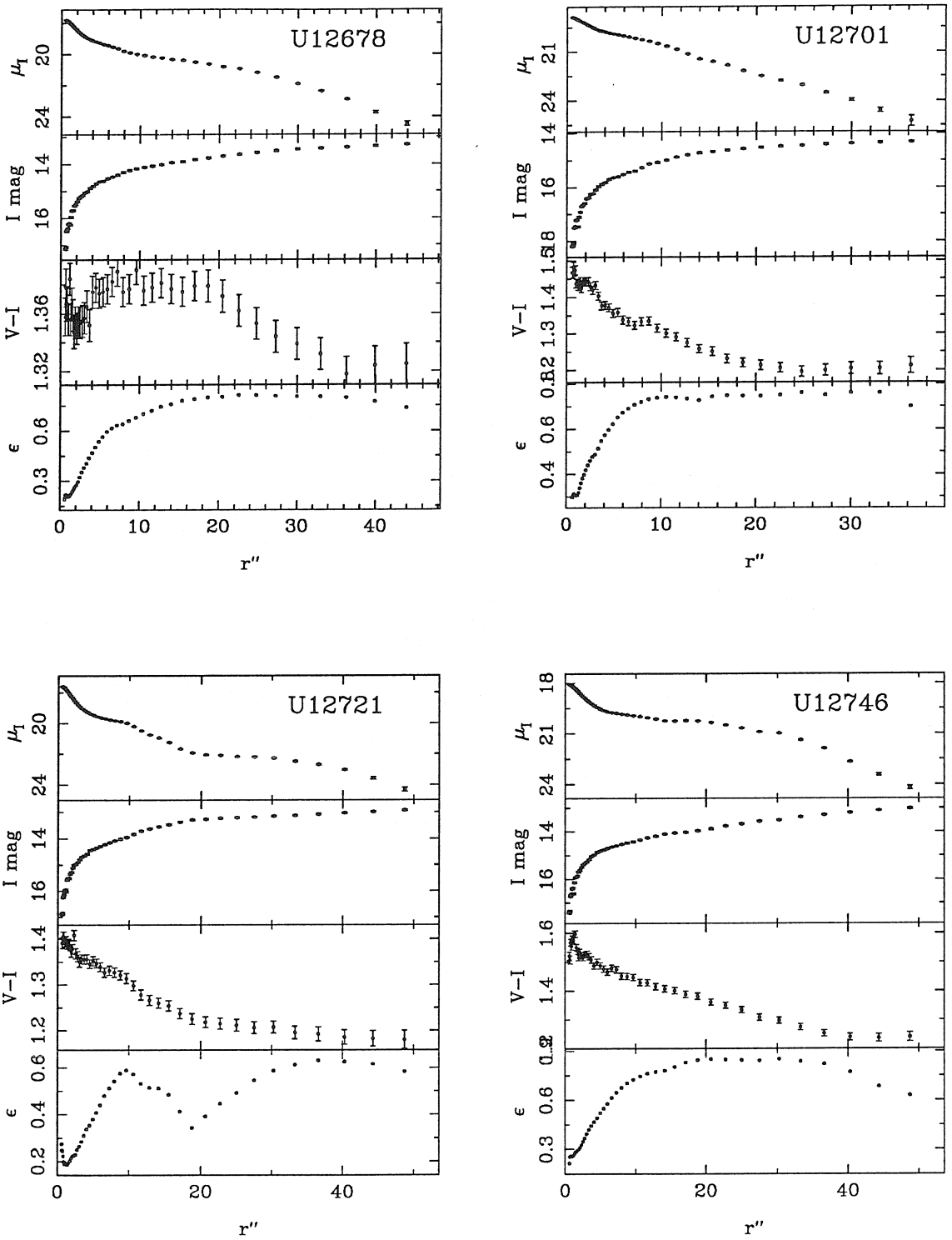

Figure 5.1 — continued

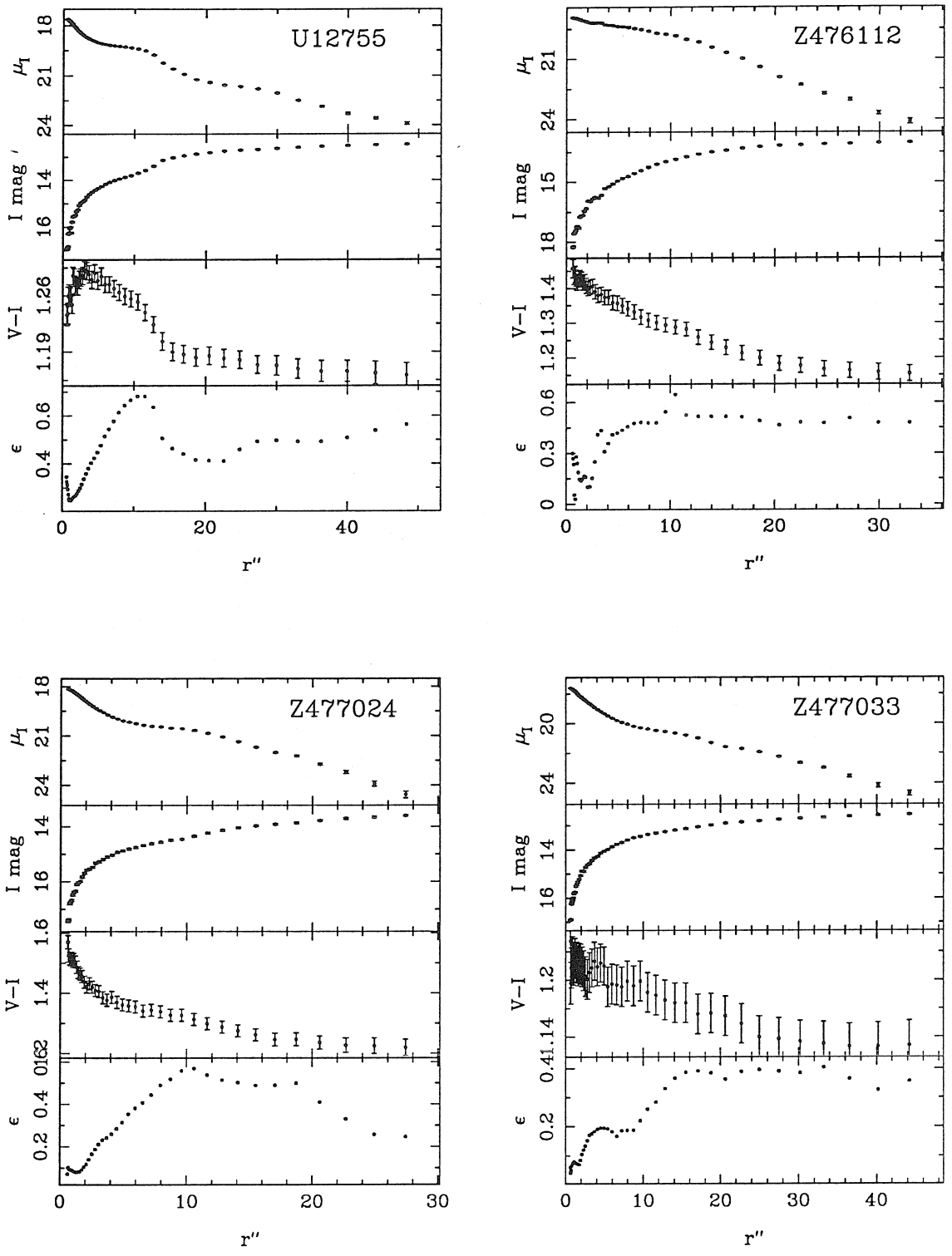

Figure 5.1 — continued

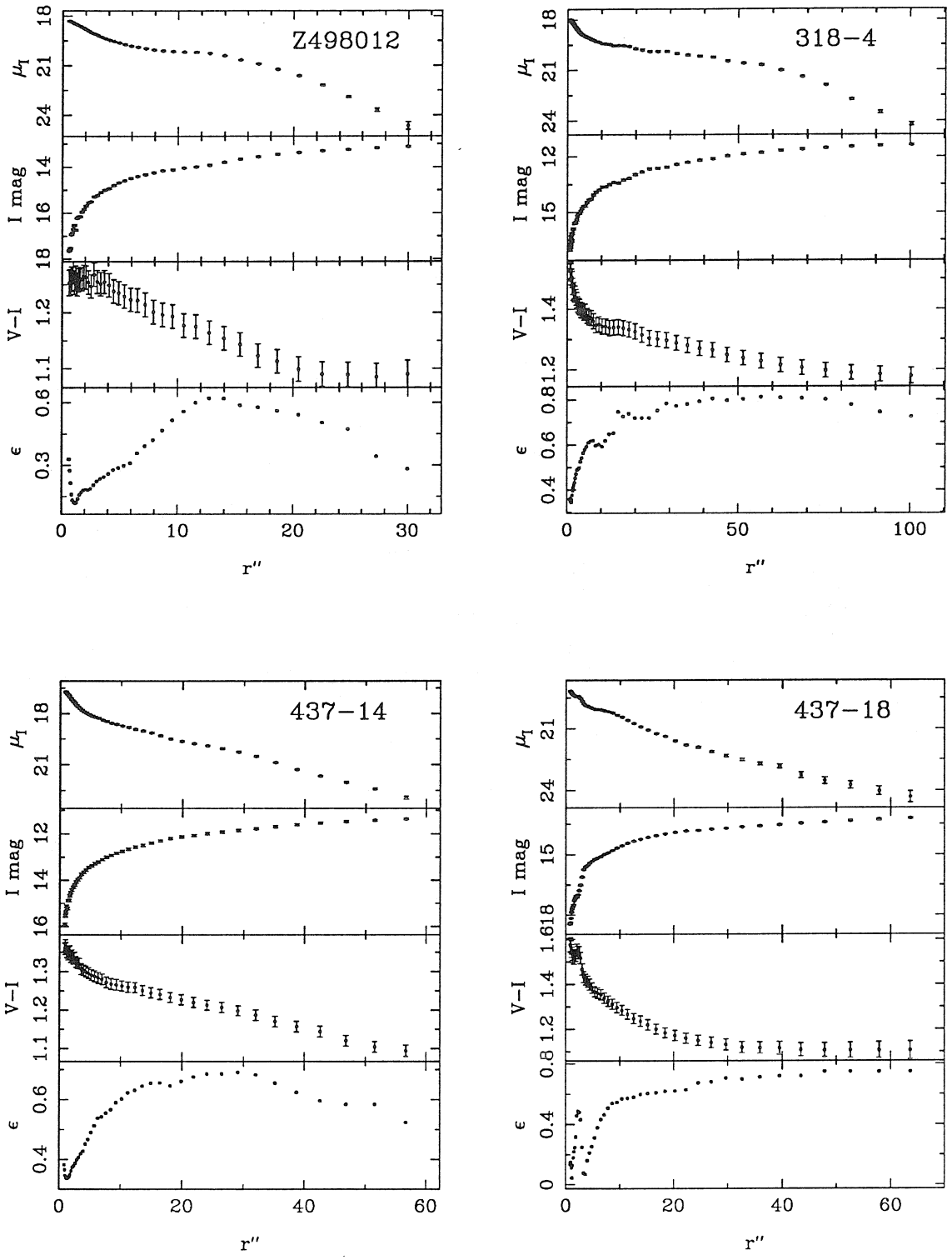

Figure 5.1 — continued

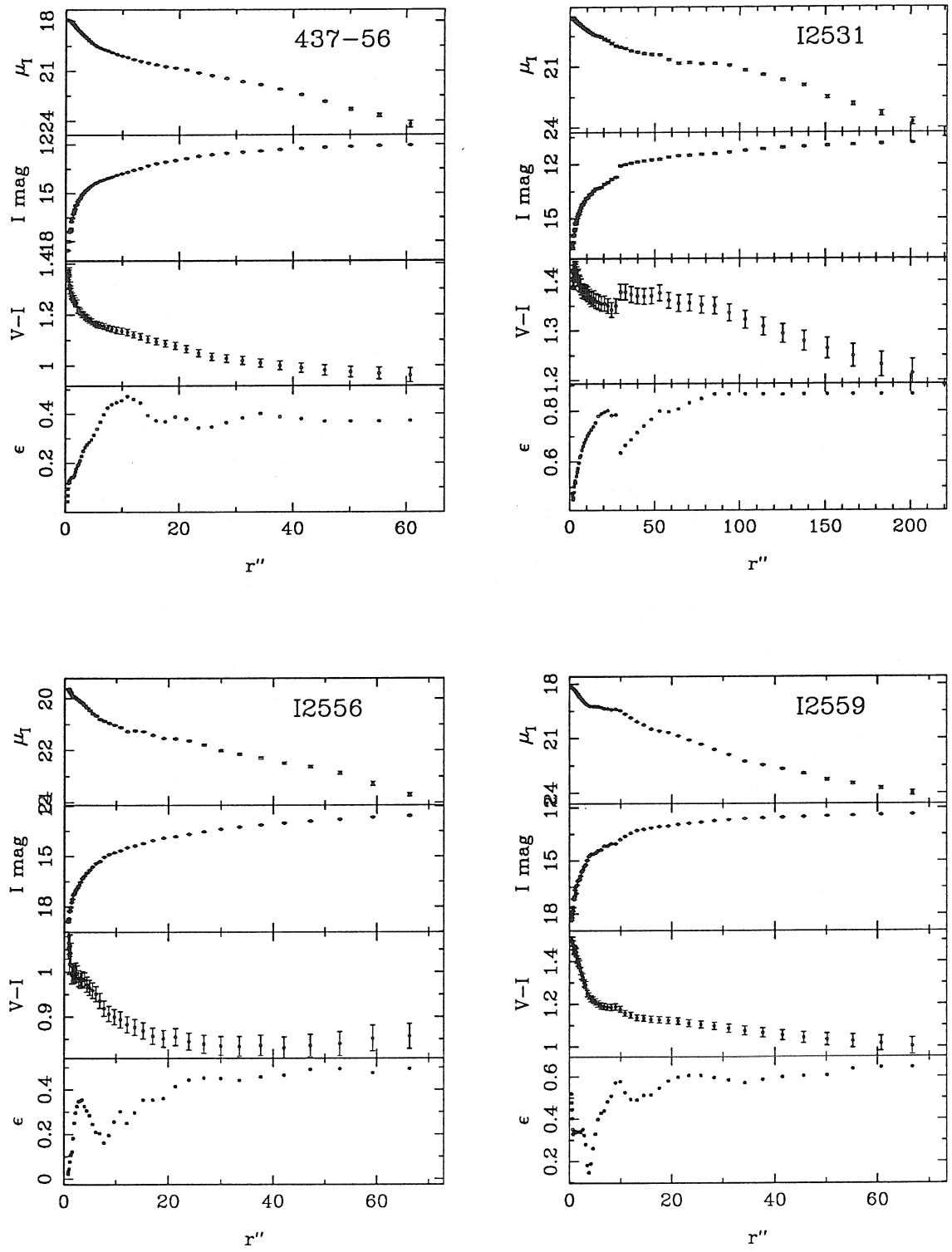

Figure 5.1 — continued

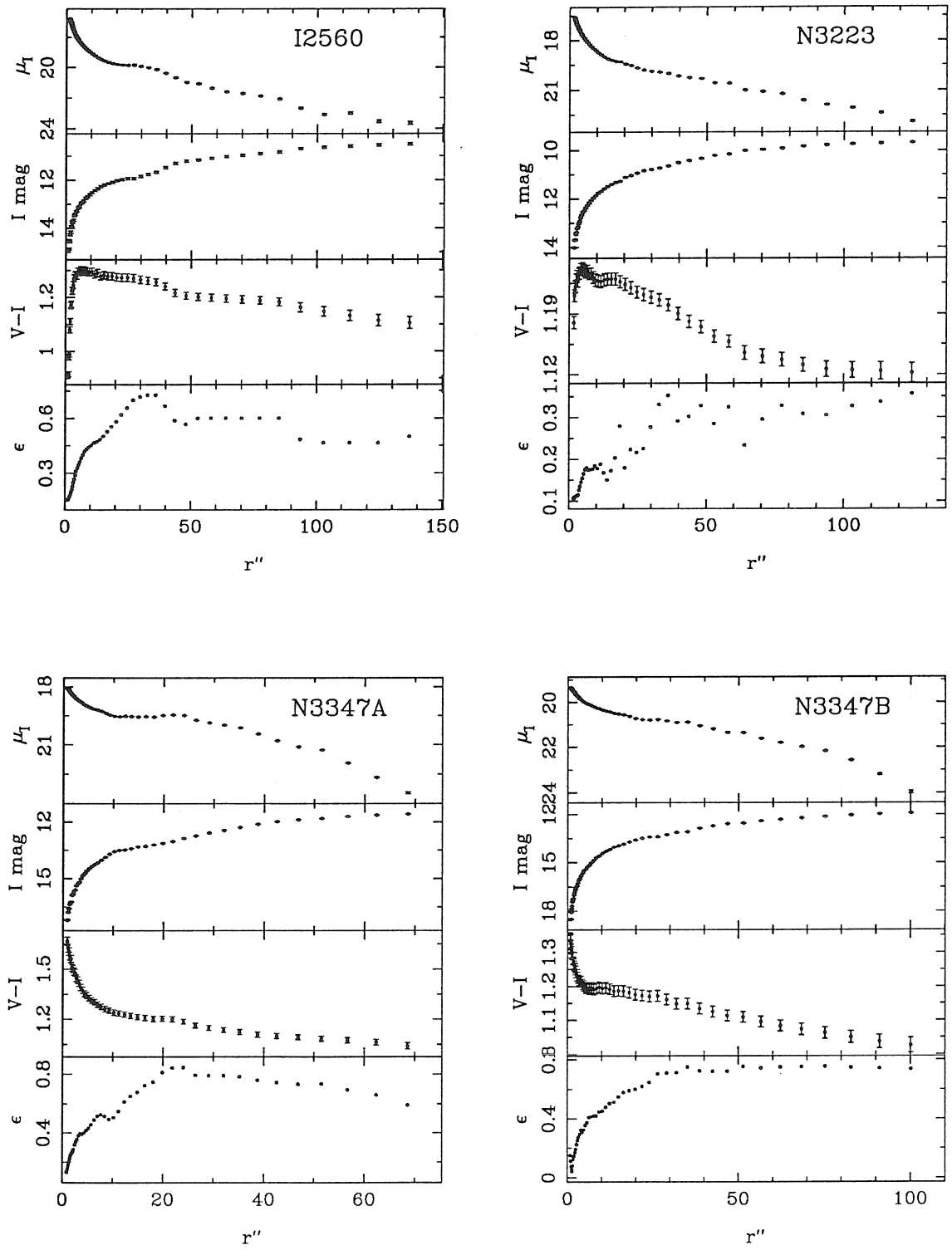

Figure 5.1 — continued

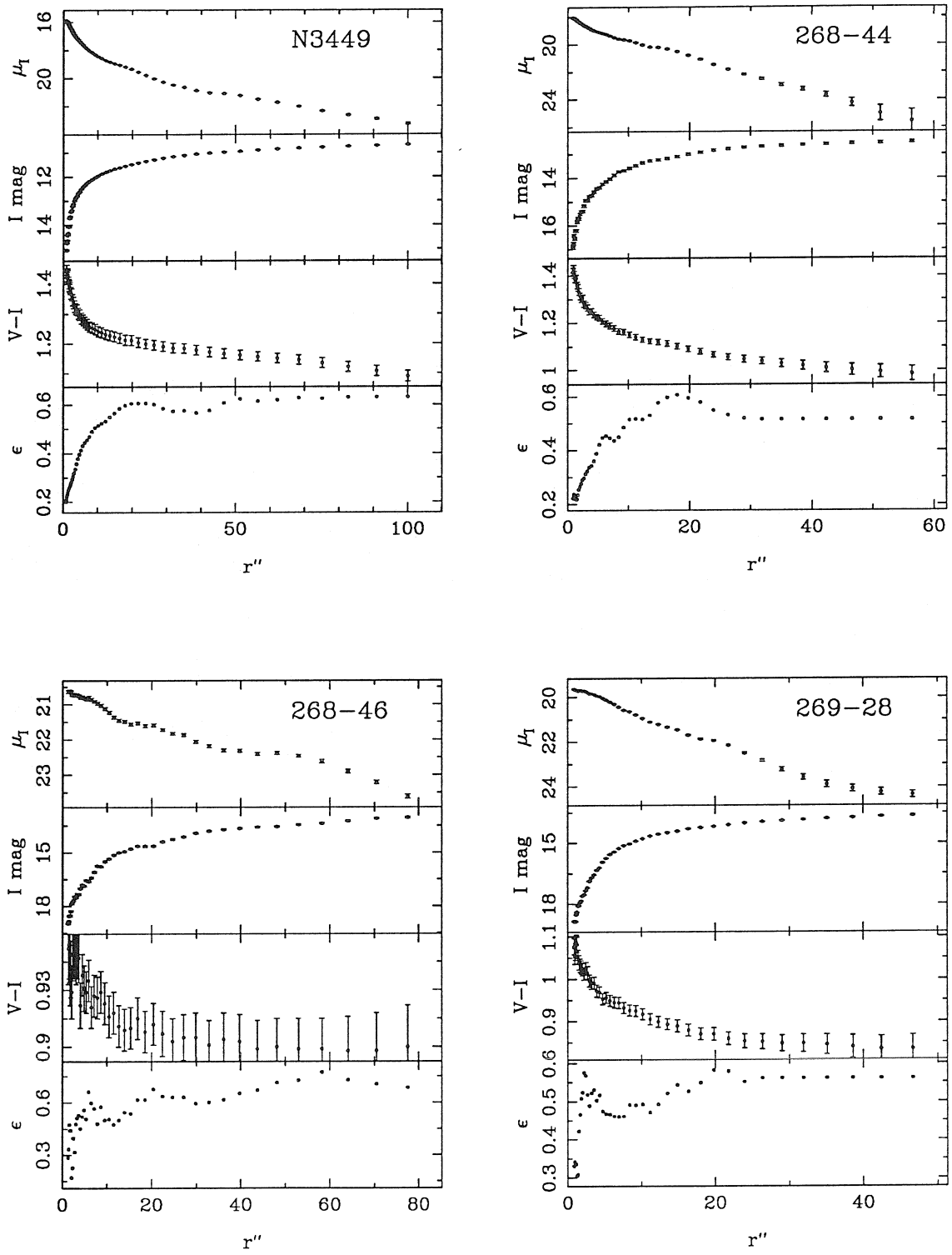

Figure 5.1 — continued

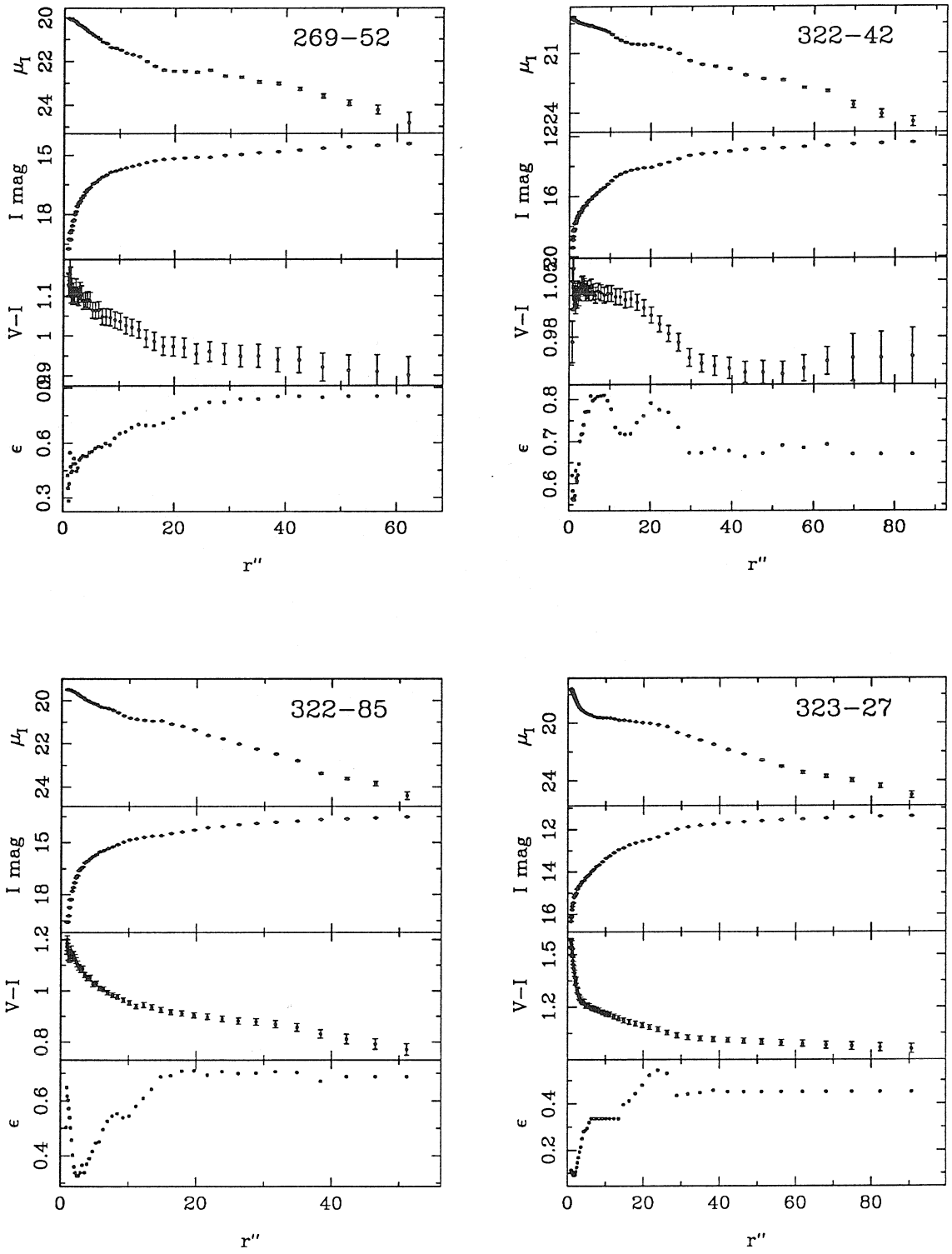

Figure 5.1 — continued

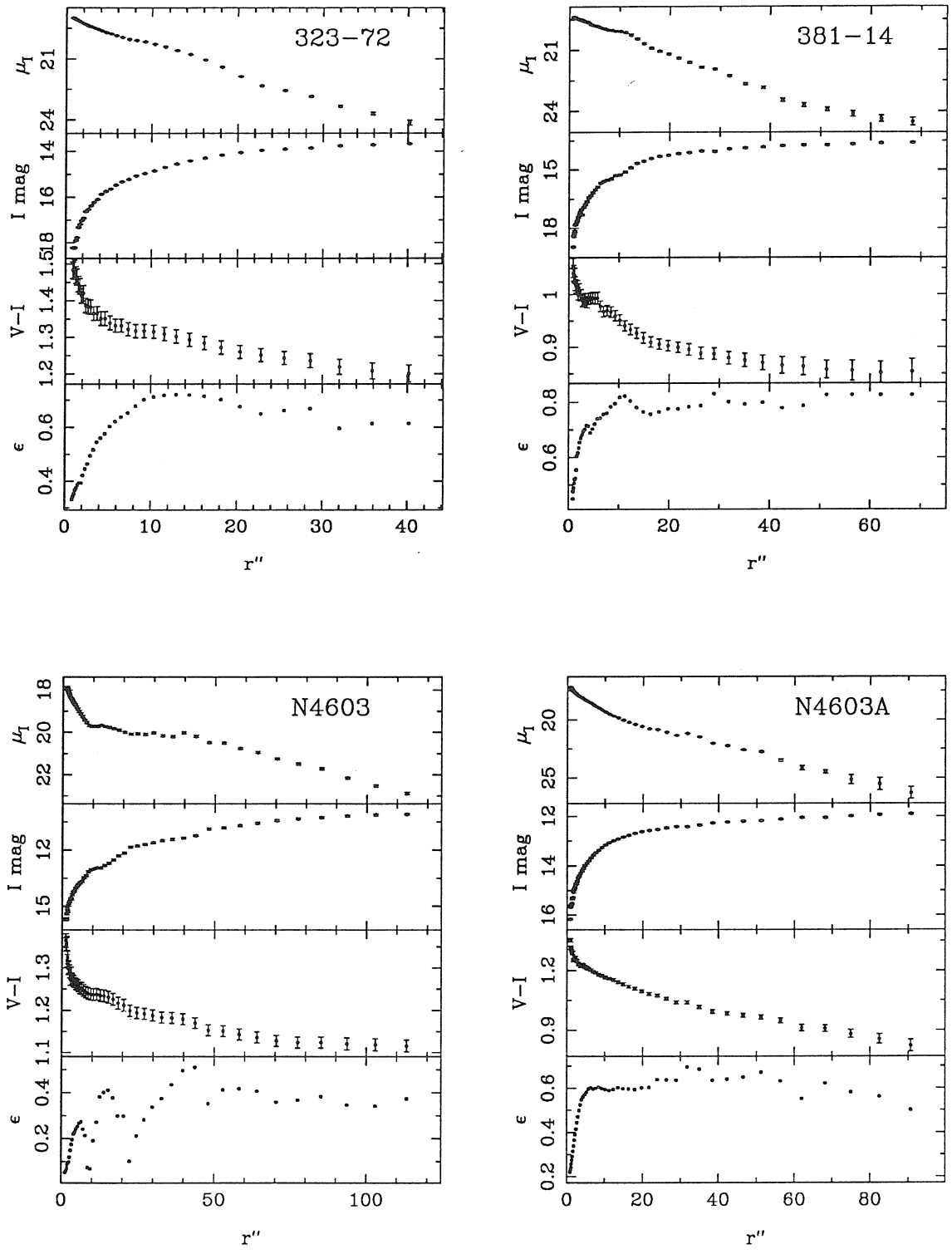

Figure 5.1 — continued

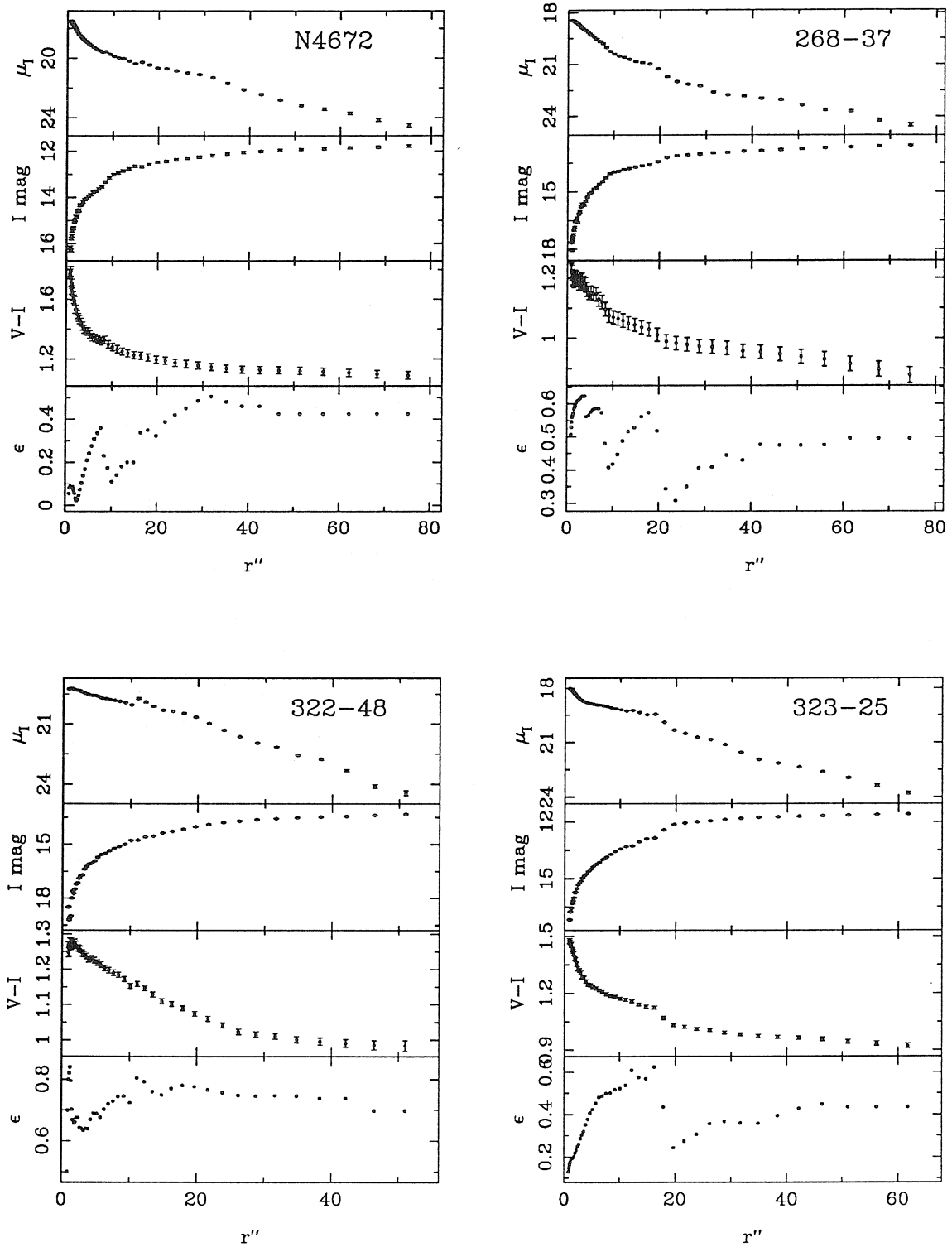

Figure 5.1 — continued

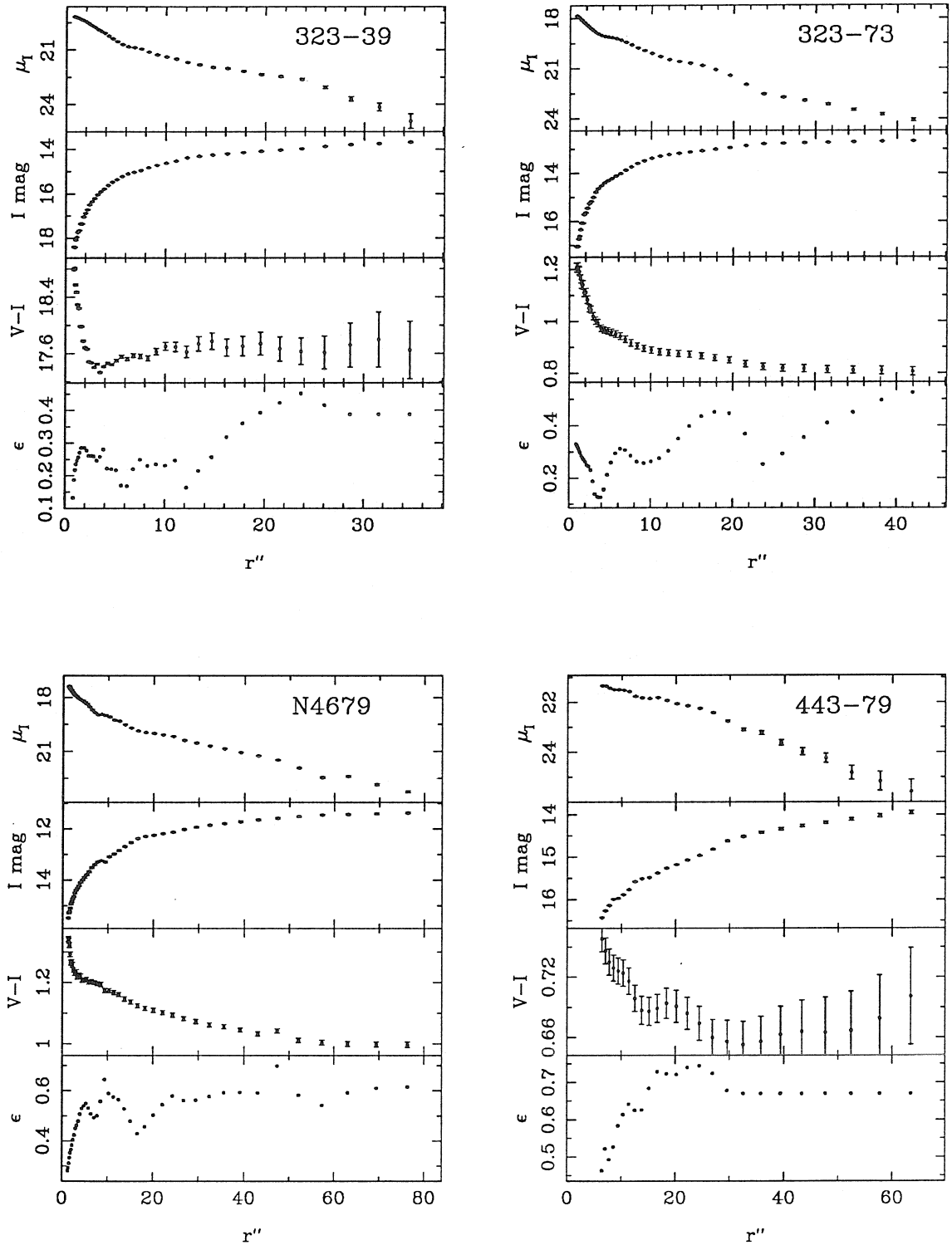

Figure 5.1 — continued

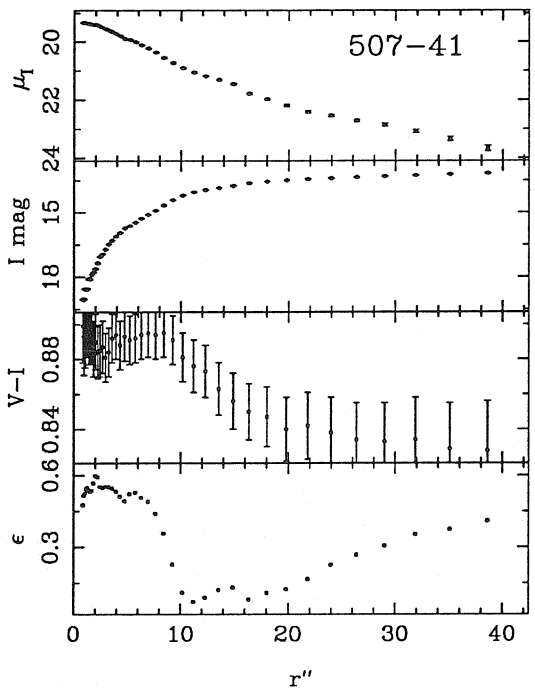

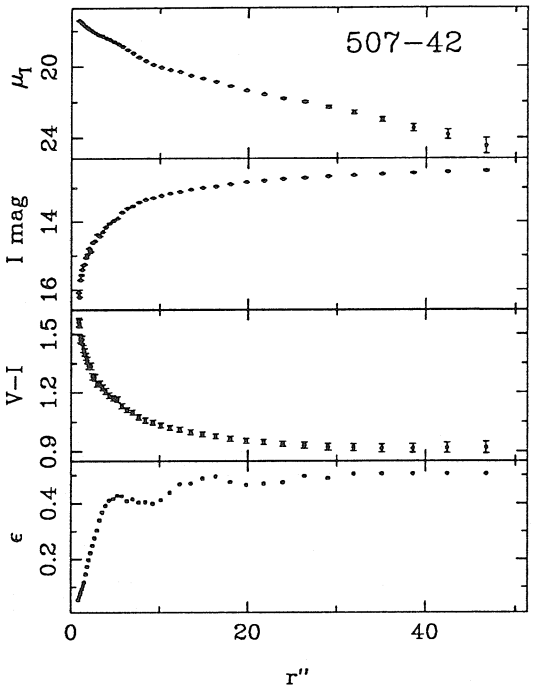

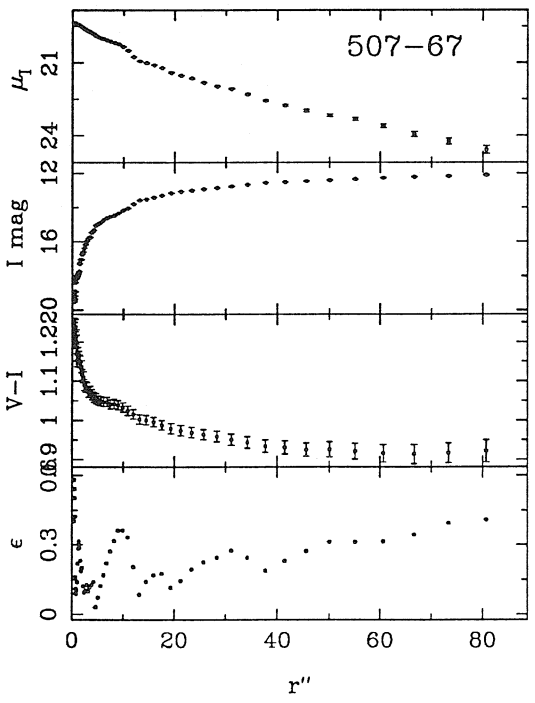

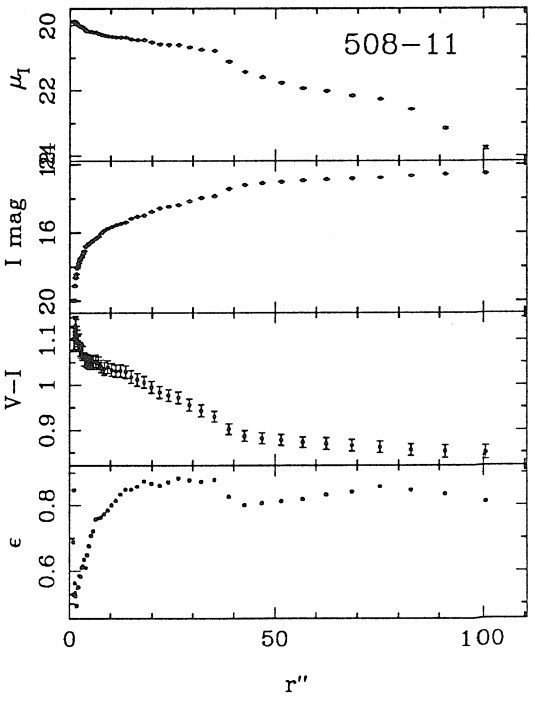

Figure 5.1 — continued

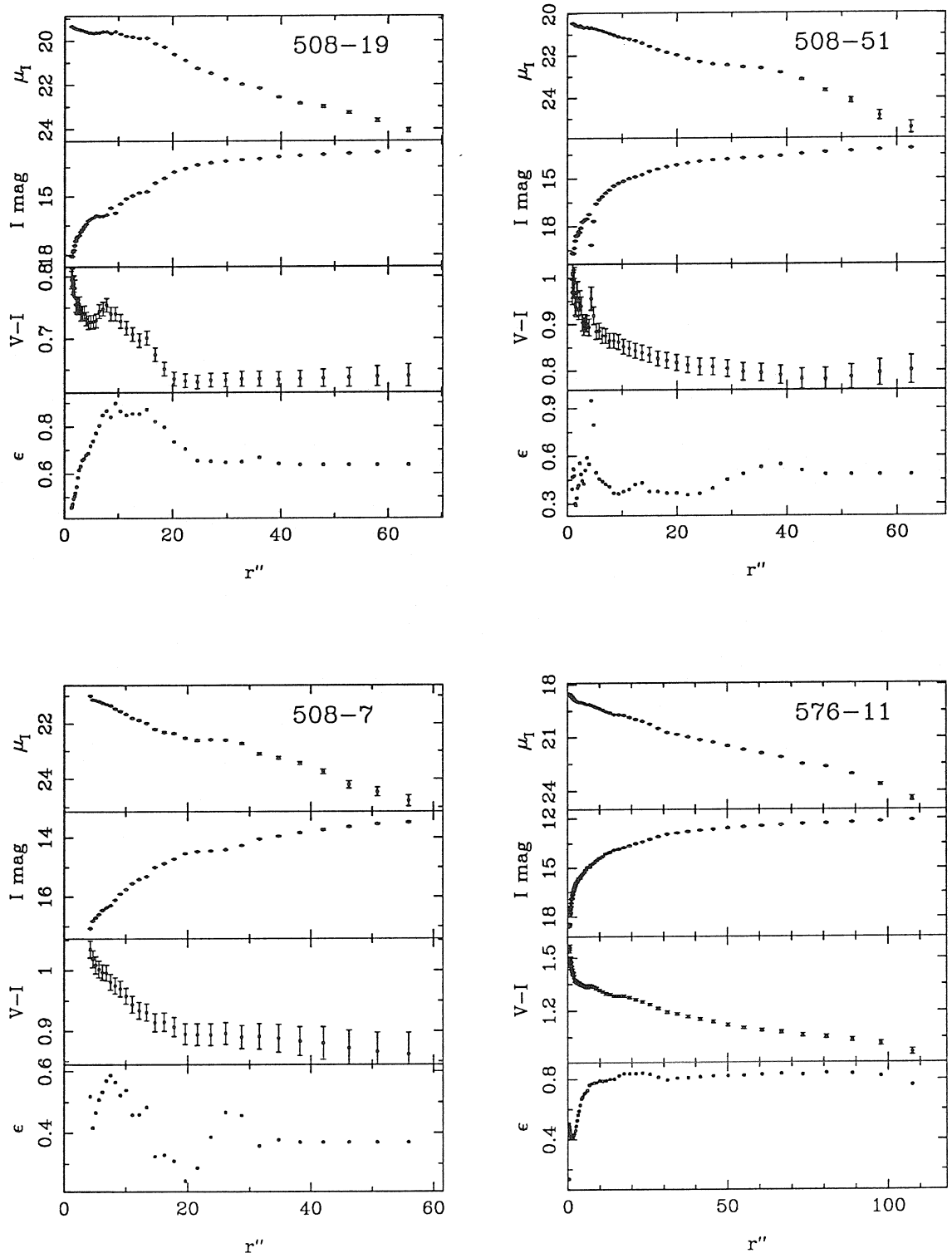

Figure 5.1 — continued

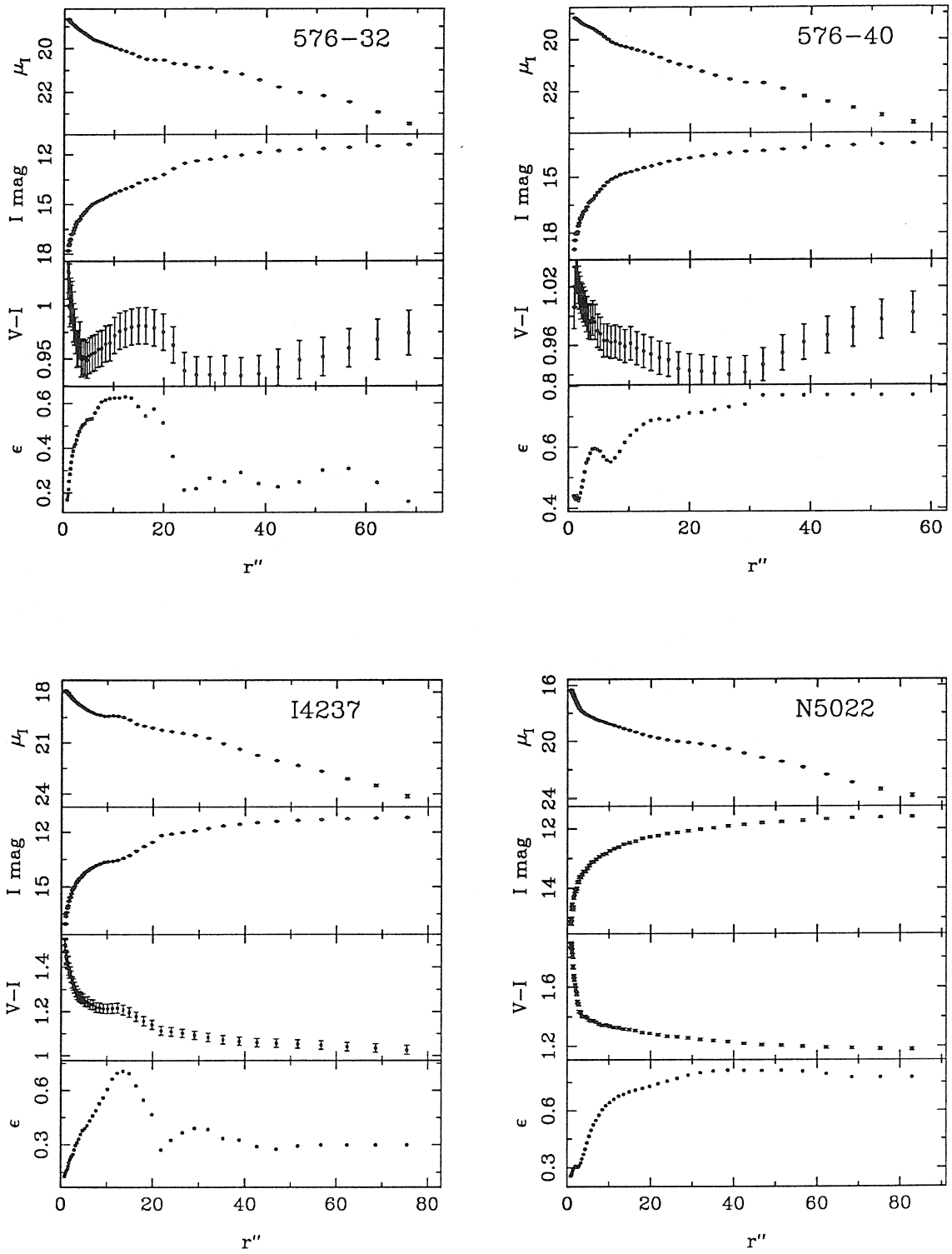

Figure 5.1 — continued

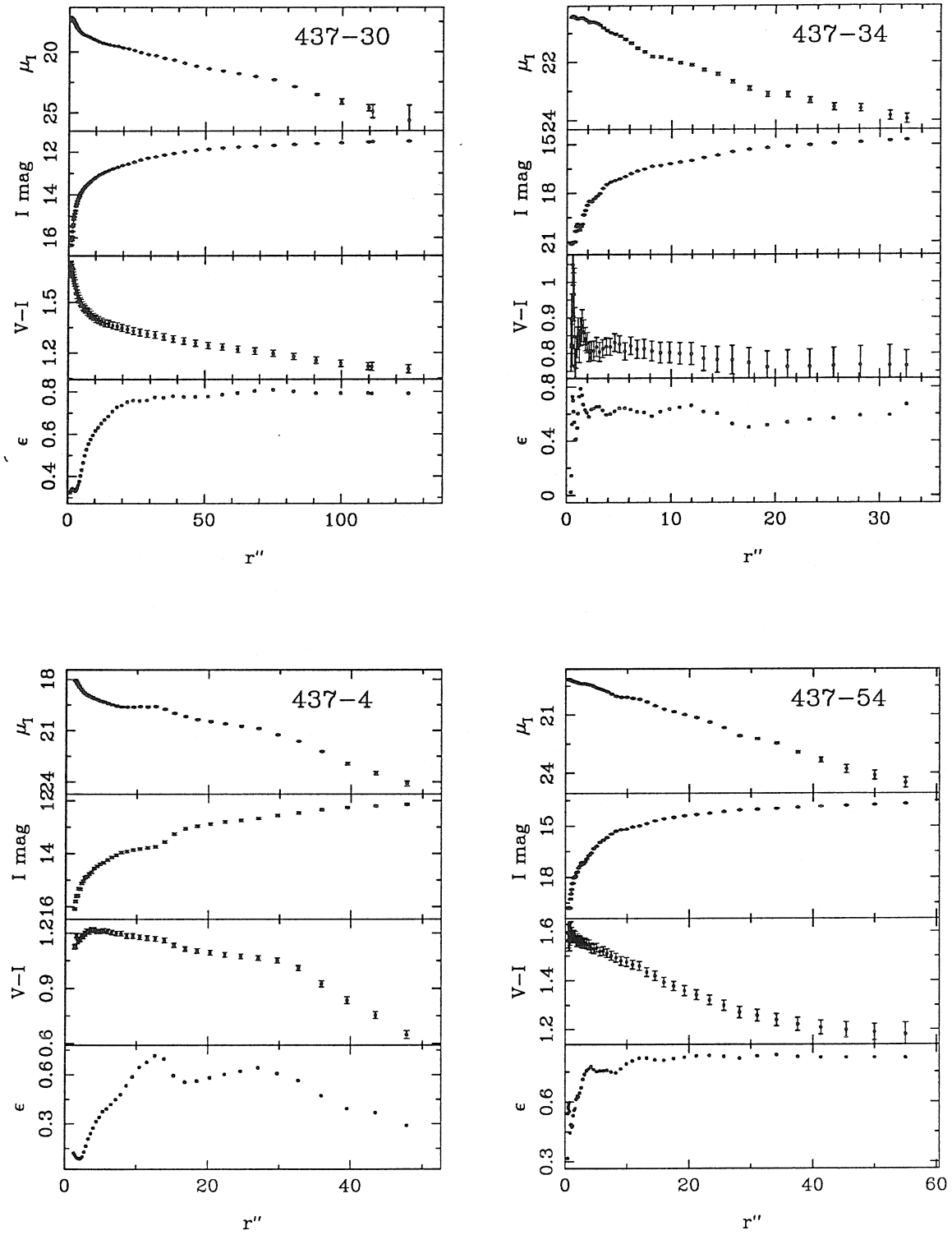

Figure 5.1 — continued

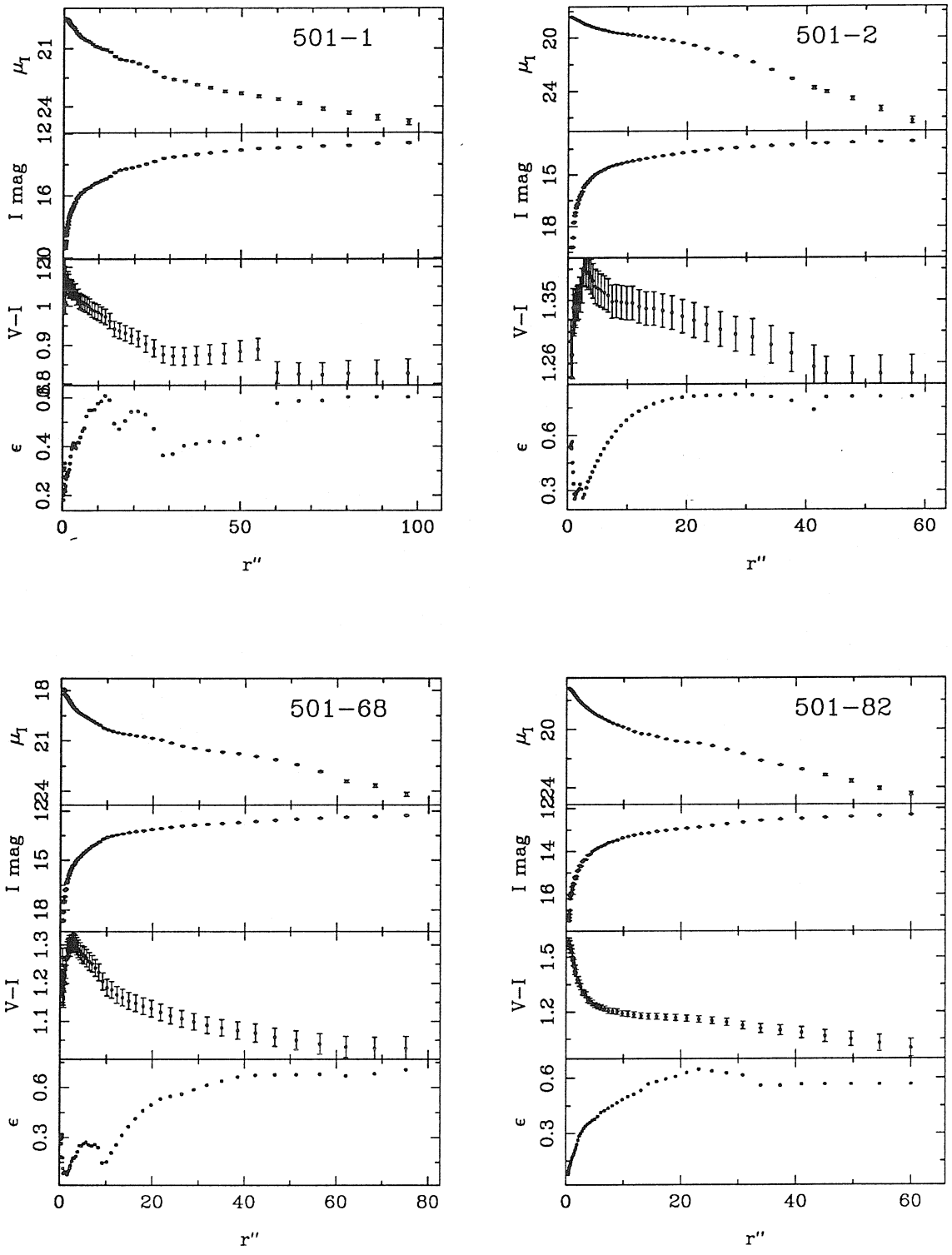

Figure 5.1 — continued

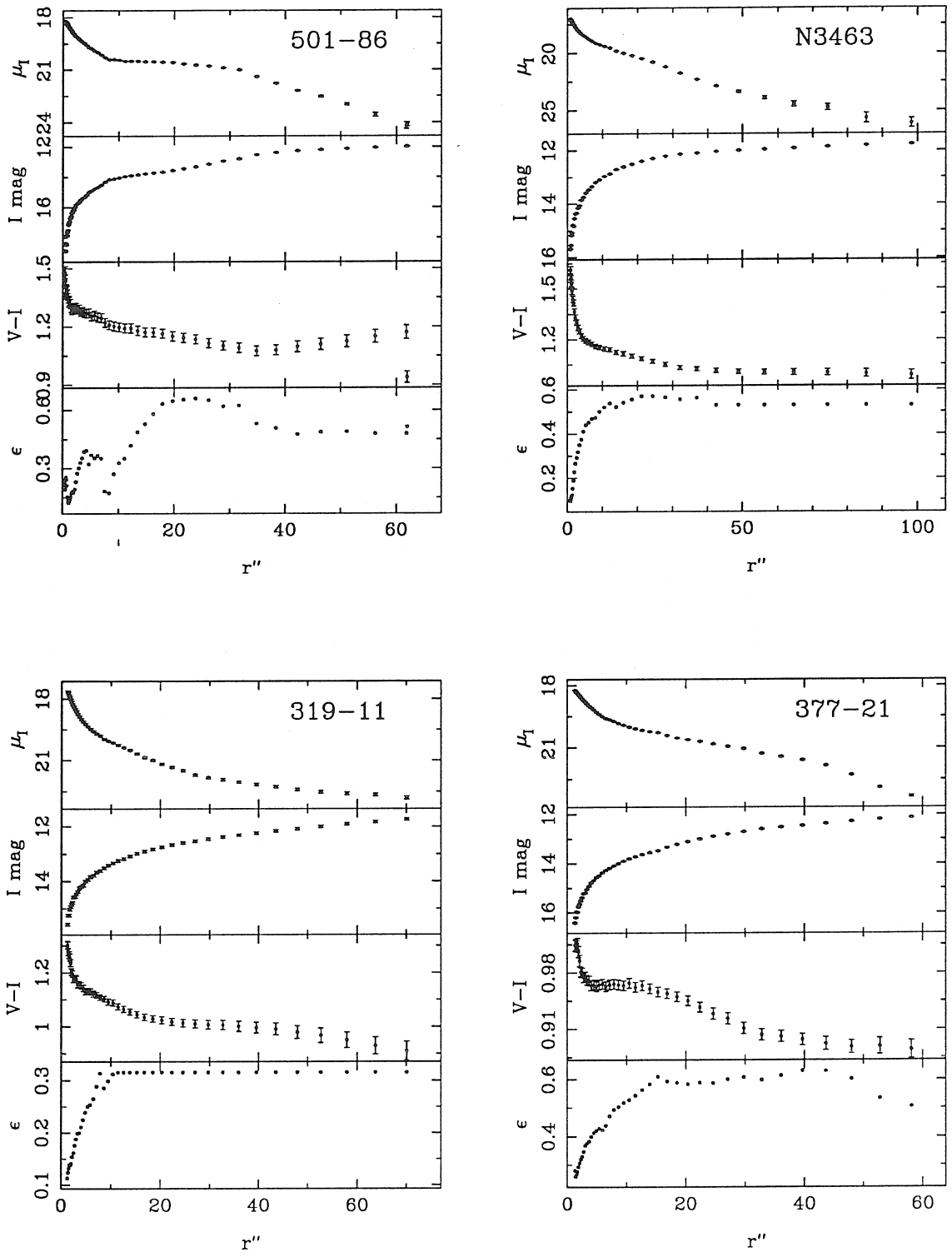

Figure 5.1 — continued

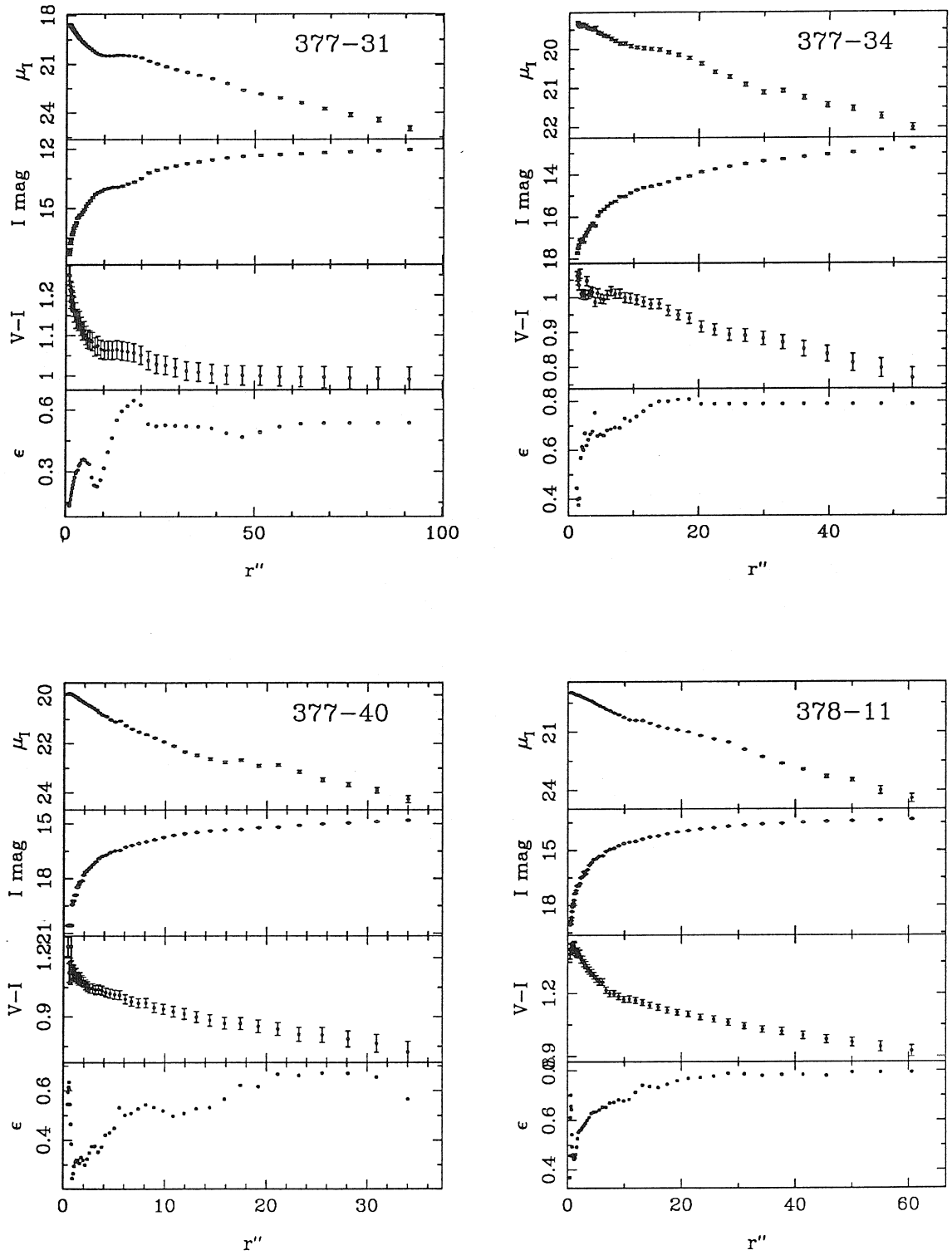

Figure 5.1 — continued

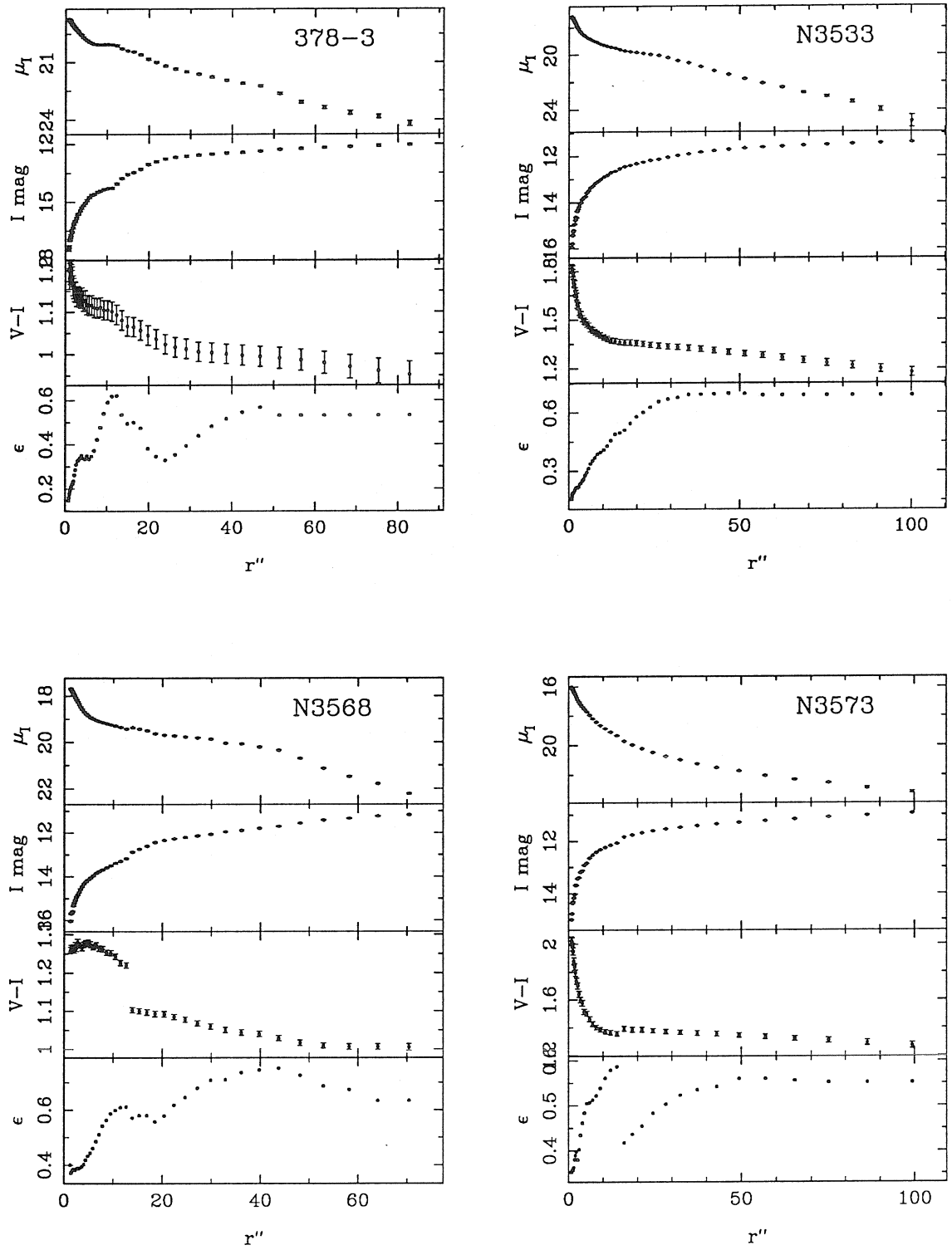

Figure 5.1 — continued

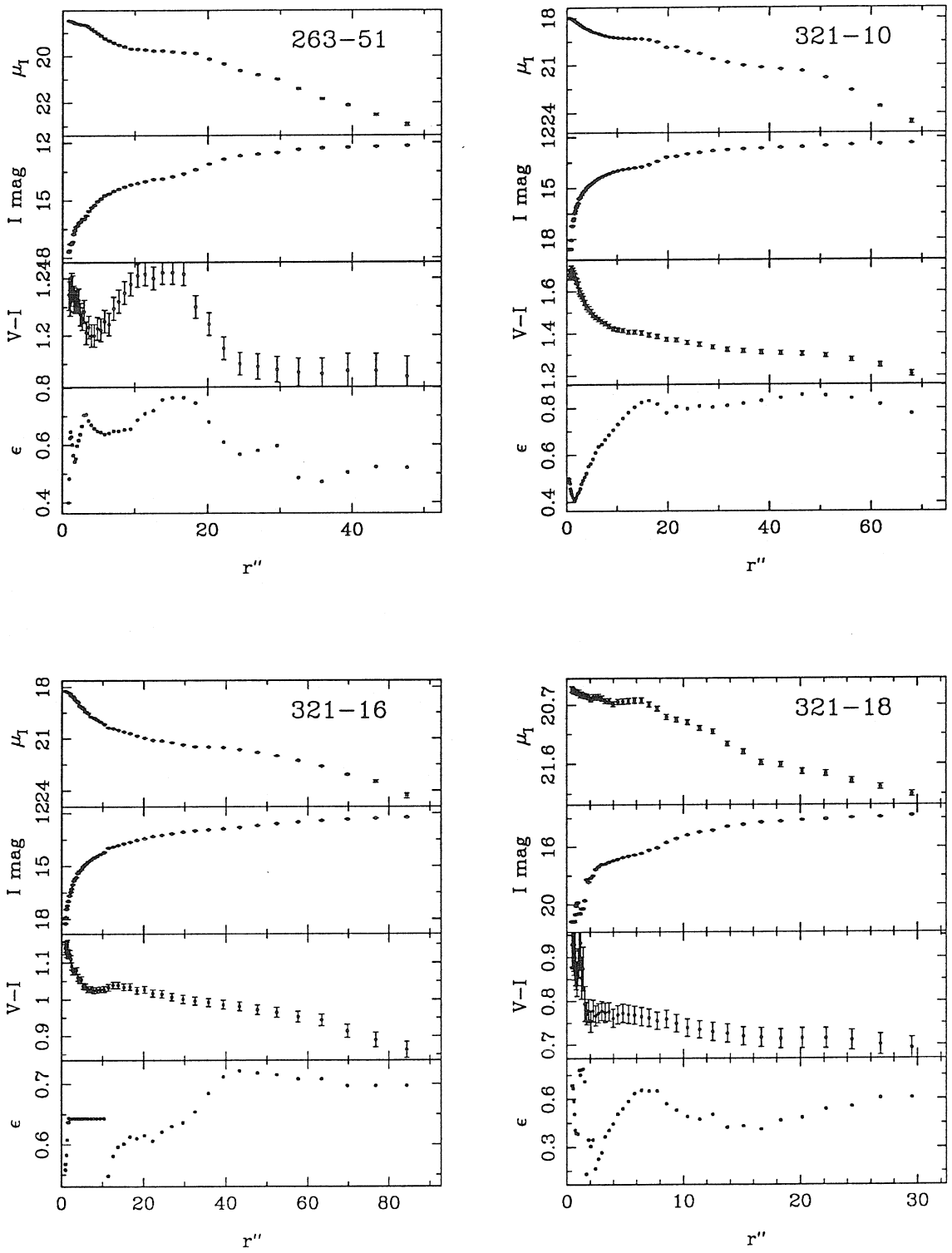

Figure 5.1 — continued

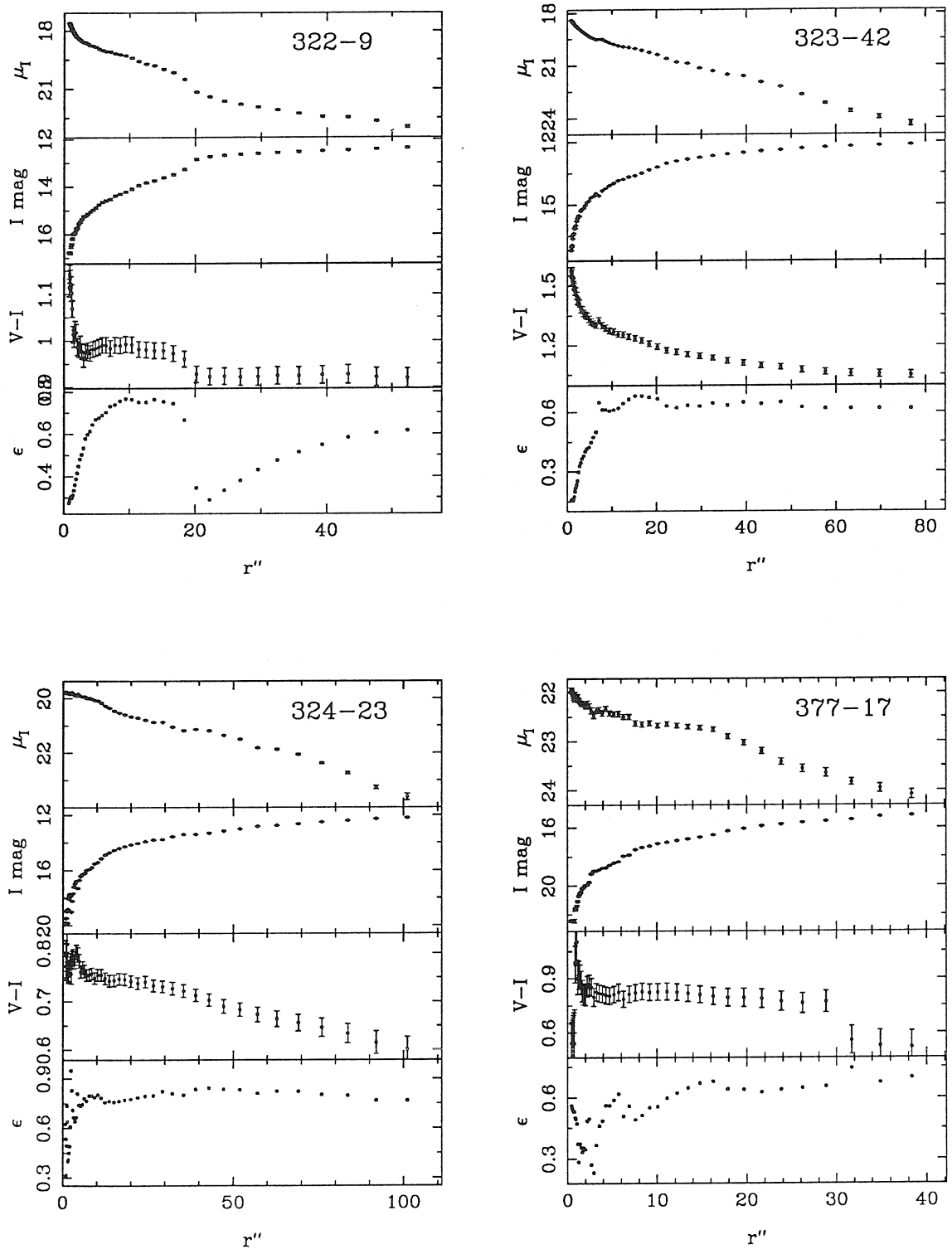

Figure 5.1 — continued

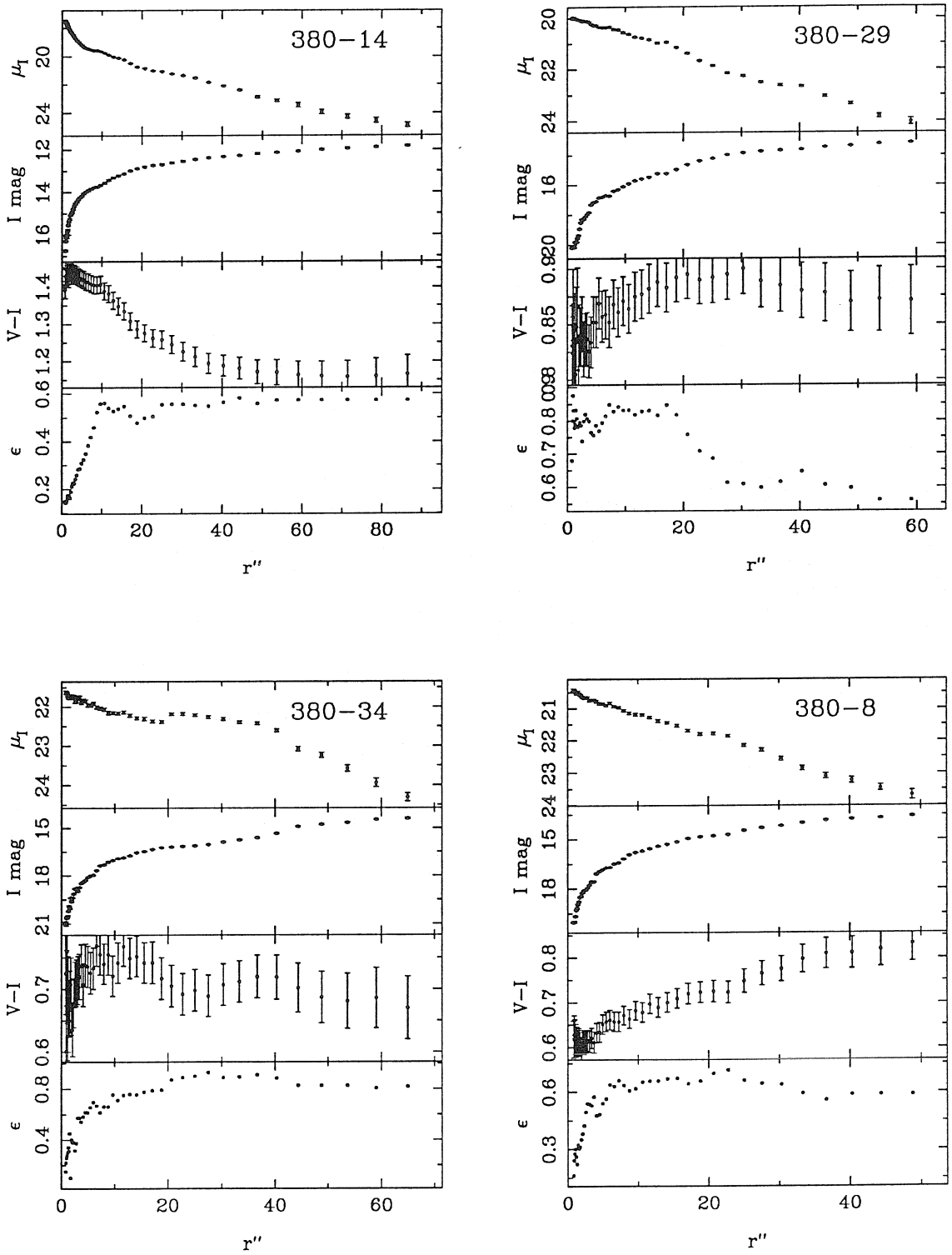

Figure 5.1 — continued

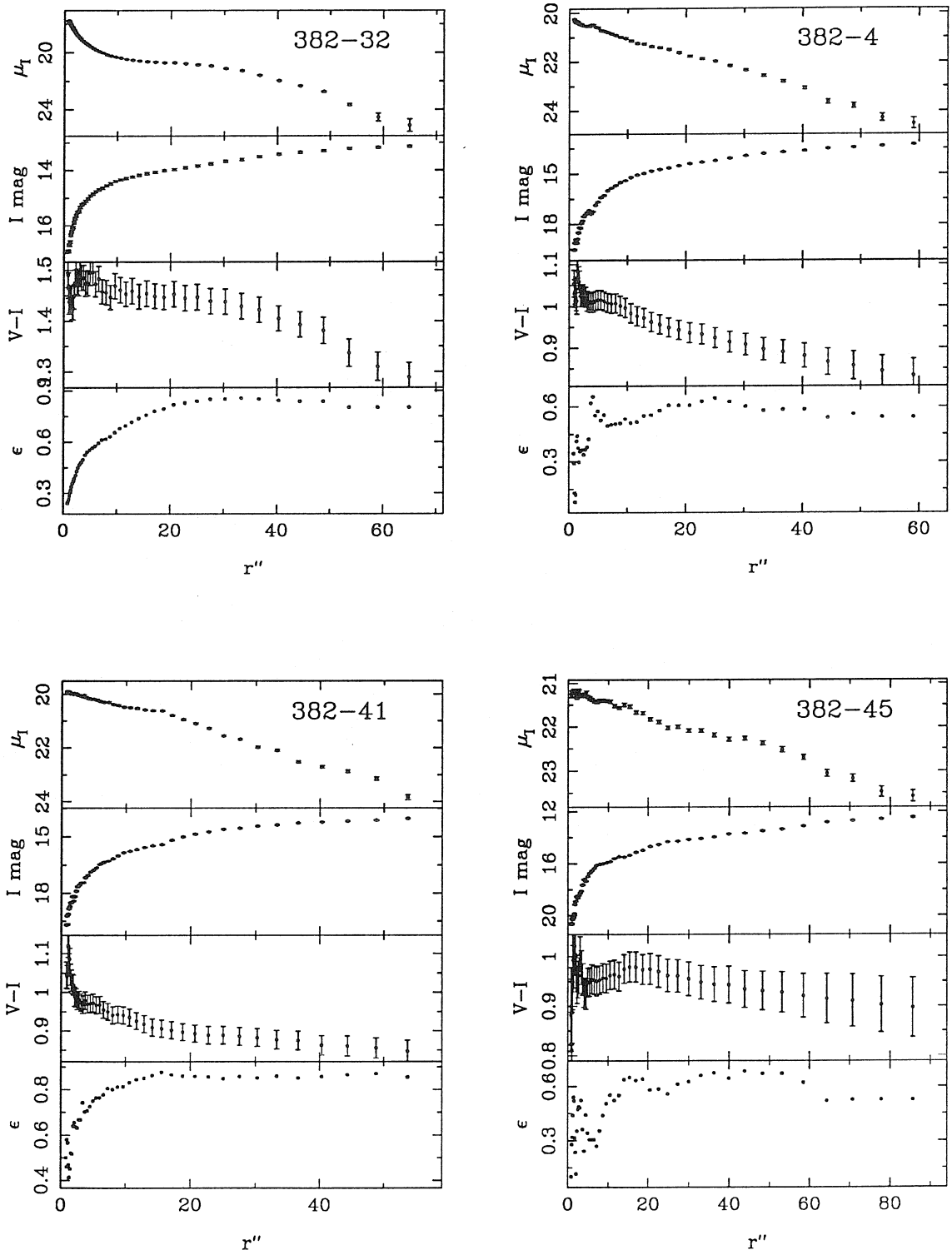

Figure 5.1 — continued

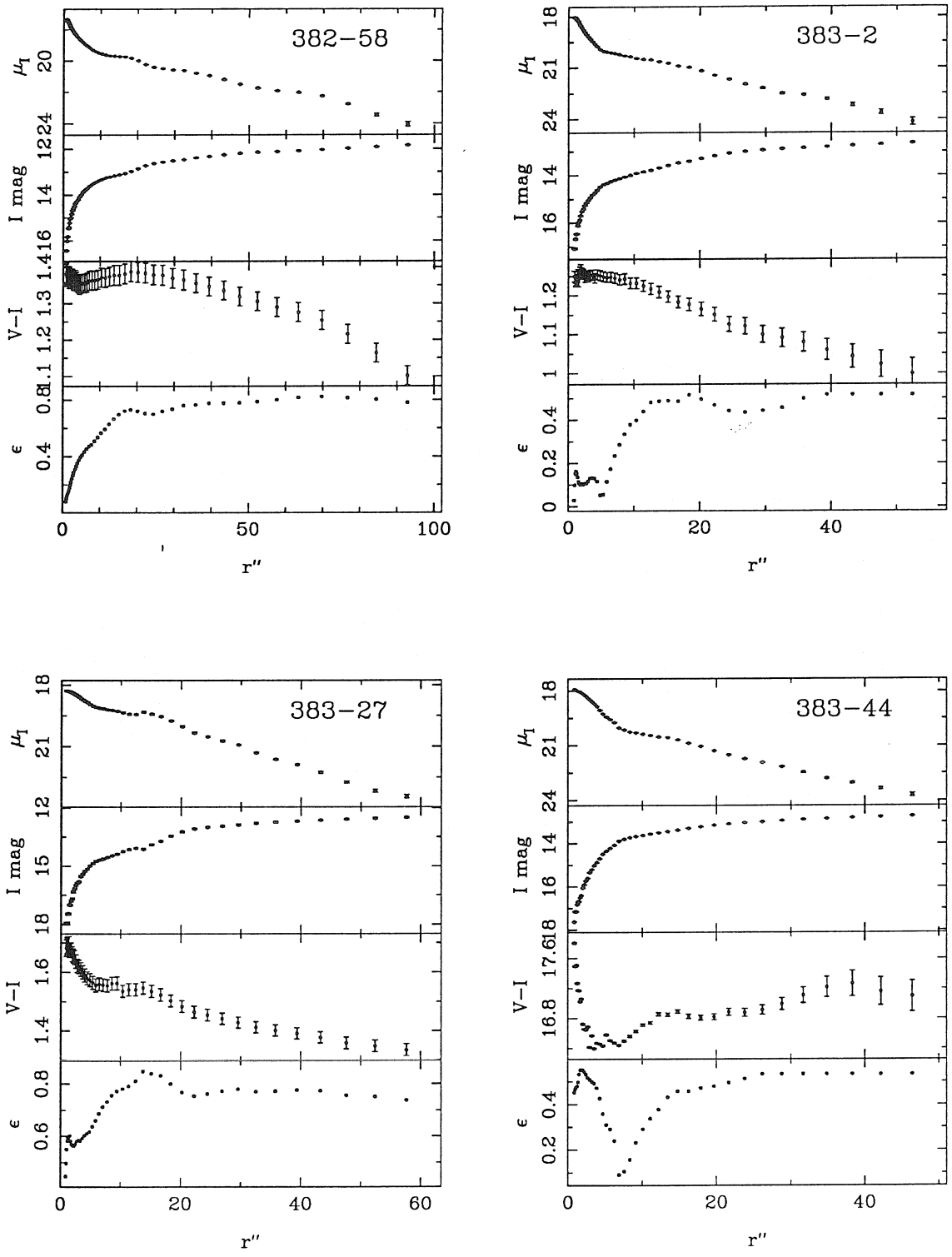

Figure 5.1 — continued

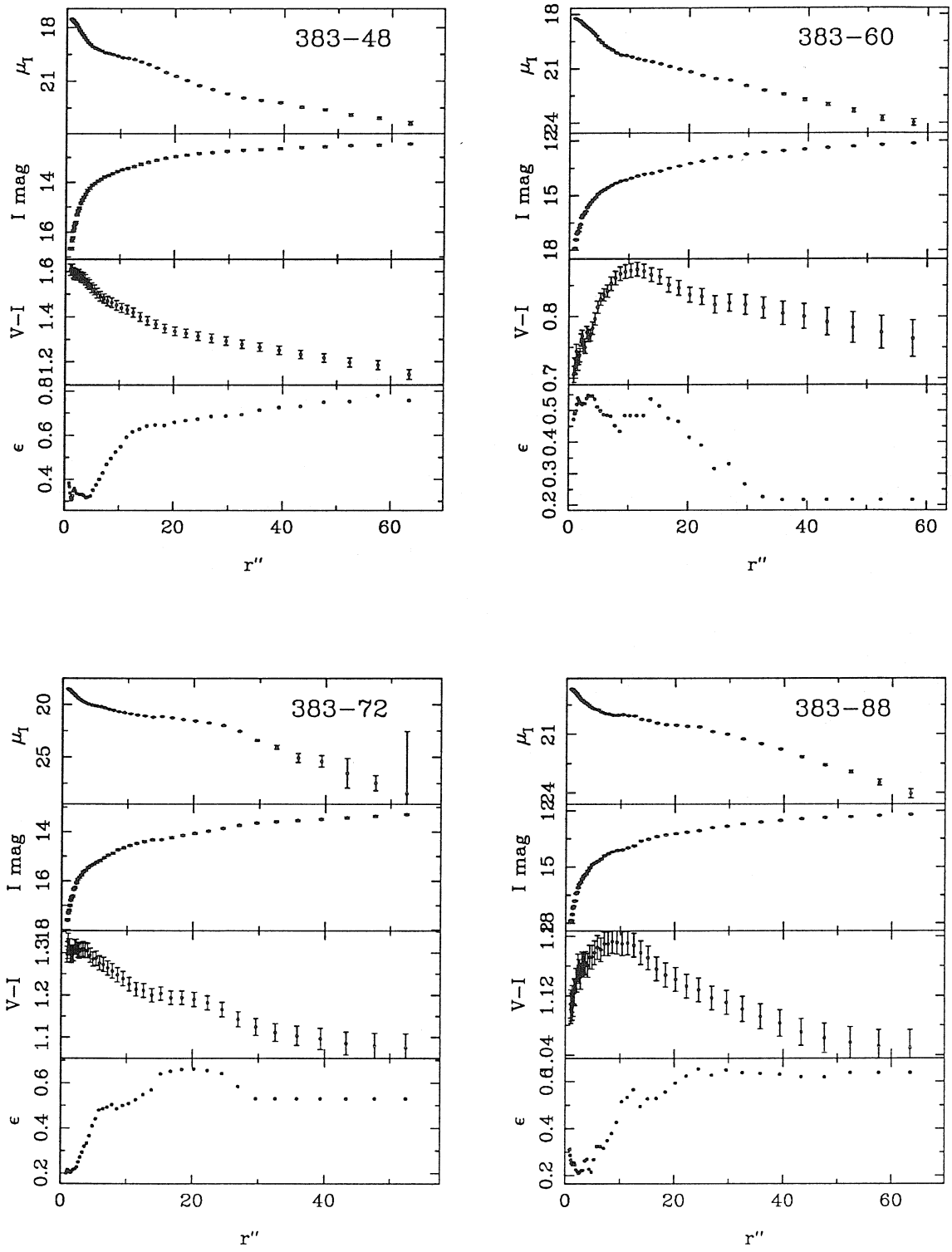

Figure 5.1 — continued

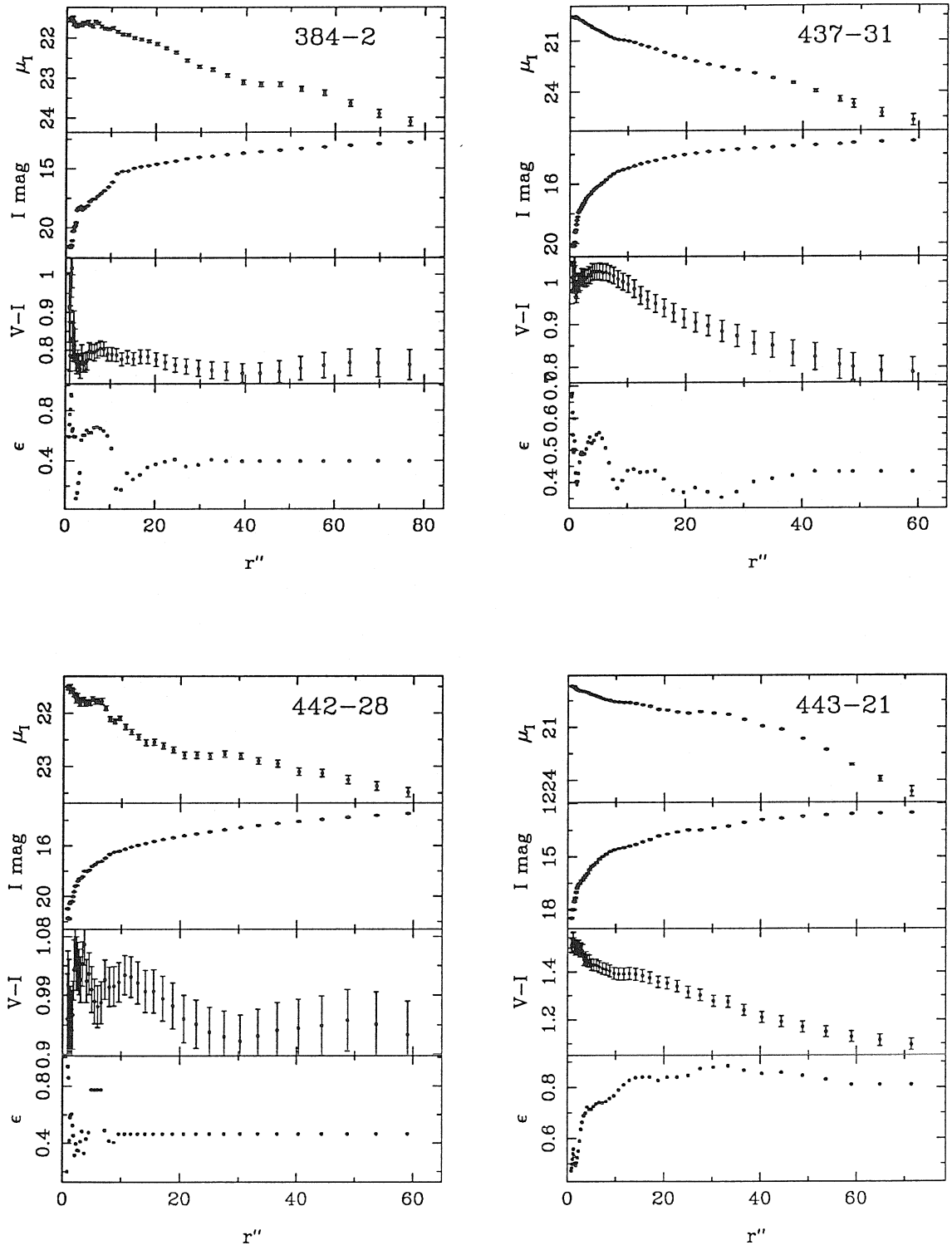

Figure 5.1 — continued

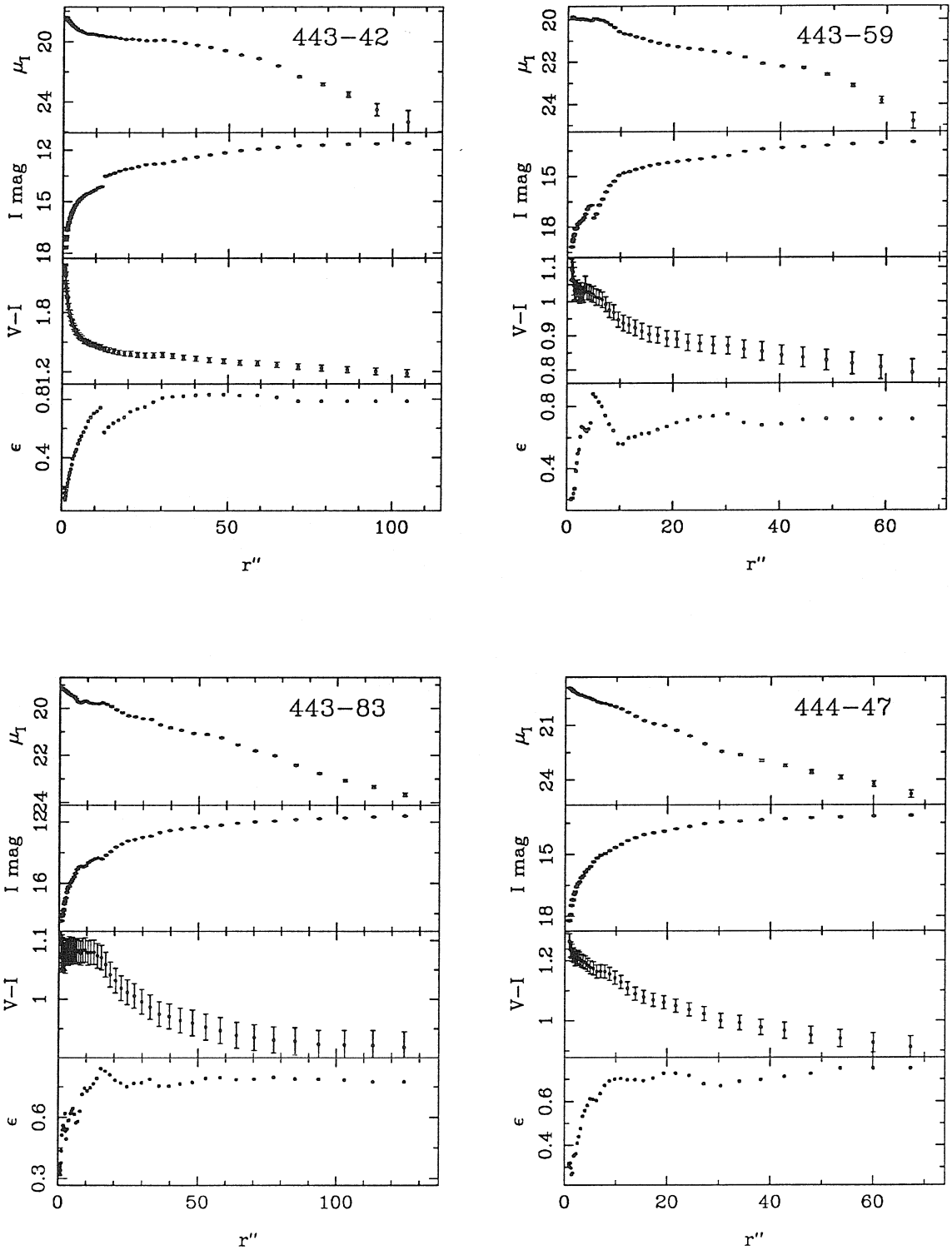

Figure 5.1 — continued

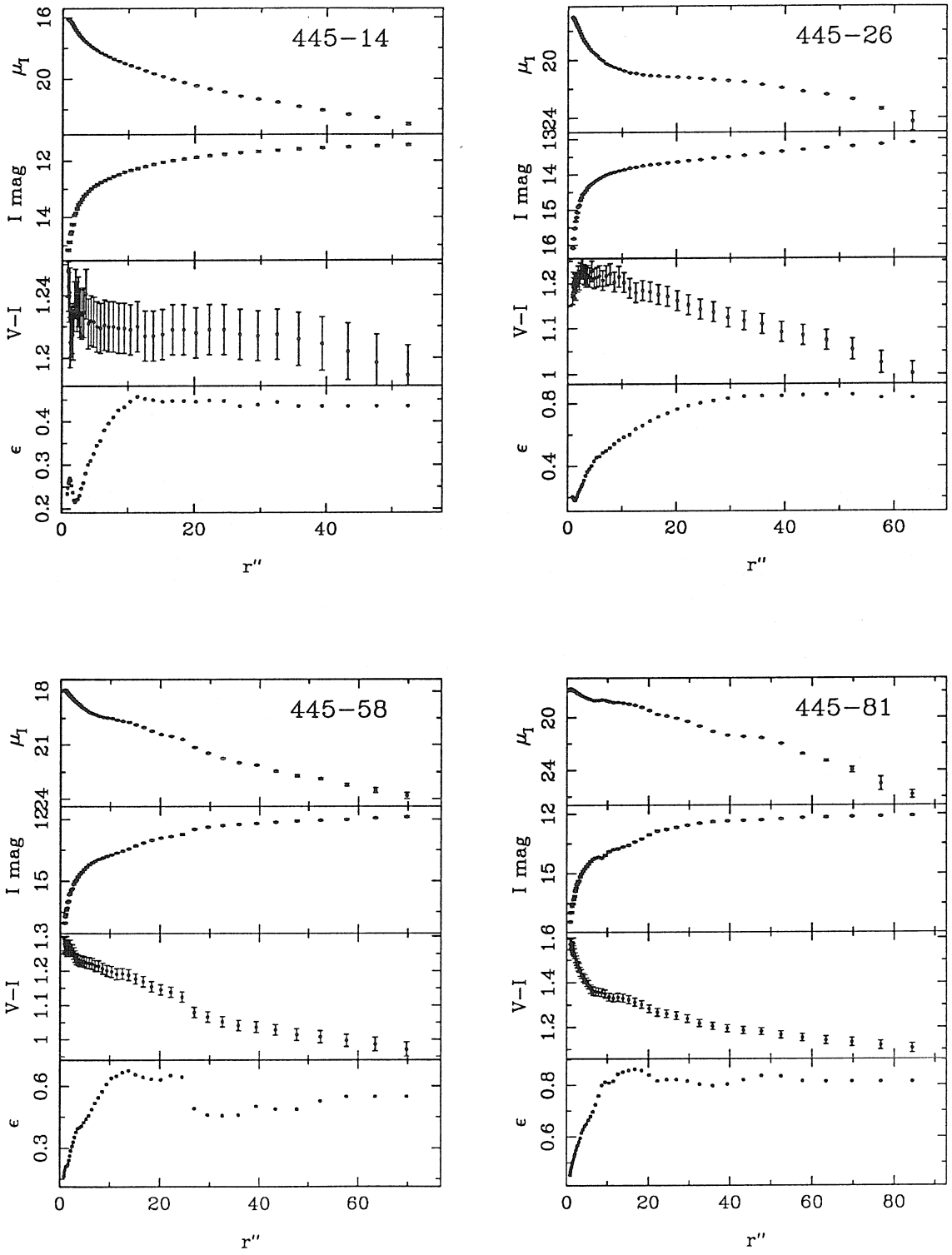

Figure 5.1 — continued

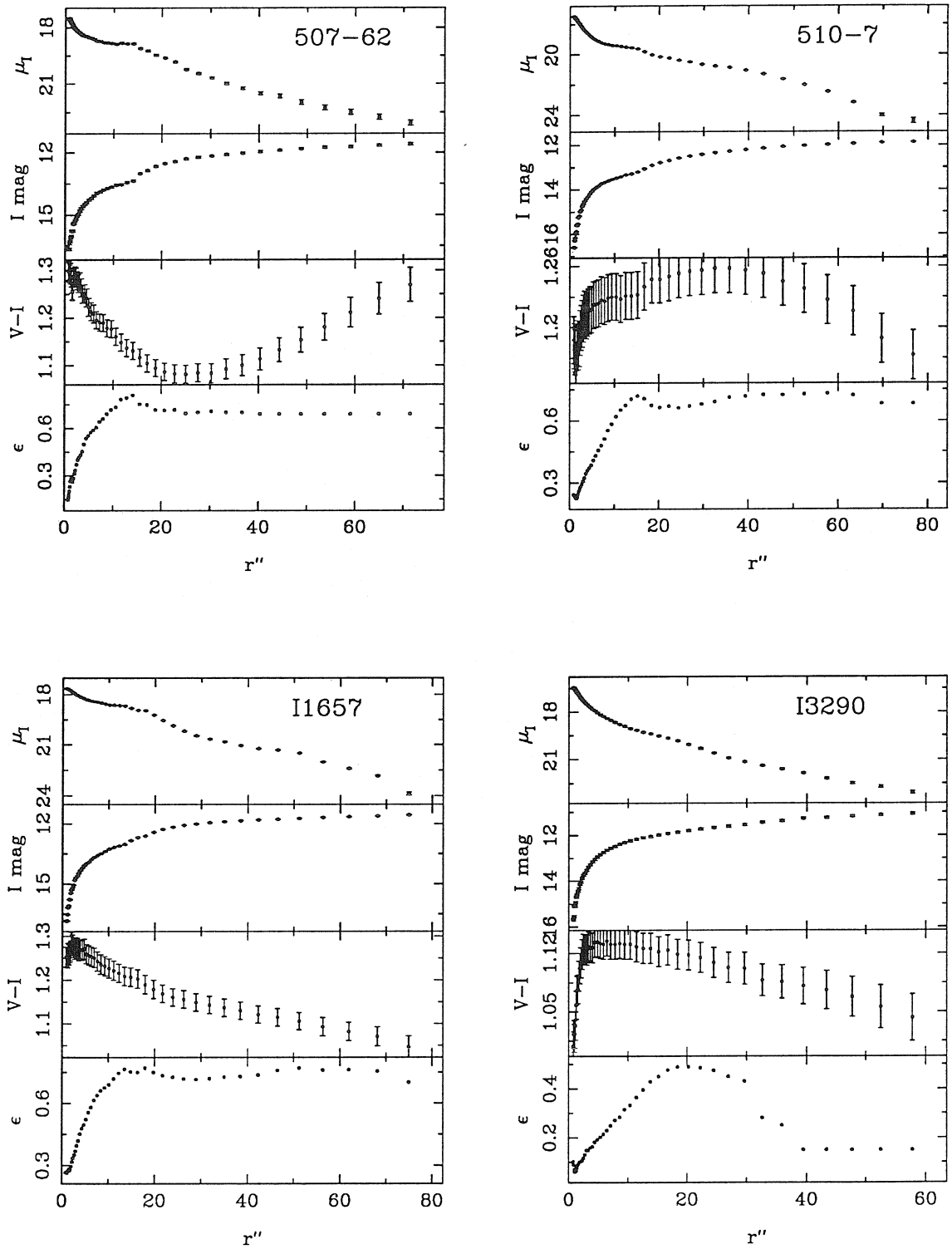

Figure 5.1 — continued

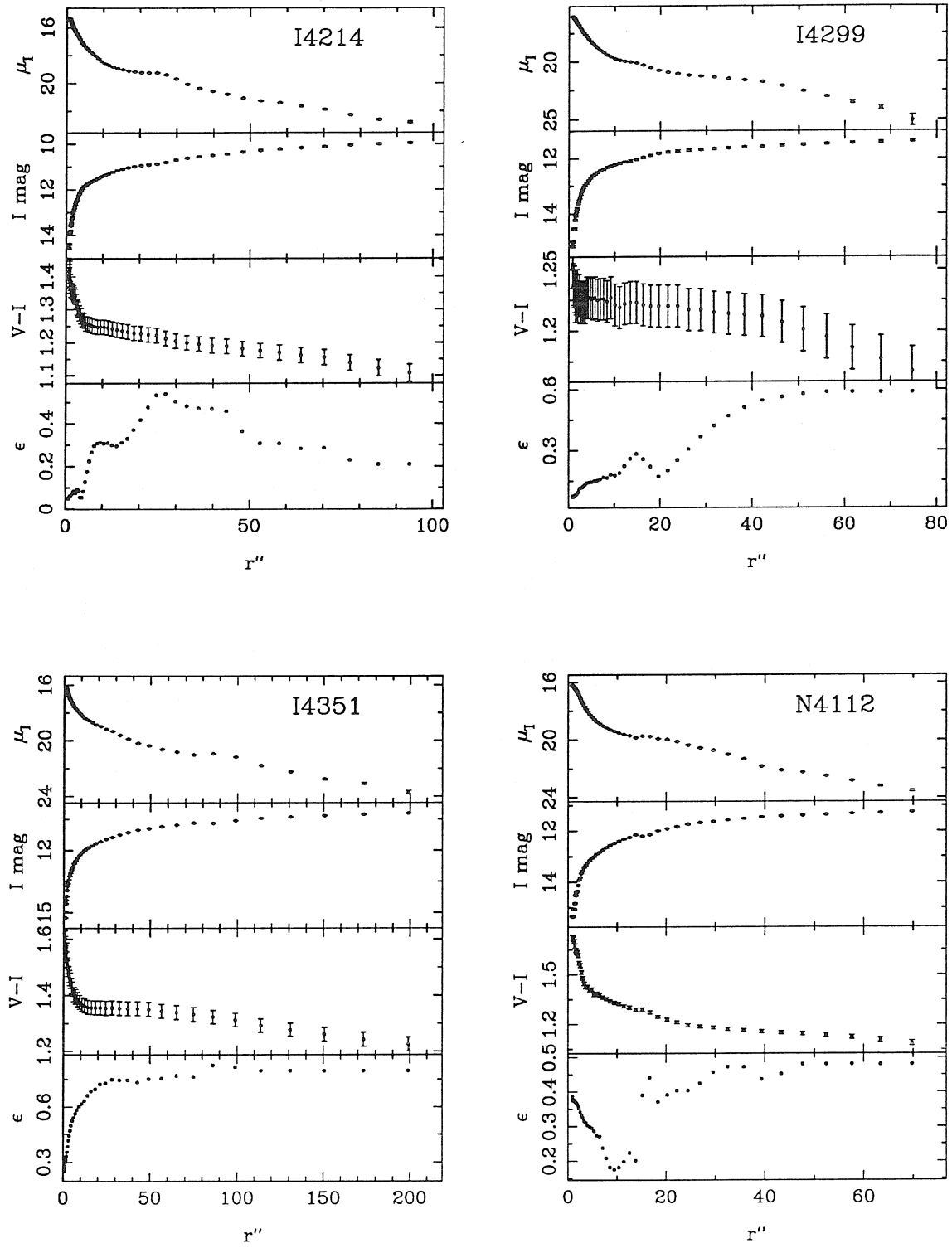

Figure 5.1 — continued

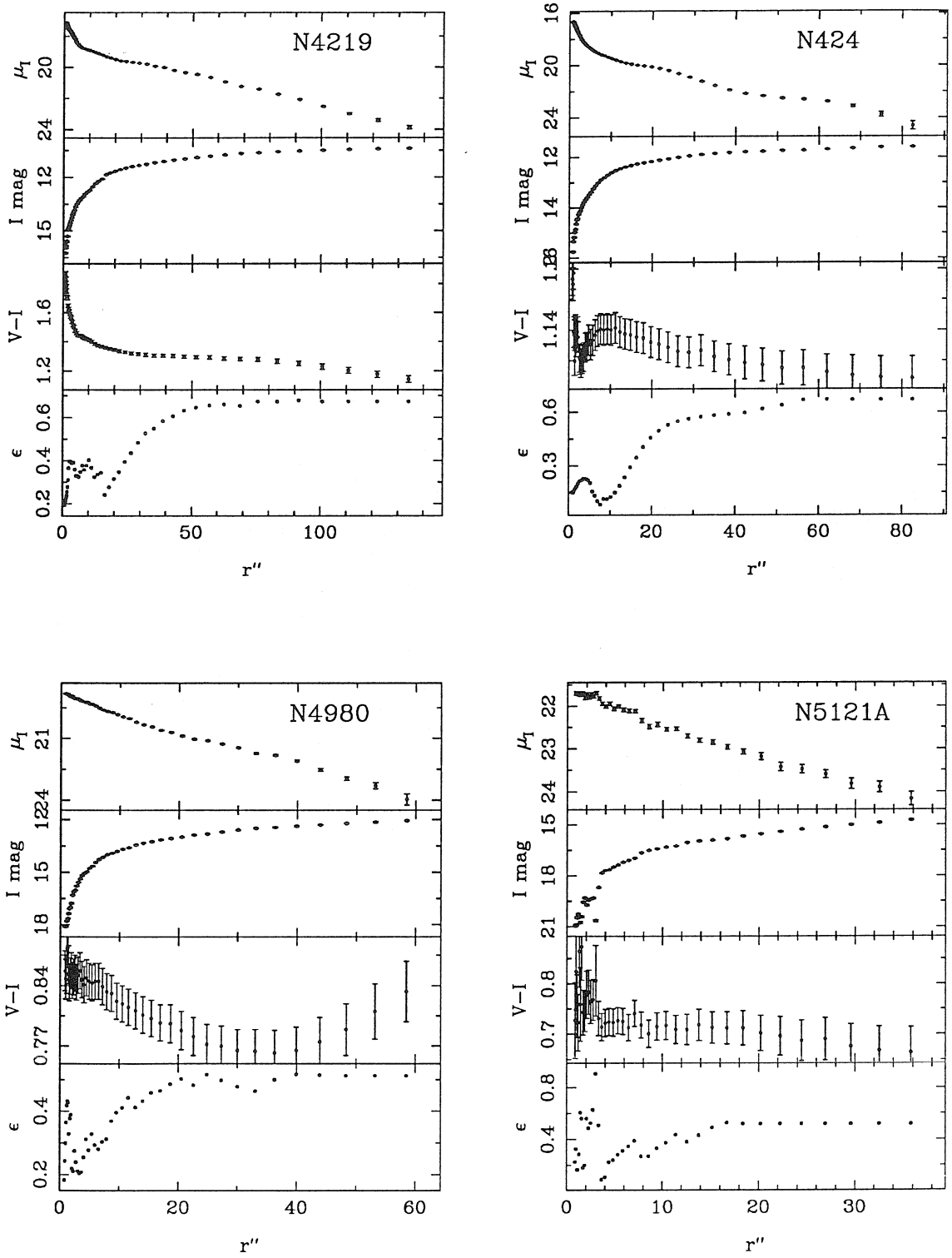

Figure 5.1 — continued

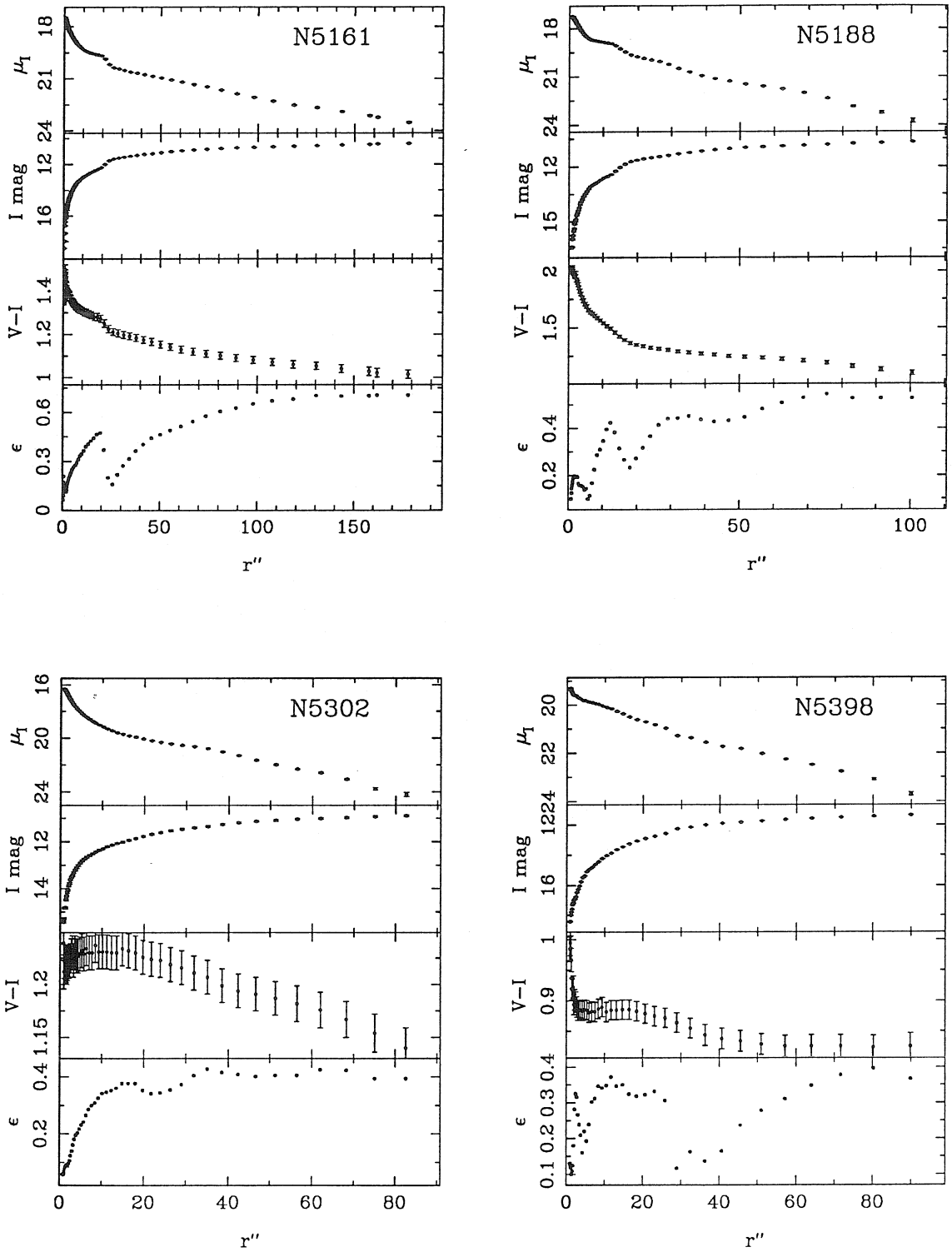

CHAPTER VI

THE TULLY-FISHER RELATION

AND ITS APPLICATION AS A DISTANCE INDICATOR

§6.1 The TF Relations of Individual Clusters

The Tully-Fisher relations, using both the isophotal magnitude $I_{23.5}$ (Col. [5] of Table 5.1) and the total magnitude I_{tot}, (Col. [6] of Table 5.1), for each cluster are presented in Figure 6.1. Non-cluster members are not plotted in Figure 6.1. The results of a double linear fit (i.e., average of χ^2 fits using each axis as independent) for each relation in Figure 6.1 are tabulated in Table 6.1; Column (1) lists the cluster names; Column (2) records the number of cluster member galaxies; Columns (3)-(5) give the fitting results for the $I_{23.5}$ - $\log W$ relation, i.e., the slope b, the dispersion about the mean relation σ_m, and the linear correlation coefficient r; Columns (6)-(8) list the same parameters for the I_{tot} - $\log W$ relation. The mean velocity width $< \log W >$ of each cluster sample and the cluster velocity v_c are also given in the last two columns.

The variation of the TF slope (col. [3] and [6]) from Table 6.1 with cluster redshift (col. [8]) and the mean velocity width (col. [7]) is shown in Figure 6.2, where the Arecibo and Parkes clusters are plotted in filled circles and open circles, respectively. From Fig 6.2 we see:

1) A weak trend of slope increasing with cluster redshift for nearby cluster (within about 5000 km/s) and then decreasing with redshift beyond 5000 km/s.

2) A similar variation of slope with cluster mean velocity width.

3) The $I_{23.5}$ and I_{tot} TF relations basically show similar apparent dependence on cluster redshift and mean velocity width. But the I_{tot} TF relation seems to have a smaller scatter about the mean variations.

4) In any case, the systematic variations are only marginally significant, at about 1 σ level.

Aaronson *et al.* (1986), in their study of the H-band TF relation of the Arecibo cluster sample, first noticed the apparent systematic variation of the TF slope with cluster redshift, and explained it as implying a curved TF relation. Mould, Han & Bothun (1989) showed that this slope variation can indeed be accounted for by the curved TF relation of the Local Supercluster, and does not indicate an intrinsic variation of the TF relation from cluster to cluster. They also pointed out that a more direct indication of a curved TF relation is presented in the slope vs mean velocity width plot. The sense of variation shown in Figure 6.2 seems to imply that the (I-band) TF relation has a flatter part at both the brighter and fainter ends. If the TF relation is universal, the reason that we see different apparent TF relations from different clusters is certainly a combined result of sample selection effects and the intrinsic properties of the universal TF relation (its shape and scatter). In other words, the selection effects allow us to extract only a piece of the complete TF relation from each cluster. Our concern here is how we can derive the relative distances of the sample clusters from these incomplete pieces of TF relations.

§6.2 The TF Relation As A Distance Indicator

As mentioned in Chapter 1, one of the fundamental questions about the TF relation is the question of its universality, i.e., whether or not it depends on the environment of galaxies. This is especially crucial when the relation is used as a distance indicator. Considering the emergence of such a relation from the processes of galaxy formation and evolution, it seems very likely that galaxy environment should have some bearing on a distance indicator relation (see, e.g., Djorgovski, de

Carvalho & Han 1989). Empirical investigations of the problem, however, indicate that the TF relation has little dependence on galaxy environment (Bothun *et al.* 1984; Mould, Han & Bothun 1989; Biviano *et al.* 1990), suggesting that the relation is qualified as a distance indicator.

Once we have a distance indicator, the next big question is how we are going to make use of this indicator to derive distances of galaxies, or clusters of galaxies from an observed dataset, which is usually subject to various selection effects. The distance indicator may yield a biased result if the selection effects are not properly handled. For example, when the TF relation is directly used on a magnitude limited galaxy sample, i.e., a sample selected according to apparent magnitude *only*, the mean distance will be under-estimated due to the familiar Malmquist bias (see Bottinelli *et al.* 1988, and references therein). A pure magnitude selection of a galaxy sample can be well quantified, and the effects of such selection on the TF relation have been studied by Teerikorpi (1984; 1987) from the theoretical point of view. In fact, the selection criterion for a real galaxy sample is usually far more complicated than just a clear apparent magnitude cut; other constraints may include, for example, the apparent size of galaxies, the HI flux of galaxies, redshift of galaxies, surface brightness of galaxies (especially with samples drawn from plate surveys), or even the inclination of galaxies. All these parameters, which are somehow inter-correlated with each other, are known to have some subtle (intrinsic or apparent) correlations with luminosity or velocity width (the two quantities in the TF relation). Obviously, without properly treating the selection effects, one would be very likely to get a biased result in employing the TF relation on such a sample. Unfortunately, there has not been a complete investigation about how the TF relation would be biased by the aforementioned sample selections; this is primarily due to a lack of knowledge about distributions of various parameters, and their inter-correlations for a complete sample of galaxies. Deriving distances using the TF relation is basically to perform a fit of the relation to the observed data; the most commonly used fitting techniques in literature are either a direct or reverse

least-squares fit, or sometimes the average of the two. In advance of applying any of these schemes to derive distances, we need to know how they are biased by real sample selection effects, which are expected to be more complicated than the single idealized Malmquist effect.

Ideally, one would like to deal with the selection effects using the Maximum Likelihood technique. Such a technique is, however, computationally more expensive than a simple χ^2 fit, and also requires a reasonably good analytical expression of the sample completeness. A formally complete Maximum Likelihood function, for the study of the TF relation and the velocity field in LSC using a *field sample* of spiral galaxies, has been developed by Han & Mould (1990). For a *cluster sample*, things are simpler in the sense that we do not need to assume a complicated velocity field model to estimate the relative cluster distances. Then how should we estimate the relative distances of clusters? If the shape of the (universal) TF relation is known *a priori*, one may directly calculate the relative mean distance moduli by applying the TF relation to the sample clusters (this is equivalent to a χ^2 fitting with the shape of TF relation fixed, and will be named the χ^2_o scheme below). This is the method employed by Aaronson *et al.* (1986, 1989), who used the H-band TF relation derived from a LSC sample of galaxies (Aaronson *et al.* 1982a, 1982b) as the calibration relation (it should be noted that the form of the TF relation deduced from a field sample may have some subtle dependence on the adopted velocity field model in the LSC). This scheme will not be adopted in this thesis, both because we do not have a reliable I-band calibrating TF relation and because this method suffers sample selection bias as shown below. Another approach is a χ^2 fitting scheme which fits the TF relation and relative cluster distances simultaneously by minimizing residuals of either magnitude (χ^2_m scheme) or velocity width (χ^2_w scheme). Willick (1990) employed a χ^2_m scheme in his study of the 10 Arecibo clusters of Aaronson *et al.* (1986) using the R-band TF relation. In §6.3, I derive a Maximum Likelihood function, which can be used to fit the TF relation and the

relative cluster distances, with the capability of removing sample selection effects. It is also demonstrated below, that for a galaxy sample selected according to both diameter and HI flux, the χ^2_o scheme and χ^2_m scheme suffer significant bias, but the χ^2_w scheme is largely free of such sample selection effects.

§6.3 A Maximum Likelihood Technique

a) The Maximum Likelihood Function

For a cluster sample, we assume all the galaxies within a single cluster are at the same distance, and that each galaxy is associated with three observed quantities relevant to the problem, the apparent magnitude m, the velocity width $\log W$, and its angular distance to the cluster center r. Now, we ask, given the sample selection limits, what is the probability for the sample galaxies to have a given distribution in the plane of the three parameters.

Let $\phi(M)$ be the luminosity function of the cluster galaxies and $D(r)$ be the surface galaxy number density of the cluster, assumed to be spherically symmetric and r be the projected distance to the cluster center. We further assume that the velocity width at a given luminosity is normally distributed with dispersion $\sigma_{\log W}$, which may include both intrinsic and observational errors. Clearly, in a projected area $r dr d\theta$ at a distance r from the cluster center, the number of galaxies with M and $\log W$ in the intervals of (M, $M + dM$), and ($\log W$, $\log W + d\log W$), respectively, is given by

$$N(M, \log W, r) dM\, d\log W\, r\, dr d\theta$$

$$\propto \exp\left[-\frac{(\log W - \langle \log W \rangle_M)^2}{2\,\sigma^2_{\log W}}\right] D(r)\,\phi\,(M)\, dM\, d\log W\, r\, dr d\theta, \qquad (6.1)$$

where $\langle \log W \rangle_M$ is the mean value of $\log W$ at constant M, which is independent of how the sample is collected (Schechter 1980). If there were not any observational constraints, we would expect that the probability of observing a galaxy with

$(M,\ \log W)$ at position r is directly proportional to equation (6.1). Unfortunately, the various observing limits and selection effects allow us only to be able to sample a portion of the complete distribution, which is usually distorted relative to the parent distribution. Define a sample completeness function $C(M, \log W)$, which is the fraction of galaxies with given $(M, \log W)$ that are sampled from the complete population. The probability of observing a single galaxy with $(M, \log W)$ at r, is given by

$$p(M, \log W, r) = \frac{1}{C_N} C(M, \log W)\, N(M, \log W, r), \tag{6.2}$$

where

$$C_N = \int_{-\infty}^{+\infty} dM \int_{-\infty}^{+\infty} d\log W \int_0^{\infty} r\, dr \int_0^{2\pi} d\theta\, [N(M, \log W, r)\, C(M, \log W)] \tag{6.3}$$

is a normalization factor. The joint probability of finding all the sample galaxies at their $(M, \log W, r)$ is $P = \prod_i p_i(M, \log W, r)$. The likelihood function is then given by

$$\begin{aligned} L = \ln P &= \sum_i \ln p_i(M, \log W, r) \\ &= -\frac{1}{2} \sum_i \frac{(\log W - \langle \log W \rangle_M)^2}{\sigma^2_{\log W}} + \sum_i \ln \Big[D(r) \phi(M) C(M, \log W) C_N^{-1} \Big]. \end{aligned} \tag{6.4}$$

To fully evaluate the likelihood given by (6.4), one has to know the following:

1) $D(r)$: the projected distribution of galaxies in the cluster. Only the relative distribution is required for our purpose, and it usually can be well determined by direct observation.

2) $\phi(M)$: the luminosity function, which can be independently determined, and of course, has to be assumed to be independent of environment. Note that we ignored the type dependence of $\phi(M)$ in the above formulae, although it can be easily included.

3) $\langle \log W \rangle_M$: the mean value of $\log W$ at constant M. This is given by the TF relation.

4) $C(M, \log W)$: the sample completeness function. This might be the most poorly known of all, because a sample of galaxies for the study of the TF relation is usually directly selected according to other properties of galaxies rather than the two parameters (M, $\log W$), which give rise the TF relation. In principle, if we know galaxies so well, we can certainly derive $C(M, \log W)$, given the constraints on other properties of galaxies. For now, however, one has to seek for other empirical methods to estimate the completeness of a sample.

Once the likelihood is reduced to a known function of some model parameters (e.g., the parameters in the TF relation, and cluster distances), one can then derive the most likely estimates of these parameters by maximizing L. It should be noted that if the second term in equation (6.4) is independent of all the model parameters, maximizing L is just equivalent to minimizing $\sum_i (\log W - \langle \log W \rangle_M)^2 / \sigma^2_{\log W}$, i.e., the ML technique reduces to the conventional χ^2_w scheme. This also makes it clear that if the second term of equation (6.4) is a strong function of some model parameters, a simple χ^2 method would yield a biased estimate of the parameters.

b) Completeness Function of Cluster Samples

Here we propose a method to simulate, using a nearby field galaxy sample, the completeness function of a distant cluster sample, which is selected according to *diameter*, *magnitude*, and *HI flux*. To do this, we have to assume that the distribution of the interesting quantities (magnitude, velocity width, HI content, galaxy size) of field galaxies is *similar* to that of cluster galaxies.*

---

* This is not true exactly, as there has been lots of evidence for the environmental dependence of various galaxy properties (see, e.g., Binggeli 1987; Whitmore *et al.* 1988; Magri *et al.* 1988, and references therein). These environmental effects, if well

Given a field galaxy sample, with distance to each galaxy known, one can put all of them to a reference distance d, and scale all the quantities accordingly. This forms an equivalent "cluster sample" at distance d, but with better completeness than we actually observe a cluster at the same distance. Now we can use our selection criterion to "observe" this simulated cluster, and see how many percent of galaxies at $(M, \log W)$ pass our selection; this percentage is just the completeness function of observing this simulated cluster at the given distance, *if the simulated cluster itself is complete.* The field galaxy sample, or the simulated cluster, is certainly not complete, since it is also subject to similar selection effects. So the percentage thus obtained is really a completeness function relative to the field sample; we denote it as $C'(M, \log W)$. Fortunately, all the quantities which constrain the selection of a galaxy sample, are roughly positively correlated. This means that the completeness of the field sample increases with, e.g., the size, HI content, or luminosity of galaxies; therefore, the relative completeness $C'(M, \log W)$ better represents the true completeness, for more stringent selection limits, or for more distant clusters.

As an experiment, I use the Local Supercluster dataset of Aaronson *et al.* (1982a) to derive relative completeness functions for distant "clusters". The kinematic distance relative to the Virgo cluster as given by these authors is used to scale the sample galaxies to an arbitrary distance. The parameters involved are the H-band magnitude $H_{-0.5}$, velocity width W, diameter A, total HI flux F, and inclination i. When simulating a cluster at distance d by pushing all the galaxies to this distance, the parameters $H_{-0.5}$, A, and F are scaled to this distance in the conventional way; A is also de-corrected for inclination effects according to the RC2 formula (see equation [4.8]). We then impose the following selection limits on such

---

understood, can certainly be accounted for in our analysis above. But this is not investigated in this thesis. As a matter of fact, as we will show below, the Maximum Likelihood method introduced in this thesis will not be implicitly employed to derive cluster distances for a number of other reasons.

a simulated cluster,

1. Apparent diameter: $A > 1'$,

2. HI flux per channel: $F/(W \sin i) > 4$ mJy.

These are approximately the selection limits for the cluster sample of this thesis, and also for most other samples currently available. It is interesting to note the influence of galaxy inclination in sample selection: highly inclined galaxies are more likely to be selected according to the diameter limit, since they appear bigger due to projection effects; on the other hand, a highly inclined galaxy would spread its HI flux into a broader frequency region, and thus makes it less easy to detect with a radio telescope. One should also note that, in order to understand how the diameter and flux limits affect the observed distribution of M and W, we are not imposing magnitude limits here, which can be easily included later by multiplying a step function with the resultant completeness function due to the selection of A and F. To "measure" the completeness of a simulated cluster with the selection limits above, we need to divide the sample galaxies into several 2-D bins according to both M and $\log W$. However, because of the small size of the sample, we choose to make 1-D bins of the data according to M and $\log W$ separately, we thus "measure" the 1-D integrations of $C'(M, \log W)$, denoted as $\overline{C}_m(M)$ and $\overline{C}_w(\log W)$, respectively. Figure 6.3a illustrates $\overline{C}_m(H)$, the relative completeness of H magnitudes (hereafter, I simply use H to denote $H_{-0.5}$), for the simulated clusters at different distances (in units of Virgo distance); Figure 6.3b shows $\overline{C}_w(\log W)$, the relative completeness of velocity width.

It will be useful to parameterize the completeness of H and $\log W$ as shown in Figure 6.3. Different forms of analytical expression have been tried; the following two provide reasonable fits to the data:

$$\overline{C}_m(H) = \left[1 + \exp\left(\frac{M - \alpha_H - \beta_H \log d}{\delta_H}\right)\right]^{-1}, \qquad (6.5a)$$

for the H completeness function, and

$$\overline{C}_w(\log W) = \left[1 + \exp\left(\frac{\log W - \alpha_W - \beta_W \log d}{\delta_W}\right)\right]^{-1}, \qquad (6.5b)$$

for the $\log W$ completeness function, where d is the distance of the simulated clusters in units of the Virgo distance. Using the data of the simulated clusters with $d > 2d_{virgo}$, we find the best fitting parameters are,

$$\begin{cases} \alpha_H &= 16.18 \pm 0.28 \\ \beta_H &= 9.87 \pm 0.40 \\ \delta_H &= 0.92 \pm 0.25 \end{cases} \qquad (6.5c)$$

$$\begin{cases} \alpha_W &= -0.62 \pm 0.05 \\ \beta_W &= -0.96 \pm 0.08 \\ \delta_W &= 0.10 \pm 0.01 \end{cases} \qquad (6.5d)$$

As just mentioned, the functions $\overline{C}_m(H)$ and $\overline{C}_w(\log W)$ so derived are the 1-D integrations of the relative completeness function $C'(H, \log W)$ over H and $\log W$, respectively. If $C_o(H, \log W)$ denotes the completeness function of the field sample we have used, then the "cluster" completeness function $C(H, \log W)$, that we are seeking for, is hidden in the following relations

$$\overline{C}_m(H) \propto \int_{-\infty}^{+\infty} C'(H, \log W) d\log W = \int_{-\infty}^{+\infty} \frac{C(H, \log W)}{C_o(H, \log W)} d\log W, \qquad (6.6a)$$

$$\overline{C}_w(\log W) \propto \int_{-\infty}^{+\infty} C'(H, \log W) dH = \int_{-\infty}^{+\infty} \frac{C(H, \log W)}{C_o(H, \log W)} dH. \qquad (6.6b)$$

It is impossible, at least mathematically, to uniquely determine the function $C(H, \log W)$ from these equations alone. We do not investigate these problems further in detail. Instead, we take two most straightforward approximations, namely,

1) $C'(H, \log W) \propto \overline{C}_m(H)\overline{C}_w(\log W)$, and 2) $C_o(H, \log W) \sim const.$

Note that the first approximation is indeed a solution of equation (6.6), and the second approximation is better for more distant clusters than for nearby clusters. We thus come to an estimate of the completeness function for a simulated cluster,

$$C(H, \log W) \sim \overline{C}_m(H)\overline{C}_w(\log W), \tag{6.7}$$

where $\overline{C}_m$ and $\overline{C}_w$ are given by equations (6.5a-d). Note that the cluster distance d in these equations is in units of Virgo distance, and $\overline{C}_m$ requires an absolute magnitude scaled to the Virgo distance.

§6.4 Test of Different Fitting Methods

An interesting test of the Maximum Likelihood scheme (and also other fitting methods: χ^2_m , χ^2_w , and χ^2_o) is to apply it on the simulated clusters as described in §6.3*b*, and see how well it predicts the "cluster" distances. To do this, I set $D(r)$ = const in the likelihood, which is not defined for the simulated clusters, although the detection of each galaxy in the original sample of Aaronson *et al.* does have some dependence on the local density in the LSC. The completeness function for the simulated clusters are taken to be equation (6.5), and the H band luminosity function is taken to be that as derived by Han and Mould (1990), i.e.,

$$\phi(H) \propto x^{\beta} e^{-x}, \tag{6.8}$$

where $x = \mathrm{dex}[-0.4(H - H_*)]$, and $\beta \sim -0.05$, $H_* \sim 7.4$. The magnitudes are scaled to the Virgo distance.

As a first attempt, we assume a linear Tully-Fisher relation. For the i^{th} galaxy in j^{th} cluster, we then have

$$H_{i,j} = a + b \log W_{i,j} + 5 \log(d/d_{virgo}), \tag{6.9}$$

where $H_{i,j}$ is apparent magnitude, d/d_{virgo} is the cluster distance in units of Virgo, which is to be found by the ML fitting. The parameters a and b define the TF relation at the Virgo distance.

We have 11 simulated clusters with distance ranging from d_{virgo} to $8d_{virgo}$, which just covers the distance range of our real cluster sample. The total number of free parameters is 12; that is, the distances of 10 clusters relative to a reference cluster (taken to be that at d_{virgo}), plus the 2 parameters characterizing the TF relation at the reference cluster. The ML fitting is then performed using the minimizing routine E04UCF of the NAG library. Figure 6.4 illustrates the fitting result (filled dots), in which the relative errors in the fitted distances of the clusters are plotted against the true distances. For comparison, the results from the conventional fitting methods of χ^2_o scheme (cross), χ^2_m scheme (open square) and χ^2_w scheme (open triangle) are also shown in the same panel. In the test of χ^2_m and χ^2_w fitting methods, a linear TF relation is assumed. In the test of the χ^2_o method, the quadratic TF relation as employed by Aaronson *et al.* (1986) is used; this test is thus directly relevant to the result of Aaronson *et al.* From Figure 6.4, it is clearly seen that the χ^2_o scheme and χ^2_m scheme both suffer large systematic bias, and their predicted cluster distances have errors as large as 10%. The ML technique and the χ^2_w scheme are almost equally good in revealing the true distances, and the uncertainties are within 5%.

It is worth noting that, according to Aaronson *et al.*, the H-band TF relation of the LSC sample is highly nonlinear. One might expect that using a quadratic TF relation in the ML or the χ^2_m and χ^2_w schemes would yield better predictions of cluster distances. The ML and χ^2 fittings are thus carried out using a quadratic TF relation. Indeed, the ML and the χ^2_w schemes predict the cluster distances slightly better; however, the χ^2_m scheme does not show any improvement at all. This reflects the complexity of sample bias. Figure 6.5 shows the fitting results with a quadratic TF relation, analogous to Figure 6.4, the solid dots represent the ML results, and the open squares and open triangles show the results of the χ^2_m and χ^2_w schemes, respectively.

The following conclusions can be drawn from the above analyses.

a) A cluster galaxy sample selected based on apparent diameter and HI flux is biased. The conventional χ^2_m scheme is very sensitive to such bias, and thus yields biased distance estimates; however, a χ^2_w fitting scheme is very robust against such sample bias (but not necessarily if the sample is selected according to other criteria).

b) Both the fitting method and the form of the TF relation (linear or quadratic) affect our prediction of cluster distances. The fitting technique seems to be more crucial.

c) The ML method does not show much advantage over the χ^2_w method; this may be due to the uncertainties in the estimated completeness functions, and uncertainty in the luminosity function.

After comparing the different fitting schemes using simulated clusters, we are now ready to study our real clusters.

§6.5 Relative Distances of the Sample Clusters

Four different methods of deriving cluster distance, namely χ^2_o , χ^2_m , χ^2_w and ML scheme, were compared in §6.4. The χ^2_w fitting method turns out to be as good as the ML method, for a cluster sample selected according to galaxy's diameter and HI flux. Based on this fact and other considerations given below, we shall primarily rely on the simple χ^2_w fitting method to estimate cluster distances in this thesis. But for comparison purposes, the χ^2_m and ML schemes are also carried out.

To estimate the relative distances of the 16 clusters in our sample, we assume a linear TF relation, and fit it to our cluster sample data using the χ^2_m , χ^2_w and ML methods. Applying a relative distance shift for each cluster, we have, for each

galaxy in the sample (similar to equation [6.9])

$$I_{i,j} = a + b \log W_{i,j} + \Delta\mu^{j}_{coma}, \tag{6.10}$$

where $I_{i,j}$ and $W_{i,j}$ are, respectively, the observed magnitude and velocity width of the i^{th} galaxy in the j^{th} cluster, and $\Delta\mu^{j}_{coma}$ is the distance module of the j^{th} cluster relative to Coma. We thus have 17 free parameters for the 16 clusters, i.e., the slope b, zero-point a of the TF relation at Coma, and the 15 distance moduli relative to Coma $\Delta\mu^{j}_{coma}$. We use both the isophotal magnitude ($I_{23.5}$) TF relation and the total magnitude (I_{tot}) TF relation, in conjunction with each of the fitting schemes.

The fittings using the χ^2_m and χ^2_w methods can be easily carried out. To apply the ML method on the real cluster samples, further approximations have to be made that may introduce uncertainties, and it is a major concern for us not to rely on the ML method in this thesis. First, we ignore the density variation in each cluster, i.e. set $D(r) = \text{const}$. Second, we estimate the completeness function $C(I, \log W)$ for each of our clusters as

$$\begin{aligned} C(I, \log W) &\sim C(I - \langle I - H\rangle_W, \log W) \\ &\sim \overline{C}_m(I - \langle I - H\rangle_W)\overline{C}_w(\log W) \end{aligned}, \tag{6.11}$$

where $\langle I - H\rangle_W$ is the mean $(I - H)$ color of spiral galaxies at constant velocity width $\log W$ as given by equation (7.5) in Chapter 7, and $\overline{C}_m$ and $\overline{C}_w$ are given by equations (6.5a-d). A relative Virgo-Coma distance modulus of 3.70 (Aaronson *et al.* 1986) is assumed in scaling the distance in these equations from Virgo to Coma. Finally, We assume the I-band luminosity function is also of the form of equation (6.8). The index β and the critical magnitude I_* at the Coma distance are taken to be –0.2 and 12., respectively. These are crudely estimated from a typical B-band luminosity ($\beta \sim -0.2$, $B_* \sim -21$, see, e.g., Binggeli, Sandage & Tammann 1988) by simply scaling B_* to I_* assuming a value of 1.5 for $(B - I)$ color, and a value of 34.5 for Coma distance modulus (Aaronson *et al.* 1986).

The three fitting methods (χ^2_m , χ^2_w , and ML) combined with two TF relations ($I_{23.5}$ and I_{tot}) give 6 different solutions. Table 6.2 lists the TF parameters of each solution, namely, the zero point a, slope b, and the TF dispersion σ_m. The relative distance moduli for the sample clusters are tabulated in Table 6.3. Columns (1) and (2) of Table 6.3 record, respectively, cluster name and number of galaxies in the cluster. Columns (3), (4) and (5) list the distance moduli relative to Coma as derived by applying, in order, the χ^2_m , χ^2_w and ML schemes with the $I_{23.5}$ TF relation. Columns (6), (7) and (8) give the relative distance moduli derived by applying the three schemes with the I_{tot} TF relation. The errors associated with the moduli represent the formal rms scatters from the fit, which is usually larger than that estimated by dividing the typical TF scatter by the square root of the number of galaxies in a cluster. As explained above, we will rely on the χ^2_w method in this thesis, our finally adopted distance modulus for each cluster is the average of the results from the χ^2_w scheme with the $I_{23.5}$ and I_{tot} TF relations, respectively, i.e., the average of columns (4) and (7). This is listed in column (9) of Table 6.3. Column (10) gives the results as derived from the H-band TF relation (Aaronson *et al.* 1989), which is based on the χ^2_o fitting method as discussed above. The last column of Table 6.3 gives the relative distance moduli based on the D_n–σ relation, from Faber *et al.* (1989), Lucey & Carter (1988) or Lucey *et al.* (1991). Conversion from distances in km/s to distance moduli is done with the relation $\mu = 5(\log R + 3.029)$ as given by Lucey *et al.* (1991).

Comparing the distance moduli from different fitting methods, we have the following interesting conclusions.

1) For each fitting method, the $I_{23.5}$ and I_{tot} TF relations yield almost identical results. The mean difference of distance moduli ($I_{23.5}$ TF – I_{tot} TF) are 0.02 $\pm$ 0.03 for both χ^2_m and χ^2_w schemes, and 0.03 $\pm$ 0.04 for the ML scheme. This indicates that the two TF relations are identical when used as distance indicators.

2) The difference of distance moduli between the χ^2_m and χ^2_w schemes systematically varies with the mean velocity width of the cluster (col. [9] of Table 6.1), as shown in Figure 6.6. This variation does not have much physical significance, but simply reflects the dispersion of TF relation and the characteristics of the fitting procedure. This does give us a clear warning that at least one of the two fitting methods is biased. As we have learn from §6.4, the χ^2_m scheme is biased and the χ^2_w scheme is almost free of bias, when applied to a sample selected according to HI flux and diameter (see the appendix of Mould *et al.* 1991 for similar discussion).

3) Considering the crude approximations we have made for the sample completeness function and especially the I-band luminosity function in the ML function, the agreement between the fitting results of ML and χ^2_w methods is surprisingly good. This implies that the ML scheme is not very sensitive to the luminosity function. Indeed, a simple test shows that varying the two parameters in the luminosity function has only a weak effect on the fitting result. The same test also shows that a slightly brighter I_* gives a better ML fit, in the sense of increasing maximum likelihood value and reducing the formal rms errors of the free parameters.

4) The agreement between the result of χ^2_w , or ML fitting schemes and that of Aaronson *et al.* (1986, 1989), who utilized a χ^2_o fitting scheme and a quadratic H-band TF relation, is not very good in general. Figure 6.7a compares the relative distance moduli derived from the H-band TF by Aaronson *et al.* (col. [10] of Table 6.3) and those of present work (col. [9] of Table 6.3). The largest discrepancies are for clusters A2634, Pegasus, Cen45, A2151, Antlia, and A1367. The discrepancy does not show a clear dependence on some global properties of individual clusters, like the individual TF slope (col. [3] and [6] of Table 6.1), the cluster mean velocity width (col. [9] of Table 6.1), and cluster redshift (col. [10] of Table 6.1). Tests were also made with a quadratic TF relation in the

above fits. The distances thus predicted are almost the same as those from the fits with the linear TF relation. This is consistent with a small value for the coefficient of the quadratic term from the fits, which is about 0.8 with a formal error of the same order. The quadratic coefficient of the H-band TF relation used by Aaronson *et al.* is, however, 7.5!

5) Comparison of the present estimation of cluster distances (col. [9] of Table 6.3) with the prediction of the $D_n - \sigma$ relation (col. [11] of Table 6.3) is presented in Figure 6.7b.

With the relative distances of the clusters in hand, we can then study the peculiar motions of the clusters relative to the isotropic Hubble flow. Before doing that, however, I will first, in Chapter 7, examine the global photometric properties of the sample galaxies, and further investigate the TF relation—its physical basis and the problem of second parameters.

REFERENCES FOR CHAPTER 6

Aaronson, M. *et al.* 1982a, *Ap. J. Suppl.*, **50**, 241.

Aaronson, M. *et al.* 1982b, *Ap. J.* , **258**, 64.

Aaronson, M. *et al.* 1986, *Ap. J.* , **302**, 536.

Aaronson, M. *et al.* 1989, *Ap. J.* , **338**, 654.

Binggeli, B. 1987, in *Nearly Normal Galaxies*, ed. S. Faber (New York: Springer), p. 195.

Binggeli, B., Sandage, A. and Tammann, G. A. 1988 *Ann. Rev. Astr. Ap.*, **26**, 509.

Biviano, A. *et al.* 1990, *Ap. J. Suppl.*, **74**, 325.

Bothun, G. 1984, *Ap. J.*, **291**, 586.

Bottinelli, L. *et al.* 1988, *Ap. J.*, **328**, 4.

Djorgovski, G., de Carvalho, R. and Han, M. 1988, in *The Extragalactic Distance Scale*, eds. S. van den Bergh and C. J. Pritchet (Provo: A.S.P.), p. 329.

Dressler, A. 1984, *Ap. J.*, **281**, 512.

Faber, S. M. *et al.* 1989, *Ap. J. Suppl.*, **69**, 763.

Han, M. and Mould, J. M. 1990, *Ap. J.*, **360**, 448.

Lucey, J. R. and Carter, D. 1988, *M.N.R.A.S.*, **235**, 1177.

Lucey, J. R. *et al.* 1991, *M.N.R.A.S.*, **248**, 804.

Magri C. *et al.* 1988, *Ap. J.*, **333**, 136.

Mould, J. R., Han, M. and Bothun, G. D. 1989, *Ap. J.*, **347**, 112.

Mould, J. R. *et al.* 1991 submitted to *Ap. J.*

Schechter, P. L. 1980, *A. J.*, **85**, 801.

Teerikorpi, P. 1984, *Astr. Ap.*, **141**, 407.

Teerikorpi, P. 1987, *Astr. Ap.*, **173**, 39.

Tully, R. B., Mould, J. R. and Aaronson, M. 1982, *Ap. J.*, **257**, 527.

Willick, J. A. 1990, *Ap. J. (Letters)*, **351**, L5.

Whitmore, B. *et al.* 1988, *Ap. J.*, **333**, 542.

Figure Captions for Chapter 6

Figure 6.1: The individual $I_{23.5}$ and I_{tot} TF relations for the 16 sample clusters.

Figure 6.2: Slopes of the two individual ($I_{23.5}$ and I_{tot}) TF relations for each cluster are plotted against a) the cluster mean velocity V_c, and b) the mean velocity width $< \log W >$.

Figure 6.3: The relative completeness functions of H-band mag and velocity width derived by applying diameter and HI flux "sample selection" limits on the simulated clusters at different distances based on the LSC data of Aaronson *et al.* (1982)

Figure 6.4: Comparison between different fitting methods for their abilities of recovering the distances of simulated clusters: plotted are the relative errors in predicted cluster distances vs input (true) distances. Results of four fitting methods, namely, ML, χ^2_m, χ^2_w, and χ^2_o (see text for details), are presented in different symbols. A linear TF relation was employed in the first three fitting methods.

Figure 6.5: Same as Fig. 6.4, but a quadratic TF relation was used in the fitting methods. The results of χ^2_o is not shown here.

Figure 6.6: Difference between the distance moduli of a sample cluster derived using the fitting methods of χ^2_w and χ^2_m is plotted against the mean velocity width of the cluster. This is a demonstration of bias in estimating cluster distances using the methods of χ^2_w or χ^2_m.

Figure 6.7a: Distance moduli relative to Coma derived from the H-band TF relation versus those from the I-band TF relation.

Figure 6.7b: Distance moduli relative to Coma derived from the $D_n - \sigma$ relation versus those from the I-band TF relation.

Table 6.1

The Tully-Fisher Relation of Individual Clusters

		$I_{23.5}$ TF relation			I_{tot} TF relation				
Cluster	N	$-b$	σ_m	r	$-b$	σ_m	r	$<\log W>$	v_c
Pisces	18	8.81 ±0.59	0.32	0.96	8.12 ±0.54	0.30	0.96	2.54	5299
A400	8	7.29 ±1.42	0.31	0.88	7.63 ±1.44	0.31	0.88	2.63	8437
A539	10	7.76 ±1.71	0.33	0.76	7.56 ±1.65	0.32	0.78	2.65	8487
Cancer	11	10.17 ±1.64	0.53	0.87	9.38 ±1.51	0.49	0.87	2.51	5193
A1367	20	9.57 ±1.10	0.41	0.87	9.07 ±1.08	0.40	0.86	2.60	6680
Coma	13	7.93 ±0.96	0.31	0.92	7.41 ±0.87	0.28	0.92	2.63	7657
Z74-23	10	9.09 ±1.16	0.36	0.93	8.54 ±1.13	0.35	0.93	2.53	4558
A2151	8	7.39 ±1.29	0.28	0.90	6.87 ±1.20	0.26	0.90	2.66	10706
Pegasus	14	8.31 ±1.20	0.46	0.87	7.77 ±1.20	0.47	0.84	2.49	4129
A2634	11	6.41 ±1.05	0.26	0.87	6.28 ±1.04	0.26	0.86	2.69	9281
Antlia	10	8.50 ±1.07	0.34	0.93	8.12 ±1.03	0.33	0.93	2.59	3032
Cen30	10	8.18 ±1.15	0.46	0.92	7.91 ±1.11	0.45	0.92	2.48	3052
Cen45	6	11.51 ±2.81	0.49	0.87	11.07 ±2.70	0.47	0.87	2.59	4469
E508	8	7.35 ±0.67	0.19	0.97	6.32 ±0.60	0.17	0.97	2.49	2847
Hydra	10	9.99 ±1.48	0.44	0.92	8.78 ±1.43	0.43	0.90	2.55	3723
N3557	5	7.39 ±2.01	0.20	0.88	9.17 ±2.96	0.30	0.82	2.57	2143
mean			0.36	0.89		0.35	0.89		

b = slope of the TF relation.

σ_m = dispersion of the TF relation in units of magnitude.

r = linear correlation coefficient of the TF relation.

$<\log W>$ = mean velocity width of the cluster member galaxies.

v_c = cluster velocity relative to the Local Group centroid.

Table 6.2

Mean TF Relations by different Fitting Schemes

	a	σ_a	$-b$	σ_b	σ_m
$I_{23.5}$-TF (χ^2_m scheme)	13.85	0.11	7.81	0.30	0.35
$I_{23.5}$-TF (χ^2_w scheme)	14.07	0.12	9.53	0.36	0.39
$I_{23.5}$-TF (ML scheme)	14.03	0.13	9.44	0.34	0.39
I_{tot}-TF (χ^2_m scheme)	13.67	0.11	7.27	0.28	0.34
I_{tot}-TF (χ^2_w scheme)	13.89	0.12	8.96	0.35	0.38
I_{tot}-TF (ML scheme)	13.81	0.07	8.74	0.33	0.37

Table 6.3

Distance Moduli Relative to Coma by Different Methods

Cluster (1)	N (2)	$\Delta\mu_1$ (3)	$\Delta\mu_2$ (4)	$\Delta\mu_3$ (5)	$\Delta\mu_4$ (6)	$\Delta\mu_5$ (7)	$\Delta\mu_6$ (8)	$<\Delta\mu>$ (9)	$\Delta\mu I$ (10)	$\Delta\mu II$ (11)
Pisces	18	−0.80±0.10	−0.95±0.11	−0.97±0.10	−0.82±0.09	−0.97±0.11	−0.95±0.09	−0.96±0.11	−0.92±0.09	−0.81±0.17
A400	8	0.01±0.12	0.01±0.14	−0.02±0.08	−0.02±0.11	−0.02±0.13	−0.02±0.06	0.00±0.13	0.04±0.14	
A539	10	0.42±0.11	0.46±0.13	0.42±0.09	0.39±0.11	0.42±0.12	0.40±0.07	0.44±0.13	0.38±0.12	
Cancer	11	−0.44±0.11	−0.64±0.13	−0.68±0.08	−0.47±0.11	−0.67±0.12	−0.66±0.07	−0.66±0.12	−0.69±0.15	
A1367	20	0.06±0.10	0.01±0.11	−0.03±0.11	0.04±0.09	−0.01±0.10	−0.02±0.07	0.00±0.10	−0.16±0.11	−0.09±0.20
Coma	13	—	—	—	—	—	—	—	—	—
Z74-23	9	−0.04±0.11	−0.20±0.13	−0.24±0.10	−0.05±0.11	−0.21±0.12	−0.22±0.06	−0.20±0.13	−0.26±0.15	
A2151	15	0.87±0.12	0.92±0.14	0.87±0.05	0.84±0.11	0.89±0.13	0.86±0.03	0.90±0.13	0.74±0.13	
Pegasus	11	−0.96±0.11	−1.20±0.12	−1.21±0.12	−0.95±0.10	−1.19±0.11	−1.15±0.08	−1.20±0.12	−1.54±0.14	−1.59±0.23
A2634	11	0.43±0.11	0.55±0.12	0.50±0.06	0.43±0.11	0.54±0.12	0.50±0.05	0.54±0.12	0.14±0.10	1.07±0.11
Antlia	10	−2.01±0.11	−2.07±0.13	−2.12±0.13	−1.98±0.11	−2.04±0.12	−2.05±0.17	−2.06±0.13	−2.17±0.09	−1.65±0.19
Cen30	10	−1.87±0.12	−2.16±0.14	−2.15±0.14	−1.85±0.11	−2.14±0.13	−2.09±0.15	−2.15±0.13	−2.07±0.19	−1.91±0.24
Cen45	6	−0.86±0.14	−0.93±0.15	−0.94±0.16	−0.86±0.13	−0.93±0.15	−0.91±0.14	−0.93±0.15	−1.18±0.23	−2.27±0.24
E508	8	−2.01±0.12	−2.24±0.14	−2.24±0.13	−1.99±0.12	−2.23±0.14	−2.17±0.16	−2.23±0.14	−2.27±0.20	
Hydra	10	−1.10±0.12	−1.24±0.13	−1.24±0.18	−1.18±0.11	−1.32±0.13	−1.28±0.12	−1.28±0.13	−1.33±0.15	−1.23±0.13
N3557	5	−1.72±0.15	−1.82±0.16	−1.82±0.17	−1.81±0.14	−1.91±0.15	−1.87±0.22	−1.86±0.16	−1.84±0.15	

Col.(1): Cluster name. Col.(2): number of galaxies. Col.(3): using χ^2_m scheme with $I_{23.5}$ - TF relation. Col.(4): using χ^2_w scheme with $I_{23.5}$ - TF relation. Col.(5): using ML scheme with $I_{23.5}$ - TF relation. Col.(6): using χ^2_m scheme with I_{tot} - TF relation. Col.(7): using χ^2_w scheme with I_{tot} - TF relation. Col.(8): using ML scheme with I_{tot} - TF relation. Col.(9): average of cols. (4) & (7). Col.(10): using H-band TF relation (adopted from Aaronson *et al.* 1989). Col.(11): using D_n–σ relation, by Faber *et al.* (1989) and Lucey & Carter (1988) (adopted from Lucey *et al.* 1991).

Figure 6.1

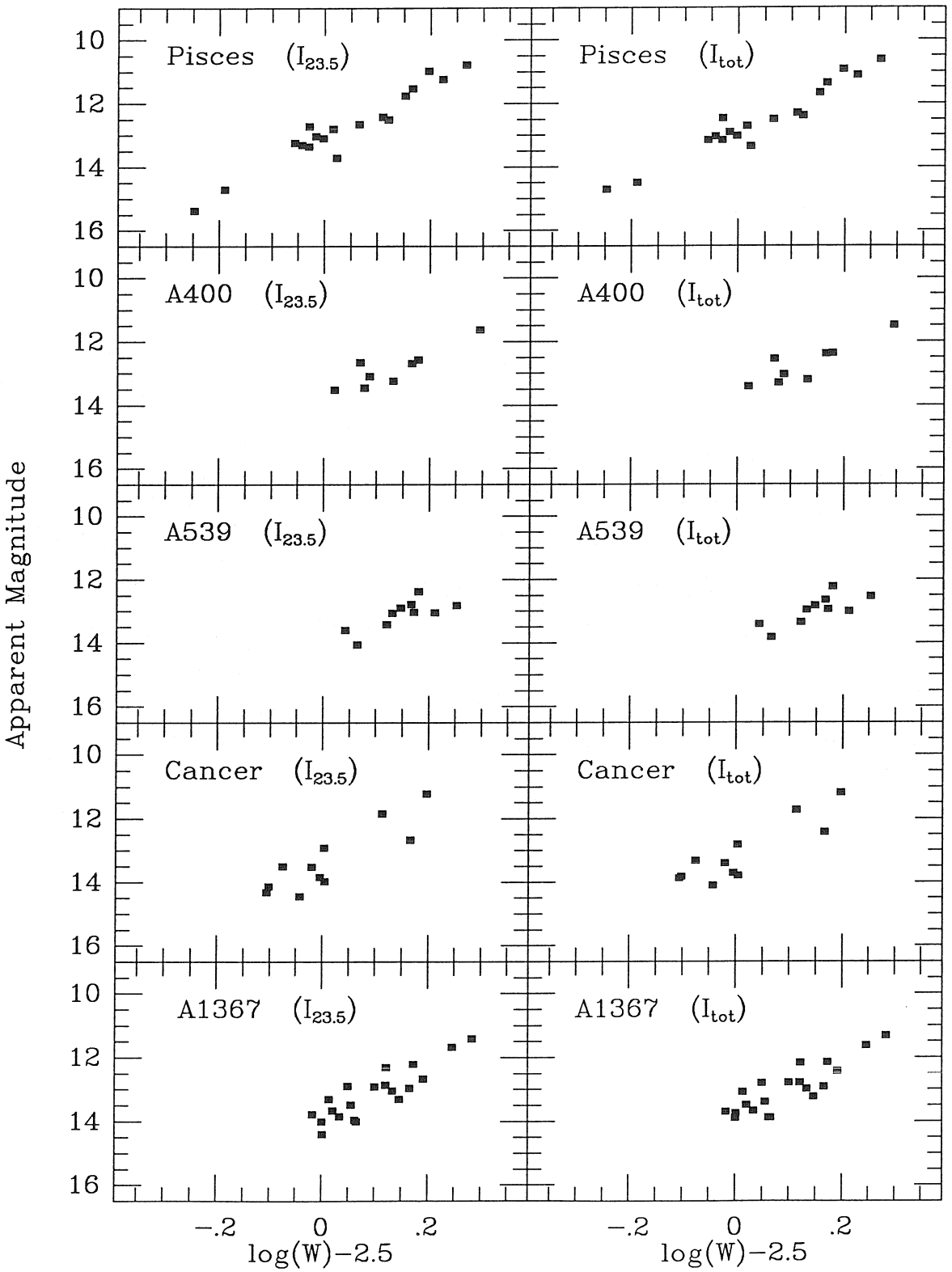
Pisces ($I_{23.5}$)
Pisces (I_{tot})
A400 ($I_{23.5}$)
A400 (I_{tot})
A539 ($I_{23.5}$)
A539 (I_{tot})
Cancer ($I_{23.5}$)
Cancer (I_{tot})
A1367 ($I_{23.5}$)
A1367 (I_{tot})
Apparent Magnitude
10
12
14
16
−.2
0
.2
log(W)−2.5

Figure 6.1 – continued

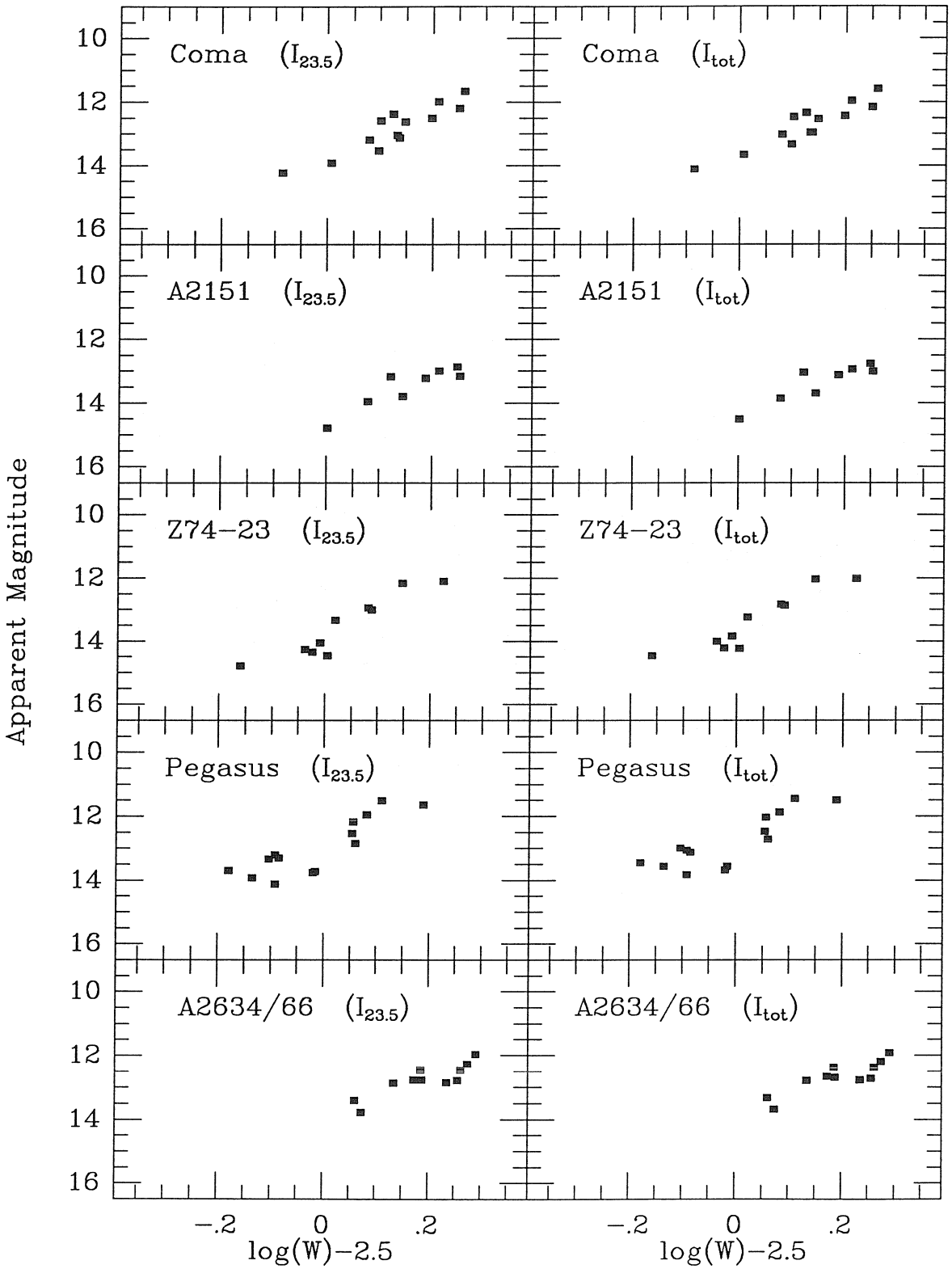

Figure 6.1 – continued

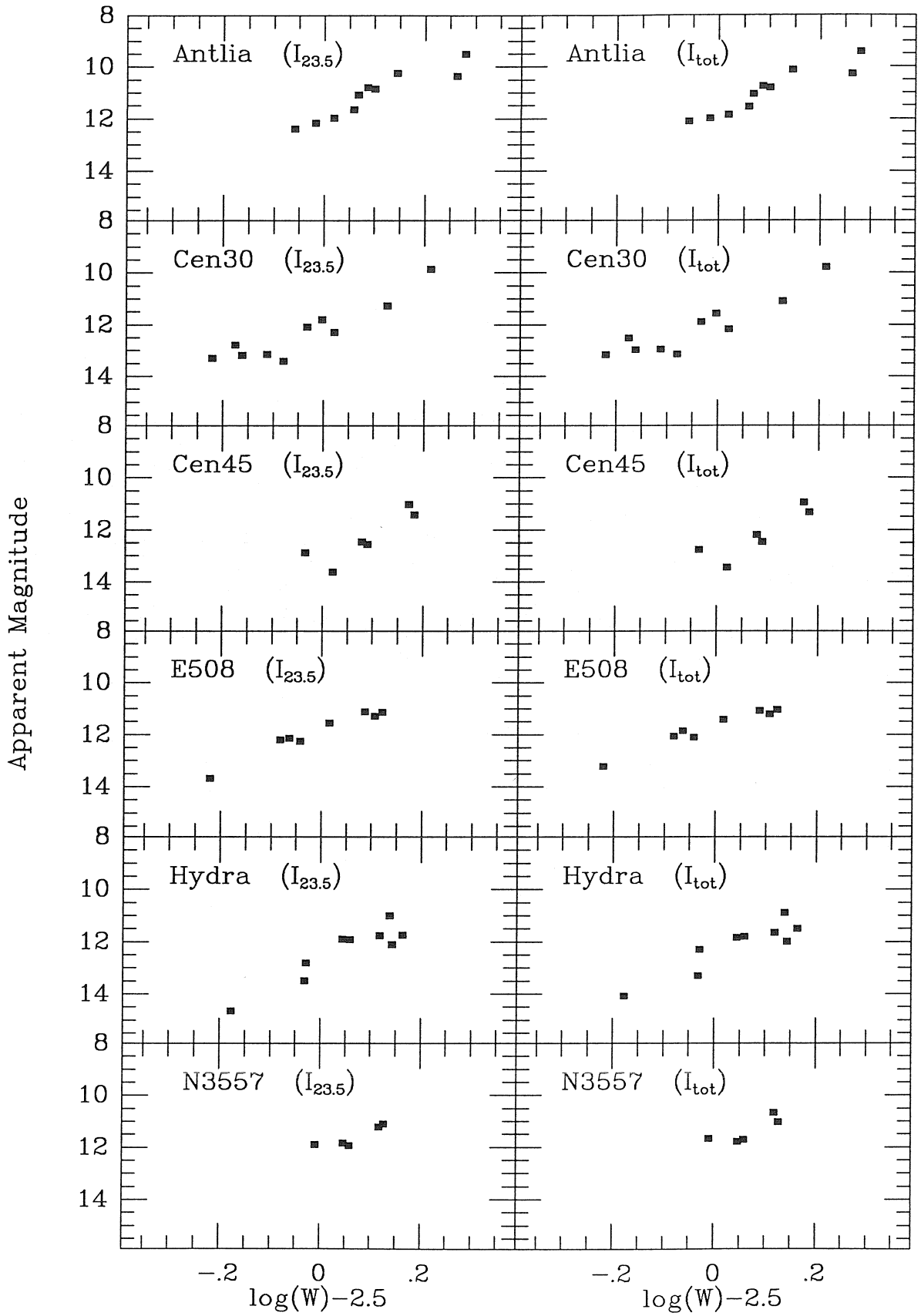

Figure 6.2

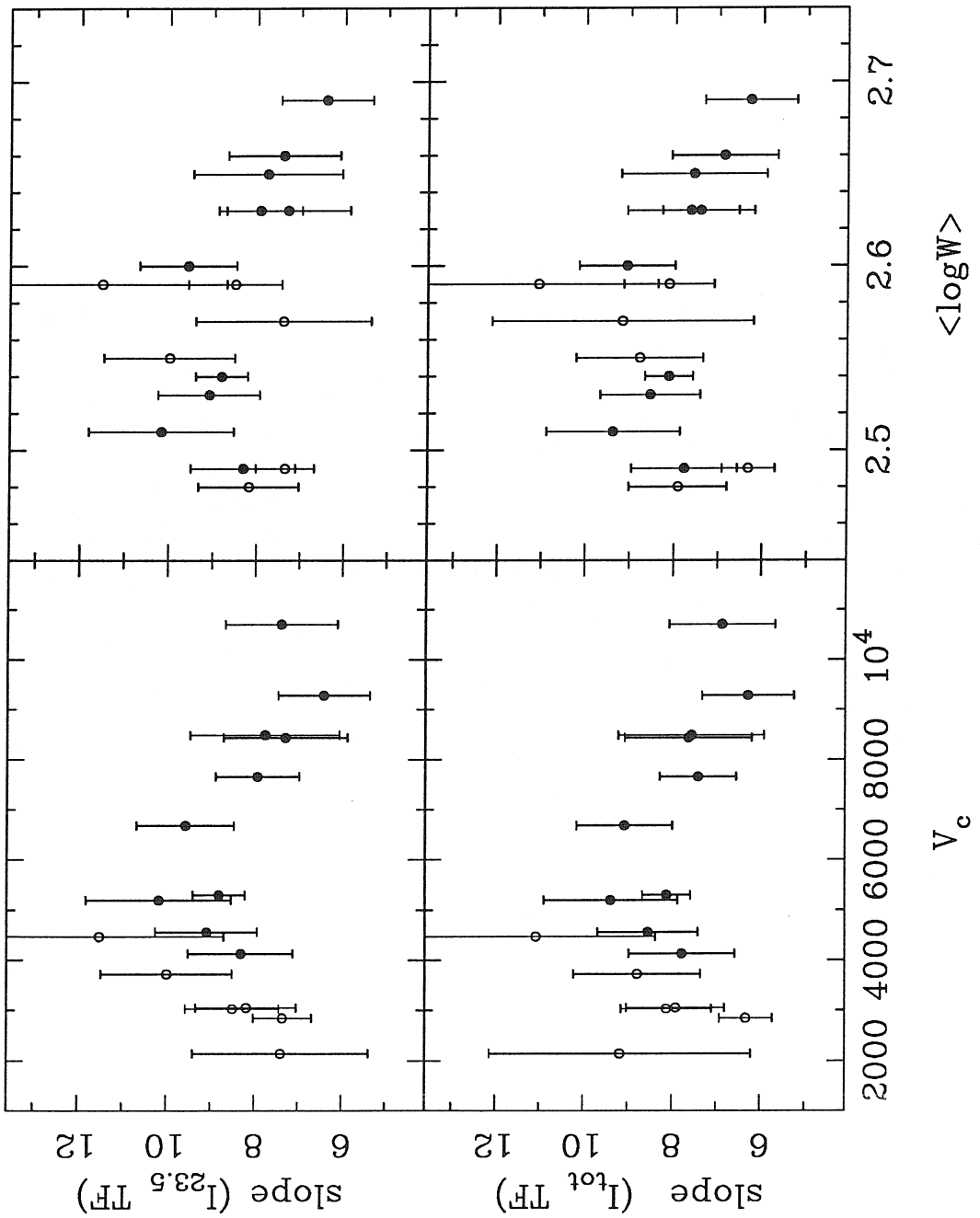
slope (I_{tot} TF)
slope ($I_{23.5}$ TF)
6
8
10
12
2000
4000
6000
8000
10^4
V_c
2.5
2.6
2.7
<logW>
<logW>

Figure 6.3

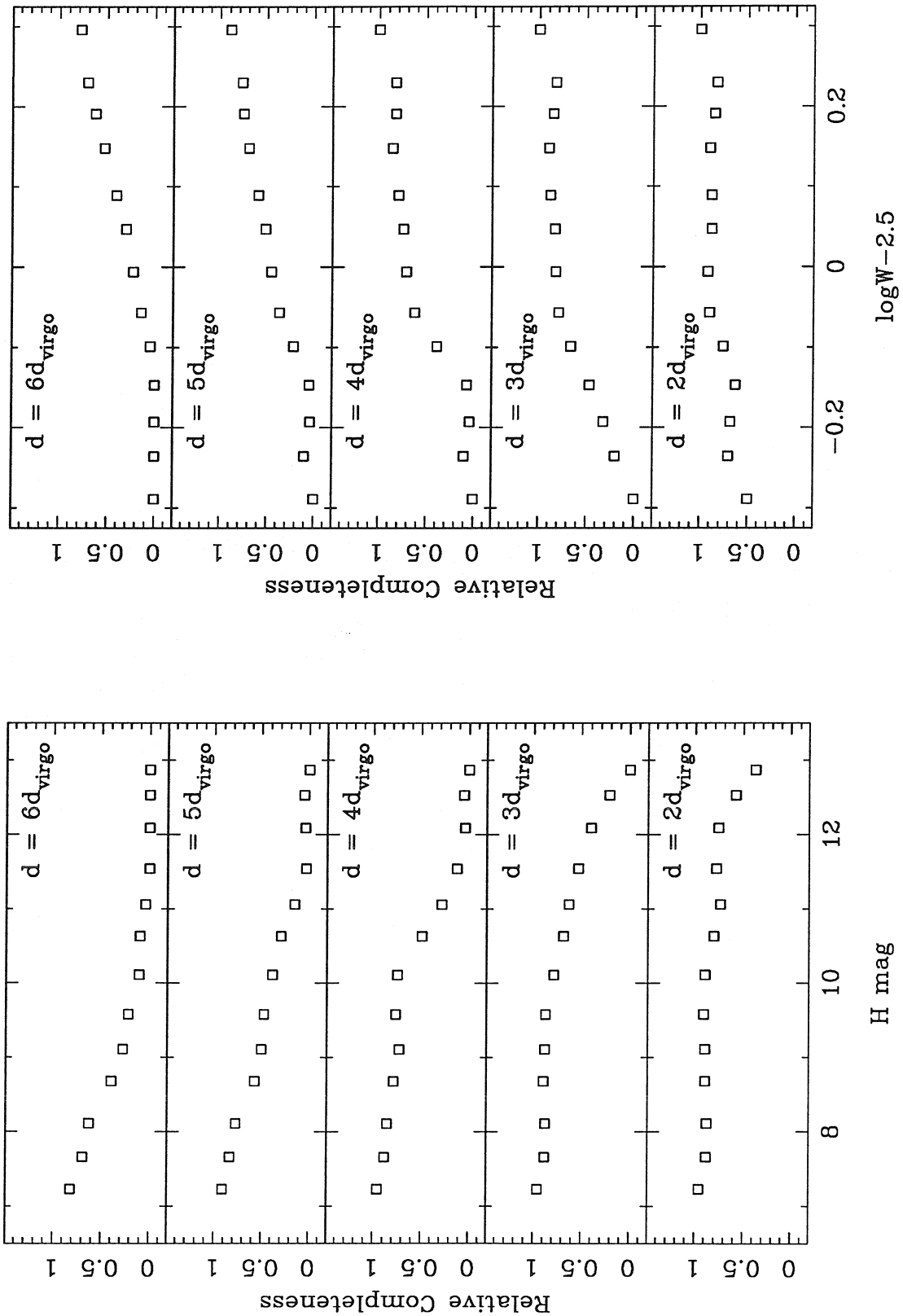
d = 6d_virgo
d = 5d_virgo
d = 4d_virgo
d = 3d_virgo
d = 2d_virgo
Relative Completeness
0
0.5
1
−0.2
0
0.2
logW−2.5
8
10
12
H mag

Figure 6.4

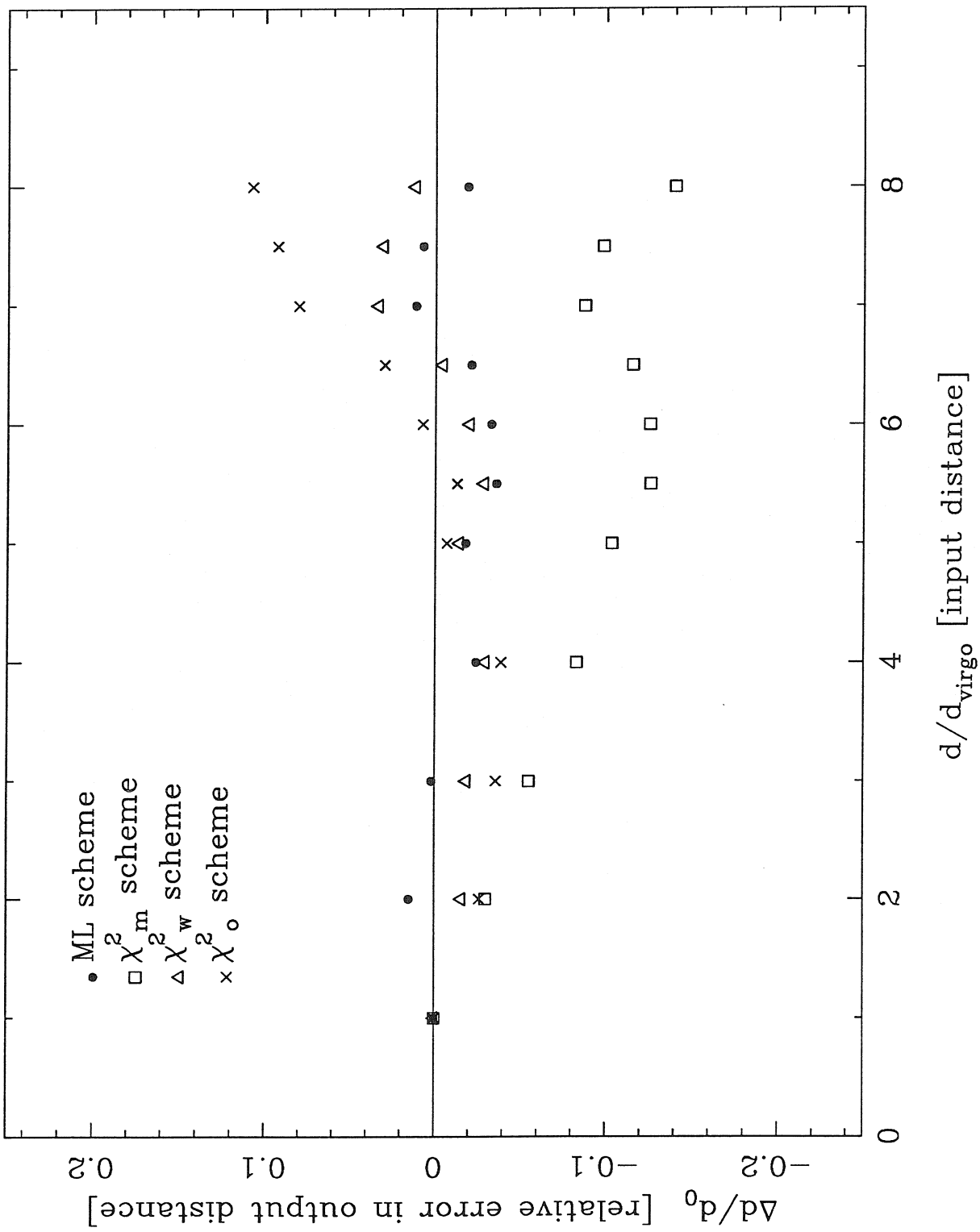
ML scheme
χ^2_m scheme
χ^2_w scheme
χ^2_o scheme
$\Delta d/d_0$ [relative error in output distance]
d/d_{virgo} [input distance]
0.2
0.1
0
−0.1
−0.2
0
2
4
6
8

Figure 6.5

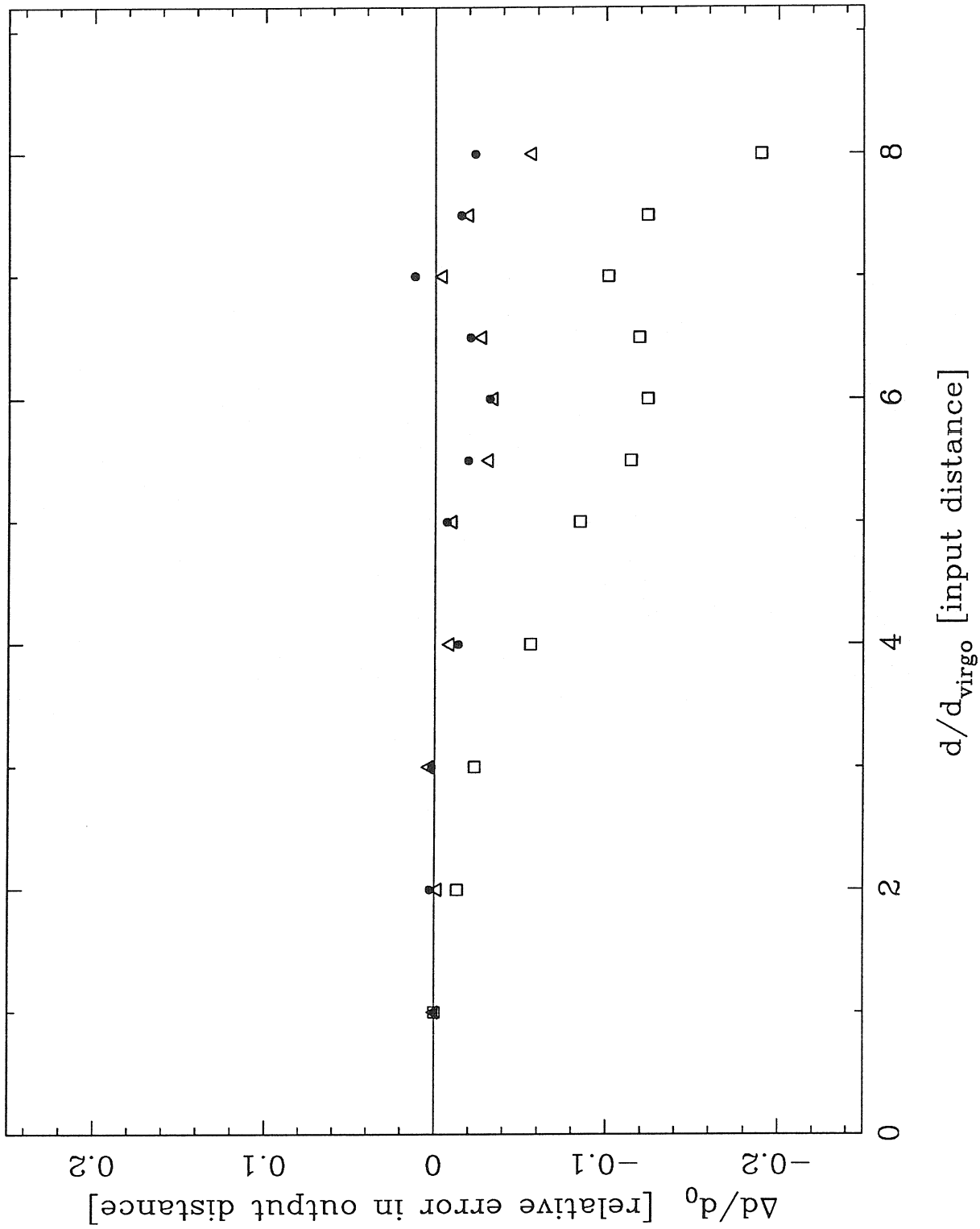
Δd/d0 [relative error in output distance]
−0.2
−0.1
0
0.1
0.2
0
2
4
6
8
d/dvirgo [input distance]

Figure 6.6

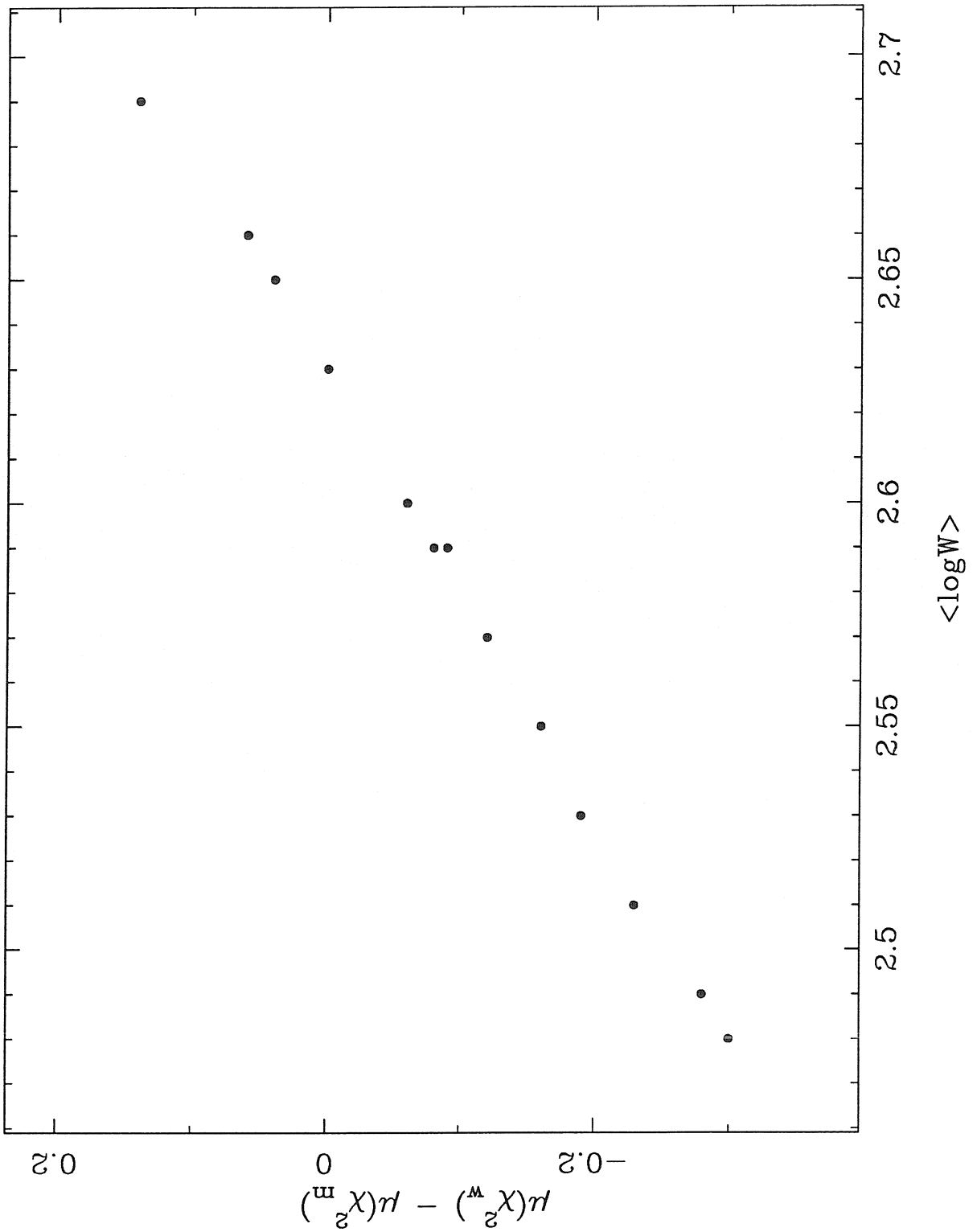

Figure 6.7

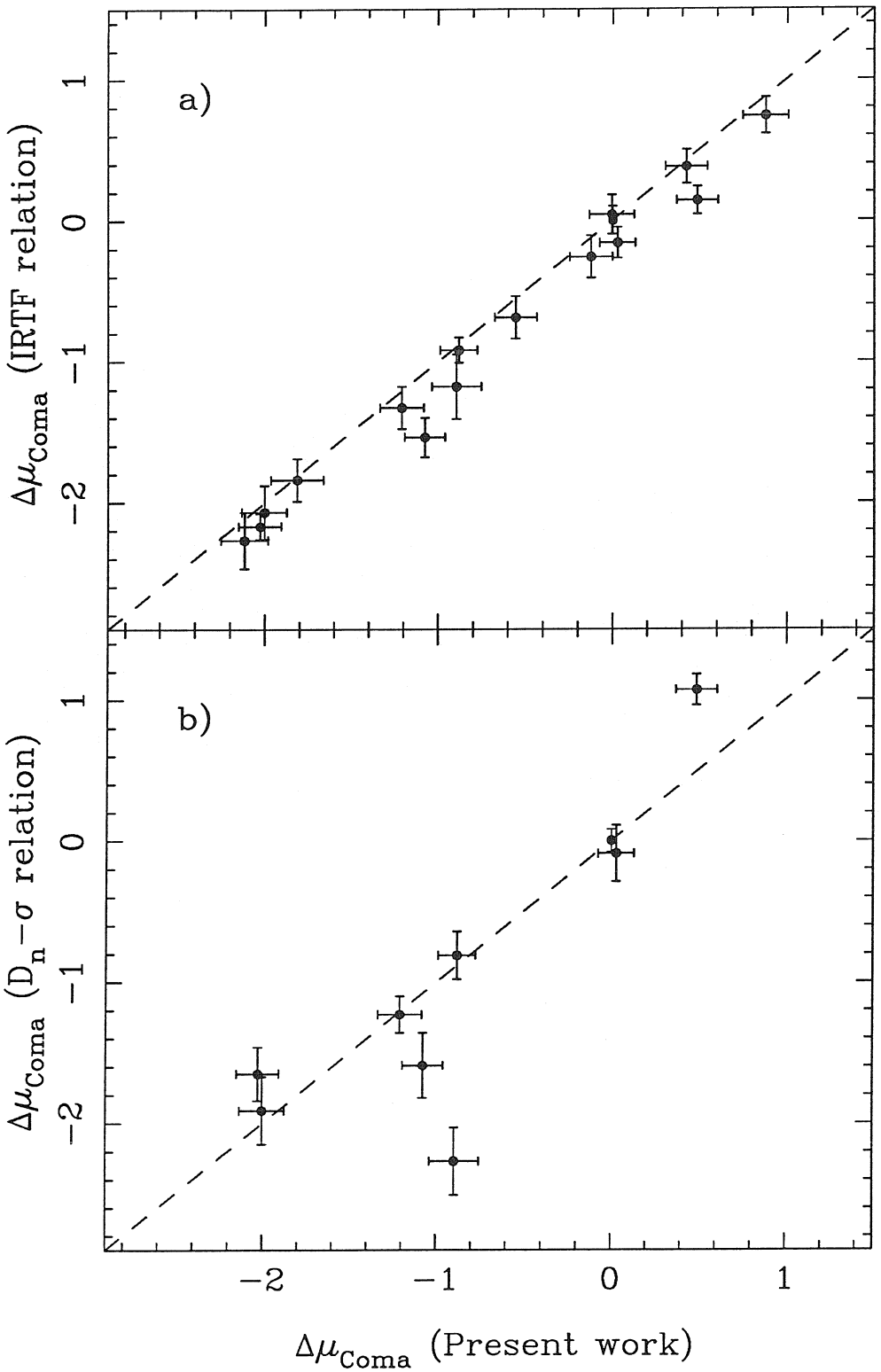
a)
b)
$\Delta\mu_{Coma}$ (IRTF relation)
$\Delta\mu_{Coma}$ ($D_n-\sigma$ relation)
$\Delta\mu_{Coma}$ (Present work)
−2
−1
0
1

CHAPTER VII

GLOBAL PHOTOMETRIC PROPERTIES OF SPIRAL GALAXIES AND SECOND PARAMETERS IN THE TF RELATION

The current photometric and kinematic appearance of a galaxy is the result of initial formation and subsequent evolution. Study of the global properties of galaxies has been a major approach to understanding the processes of galaxy formation and evolution. In making use of the extensive data from the surface photometry of this thesis, below I will briefly examine the photometric properties of the sample galaxies. But I will not discuss the implications in detail, as they lie beyond the scope of this thesis. The TF relation, as one of the important integrated photometric–kinematic relations of spiral galaxies, will also be investigated in this chapter. I seek to study the dependence of the TF relation on other galaxy properties, i.e., the problem of second parameters, and propose physical explanations for the empirical properties of the TF relation.

§7.1 Distance Independent Photometric Parameters

The following distance-independent photometric quantities are extracted from Table 5.1

(1). $\Sigma_{23.5} \equiv I_{23.5} + 5 \log A^0_{23.5}$, the mean (face-on) surface brightness.

(2). C_{20}/C_{80}, the ratio of concentration radius at level 20% to that at level 80% — an index measuring the degree of light concentration in a galaxy.

(3). $C_{20}/A^0_{23.5}$, $C_{50}/A^0_{23.5}$, and $C_{80}/A^0_{23.5}$, the ratios of concentration radii at level 20%, 50% and 80% to the isophotal radius at $\mu_I = 23.5$ mag/arcsec^2. These

parameters reflect the degree of light concentration as normalized to an absolute brightness level.

(4). $V-I$, the $(V-I)$ color within isophote $\mu_I = 23.5$ mag/arcsec^2.

(5). $I-H \equiv I_{tot} - H_{-0.5}$, an indicative $(I-H)$ color.

Morphological type dependence of the parameters $\Sigma_{23.5}$, C_{20}/C_{80}, $(V-I)$, $(I-H)$ and $C_{20}/A^0_{23.5}$ are shown in Figures 7.1a-e. Note that a few galaxies with types larger than 10 are plotted at 10 in the figures. All these parameters show strong dependence on type.

Velocity width dependence of these parameters are presented in Figures 7.2a-g. Linear fits to these relations (assuming equal vertical errors) yield,

$$\Sigma_{23.5} = 26.16(\pm 0.54) - 2.24(\pm 0.21)\log W, \tag{7.1}$$

$$C_{20}/C_{80} = 0.78(\pm 0.09) - 0.23(\pm 0.03)\log W, \tag{7.2}$$

$$C_{20}/A^0_{23.5} = 1.60(\pm 0.11) - 0.54(\pm 0.04)\log W, \tag{7.3}$$

$$V-I = -1.50(\pm 0.28) + 0.94(\pm 0.21)\log W, \tag{7.4}$$

$$I-H = -5.61(\pm 0.39) + 2.40(\pm 0.15)\log W. \tag{7.5}$$

It is seen from Figure 7.2a and 7.2d that both the $\Sigma_{23.5}$ – $\log W$ relation and the $(I-H)$ – $\log W$ relation undergo a change in slope at a critical velocity width (or luminosity) $\log W \sim 2.6$. Such *discontinuities*, or *nonlinearity*, in the two global photometric–kinematic relations might be an indication of the intrinsic variation in the structure of spiral galaxies or just reflect the improper operational definition of the observables (Mould, Han & Bothun 1989; Persic & Salucci 1991). Other (or similar) "discontinuities" in the global photometric properties of both spiral and elliptical galaxies have been reported and investigated by a number of authors (Binggeli, Sandage & Tarenghi 1984; Kormendy 1987; Dekel & Silk 1986; Pierce 1989). Whatever the physical explanations for such "discontinuities" of galaxy properties might be, we note that an interesting and practical implication of a

nonlinear $(I-H)$ – $\log W$ relation is that the degree of the nonlinearity of I-band TF relation is different from that of H-band TF relation; the latter has been reported to be highly nonlinear (Aaronson *et al.* 1982a, 1982b). The sense of the curvature seen in the $(I-H)$ – $\log W$ relation implies that the I-band TF relation is less curved (if not perfectly straight) than the H-band TF relation.

A color-color diagram, i.e., $(I-H)$ vs $(V-I)$, is illustrated in Figure 7.3.

A traditional method to study the luminosity structure of galaxies is to divide it into distinct components, most often, an exponential disk and a $r^{1/4}$ bulge (e.g., Freeman 1970; de Vaucouleurs 1977; Kormendy 1977a,b; Burstein 1979; Boroson 1981; Kent 1985; Kodaira *et al.* 1986). Decomposition of the light distribution into such components is not, however, very reliable for most galaxies (at least in this thesis sample), and also requires a careful correction for seeing effects. The (bulge/disk) structure properties, as well as other important photometric properties (like color gradient and color asymmetry about major axis) of the sample galaxies will not be investigated in this thesis.

§7.2 Distance Dependent Photometric Parameters

Using the relative distances of the sample clusters listed in Col. (4) of Table 6.4, we can put them all to a reference distance, and investigate the distance-dependent photometric properties of the cluster galaxies. Again, we choose Coma as a reference cluster, and define the following (distance-dependent) parameters for each of the cluster galaxies in Table 5.1. Non-cluster-members are excluded from the following discussions.

(1) $I_{23.5}^{abs} \equiv I_{23.5} - 5\log(d/d_{Coma})$, the absolute isophotal magnitude (or magnitude that would be observed, if the galaxy were at Coma distance).

(2) $I_{tot}^{abs} \equiv I_{tot} - 5\log(d/d_{Coma})$, the absolute total magnitude.

(3) $R_{23.5} \equiv A^0_{23.5} d/d_{Coma}$, physical isophotal radius.

(4) $J/M \equiv R_{23.5} W$, an indicative parameter for specific angular momentum of a galaxy (i.e., angular momentum per unit mass).

(5) $M \equiv R_{23.5} W^2$, a mass indicator of the galaxy.

(6) $\rho_m \equiv W^2/R^2_{23.5}$, an indicative mass density of a galaxy.

(7) $M/L \equiv M \mathrm{dex}(0.4\, I^{abs}_{tot})$, a mass-to-light ratio indicator (not in the conventional solar units).

Note that in defining $\log(J/M)$, M and $\log \rho_m$, I used the isophotal radius rather than any of the three concentration radii. This choice is merely based on the fact that the isophotally defined $\log(J/M)$ and M show much better correlation with each other and with absolute magnitude or velocity width than those defined concentrationally (we believe that close correlations should exist between *true* specific angular momentum and mass and between mass and luminosity for normal galaxies). This preference of isophotal radius over the concentration radii in the definition of the three global "kinematic" quantities might have interesting implications. Does it indicate that the relative light distribution of a galaxy carries less information about the mass and angular momentum contents of a galaxy than does the absolute isophotal size of the galaxy?

a) Specific Angular Momentum

Figures 7.4a-f present the correlations of the specific angular momentum indicator $\log(J/M)$ with, in order, a) indicative mass $\log M$, b) absolute total magnitude I^{abs}_{tot}, c) mean surface brightness $\Sigma_{23.5}$, d) galaxy type, e) density indicator $\log \rho_m$, and f) concentration index C_{20}/C_{80}. Linear fits to Figures 7.4a, 7.4b and 7.4e yield the following expressions,

$$\log(J/M) = -0.69(\pm 0.04) + 0.71(\pm 0.01) \log M, \qquad (7.6)$$

$$\log(J/M) = 7.57(\pm 0.07) - 0.27(\pm 0.01) I_{tot}^{abs}, \tag{7.7}$$

$$\log(J/M) = 1.81(\pm 0.04) + 1.54(\pm 0.03) \log R_{23.5}, \tag{7.8}$$

or equivalently,

$$J/M \propto M^{0.71\pm 0.01}, \tag{7.9}$$

$$J/M \propto L_{tot}^{0.68\pm 0.02}, \tag{7.10}$$

$$J/M \propto R_{23.5}^{1.54\pm 0.03}, \tag{7.11}$$

where L_{tot} is the total I-band luminosity. It should be noted that the correlation in equations (7.6) and (7.8) may largely be artificial because of the correlation introduced in the definition of the parameters. However, the slopes certainly carries important information about the kinematic and photometric structures of galaxies and also the process of angular momentum origin (Peebles 1969; Efstathiou & Jones 1969). Very similar dependence of the specific angular momentum on mass has been empirically derived by other authors (Heidmann 1968; Vettolani *et al.* 1980; Pierce 1989), and has several theoretical explanations (Thuan & Gott 1977; Shaya & Tully 1984). The anti-correlation between specific angular momentum and density seen in Figure 7.4e is consistent with theoretical predictions (e.g., Hoffman 1986). It is important to note that the correlation between J/M and luminosity (equation [7.7] or [7.10]) is remarkably good, which is not caused by artificial effects as could be for the $J/M - M$ correlation. As we will discuss below, this might have significant impact on our study of the TF relation.

b) Mass and Mass Density

In Figures 7.5a-f, the mass density indicator $\log \rho_m$ is plotted against, in the order, a) indicative mass $\log M$, b) absolute total magnitude I_{tot}^{abs}, c) mean surface brightness $\Sigma_{23.5}$, d) galaxy type, e) $(V - I)$ color, and f) concentration index C_{20}/C_{80}.

Figures 7.6a-f present the relations of the indicative mass $\log M$, with, in order, a) velocity width $\log W$, b) the physical isophotal radius $R_{23.5}$, c) the mean

surface brightness $\Sigma_{23.5}$, and d) galaxy type. Double linear fits to the relations of mass/radius, and mass/width yield

$$\log M = 3.39(\pm 0.15) + 2.25(\pm 0.07) \log R_{23.5}, \tag{7.12}$$

$$\log M = -1.96(\pm 0.10) + 3.31(\pm 0.07) \log W. \tag{7.13}$$

c) Luminosity and Mass-to-Light Ratio

The correlation of M/L with various parameters are shown in Figures 7.7a-l, these parameters are, in the order, a) mean surface brightness $\Sigma_{23.5}$, b) absolute magnitude I_{tot}^{abs}, c) morphological type, d) $(V-I)$ color, e) velocity width $\log W$, f) physical isophotal radius $R_{23.5}$, g) density indicator $\log \rho_m$, h) specific angular momentum indicator $\log(J/M)$, i) concentration index C_{20}/C_{80}, j) the physical concentration radius C_{80}, k) concentration parameters $C_{20}/A^0_{23.5}$, and l) $C_{80}/A^0_{23.5}$. A quick visual inspection of these relations leads to the following preliminary conclusions:

1) M/L is not a strong function of luminosity, though it does show a weak decreasing with increasing luminosity (see also Pierce 1989). This is qualitatively consistent with the prediction of the galaxy models of Tinsley (1981) and Rubin *et al.* (1982).

2) high M/L galaxies tend to have low surface brightness.

3) M/L does not show clear dependence on the light concentration parameters, C_{20}/C_{80}, $C_{20}/A^0_{23.5}$ or $C_{80}/A^0_{23.5}$.

4) M/L does not show clear dependence on galaxy type.

5) It is interesting to note that the mass-to-light ratio M/L, a crude measure of stellar population or the initial mass function (IMF), is almost independent of the mean mass density of the galaxy.

Figures 7.8a-d and 7.8a$'$-d$'$ illustrate, respectively, the correlations of the absolute isophotal and total magnitudes with, a) radius $R_{23.5}$, b) mean surface brightness $\Sigma_{23.5}$, c) morphological type, d) mass, and e) $V-I$ color, Familiar correlations are seen in these plots, i.e., higher luminosity galaxies tend to be earlier types, or to have higher mean surface brightness, or redder colors. It is also noticed from these plots that the scatter in a relation with total magnitude is smaller than that of the corresponding relation with isophotal magnitude. This is an indication of the validity of the method we employed in Chapter 5 to estimate the total magnitude by extrapolation.

§7.3 Second Parameter in the TF Relation

It is of great significance, from both theoretical and practical points of view, to investigate the possibility of second parameters in the TF relation. On one hand, it helps us to understand the physical bases of the TF relation and the formation and evolution of galaxies; on the other hand, it may provide a method of improving the TF relation as a distance indicator.

The combined I_{tot} TF relation, $I_{23.5}$ TF relation and also H-band TF relation are presented, in order, in Figures 7.9a, 7.9b and 7.9c, which all have equal vertical scales. The scatters in the relations (i.e., dispersion about the mean relation), are shown in the plots, that is, 0.37 mag for $I_{23.5}$ TF relation, 0.35 mag for I_{tot} TF relation, and 0.44 mag for H-band TF relation. The combined TF relations show a mild change of slope at about $\log W = 2.7$, however, the effect of this nonlinearity on the derived distance is small as demonstrated in Chapter 6.

The magnitude residuals about the mean relation are calculated from the I_{tot} TF relation, and are examined for correlations with other available parameters. Table 7.1 summarizes the results based on visual inspections. For each parameter, a code ranging from 0 to 10 is given to indicate the relative strength of the correlation; a number of 0 represents no correlation and a number of 10 represents the highest

correlation. Figures 7.10a-h graphically show the correlations of the residuals with some of the parameters listed in Table 7.1, which are, a) the mean surface brightness $\Sigma_{23.5}$, b) $V-I$ color, c) galaxy type, d) specific angular momentum $\log(J/M)$, e) density indicator $\log \rho_m$, f) mass-to-light ratio $\log(M/L)$, g) the physical concentration radius $\log C_{80} + \log(d/d_{coma})$, and h) the residuals of $\log R_{23.5}/\log W$ relation, denoted as Res$[\log R_{23.5}/\log W]$.

Strong correlations with Res$[\log R_{23.5}/\log W]$, density indicator $\log \rho_m$, mass-to-light ratio M/L and also the physical concentration radius C_{80} are clearly seen (Figures 7.10e-h). A correlation with type appears to present for very early (T $<$ 2) and very late (T $>$ 7) type galaxies, but this is not significant because of the small number of galaxies in these extreme types.

Now there are a number of interesting questions regarding these correlations. First of all, are they really caused by some physical properties of galaxies or just reflect some artificial effects? Second, if they are physically meaningful, what can we learn from all these about the physical basis of the TF relation, or can we find a reasonable physical explanation for the correlations? And third, can we use these correlations to improve the TF relation as a distance indicator?

To answer the first question, let us examine the "basic constitutes" of the TF residuals and the quantities which show correlations with TF residuals, and treat them as pure mathematical independent variables, and then see whether the correlations observed in Figures 7.10e-h are due to the self-correlation of these variables (note we do not consider the inter-correlations among such variables, which are awaiting physical interpretations).

a) TF residuals $\sim I_{tot}^{abs} - b \log W$, where $b = -8.8$ is the slope of the I_{tot} TF relation.

b) Res$[\log R_{23.5}/\log W] \sim -\log R_{23.5} - p \log W$, where $p = 1.5$ is the slope of the $\log R_{23.5}/\log W$ relation (Figure 7.11).

c) density indicator $\log \rho_m \sim 2 \log W - 2R_{23.5}$.

d) mass-to-light ratio indicator $\log(M/L) \sim I_{tot}^{abs}/2.5 + 2 \log W + R_{23.5}$.

Clearly, the TF residuals and the three parameters have common variables: I_{tot}^{abs} and/or $\log W$, the latter three parameters also depend on $R_{23.5}$. Let us check whether the correlations presented in Figures 7.10e-h simply reflect the self-correlation of the two common variables, I_{tot}^{abs} and $\log \rho_m$.

♣. The correlation of TF residuals with Res[$\log R_{23.5}/\log W$] (Figure 7.10h): The common variable in this case is just $\log W$. Obviously, the TF residual does not have overall correlation with $\log W$, the correlation of TF residuals with Res[$\log R_{23.5}/\log W$] thus arises from the combination of $\log W$ and radius $R_{23.5}$ *in the particular manner* (note a different combination of $\log W$ and $R_{23.5}$: $\log(J/M) = R_{23.5} + \log W$, does not correlate with the TF residual as shown in Figure 7.10d). This implies that the correlation between TF residual and Res[$\log R_{23.5}/\log W$] is not produced by self-correlation of the variable $\log W$, but reflects something that is beyond a simple mathematical explanation.

♡. The correlation of TF residuals with $\log \rho_m$ (Figure 7.10e): Same as above, $\log W$ is the only common variable in this case, and the correlation of TF residuals with $\log \rho_m$ can not be due to the self-correlation of $\log W$, but reflects the very involvement of radius $R_{23.5}$.

♠. The correlation of TF residuals with $\log(M/L)$ (Figure 7.10f): Now both $\log W$ and I_{tot}^{abs} are common variables. Self-correlation of these two variables does contribute to the correlation seen in Figure 7.10f, which can be easily verified by checking the relation between TF residuals and the quantity $I_{tot}^{abs}/2.5 + 2 \log W$ (i.e, set $R_{23.5}$ at constant in the expression of $\log[M/L]$). However this relation clearly has larger scatter than the original relation of Figure 7.10f, indicating that the correlation between TF residuals and $\log(L/M)$ in Figure 7.10f partly

reflects an artificial effect, but certainly contains some physical information.

Now, we come to a simple conclusion: the correlations in Figures 7.10e-f are physically meaningful, and reflect the inter-correlations among the fundamental parameters, $R_{23.5}$, I_{tot}^{abs} and W. These correlations *as shown in the particular forms* above may contain important information about the formation and/or structures of galaxies. Below, in the subsections a) and b), I seek two possibilities to interpret these correlations physically; and in subsection c), I discuss the question of improving the TF relation as a distance indicator.

a) The TF Relation from Initial Density Fluctuation

As a matter of fact, all the above correlations can be qualitatively interpreted using the basic concept of CDM galaxy formation scenario. Blumenthal *et al.* (1984) have demonstrated that the protogalaxies (the equilibrium structures that collapse dissipationlessly from the CDM initial fluctuation spectra) satisfy a relation between mass (M) and kinetic energy (E_k) of the form $\log M \sim \alpha \log E_k$ (their Figure 4). The slope of this relation α depends on the slope of the initial fluctuation spectrum, while the zero point of the relation is a decreasing function of the amplitude of the fluctuation, or roughly the mass density of a protogalaxy. This relation can be considered as the seed of the TF relation, and the observed version of the TF relation (the relation between luminosity and rotation velocity) is just an image of this *initial TF relation*, after the protogalaxies have undergone various processes (e.g., star formation, dissipation collapse). The correlations presented in Figures 7.10e-h can then be understood within this gross picture:

(1) The residual correlation with density shown in Figure 7.10e, i.e., lower density galaxies tend to be brighter than an average galaxy of the same velocity width. This is in the right sense of the correlation between density and the zero-point of the *initial TF relation*. So the correlation of Figure 7.10e can be regarded as reflecting the intrinsic dispersion of the initial TF relation.

(2) The correlation with M/L (Figure 7.10f), i.e., higher M/L galaxies tend to be fainter than an average galaxy of the same velocity width, can be understood as the result of deviation from the "initial TF relation" due to a too low (or too high) luminosity, i.e., reflecting the peculiar star formation history (IMF).

(3) The dependence of TF residual on C_{80} (Figure 7.10g) is in the sense that galaxies of larger concentration radii appear to be brighter than an average galaxy of the same rotation velocity, or equivalently that galaxies of larger concentration radii tend to have lower rotation velocity than an average galaxy of same luminosity. This can be interpreted as a result of deviation from the "initial TF relation" due to a too large or too small collapse factor, because angular momentum is conserved during collapse. This explanation is consistent with the fact that angular momentum is independent of TF residuals (Figure 7.10d).

(4) The correlation between TF residual and Res[$\log R_{23.5}/\log W$] (Figures 7.10h) is such that galaxies with radii larger than an average galaxy of the same rotation velocity ($\log W$) is also brighter than the average galaxy. Equivalently, such a correlation can be described as: a galaxy with radius larger than the prediction of $\log R_{23.5}/\log W$ relation have rotation velocity smaller than the prediction of TF relation. This can also be naturally interpreted as the result of deviation of the galaxy from the "initial TF relation" due to a too large or too small collapse factor (angular momentum is conserved during collapsing). As a matter of fact, if we assume *the scatter in the galaxy collapse factor is the common source of the dispersions in both TF relation and* $R_{23.5}/W$ *relation*, we can then predict the slope of the relation between TF residuals and Res[$\log R_{23.5}/\log W$] : if a galaxy collapsed by an extra amount of radius, $\Delta R_{23.5}$, from the mean defined by the relation $\log R_{23.5} \sim p \log W$, then angular momentum conservation implies that it would have an extra rotation velocity of $\Delta W/W \sim -\Delta R_{23.5}/R_{23.5}$. Thus the total deviation of $R_{23.5}$ from the relation $\log R_{23.5} \sim p \log W$ is given by $\Delta[\log R_{23.5}] = -(1+p)\Delta[\log W]$ (not just $p\Delta[\log W]$!). On the other hand,

the extra rotation velocity $\Delta[\log W]$ would produce a residual from the mean TF relation ($I_{tot} \sim b \log W$) of $-b\Delta[\log W]$. Therefore, the relation between the TF residuals and $\log R_{23.5}/\log W$ residuals is expected to have a slope of $b/(1+p)$, which is -3.52 ± 0.18 for $b \sim -8.8 \pm 0.3$ and $p \sim 1.5 \pm 0.1$ from our data. A direct fit to Figure 7.10h yields a slope of -3.55 ± 0.23! This incredible coincidence is not trivially understood (by the author), and I would consider it as preliminary evidence for the assumption that *the scatter in the TF relation is largely caused by the scatter in the galaxy collapse factor (or scatter in the degree of energy dissipation).* The interesting consequence of this explanation is that the luminosity is better correlated with angular-momentum rather than with rotation-velocity, because angular momentum is a conserved quantity in the process of galaxy dissipational collapse. Indeed, Figure 7.4b shows a very good correlation between luminosity and angular momentum, with a dispersion of about 0.23 mag.

b) The TF Relation from Virial Theorem

Another way to understand the TF relation and its dependence on other properties of galaxies (e.g., $\log \rho_m$ and M/L) is to scale the Virial Theorem as traditionally done to derive the TF relation (e.g., Aaronson, Huchra & Mould 1979). For a galaxy bound by gravity, the Virial Theorem implies

$$\overline{M}/\overline{R} = k\overline{W}^2, \tag{7.14}$$

where $\overline{M}$ is the total mass of the galaxy, $\overline{R}$ is a suitable radius, $\overline{W}$ is a typical velocity dispersion measuring the kinetic energy of the galaxy, and k is a virialization constant reflecting the dynamical relaxation of the galaxy. Let L be the luminosity of the galaxy and $\overline{\rho}_m$ be an average density parameter defined as $\overline{M}/\overline{R}^3$, equation (7.14) can then be expressed as

$$L = k^{\frac{3}{2}} (\overline{M}/L)^{-1} (\overline{M}/\overline{R}^3)^{-\frac{1}{2}} V^3 = k^{\frac{3}{2}} (\overline{M}/L)^{-1} \overline{\rho}_m^{-\frac{1}{2}} \overline{W}^3. \tag{7.15}$$

Now, let us relate the parameters $\overline{M}$, $\overline{\rho}_m$ and $\overline{W}$ with their operationally defined correspondences using linear relations:

$$\overline{M} = k_m M, \tag{7.16a}$$

$$\overline{\rho}_m = k_\rho \rho_m, \tag{7.16b}$$

$$\overline{W} = k_v W, \tag{7.16c}$$

here the parameters k_m and k_ρ reflect the density structure of the galaxy, and k_v reflects the kinematical structure of the galaxy. Equation (7.15) can then be expressed in the operationally defined parameters:

$$L = K\,(M/L)^{-1} \rho_m^{-\frac{1}{2}}\, W^3, \tag{7.17}$$

and K is a combined structural parameter, given by

$$K \equiv k^{\frac{3}{2}} k_m^{-1} k_\rho^{-\frac{1}{2}} k_v^3. \tag{7.18}$$

Equation (7.17) is our derived relation between luminosity and velocity width. The product $K\,(M/L)^{-1}\rho_m^{-\frac{1}{2}}$ ought to be constant or a weak power-law function of W, in order for L and W to have a power law relationship. Any properties of this product, e.g., scatter, or dependence on other parameters, will directly translate into the L–W relation (i.e., the apparent TF relation). Note that equation (7.17) is different from that of Aaronson, Huchra & Mould (1979) or Djorgovski, de Carvalho & Han (1989). The difference comes from the fact that here we do not directly scale radius and luminosity as did the above mentioned authors, and thus do not introduce a surface brightness term in the relation, but alternatively, we introduce a mean mass density indicator. The coefficient K in our equation (7.17) is therefore not sensitive to the luminosity structure of a galaxy, and reflects only the density and kinematical structures of a galaxy. This is considered to be an advantage of equation (7.17).

If $K(M/L)^{-1}\rho_m^{-\frac{1}{2}}$ is constant for all the galaxies, and M/L is independent of ρ_m, equation (7.17) then predicts:

(1) the TF relation has a slope of –7.5.

(2) the residuals of the TF relation linearly vary with $\log(M/L)$, with a slope of 2.5.

(3) the residuals of the TF relation linearly vary with $\log \rho_m$, with a slope of 1.25.

These predictions are compared with what we just found from the real galaxy sample:

(1′) slope of the I_{tot} TF relation is around – 8.8 with dispersion of 0.35 (see Table 6.2).

(2′) slope of the relation between TF residual and $\log(M/L)$ (Figure 7.10e) is about 3.7 ± 0.3 (with a double linear fit).

(3′) slope of the relation between TF residual and $\log \rho_m$ (Figure 7.10f) is about 1.6 ± 0.2 (double linear fit).

It is seen that the differences between the observed and predicted slopes are at several σ levels (according to the formal rms error). However, considering the crudeness of our mass and density indicators, the overall qualitative agreement is still very impressive. It is also noted that the predictions (2) and (3) above are subject to the condition that M/L and ρ_m are not correlated. While our data reasonably well agrees with these two predictions, consistently, there is indeed no correlations between M/L and ρ_m as seen from Figure 7.7g.

c) The TF Relation as Distance Indicator

The above analyses of the TF relation and its correlations with the quantities $\mathrm{Res}[\log R_{23.5}/\log W]$, M/L, $\log \rho_m$ and C_{80} as presented in Figures 7.10e-h are just simple attempts towards an understanding of the physics underlying the TF relation. Practically, we are certainly more interested in the question of whether

these correlations can be employed to improve the TF relation as distance indicator. Forgetting any physical implications for the moment, the correlations shown in Figures 7.10e-h can be empirically interpreted as the result of a correlation among the three basic observables, i.e., magnitude I_{tot} (or $I_{23.5}$), velocity width W, and isophotal radius $R_{23.5}$. A direct fit to this relation yield:

$$I_{tot}^{abs} = 28.90(\pm 0.24) - 4.65(\pm 0.26)\log W - 2.64(\pm 0.18)\log R_{23.5}, \quad (7.19a)$$

$$I_{23.5}^{abs} = 30.80(\pm 0.24) - 5.46(\pm 0.31)\log W - 2.40(\pm 0.21)\log R_{23.5}, \quad (7.19b)$$

and the dispersions of the two relations are, respectively, 0.23 mag and 0.28 mag. Do these two relations predict distance better than does the TF relation? The answer is unfortunately no, because the radius that enters these relations is also a distance dependent parameter. In fact, it is easy to show that the uncertainties in distance as predicted by these two relations are, respectively, 22% and 24% per galaxy, which are worse than the TF relations.

In sum, the analyses presented above provide preliminary evidence for the second parameter of the TF relation. The second parameter may simply be a measure of the global mass and luminosity structures of galaxies, or a quantity characterizing the "peculiarity" of galaxy dissipational collapse. However, such parameters constructed using distance-dependent observables do not help to improve the TF relation as a distance indicator. In order to improve the accuracy of distance prediction by TF relation and also test our analyses presented above, it is desirable to investigate alternative distance independent parameters, which reflect the variation of M/L, or $\log \rho_m$, or galaxy collapse factor.

REFERENCES FOR CHAPTER 7

Aaronson, M., Huchra, J. and Mould, J. R. 1979, *Ap. J.*, **229**, 1.

Aaronson, M. *et al.* 1982a, *Ap. J. Suppl.*, **50**, 241.

Aaronson, M. *et al.* 1982b, *Ap. J.* , **258**, 64.

Binggeli, B., Sandage, A. & Tarenghi, M. 1984, *A. J.*, **89**, 64.

Blumenthal, G. R. *et al.* 1984, *Nature*, **311**, 517.

Boroson, T. A. 1981, *Ap. J. Suppl.*, **46**, 177.

Burstein, D. 1979, *Ap. J.*, **234**, 435.

Dekel, A. and Silk, J. 1986, *Ap. J.* , **303**, 39.

de Vaucouleurs, D. 1977, *Ap. J. Suppl.*, **33**, 211.

Efstathiou, G. and Jones, B. J. T. 1969, *M. N. R. A. S.*, **186**, 133.

Freeman, K. C. 1970, *Ap. J.*, **160**, 1.

Heidmann, N. 1968, *Ap. (Letters)*, **3**, 153.

Hoffman, Y. 1986, *Ap. J.*, **301**, 65.

Kent, S. M. 1985, *Ap. J. Suppl.*, **59**, 115.

Kodaira, K. *et al.* 1986, *Ap. J. Suppl.*, **62**, 703.

Kormendy, J. 1977a , *Ap. J.*, **214**, 359.

Kormendy, J. 1977b , *Ap. J.*, **217**, 406.

Kormendy, J. 1987 in *Nearly Normal Galaxies*, ed. S. M. Faber, (New York: Springer-Verlag), p. 163.

Mould, J. R., Han, M. and Bothun, G. 1989, *Ap. J.*, **347**, 112.

Peebles, P. J. E. 1969, *Ap. J.*, **155**, 351.

Persic, M. and Salucci, P. 1991, *M. N. R. A. S.*, **248**, 325.

Pierce, M. J. 1989, Ph.D. Thesis, University of Hawaii.

Rubin, V. *et al.* 1982, *Ap. J.*, **289**, 81.

Shaya, E. J. and Tully, R. B. 1984, *Ap. J.*, **281**, 56.

Thuan, T. X. and Gott, J. R. 1977, *Ap. J.*, **216**, 194.

Tinsley, B. M. 1981, *M. N. R. A. S.*, **194**, 63.

Vettolani, G. *et al.* 1980, *M. N. R. A. S.*, **193**, 269.

Figure Captions for Chapter 7

Figure 7.1a-e: Morphological type dependence of the global photometric parameters, a) mean surface brightness $\Sigma_{23.5}$, b) concentration index C_{20}/C_{80}, c) $(V-I)$ color, d) $(I-H)$ color, and e) concentration parameter $C_{20}/A_{23.5}$.

Figure 7.2a-e: Velocity width dependence of the same parameters in Fig. 7.1.

Figure 7.3: The $(V-I)$ color is plotted against the $(I-H)$ color.

Figure 7.4a-f: Specific angular momentum indicator is plotted against a) indicative mass, b) total absolute mag, c) mean surface brightness, d) morphological type, e) density indicator, and f) concentration index.

Figure 7.5a-f: Mass density indicator is plotted against a) indicative mass, b) total absolute mag, c) mean surface brightness, d) morphological type, e) $(V-I)$ color, and f) concentration index.

Figure 7.6a-d: Mass indicator is plotted against a) velocity width, b) physical radius, c) mean surface brightness, and d) galaxy type.

Figure 7.7a-l: Mass-to-light ratio verses, a) mean surface brightness, b) total absolute mag, c) galaxy type, d) $V-I$ color, e) velocity width, f) physical radius, g) density indicator, h) specific angular momentum, i) concentration index, j) physical concentration radius, k) concentration parameter $C_{20}/A_{23.5}$, and l) $C_{80}/A_{23.5}$.

Figure 7.8a-d: Absolute isophotal mag is plotted against a) physical radius, b) mean surface brightness, c) type, d) mass indicator, and e) $(V-I)$ color.

Figure 7.8a′-d′: Absolute total mag is plotted against a) physical radius, b) mean surface brightness, c) type, d) mass indicator, and e) $(V-I)$ color.

Figure 7.9: The combined TF relations, i.e., the individual TF relations of sample clusters scaled to Coma distance: a) $I_{23.5}$ TF relation, b) I_{tot} TF relation, and c) H-band TF relation.

Figure 7.10: The residual of I_{tot} TF relation is plotted against a) the mean surface brightness, b) $(V-I)$ color, c) morphological type, d) specific angular momentum indicator, e) mass density indicator, f) mass-to-light ratio, g) physical concentration radius, and h) residual of radius/velocity-width relation.

Figure 7.11: The relation between physical radius and velocity width.

Table 7.1

Correlation of TF Residuals With Various Parameters

Parameter	Correlation[a]	Correlation Sense
$\log \rho_m$	9	higher ρ_m galaxies are fainter than TF predictions
$\log(M/L)$	9	higher M/L galaxies are fainter than TF predictions
Type	4	later types are brighter than TF predictions
$\log(J/M)$	0	
$\log C_{80}$	7	larger C_{80} galaxies are brighter than TF predictions
$\log R_{23.5}$	5	larger $R_{23.5}$ galaxies are brighter than TF predictions
Res$[\log R_{23.5}/\log W]^b$	10	galaxies larger than $\log R_{23.5}/\log W$ predictions are brighter than TF predictions
Res$[\Sigma_{23.5}/\log W]^b$	0	
$\log M$	0	
$\Sigma_{23.5}$	1	lower $\Sigma_{23.5}$ galaxies are brighter than TF predictions
$V-I$	0	
$I-H$	0	
C_{20}/C_{80}	0	
$C_{20}/A^0_{23.5}$	0	
$C_{80}/A^0_{23.5}$	0	
$\log(M_H)^c$	0	
$\log(M_H/L_B)^d$	0	

[a] a visually defined code from 0 to 10, indicating the strength of the correlation.

[b] Res$[Y/X]$: residuals of the Y/X relation

[c] HI mass from Aaronson *et al.*

[d] HI mass to blue light ratio from Aaronson *et al.*

Figure 7.1

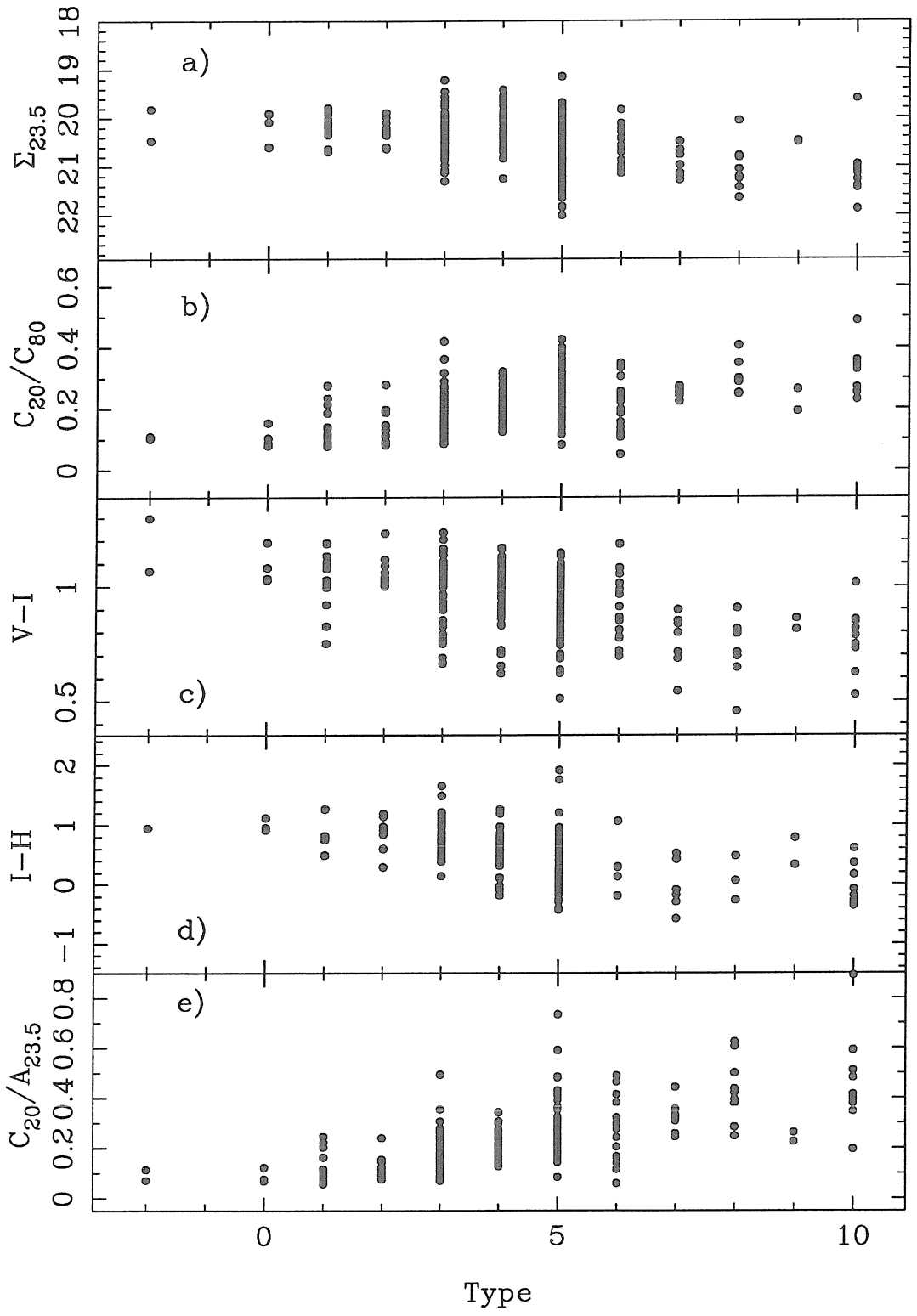
a)
b)
c)
d)
e)
$\Sigma_{23.5}$
C_{20}/C_{80}
V−I
I−H
$C_{20}/A_{23.5}$
18
19
20
21
22
0
0.2
0.4
0.6
0.5
1
2
−1
0.8
0
5
10
Type

Figure 7.2

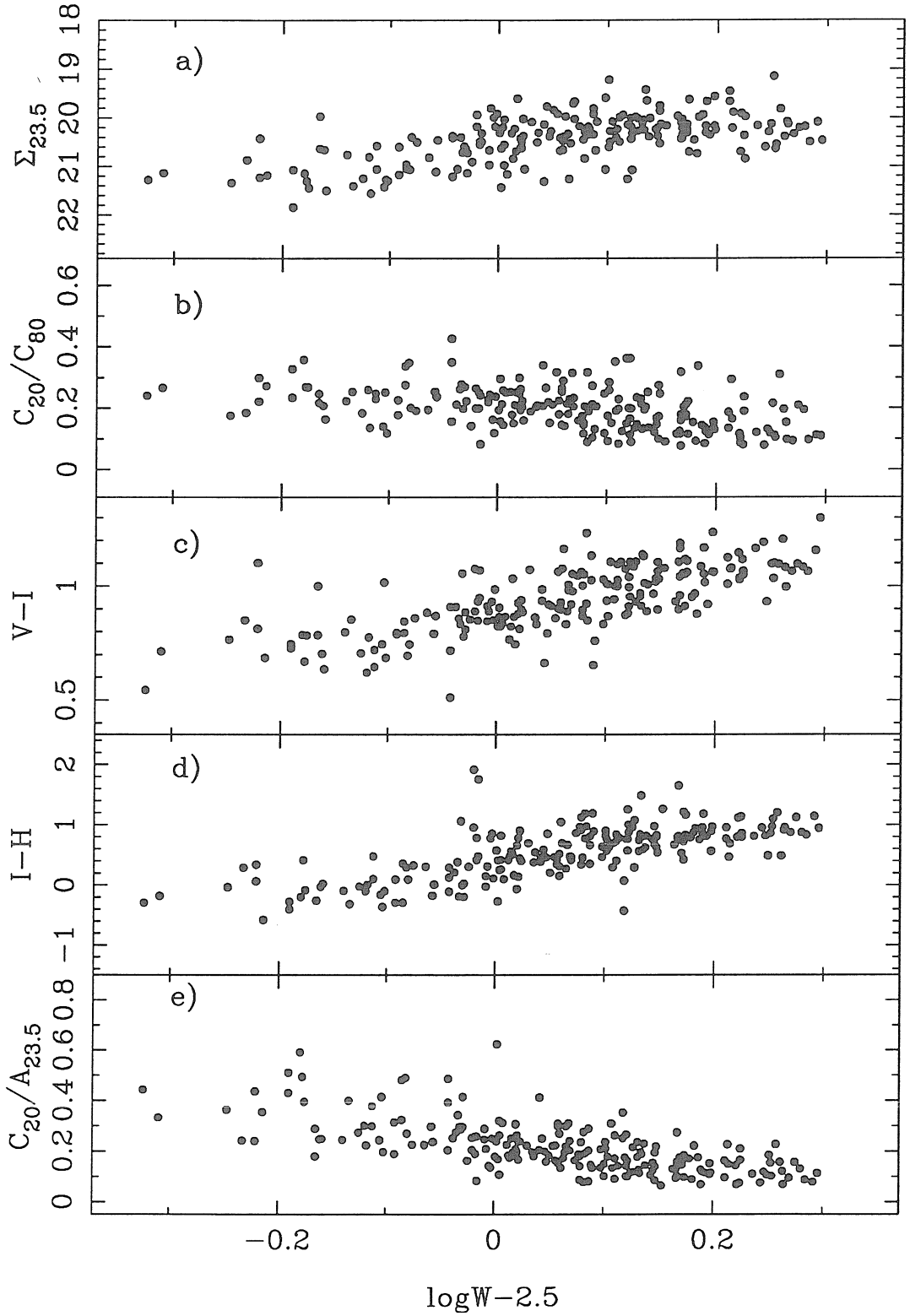

Figure 7.3

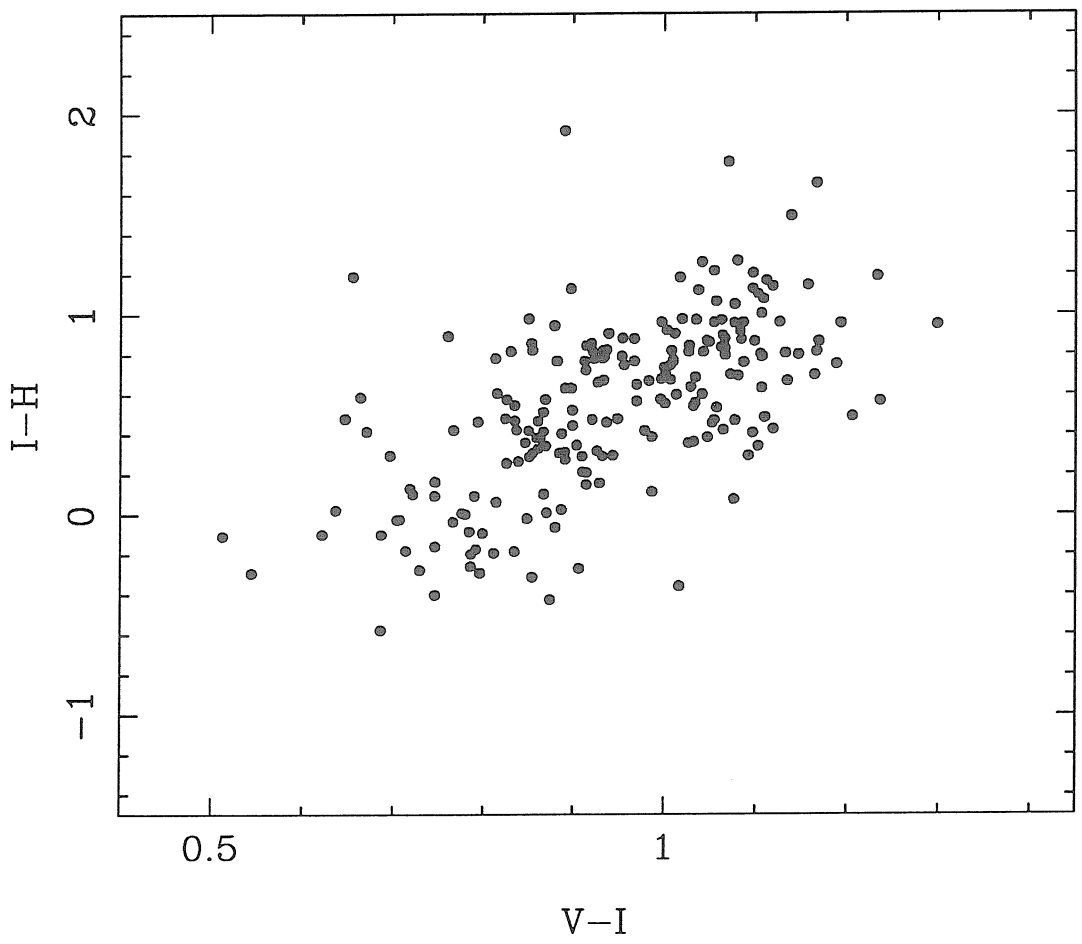

Figure 7.4

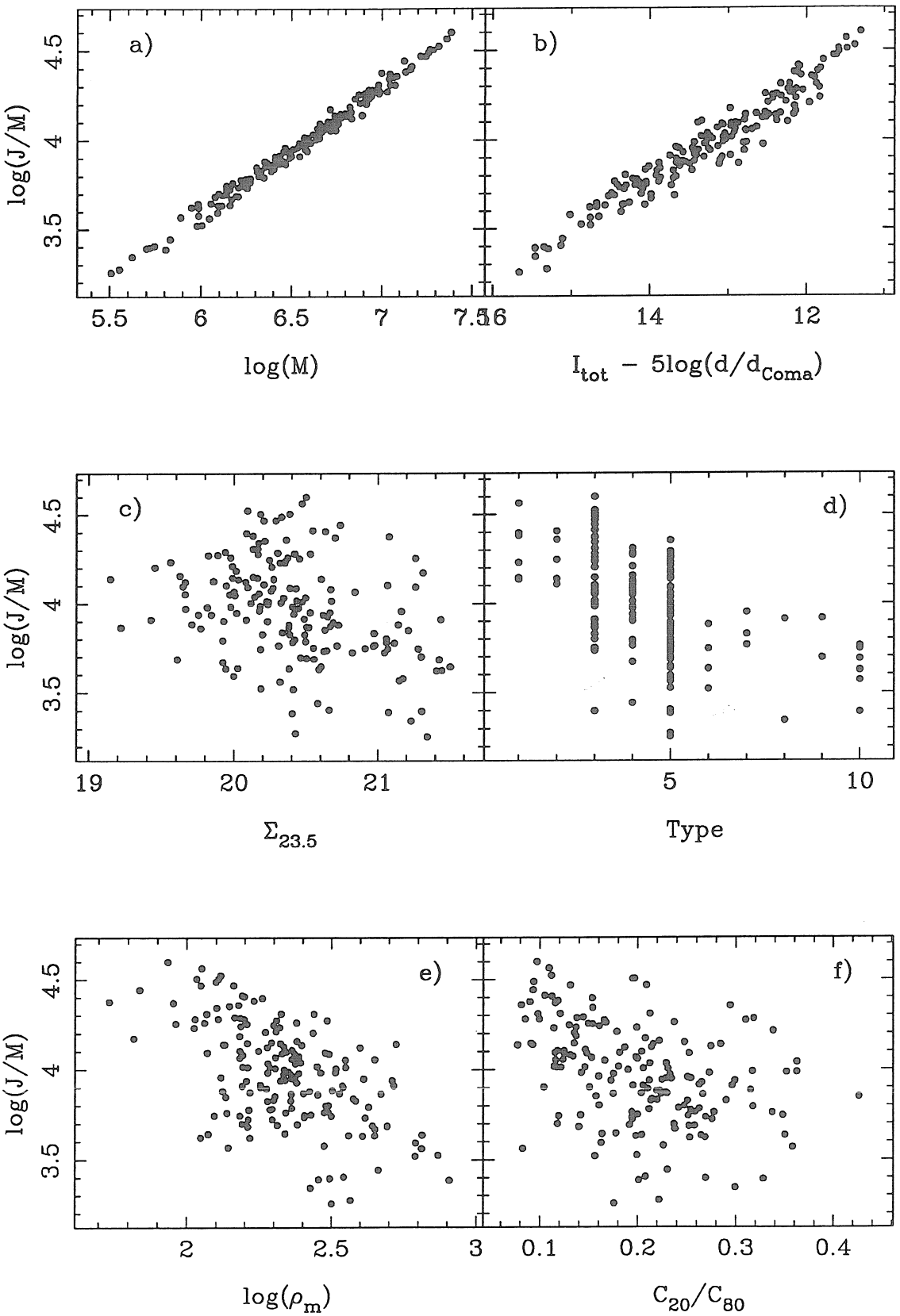
a)
b)
c)
d)
e)
f)
log(J/M)
log(M)
$I_{tot} - 5\log(d/d_{Coma})$
$\Sigma_{23.5}$
Type
$\log(\rho_m)$
C_{20}/C_{80}

Figure 7.5

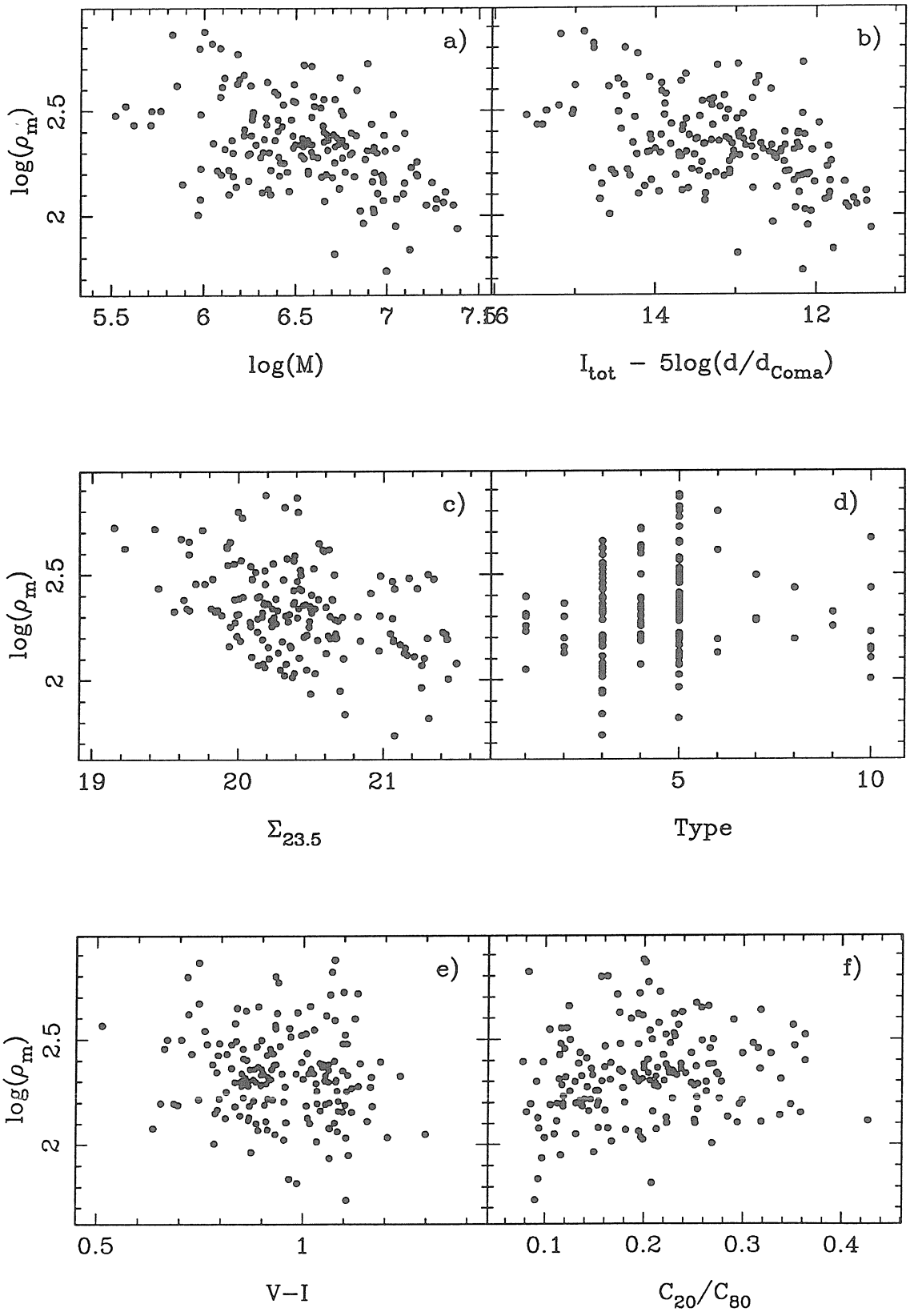

Figure 7.6

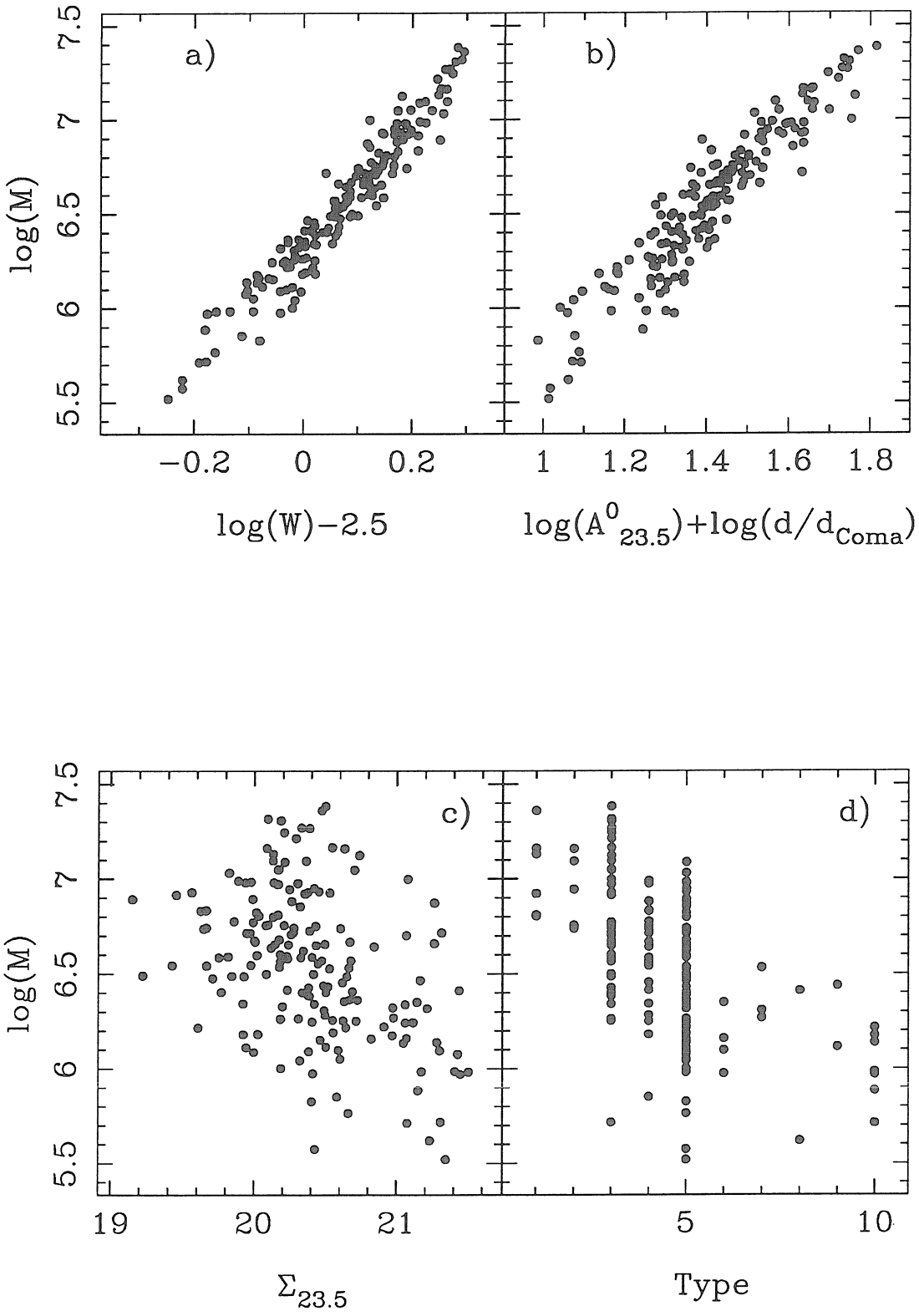
a)
b)
c)
d)
log(M)
7.5
7
6.5
6
5.5
−0.2
0
0.2
log(W)−2.5
1
1.2
1.4
1.6
1.8
log(A$^0_{23.5}$)+log(d/d$_{Coma}$)
19
20
21
$\Sigma_{23.5}$
5
10
Type

Figure 7.7

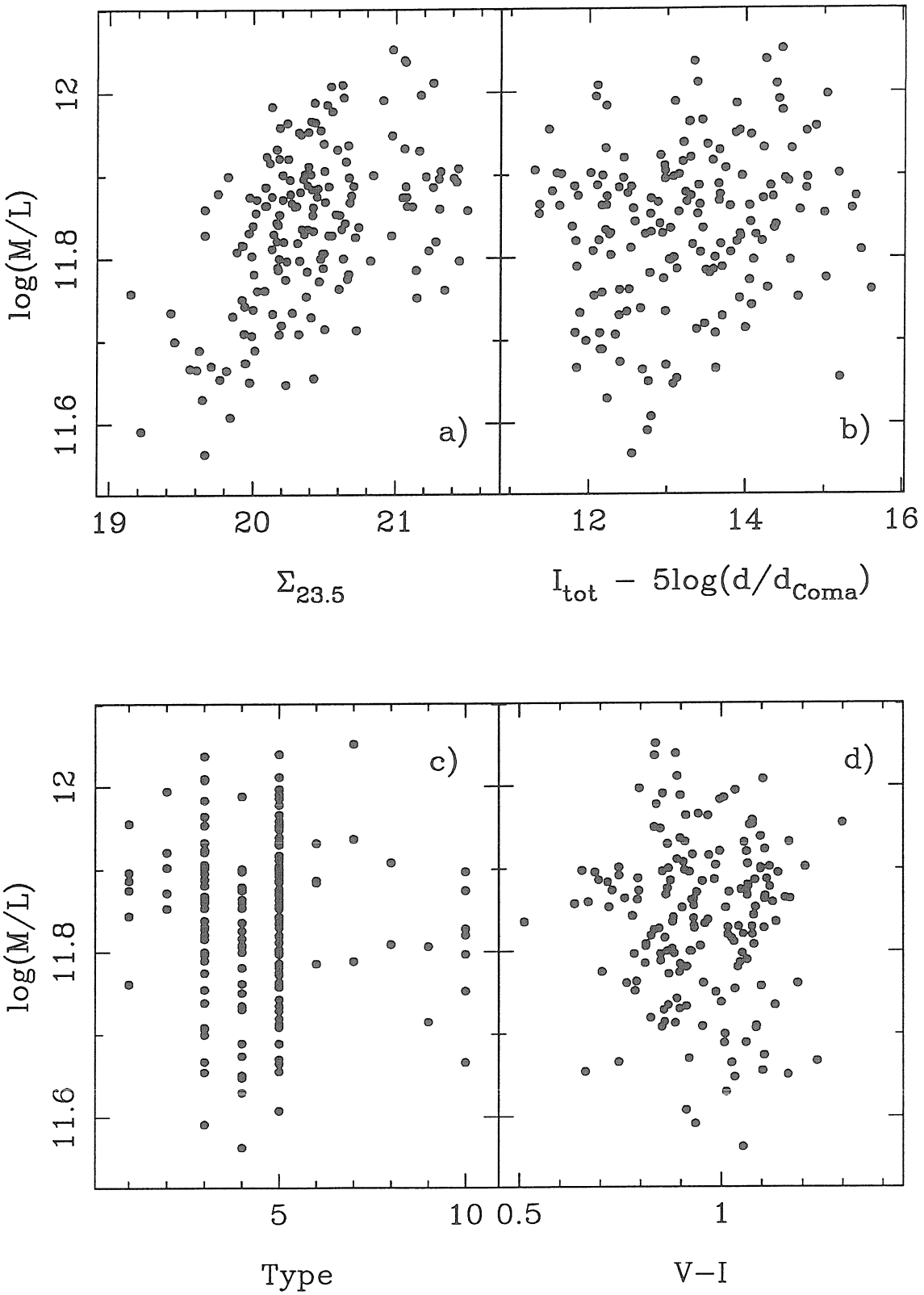
log(M/L)
12
11.8
11.6
a)
b)
19
20
21
12
14
16
$\Sigma_{23.5}$
$I_{tot} - 5\log(d/d_{Coma})$
c)
d)
5
10
0.5
1
Type
V−I

Figure 7.7 — continued

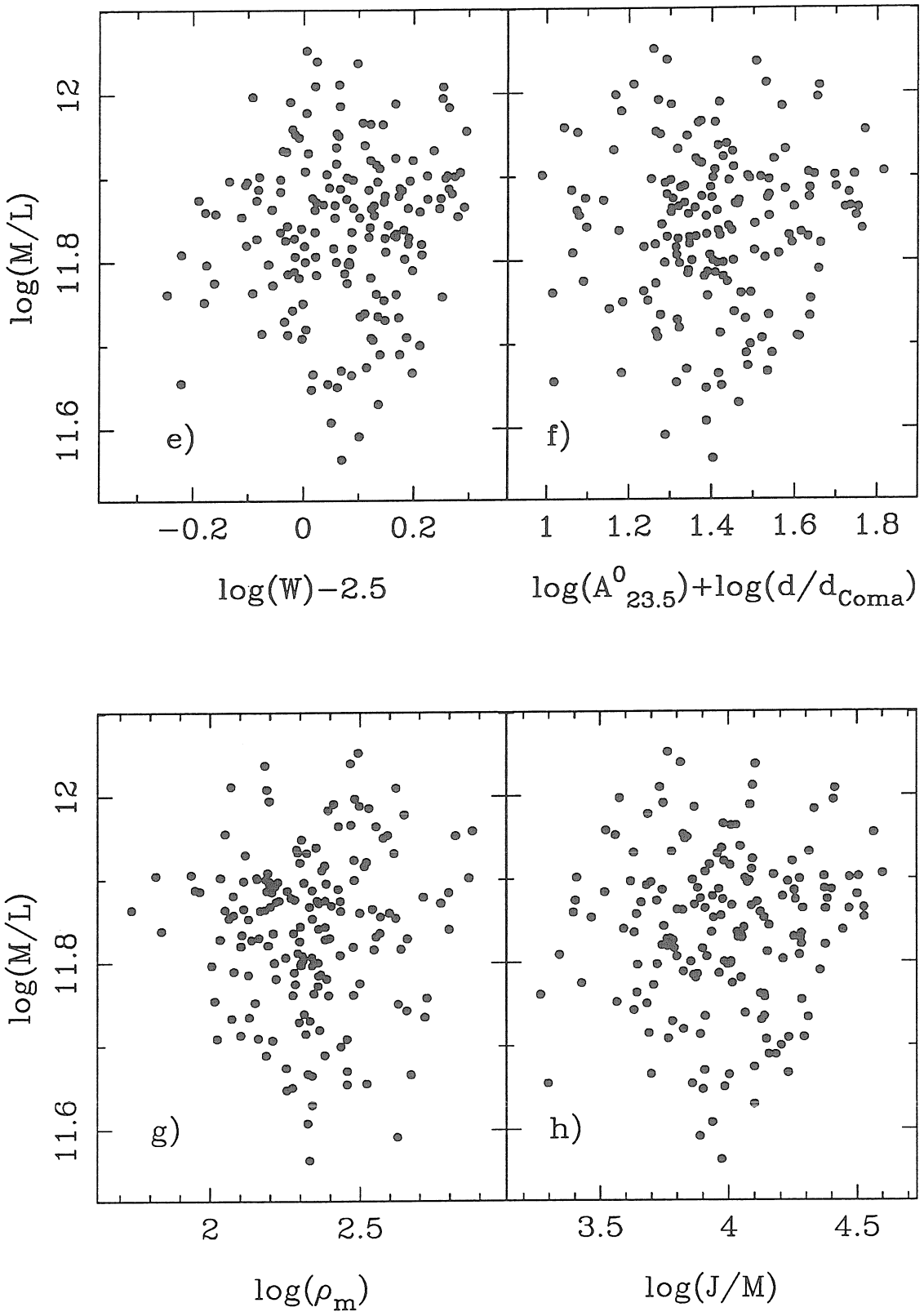

Figure 7.7 — continued

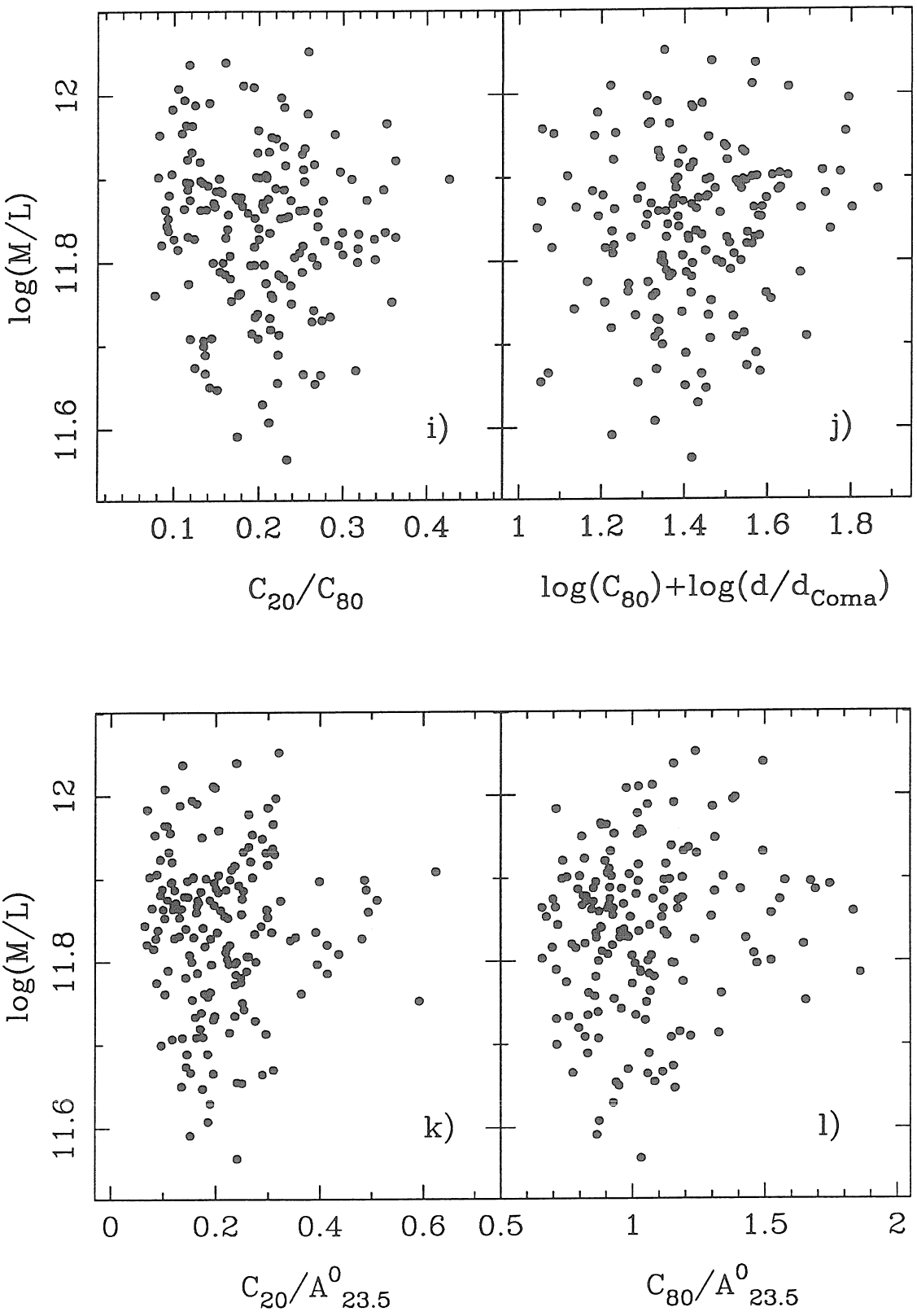

Figure 7.8

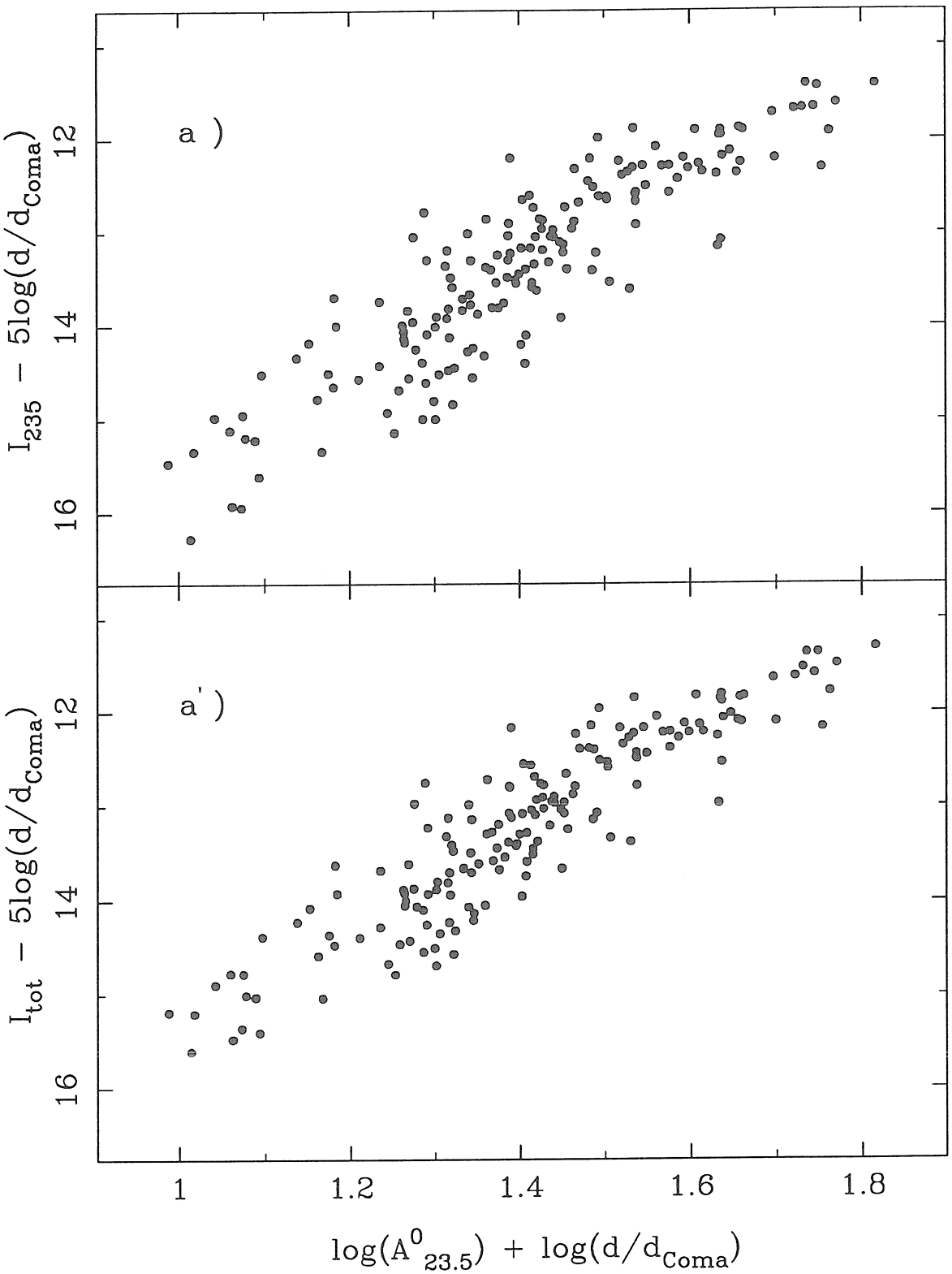
a)
a')
$I_{235} - 5\log(d/d_{Coma})$
$I_{tot} - 5\log(d/d_{Coma})$
12
14
16
1
1.2
1.4
1.6
1.8
$\log(A^0_{23.5}) + \log(d/d_{Coma})$

Figure 7.8 — continued

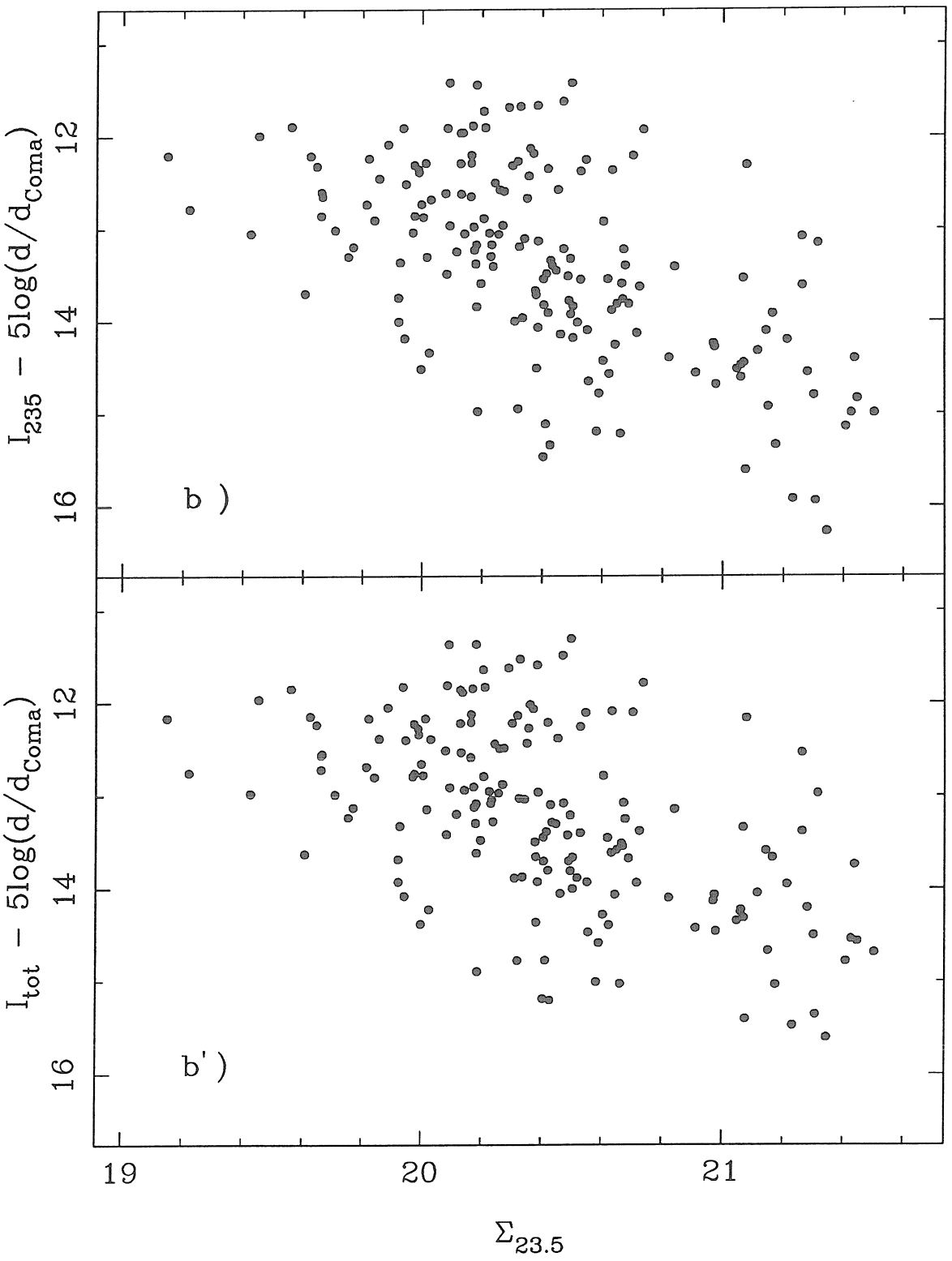

Figure 7.8 — continued

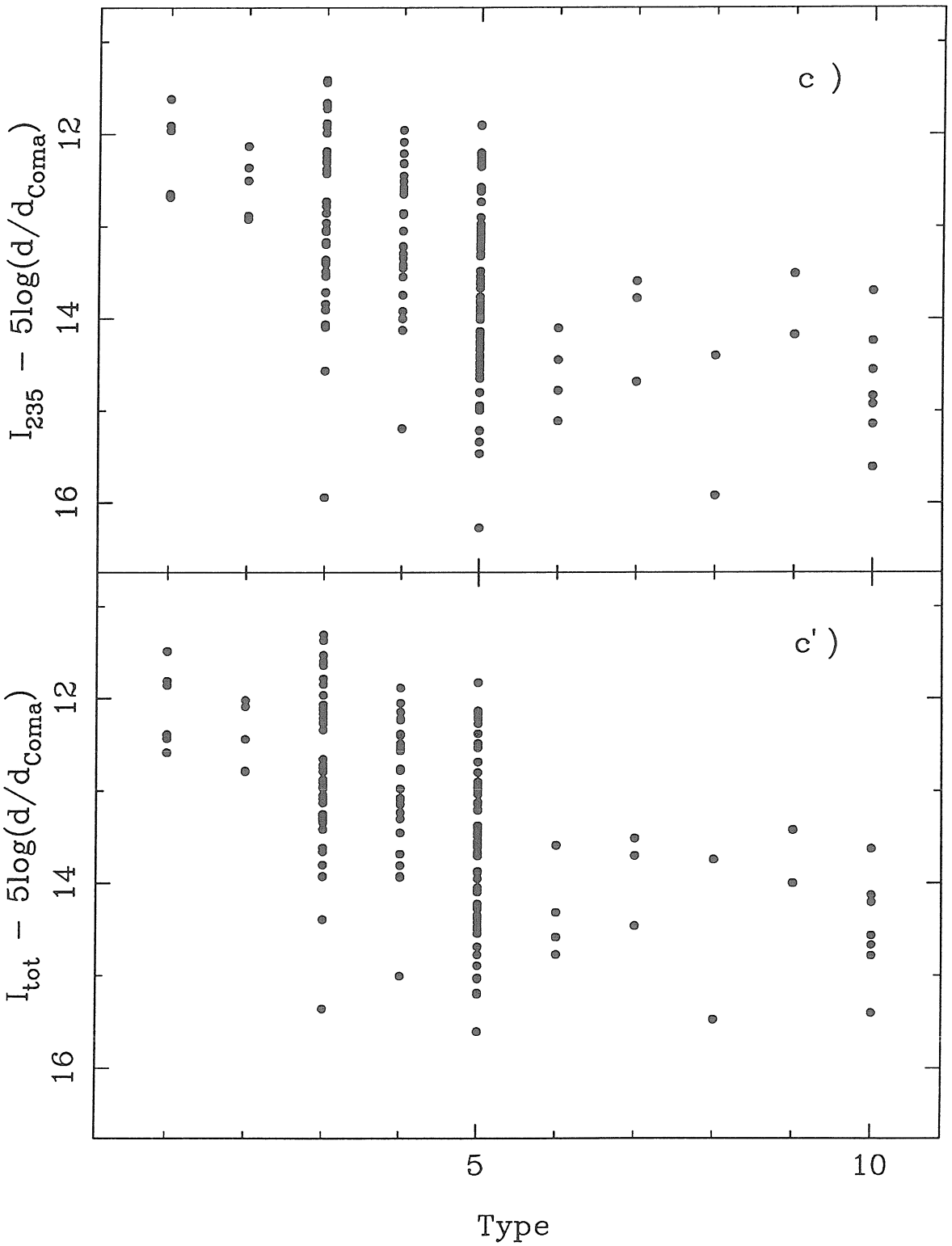

Figure 7.8 — continued

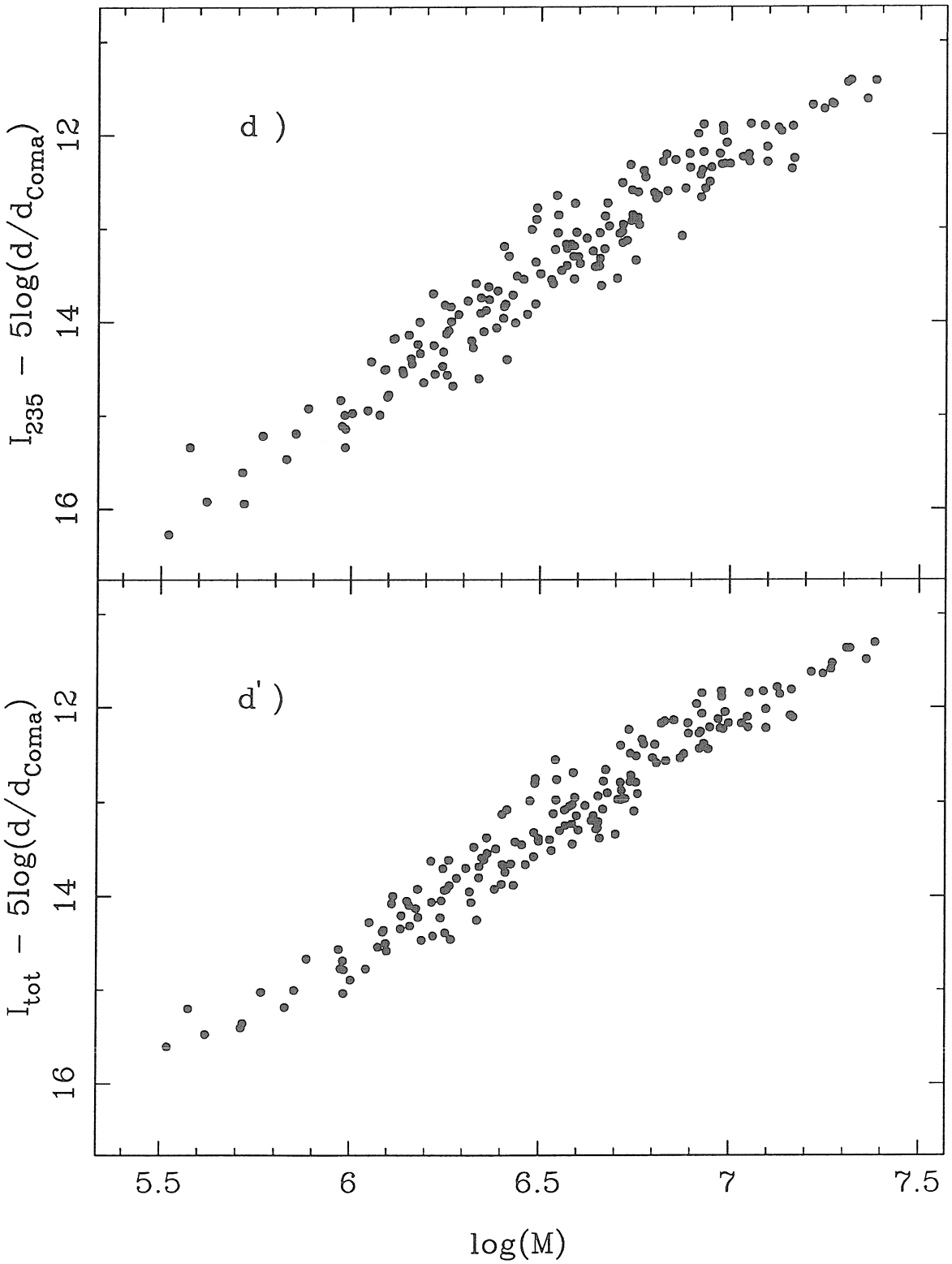

Figure 7.8 — continued

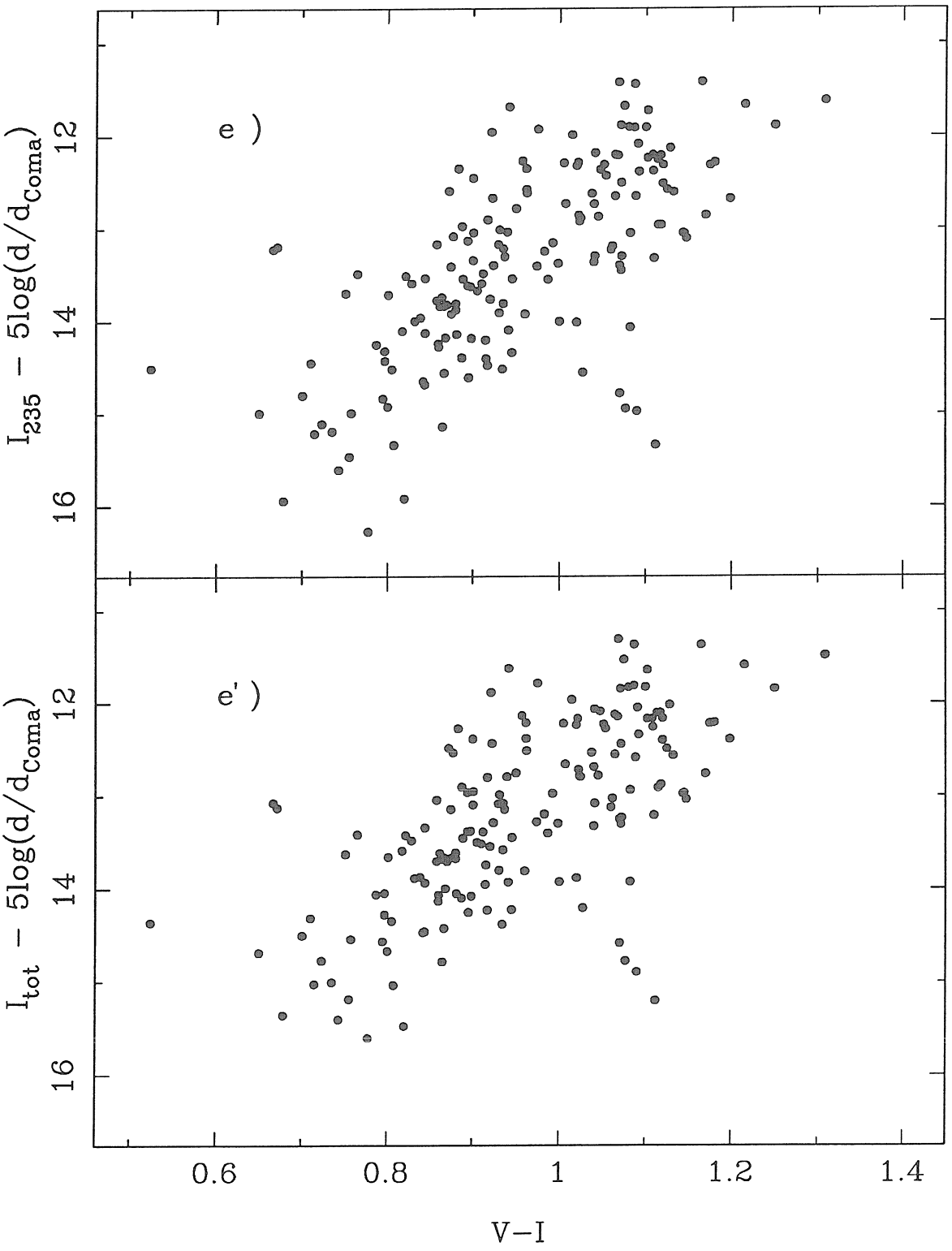

Figure 7.9

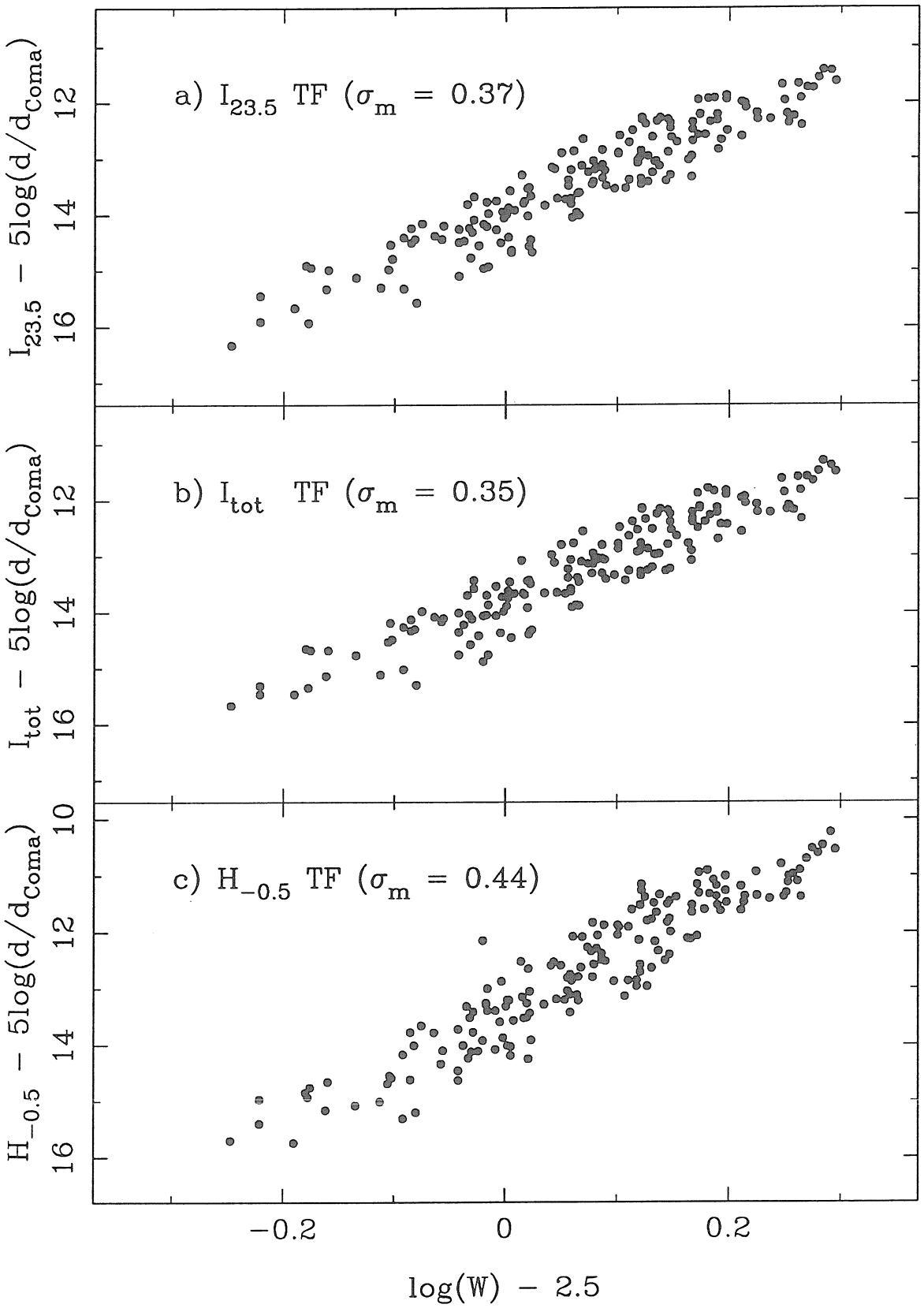
a) $I_{23.5}$ TF (σ_m = 0.37)
b) I_{tot} TF (σ_m = 0.35)
c) $H_{-0.5}$ TF (σ_m = 0.44)
$I_{23.5}$ − 5log(d/d_{Coma})
I_{tot} − 5log(d/d_{Coma})
$H_{-0.5}$ − 5log(d/d_{Coma})
16
14
12
10
−0.2
0
0.2
log(W) − 2.5

Figure 7.10

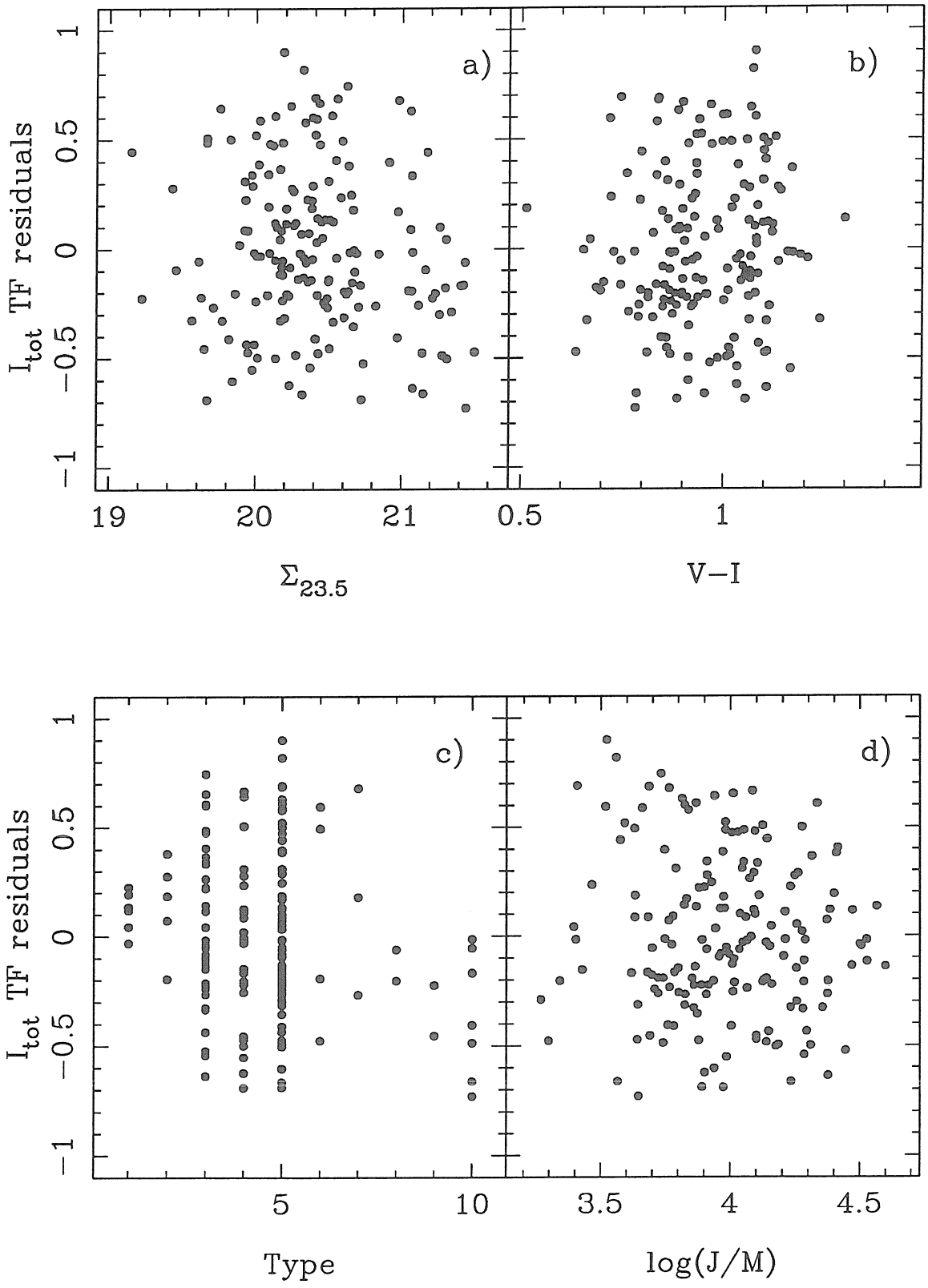

Figure 7.10 — continued

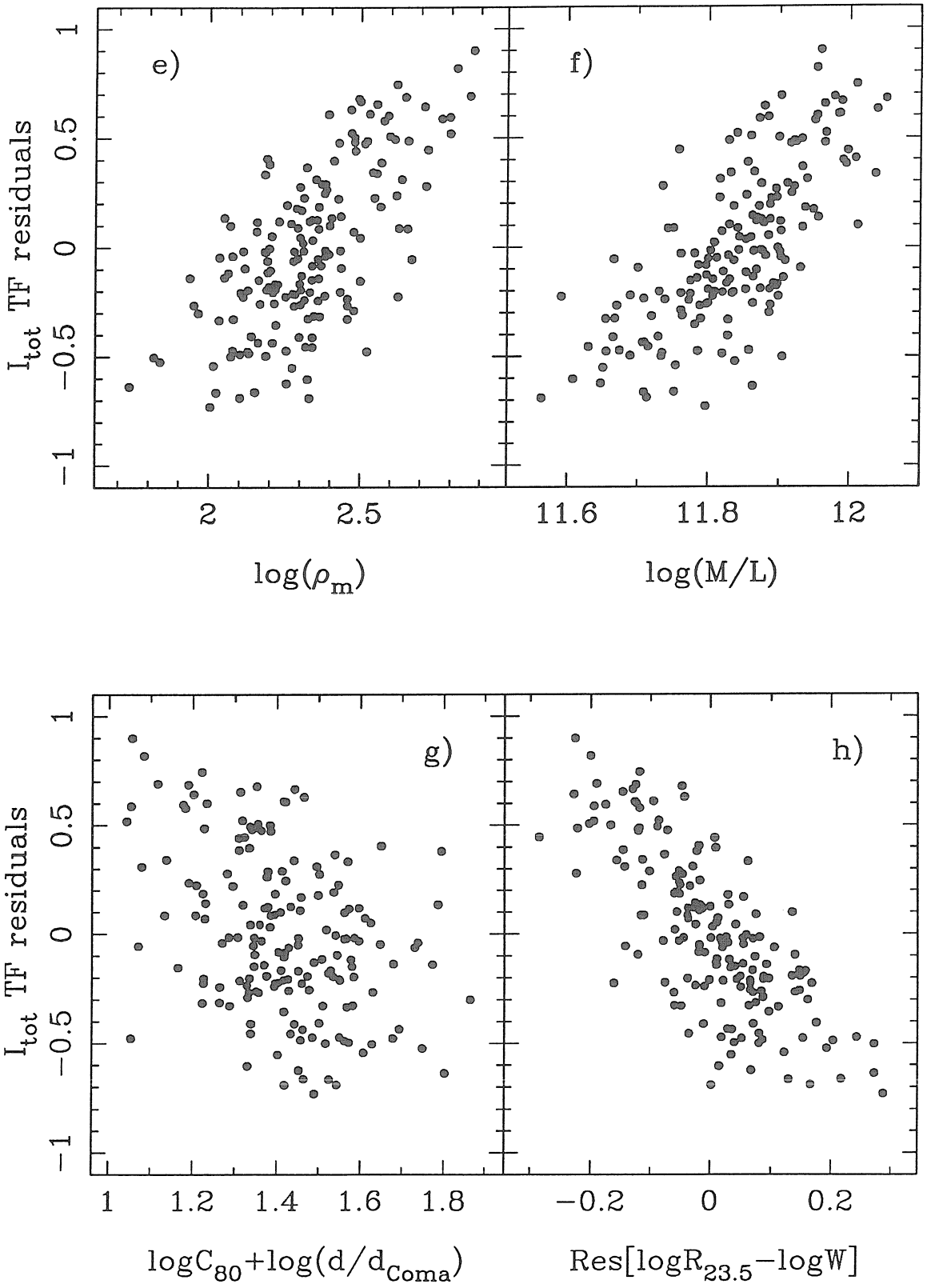

Figure 7.11

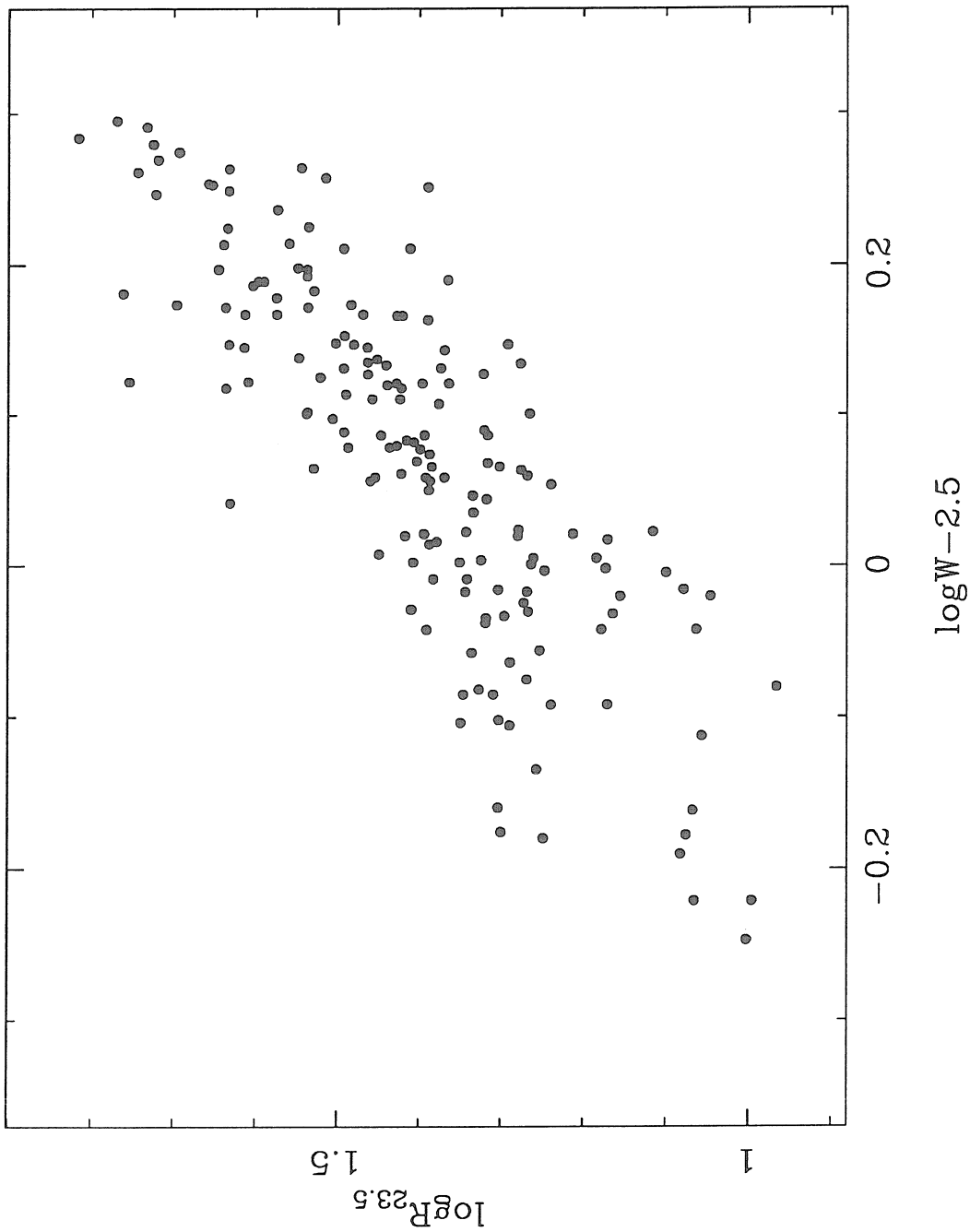

CHAPTER VIII

THE LARGE-SCALE VELOCITY FIELD

§8.1 Basic Evidence for Large-Scale Motions

The relative distances of the sample clusters were derived from the TF relation in Chapter 6. These distances together with redshifts and coordinates of the clusters provide the basic information about the large-scale velocity field traced by the sample clusters. Table 8.1 presents all these basic data: Column (1) gives the cluster name; Column (2) and (3) are the galactic coordinates of clusters; Columns (4) and (5) list the distance moduli and errors of the sample clusters relative to Coma (from column [9] of Table 6.3); Column (6) and (7) record the mean velocities of clusters in the LG frame and the CMB frame, respectively; Column (8) is the dispersion in the mean cluster velocity; Columns (9) and (10) give the apparent Hubble ratio and its uncertainty derived from Columns (5) and (7).

Figure 8.1a shows the variation of the apparent Hubble ratio with cluster velocity. A general trend of decreasing Hubble ratio with distance is seen, indicating that these clusters have large relative peculiar motions in the CMB frame. Standing out of this mean trend, at the lower left corner of Figure 8.1a, is the cluster Pegasus. This cluster lies at about the same distance of the GA, but in the opposite side of the sky. Figure 8.1b plots the Hubble ratio against the cosine of the angle between the cluster and the GA (l=309°, b=18°, from Faber and Burstein 1988). Pegasus now looks very normal in Figure 8.1b. The broad trend of increasing Hubble ratio with COS(GA) in Figure 8.1b is suggestive of a coherent peculiar motion of the clusters in the general direction of GA.

In sum, the fact that the Hubble ratios of the sample clusters show systematic variations with both distances and positions of the clusters leads the most

fundamental and safe conclusion of our study: *the sample clusters have large relative peculiar motions, and the motions are highly correlated, showing a general flow towards approximately the GA direction; the source of this coherent motion, if gravitational in origin, must lie beyond the limit of our sample.* To further quantify the picture of the peculiar motions, one may need to make additional assumptions, and utilize proper mathematical methods.

§8.2 Model of the Large-Scale Motions

A formal procedure of modeling the peculiar velocity field is to fit a presumed model to the observed data. Let H_o be the Hubble constant, and $V_{pec}(\vec{r})$ the radial component of a peculiar velocity field model, characterized by a number of model parameters. Evidently, the predicted velocity of a cluster at $\vec{r}$ is given by

$$V_{pred} = H_o r - V_{pec}(\vec{r}). \tag{8.1}$$

The fit can then be accomplished, e.g., by minimizing the quantity

$$\chi^2 = \sum_{i=1}^{n} \frac{[V_{obs} - H_o\, r + V_{pec}(\vec{r})]^2}{\sigma_V^2 + H_o^2 \sigma_r^2}, \tag{8.2}$$

where V_{obs} is the observed velocity of a cluster (column [7] of Table 8.1), and r is the estimated distance of a cluster in arbitrary units (Coma distance in our case). σ_V and σ_r are, respectively, the uncertainty in V_{obs} (column [8] of Table 8.1) and uncertainty in estimated distance r (from column [5] of Table 8.1).

a) Bulk Flow Model

Figure 8.1b gives us an impression that the sample clusters are comoving in the CMB frame toward approximately the GA direction. For a more accurate description, we now fit the data with a bulk flow model. The model can be parameterized as

$$V_{pred} = H_o r + W_{blk} \cos A, \tag{8.3}$$

where W_{blk} is the amplitude of the flow in the CMB frame, and A is the angle between a cluster and the flow direction (l, b) (as free parameters of the model).

The best fitting parameters are $H_o = 7150 \pm 147$ kms$^{-1}/d_{coma}$, $W_{blk} = 538 \pm 183$ kms^{-1}, and $(l, b) = (308° \pm 19°, -2° \pm 12°)$, which are tabulated in Table 8.2 as solution 1. The last two columns of Table 8.2 list, respectively, the value of χ^2 per degree-of-freedom and the dispersion of model (velocity) residuals. Figure 8.2 plots the peculiar velocities of clusters, calculated using $V_{pec} = V_{obs} - H_o r$, against the cosine angle between clusters and the bulk flow direction. This plot illustrates how well the large-scale velocity field can be represented by a bulk flow model. Note that the leftmost point in the figure, which appears to have the largest deviation from the mean flow, is cluster Pisces at distance of 4771 kms^{-1} .

b). The Great Attractor Model

The GA model of the Seven Samurai (Lynden-Bell *et al.* 1988; Faber & Burstein 1989) has been widely discussed in the literature, and is the current most popular empirical model of the large-scale peculiar motions. Han & Mould (1990), which can be regarded as a complementary paper of this thesis, studied the velocity field in the LSC using a model including both the Virgo-infall and GA-infall. They outlined the detailed formula of a bi-infall model expressed in the frame of the LG. In this thesis, we are more interested in the large-scale motions beyond the LSC. It is thus advantageous to express everything in the frame of the CMB, which bypasses the problems of Virgo-infall motion and the random motion of the LG. Let the profile of density excess of the GA be $r^{-\gamma}$. The peculiar velocity caused by such a mass overdensity is proportional, in the linear approximation, to $r^{1-\gamma}$ (Peebles 1976). The predicted radial velocity of a cluster in the CMB frame is then given by

$$V_{pred} = H_o r - W_{GA} \left(\frac{r - d_{GA} \cos\theta}{r_{GA}} \right) \left(\frac{r_{GA}}{d_{GA}} \right)^{1-\gamma}, \qquad (8.4)$$

where W_{GA} is the amplitude of the GA infall pattern at our position, d_{GA} is the

distance from us to the GA, θ is the angle between a cluster and the GA, and r_{GA} is the distance from the cluster to the GA, and is given by the following relation

$$r_{GA} = \sqrt{d_{GA}^2 + r^2 - 2\,r\,d_{GA}\cos\theta}. \tag{8.5}$$

The solution of such a GA model can also be obtained by minimizing equation (8.2). The model parameters may include everything unknown in equation (8.4), i.e., H_o, W_{GA}, d_{GA}, position of the GA (l, b), and γ. We fit the model with three different choices for model parameters:

1. model parameters are H_o, W_{GA} and d_{GA}; and the GA direction (l, b) is fixed at $(309°, 18°)$ (Faber & Burstein 1989), the parameter γ is fixed at a value of 2 (see Han & Mould 1990 for more discussion).

2. model parameters are H_o, W_{GA}, d_{GA}, and GA direction (l, b); γ fixed at 2.

3. model parameters are H_o, W_{GA}, d_{GA}, GA direction (l, b), and γ.

Solutions of these three models are given in Table 8.2 numbered as 2, 3 and 4 in the order. It is worth to note the following:

a) the three solutions give almost identical prediction for the GA distance, i.e., $d_{GA} \sim 0.67$ in units of Coma distance. This formally corresponds to an apparent velocity of $0.67 H_o d_{GA} - W_{GA}$, which is about 4400 kms^{-1} and very close to the centroid of the radial velocity distribution of galaxies in the GA region (Dressler 1988, 1991).

b) the infall velocities at LG by the three solutions are also in good agreement within formal errors, although the best estimate for GA direction is some 15° away from that of Faber & Burstein (1989).

c) H_o and W_{GA} is sensitive to γ as seen from solution 4. But the position and distance of the GA show little dependence on other parameters. The parameter

γ does not seem to be well constrained by our data.

c) Comparison of Different Solutions

Which of the models in Table 8.2 best features the peculiar velocity field traced by our sample clusters? Let us now examine the four solutions in more detail from different views —— both mathematical and more-or-less physical.

c1. Goodness-of-fit

A pure mathematical judge of the goodness of a model fit using the χ^2 technique relies on the value of χ^2/dof (the second last column of Table 8.2). According to this parameter, the GA model seems to give a mildly better fit to the data than does the bulk flow model. But we have to note that while this parameter can tell us the goodness of representing the data by an analytical model, it does not conclusively verify the correctness of the model.

c2. Model Velocity Residuals

Another way to judge the "goodness" of a model fit is to check the global variation of the model residuals, i.e., the deviation of cluster velocity from model prediction, $V_{obs} - V_{pred}$. Figures 8.3–8.6, corresponding to the four solutions in Table 8.2, show the variation of model residual with cluster distance and the cosine angle between the cluster and the streaming/infall direction. The following interesting features are noticed from these figures:

a) The relation of velocity residual with both cluster distance and COS(A) shows no overall systematic variation in all cases, a necessary condition for a right model.

b) The velocity of A2151, the most distant cluster in our sample, appears to be underestimated by a GA model with $\gamma \equiv 2$ (solution 2 and 3), but better

predicted by either a bulk flow model or a GA model with smaller value of the γ parameter. An apparent explanation for this is that there is more correlation of peculiar velocities on large scales than predicted by a GA model with $\gamma = 2$.

c) The cluster A2634 has the largest negative residuals in all cases, while the Pisces cluster always has very large positive residuals, especially in the case of the bulk flow model. We note that a positive/negative residual could result if the cluster distance is under/over estimated. As seen from Table 6.3, our estimated distance for Pisces is indeed a little bit nearer than that implied by the IRTF relation or the $D_n - \sigma$ relation, however, an error of 0.1 mag in distance modulus corresponds to a residual shift of only ~ 200 kms^{-1} at the Pisces distance. The cluster A2634 is really not a single cluster, but a combined system of A2634 and A2666 (Aaronson *et al.* 1986), the predicted distance for this "cluster" by different distance indicators is very controversial (see also Table 6.3).

d) The dispersion of model residuals from each of the four solutions is also calculated and is given in the last column of Table 8.2; this quantity decreases with the number of model parameters, from 304 kms^{-1} for solution 2 (3 free parameters) to 288 kms^{-1} for solution 4 (6 free parameters). But we have to note that the estimation of the dispersion parameters is largely affected by the few clusters with extreme residuals.

Pretending that there is something wrong with the two clusters Pisces and A2634, we then exclude these two clusters from the sample and refit each of the four models. The corresponding solutions thus obtained are listed in Table 8.2 numbered as $N.1$, with N being the original solution number. We see that all the four fittings are significantly improved according to the parameters χ^2 and $\sigma(v)$. Again, the GA model appears to fit the data slightly better than does a bulk flow model. Note that, while the model fitting is largely improved, the model parameters undergo only weak change, except for solution 4.1, which, relative to solution 4, shows a large

increase of H_o and W_{GA} in accordance with a decrease in γ. A value of γ less than 1 as that given by solution 4.1 corresponds to an extremely low density perturbation on large scales, and the infall velocity, according to linear approximation formula, increases with distance to the infall center. This again indicates more correlation of peculiar velocities on large scales.

The above discussions may be summarized as: 1) both the GA model and the Bulk Flow model fits the data reasonably well, although there seems to be a weak preference for the GA model over the Bulk Flow model; 2) our sample may be statistically too small to well constrain a GA model especially when the parameter γ is set free; and 3) there is also an indication that the peculiar velocity correlation on large scales is stronger than solutions 2 and 3 predict.

c3. Prediction of the CMB Dipole Anisotropy

It is also very instructive to compare how well different models predict the dipole anisotropy in the CMB, i.e., the motion of the LG relative to the CMB. In general, the motion of the LG with respect to the CMB can be decomposed into two major components:

1) the motion of the LG within the LSC, which includes a Virgocentric infall motion and a random motion of the LG. In the paper of Han & Mould (1990), we studied the peculiar velocity field within the LSC, and found that, at the position of the LG, the Virgocentric infall amplitude is 197 $\pm$37 kms^{-1} and the random motion (the motion of Local Anomaly) is 230 $\pm$23 kms^{-1} towards (l, b) = (205°$\pm$4°, 11°$\pm$3°). The sum of these two vectors gives the motion of the LG within the LSC: 341 $\pm$30 kms^{-1} towards (l, b) = (217°$\pm$4°, 44°$\pm$5°).

2) the motion of the whole LSC with respect to the CMB; this can be naturally inferred from the flow models of Table 8.2, which describe how the sample clusters move in the CMB. We simply assume the LSC follows the flow pattern

defined by the sample clusters, and has no additional random motion above the flow model.

For each solution in Table 8.2, we can then predict the motion of the LG in the CMB by adding up the total velocity of the LG within the LSC and the velocity of LSC in the CMB frame as given by the solution. Table 8.3 lists the results predicted by the solutions in Table 8.2, where U is the predicted amplitude of the motion of LG relative to CMB, (l, b) is the apex of this motion; ΔU is the difference between the predicted amplitude and the true amplitude of the dipole motion, $\Delta\phi$ is the angle between predicted and the true dipole directions. The agreements between the predictions and the true dipole are generally good within 1 σ.

Note that the two velocity components which give rise to the prediction of the anisotropy dipole were independently estimated from two different datasets. The satisfactory success for their combination to predict the dipole anisotropy adds credence to the reality of the two velocity components.

d) Comparison With Previous Work

In Table 8.4, we list the inferred peculiar velocity of the LSC relative to the CMB (i.e., l, b and U in cols. [2-4]) from our solutions 1-4 and also from other selected studies. Note that the peculiar velocity of the LSC in CMB is usually deduced by fitting a presumed model (column[5]) to a data set (column [6]); fitting a Bulk flow or GA-infall model can be carried out in the frame of CMB; whereas fitting a model that includes the motion of the LG within the LSC (e.g., the model of Virgo+LA+GA or Virgo+GA, here LA stands for Local Anomaly, see e.g., Han & Mould 1990) will have to be done in the frame of the LG. In both cases, the motion of the LSC is taken to be the GA-infall (or bulk flow) velocity at the position of the LG, which relies on the assumption that the GA is at rest with respect to the CMB. It is also important to note that a GA model and a Bulk Flow model have very different implications on the large-scale patterns of peculiar velocity in the universe,

even if they give identical values for the motion of the LSC relative to the CMB.

Our bulk flow model (solution 1 and especially 1.1) is in very good agreement with that of Lynden-Bell *et al.* (1988). Our solution 2 for the GA model (with GA direction fixed) also agrees well with the corresponding solutions of Han & Mould (1990) and Aaronson *et al.* (1989). The direction of GA given by our solution 3 and 4 is however about 15° higher above the galactic plane than that of Faber & Burstein (1988), and the resultant infall velocities are also lower by about 100 kms^{-1} than their best estimate. these differences are significant at 1 σ.

A relevant work, which is not included in Table 8.4, is the that of Mathewson, Ford & Buchhorn (1991). These authors studied the large-scale flow in the Supergalactic Plane along the line joining the GA region and the Perseus-Pisces supercluster using their survey of peculiar velocities of spiral galaxies in the GA region and that in Perseus-Pisces by Willick (1990). They found that the median lines of peculiar velocities are offset from zero by +500 kms^{-1} in the direction of GA and –500 kms^{-1} in the direction of Perseus-Pisces, indicating a bulk flow of amplitude 500 kms^{-1} and with coherent length some 20000 kms^{-1} in the Supergalactic Plane. This qualitative result is in good agreement with our bulk flow solution.

The results from a recent survey of peculiar velocities of eight additional southern clusters by Mould *et al.* (1991) using an I-band TF relation also agrees with the basic peculiar velocity picture presented by our sample clusters, i.e., large outflows of clusters in the CMB dipole direction.

It is noted that a coherent large-scale motion picture (or a GA-infall picture) is not consistent with the study of Rowan-Robinson *et al.* (1990), who believe, from a redshift survey of IRAS galaxies and an analytical model, that the LG's motion in CMB is generated by a number of known superclusters (with presumed large halos) in the local universe, and each cluster has its own peculiar velocity of the same order but in diverse directions. A very large-scale coherent motion does not either seem to

agree well with the results of other investigations about the relationship between the CMB and optical/IRAS dipoles (Yahil, Walker & Rowan-Robinson 1986; Strauss & Davis 1988; Yahil 1988; Lahav *et al.* 1988; Lynden-Bell *et al.* 1989). These studies in general come to the conclusion that the CMB dipole is generated largely within relatively small regions and the peculiar motions on large scales do not have much correlation. It is interesting to note that the source of such disagreement can be largely traced to the Perseus-Pisces supercluster, which lies on the opposite side of the sky from the GA. This supercluster counts a lot in the dipole investigations, and acts to balance the GA (Strauss 1991); however, it appears not so important according to the studies based on distance indicators.

In sum, our data appears to support the idea of large-scale coherent motions on scales beyond the LSC; conceptually similar conclusions seem to be favored by most other investigations which explicitly rely on either the $D_n - \sigma$ or the TF relation as distance indicator.

§8.3 Reliability of Model Solutions

Our solutions for the large-scale motion above were carried out by fitting analytical models to the fundamental data of the sample clusters listed in Table 8.1, i.e., distances deduced from the TF relation and the apparent cluster redshifts and positions. Both the distance and redshift carry statistical uncertainties as characterized by the formal errors in columns [5] and [8] of Table 8.1. The effects of such statistical uncertainties in the data on our model fitting are partly reflected in the formal errors of the model parameters. To test how likely it is that our solutions can arise, by chance, from such statistical fluctuations in the data, we conduct the following numerical experiment.

We produce counterfeit datasets by perturbing the distance and redshift of each cluster (column [4] and [7] of Table 8.1) with Gaussian noise of σ equal to respectively the corresponding formal errors as given in columns [5] and [8] of Table

8.1. Sixty such counterfeit datasets are produced. Figure 8.7, analogous to Figure 8.1 but based on these simulated datasets, illustrates the variation of the Hubble ratio with cluster redshift and the cosine angle between cluster and the GA direction of Faber & Burstein (1988). The vertical scatter in this plot reflects the reliability of our reduced solutions for the large-scale motion due to the statistical uncertainties in the estimated cluster distance and redshift. We fit a bulk flow model and a GA model (with direction set free and γ fixed at 2) to each of the simulated datasets. The averaged solutions are listed in Table 8.2 as solutions 1.2 and 3.2, respectively. These two solutions are compared with their analogues, solutions 1 and 3. The deviations of all the model parameters are seen to be within 1 σ. The quoted uncertainties in the model parameters from the simulation are calculated from the variance of individual solutions, and thus are better measures of the effects of the statistical errors in cluster distances and redshifts on our reduced solutions of large-scale motions. These uncertainties are seen to be comparable to, or a bit higher than the original formal errors in the model parameters given by the fitting procedure, which largely reflect the goodness of fitting the analytical model to the original data. Anyway, we conclude from these simulation tests that the detection of the large-scale coherent motion is reliable, in the sense that it is very unlikely to arise from the statistical uncertainties in our dataset.

Besides statistical uncertainties in the original dataset of our cluster sample, there is still a concern of bias, or systematic errors in the dataset, both in the estimated distances and the cluster redshifts. In Chapter 6, we discussed in great detail the problem of sample selection biases in predicting distances of clusters of galaxies. To our best understanding, the relative distances for the sample clusters derived in Chapter 6 are largely free of bias due to selection effects. Then what about the redshifts of the clusters? We utilized the *cluster mean redshifts* from the literature in our analyses above. However, we note that the *sample mean redshifts* (column [6] of Table 2.1) estimated from the cluster galaxies in our sample show large deviations from the *mean cluster redshifts* for some of the clusters. Note that

the *cluster mean redshifts* are heavily weighted by galaxies in cluster cores where more elliptical galaxies are found, whereas our sample galaxies are gas-rich spirals and are more often found in the outer peripheries of clusters. The discrepancies between the two mean velocities from Table 2.1 (sample mean – cluster mean) are plotted against the cluster mean values in Figure 8.8. The discrepancies are seen to be dominantly positive, i.e., sample mean redshifts are more often higher than cluster mean redshifts. Interestingly, we note that such a redshift asymmetry is in accordance with that in groups of galaxies as reported by Sulentic (1984) and Arp & Sulentic (1985), who also raised the question of nonvelocity redshift component for companion galaxies in groups. A less exotic explanation might be that some clusters are not well bounded and have substructures. This seems to be the case for Cancer, Z74-23 and possibly A400 (Bothun *et al.* 1983; Aaronson *et al.* 1986); these three clusters indeed show relatively large discrepancies between sample and cluster mean velocities. The other three clusters with large discrepancies are Cen30, Pegasus and A2151; these clusters however as known to the author have not been reported to have substructures in literature. Whatever the origin of such discrepancies is, it is an important issue in studying the velocity field using clusters as velocity field tracers, and merits detailed investigation. For the purpose of this thesis, our concern is whether a discrepancy between sample mean velocity and cluster mean velocity of a cluster indicates the mean distance (as derived from Chapter 6) of our sampled galaxies in the cluster fairly sample the cluster distance, and if not, to what extent, it would affect our solution for the large scale motions. To test this, we repeat the above analyses using the *sample mean redshifts*, i.e., assuming the mean distance as derived in Chapter 6 for a cluster is not the same of cluster-core distance, and is better associated with the sample mean velocity rather than the cluster mean velocity. First of all, in Figure 8.9 we plot the Hubble ratio calculated using sample mean velocity (in the frame of CMB) against, a) sample mean velocity and b) cosine of the angle between cluster and the GA direction of Faber & Burstein (1988). This is compared with its counterpart Figure 8.1 which was based on the cluster mean

velocities. It is seen that Figure 8.9 retains the general trend of Figure 8.1, but the scatter appears to be increased.

For further comparison, we also carried out the (bulk flow and GA) model fittings analogous to solutions 1 – 4 in Table 8.2. The corresponding solutions numbered as $1'$– $4'$ are tabulated in Table 8.5. The bulk flow solution undergoes a large change both in flow amplitude and direction; the three GA model solutions in contrast are relatively stable, especially the GA distance d_{GA} here is in remarkable agreement with that in Table 8.2. As seen from the dispersions of model residuals, the quality of these fits is poor compared with those of solutions 1 – 4 in Table 8.2. It is also noted that the formal errors of the model parameters of these solutions are generally larger than their counterparts in Table 8.2, especially for solutions $3'$ and $4'$. These largely reflect the fact that the GA direction is not well constrained by the data, due to large intrinsic dispersion of the dataset (the vertical scatter in Figure 8.9 at constant redshift). If we refit the model with the GA direction fixed at that of solution $3'$ or $4'$, we then have a very significant detection of GA infall.

The fact that the analytical models of both bulk-flow and GA shows poor fit to the data with sample mean redshift might suggest that the redshift discrepancies seen in some clusters are of statistical origin. Anyway, the above simple experiments allow us to draw the following conclusions:

1) The redshift discrepancies found in some clusters do not affect our basic conclusion that the sample clusters have large coherent motions in the CMB frame.

2) But it does seem to modify the detailed analytical models for the large-scale motions, especially the bulk flow model.

3) The GA model fits the data mildly better than a bulk flow model, but the GA direction can not be well determined.

§8.4 Summary

We derived relative distances of 16 clusters of galaxies using the I-band TF relation as distance indicator. When these distances are combined with the mean redshifts of the clusters and their positions on the sky, a gross large-scale peculiar motion picture emerges. Study of this peculiar motion picture allows us to draw the following conclusions:

1) The large-scale motions of the sample clusters are highly non-random, and appear to form a pattern of coherent flow towards roughly the GA direction, with an amplitude of some $400 \sim 600$ kms^{-1} at the LG.

2) The large-scale coherent motion is statistically significant, in the sense that it is unlikely to be caused by the statistical uncertainties in the dataset, nor is it an artifact of the redshift discrepancies of the sample clusters. The problem of redshift discrepancies in clusters is crucially important for the study of peculiar motions of clusters, and should be carefully stressed in any of such investigations.

3) The peculiar velocity field is fitted using analytical models of both Bulk Flow and GA-infall; both model fits the data reasonably well, although there is a weak preference for the GA model over the bulk flow model. Our best estimated GA parameters differ from those of the 7 Samurai with marginal significance.

4) The motion of the LSC in the rest frame of the CMB, predicted by assuming it follows the coherent flow field of the 16 sample clusters, is in good agreement with that just required by the LG, apart from its motion within the LSC, to generate the CMB dipole anisotropy. This adds credence to the reality of the large-scale flow.

The existence of large-scale coherent motion in the universe, which is seeing more and more support from different investigations (primarily those based on the TF or $D_n - \sigma$ relations), does not seem to be expected by the current theories

of structure formations based on cold or hot dark matter (Vittorio & Silk 1985; Bertschinger & Juszkiewicz 1988; Gorski *et al.* 1989; Groth *et al.* 1989, but see also Kaiser 1988, 1991). However, it is worth keeping in mind that there also exist questions regarding the reality of large-scale motions. One of them is again the possibility of environmental dependence of the zero-point of distance indicators (Djorgovski, de Carvalho & Han 1988; Silk 1989), although, according to a number of empirical investigations, this appears not to be the case for both the TF relation and the $D_n - \sigma$ relation (Mould, Han & Bothun 1989; Biviano *et al.* 1990; Burstein, Faber & Dressler 1990). Another possibility is that the conventional assumption of the CMB defining a standard rest frame and its temperature dipole being the result of the motion of the LG is wrong (Mathewson, Ford & Buchhorn 1991). Abandoning this assumption would certainly rule out the problem of large-scale motion, but also brings other theoretical problems. In fact, Burstein, Faber & Dressler (1990) have listed a number of arguments in favor of this assumption.

In any case, large-scale coherent motions as well as the distance indicator relations employed in the relevant studies contain valuable information about the formation and evolution of galaxies and large scale structures in the universe. A successful theoretical model is expected to tell us the very physics underlying the apparent properties of the universe that we are *seeing*.

REFERENCES FOR CHAPTER 8

Aaronson, M. *et al.* 1986, *Ap. J.*, **302**, 536.

Aaronson, M. *et al.* 1989, *Ap. J.*, **338**, 654.

Arp, H. and Sulentic, J. W. 1985, *Ap. J.*, **291**, 88.

Bertschinger, E. and Juszkiewicz, R. 1988, *Ap. J.*, **334**, L59.

Biviano, A. *et al.* 1990, *Ap. J. Suppl.*, **74**, 325.

Bothun, G. D. *et al.* 1983, *Ap. J.*, **268**, 47.

Burstein, D., Faber, S. M. and Dressler, A. 1990, *Ap. J.*, **354**, 18.

Djorgovski, G., de Carvalho, R. and Han, M. 1988, in *The Extragalactic Distance Scale*, eds. S. van den Bergh and C. J. Pritchet (Provo: A.S.P.), p. 329.

Dressler, A. 1988, *Ap. J.*, **329**, 519.

Dressler, A. 1991, *Ap. J. Suppl.*, **75**, 241.

Faber, S. M. and Burstein, D. 1988, in *Large Scale Motions in the Universe*, ed. V. C. Rubin and G. Coyne (Princeton: Princeton University Press), p. 115.

Gorski, K. *et al.* 1989, *Ap. J.*, **344**, 1.

Groth, E. J. *et al.* 1989, *Ap. J.*, **346**, 558.

Han, M. and Mould, J. R. 1990, *Ap. J.*, **360**, 448.

Kaiser, N. 1988, *M.N.R.A.S.*, **231**, 149.

Kaiser, N. 1991, *Ap. J.*, **366**, 388.

Lahav, O. *et al.* 1988, *M.N.R.A.S.*, **234**, 677.

Lilje, P. B., Yahil, A. and Jones, B. J. T. 1986, *Ap. J.*, **307**, 91.

Lynden-Bell, D. *et al.* 1988, *Ap. J.*, **326**, 19.

Lynden-Bell, D., Lahav, O. and Burstein, D. 1989, *M.N.R.A.S.*, **241**, 325.

Mathewson, D. S., Ford, V. L., and Buchhorn, M. 1991 *Ap. J. (Letters)*, in press.

Mould, J. R. *et al.* 1991, submitted to *Ap. J.*.

Peebles, P. J. E. 1976, *Ap. J.*, **205**, 318.

Rowan-Robinson, M. *et al.* 1990, *M.N.R.A.S.*, **247**, 1.

Staveley-Smith, L. and Davies, R. D. 1989, *M.N.R.A.S.*, **241**, 787.

Strauss, M. A. and Davis, R. D. 1988, in *Large Scale Motions in the Universe,* ed. V.C. Rubin and G. Coyne (Princeton University Press), p. 255.

Strauss, M. A. 1991, private communication.

Sulentic, J. W. 1984, *Ap. J.*, **286**, 442.

Vittorio, N. and Silk, J. 1985, *Ap. J. (Letters)*, **293**, L1.

Willick, J. 1990, *Ap. J. (Letters)*, **351**, L5.

Yahil, A. 1988, in *Large Scale Motions in the Universe,* ed. V.C. Rubin and G. Coyne (Princeton University Press), p. 219.

Yahil, A., Walker, D. and Rowan-Robinson, M. 1986, *Ap J.*, **301**, L1.

Figure Captions for Chapter 8

Figure 8.1: a) Hubble ratio against cluster velocity in the CMB frame; b) Hubble ratio against cosine angle between a cluster and the direction of the GA (l=309°, b=18°) given by Faber & Burstein (1988).

Figure 8.2: Peculiar velocity versus the cosine angle between cluster and bulk flow apex (solution 1 of Table 8.2).

Figure 8.3: Model residuals calculated using solution 1 in Table 8.2 is plotted against a) velocity in CMB frame and b) cosine angle between cluster and the model flow direction.

Figure 8.4: Same as Figure 8.3, but the model residuals is based on solution 2.

Figure 8.5: Same as Figure 8.3, but the model residuals is based on solution 3.

Figure 8.6: Same as Figure 8.3, but the model residuals is based on solution 4.

Figure 8.7: Analogous to Figure 8.1, but here the Hubble ratio is based on 60 counterfeit datasets, which were generated by normally disturbing the true cluster dataset (distance and velocity).

Figure 8.8: Cluster redshift discrepancy (sample mean velocity minus cluster mean velocity) versus cluster mean velocity.

Figure 8.9: Analogous to Figure 8.1 and Figure 8.7, but here the Hubble ratio is calculated using the *sample mean redshifts* of the clusters in our sample.

Table 8.1

Distances and Hubble Ratios of the Sample Clusters

Cluster	l	b	$\Delta\mu$	$\sigma_{\Delta\mu}$	v_{LG}	v_{CMB}	σ_v	H	σ_H
(1)	(2)	(3)	(4)	(5)	(6)	(7)	(8)	(9)	(10)
Pisces	125.8	–32.5	–0.96	0.11	5274	4771	58	7221	373
A400	170.3	–44.9	0.00	0.13	7154	6910	90	6910	420
A539	195.7	–17.7	0.44	0.13	8561	8633	123	7033	405
Cancer	202.5	28.7	–0.66	0.12	4790	5115	89	6964	406
A1367	234.8	73.0	0.00	0.10	6427	6818	73	6818	330
Coma	57.2	87.9	0.00	0.11	6931	7186	45	7186	415
Z74-23	349.6	65.5	–0.20	0.13	6025	6305	153	6961	430
A2151	31.7	44.5	0.90	0.13	11077	11056	97	7288	438
Pegasus	87.8	–48.4	–1.20	0.12	4078	3519	78	6158	346
A2634	103.5	–36.0	0.54	0.12	8783	8206	115	6355	360
Antlia	273.0	20.0	–2.06	0.13	2667	3260	84	7967	537
Cen30	302.5	21.5	–2.15	0.13	2804	3313	52	8478	551
Cen45	302.5	21.5	–0.93	0.15	4337	4846	35	7472	490
E508	309.2	39.2	–2.23	0.14	2728	3211	60	9052	586
Hydra	269.6	26.5	–1.28	0.13	3455	4054	85	7344	461
N3557	282.0	22.0	–1.86	0.16	2702	3284	79	7772	587

Table 8.2

Peculiar Velocity Field Models

Solution	H_o	W_{blk}	l	b	χ^2/dof	$\sigma(v)$
			Bulk Flow Model			
1.....	7150 ±147	538 ±183	308 ±19	−2 ±12	1.56	304
1.1.....	6988 ±130	625 ±120	310 ±16	7 ±11	0.86	255
1.2.....	7155 ±127	628 ±139	309 ±21	−2 ±13	—	—

Solution	H_o	W_{GA}	d_{GA}	l	b	γ	χ^2/dof	$\sigma(v)$
				Great Attractor Model				
2.....	7193 ±107	387 ±68	0.67 ±0.03	≡ 309	≡ 18	≡ 2	0.99	313
2.1.....	7187 ±100	396 ±60	0.67 ±0.02	≡ 309	≡ 18	≡ 2	0.72	230
3.....	7140 ±118	345 ±76	0.69 ±0.06	300 ±7	34 ±10	≡ 2	1.00	296
3.1.....	7130 ±109	359 ±68	0.70 ±0.05	301 ±6	35 ±8	≡ 2	0.67	197
3.2.....	7238 ±165	495 ±169	0.76 ±0.16	308 ±14	26 ±16	≡ 2	—	—
4.....	7332 ±300	490 ±177	0.67 ±0.06	305 ±13	32 ±15	1.3 ±0.7	1.03	288
4.1.....	7661 ±333	687 ±123	0.61 ±0.11	312 ±10	29 ±12	0.7 ±0.3	0.38	147

H_o = Hubble constant ($\mathrm{kms}^{-1}/d_{coma}$); W_{blk} = bulk flow velocity in CMB frame (kms^{-1}); W_{GA} = GA-infall velocity at LG (kms^{-1}); (l, b) = galactic coordinates of the flow/infall direction; d_{GA} = GA distance relative to Coma; γ = exponent of the GA density profile. χ^2/dof = χ^2 per degree-of-freedom; $\sigma(v)$ = dispersion of model residuals (kms^{-1}).

Table 8.3

Prediction of Dipole Anisotropy

	Predicted Dipole[a]			(pred. – true)[b]	
Solution	U	l	b	ΔU	$\Delta\phi$
1	626 ±176	283 ±17	20 ±11	26 ±176	15 ±16
1.1	725 ±143	288 ±13	25 ±10	125 ±143	18 ±13
1.2	699 ±184	287 ±17	18 ±14	99 ±184	20 ±16
2	562 ±72	274 ±9	39 ±7	–38 ±72	13 ±8
2.1	569 ±70	275 ±9	39 ±7	–31 ±70	13 ±8
3	586 ±70	262 ±7	47 ±7	–14 ±70	20 ±7
3.1	598 ±62	263 ±7	48 ±6	–2 ±62	21 ±7
3.2	678 ±158	279 ±15	42 ±13	78 ±158	17 ±13
4	697 ±147	275 ±14	45 ±12	197 ±147	18 ±12
4.1	848 ±131	289 ±11	42 ±10	248 ±131	23 ±9
true dipole	600 ±30	268 ±5	27 ±3	———	———

[a] The predicted dipole ≡ the sum of LSC's motion relative to CMB as implied by the solutions from Table 8.2, and the LG's motion within LSC from Han & Mould (1990). U = amplitude in kms^{-1}, (l, b) = direction in galactic coordinate system. See text for details.

[b] The difference between predicted dipole and the true dipole. ΔU = difference in amplitude, $\Delta\phi$ = difference in direction.

Table 8.4

The Motion of LSC in the CMB Frame

Reference	l	b	U	Sample[a]	Model[b]
Solution 1	308 ±19	–2 ±12	538 ±183	CS	Bulk Flow
Solution 2	≡309	≡18	387 ±68	CS	GA
Solution 3	300 ±7	34 ±10	345 ±76	CS	GA
Solution 4	305 ±13	32 ±15	490 ±123	CS	GA
Aaronson *et al.* 1989	≡309	≡18	486 ±91	CS	Virgo+GA
Lynden-Bell *et al.* 1988	307 ±11	9 ±8	521 ±89	E	Bulk Flow
	≡307	≡9	570 ±60	E	GA
Faber & Burstein 1988	309 ±10	18 ±10	535 ±77	E	Virgo+LA+GA
Lilje, Yahil & Jones 1986	288 ±9	–9 ±10	503 ±75	FS	quadrupole solution with CMB constraint
Staveley-Smith & Davies 1989. . . .	295 ±7	23 ±7	543 ±68	FS	Virgo+GA model
Han & Mould 1990	≡309	≡18	400 ±91	FS	Virgo+LA+GA

[a] CS = cluster spirals; FS = field spirals; E = elliptical galaxies.

[b] LA stands for Local Anomaly, see Han & Mould (1990) for details.

Table 8.5

Peculiar Velocity Field Models[a]

			——— Bulk Flow Model ———					
Solution	H_o	W_{blk}		l	b		χ^2/dof	$\sigma(v)$
$1'$	7325 ±169	815 ±281		323 ±18	−20 ±14		1.65	405
			——— Great Attractor Model ———					
Solution	H_o	W_{GA}	d_{GA}	l	b	γ	χ^2/dof	$\sigma(v)$
$2'$	7276 ±115	433 ±74	0.67 ±0.03	≡ 309	≡ 18	≡ 2	1.00	376
$3'$	7295 ±271	471 ±429	0.68 ±0.11	310 ±17	14 ±27	≡ 2	1.18	375
$4'$	7379 ±443	554 ±563	0.68 ±0.13	311 ±20	13 ±31	1.7 ±0.7	1.28	380

[a] Similar to Table 8.2, but based on sample mean velocities.

H_o = Hubble constant ($\mathrm{kms}^{-1}/d_{coma}$); W_{blk} = bulk flow velocity in CMB frame (kms^{-1}); W_{GA} = GA-infall velocity at LG (kms^{-1}); (l, b) = galactic coordinates of the flow/infall direction; d_{GA} = GA distance relative to Coma; γ = exponent of the GA density profile. χ^2/dof = χ^2 per degree-of-freedom; $\sigma(v)$ = dispersion of model residuals (kms^{-1}).

Figure 8.1

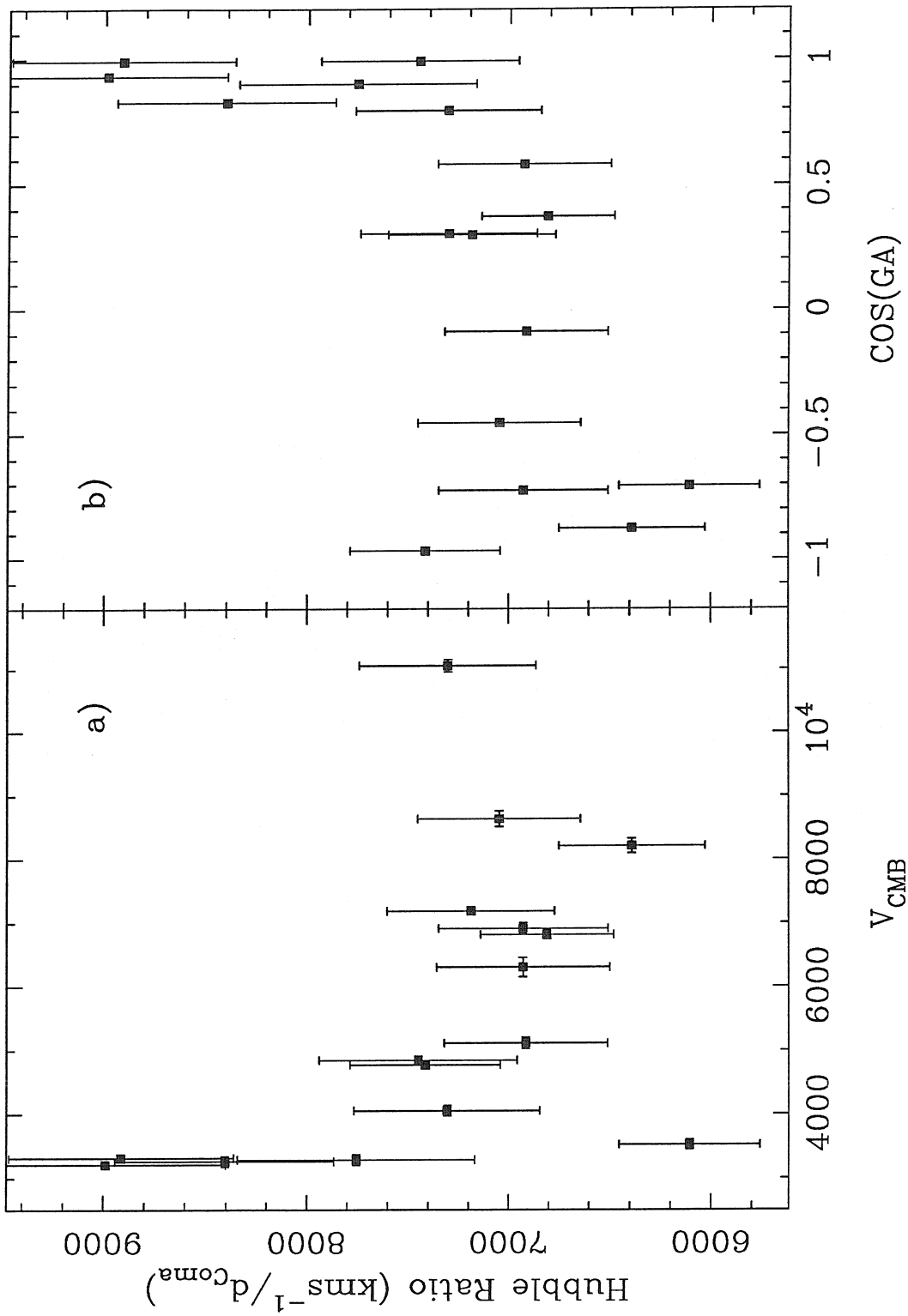
Hubble Ratio (kms^{-1}/d$_{coma}$)
6000
7000
8000
9000
a)
b)
4000
6000
8000
10^4
V_{CMB}
−1
−0.5
0
0.5
1
COS(GA)

Figure 8.2

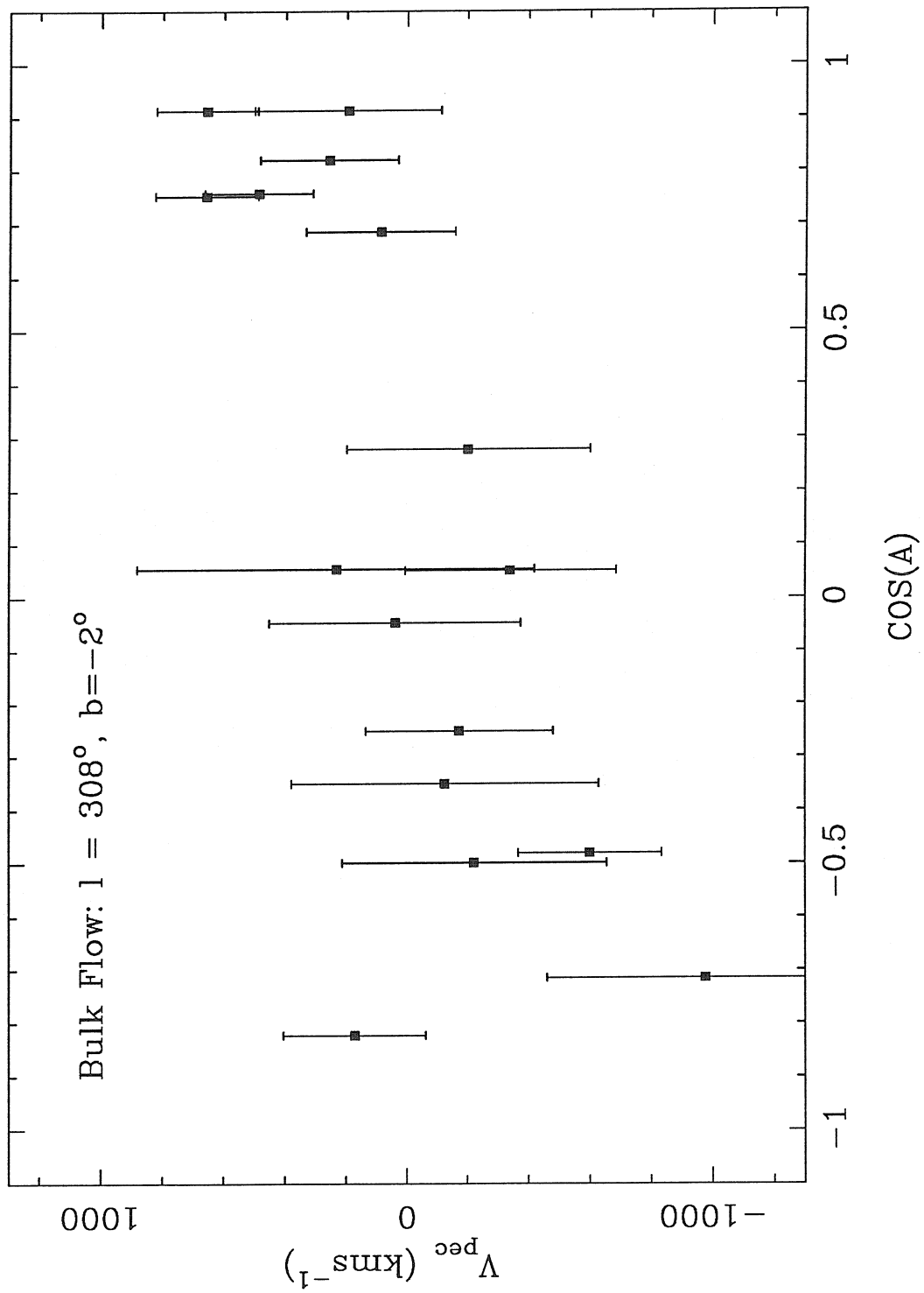

Figure 8.3

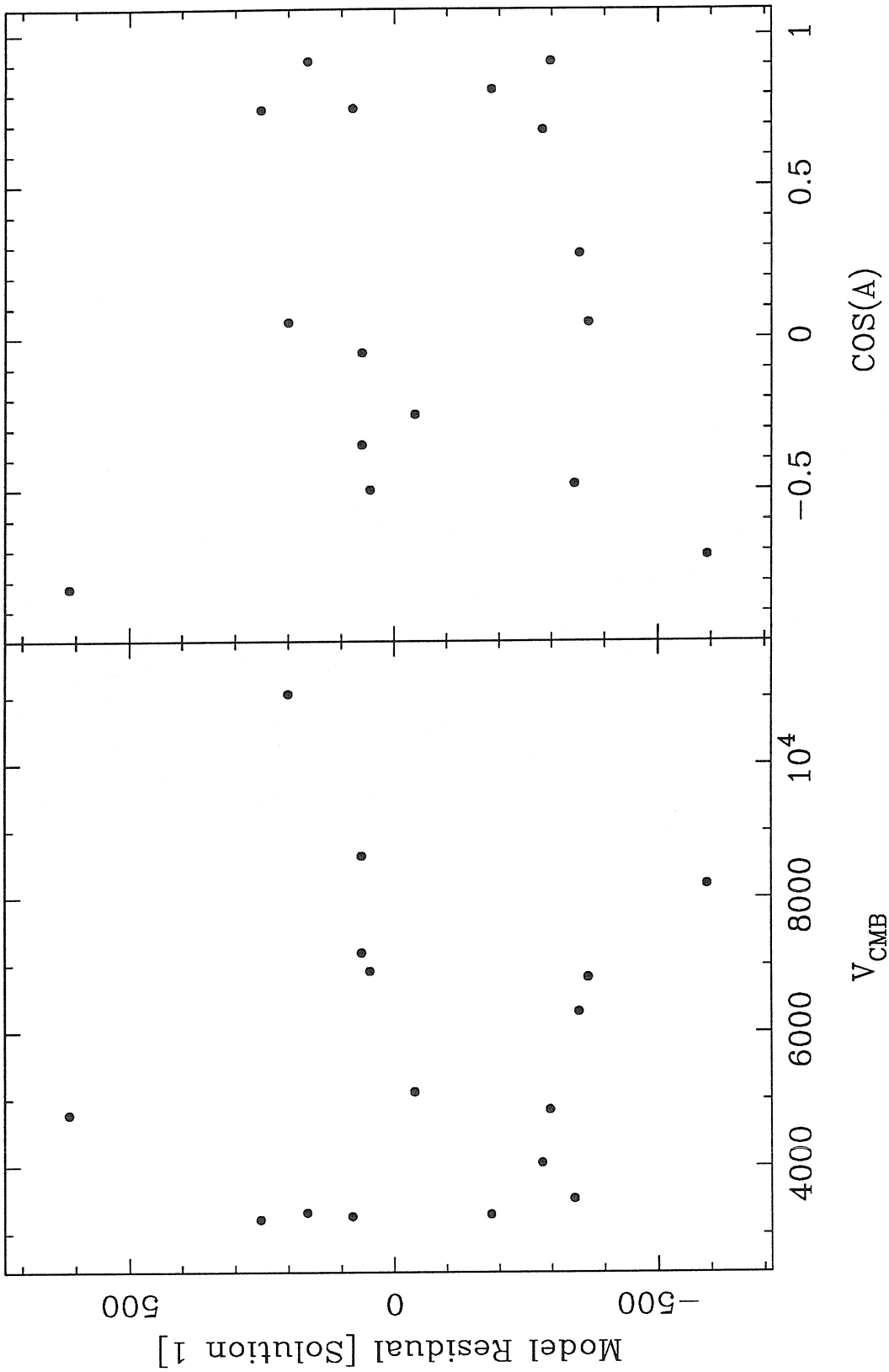
Model Residual [Solution 1]
−500
0
500
4000
6000
8000
10^4
V_{CMB}
−0.5
0
0.5
1
COS(A)

Figure 8.4

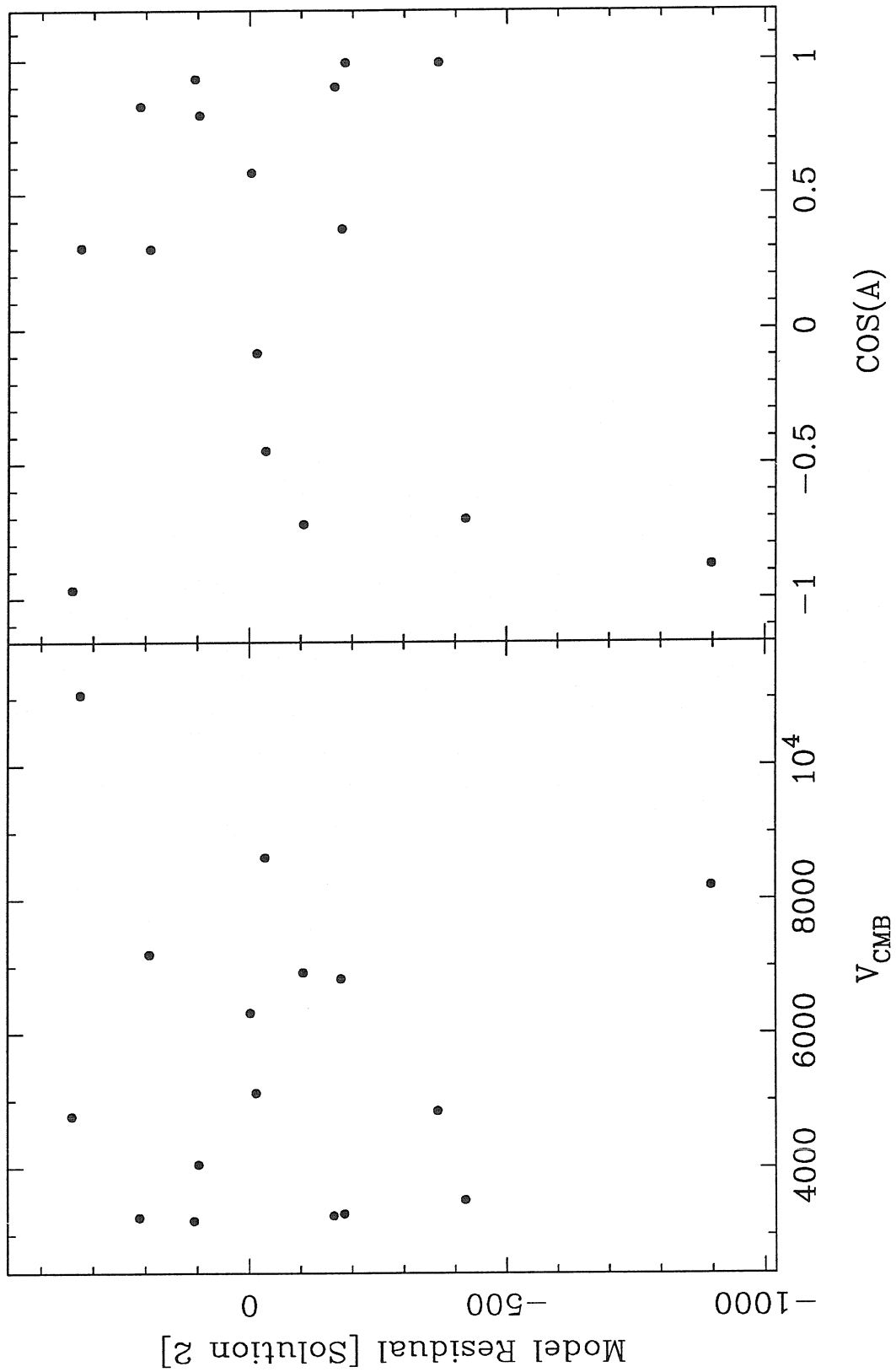
Model Residual [Solution 2]
−1000
−500
0
4000
6000
8000
10^4
V_CMB
−1
−0.5
0
0.5
1
COS(A)

Figure 8.5

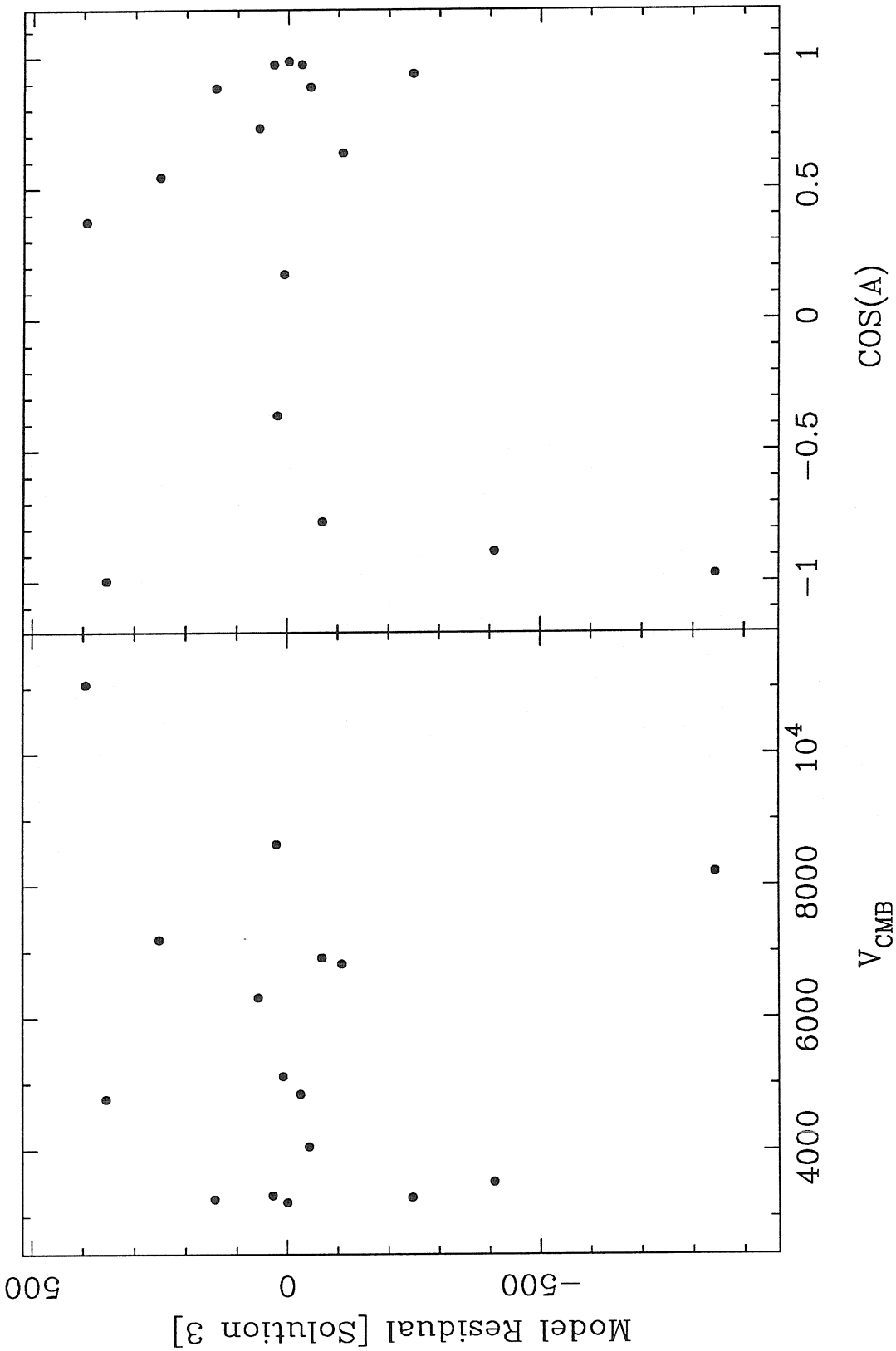
Model Residual [Solution 3]
−500
0
500
4000
6000
8000
10^4
V_{CMB}
−1
−0.5
0
0.5
1
COS(A)

Figure 8.6

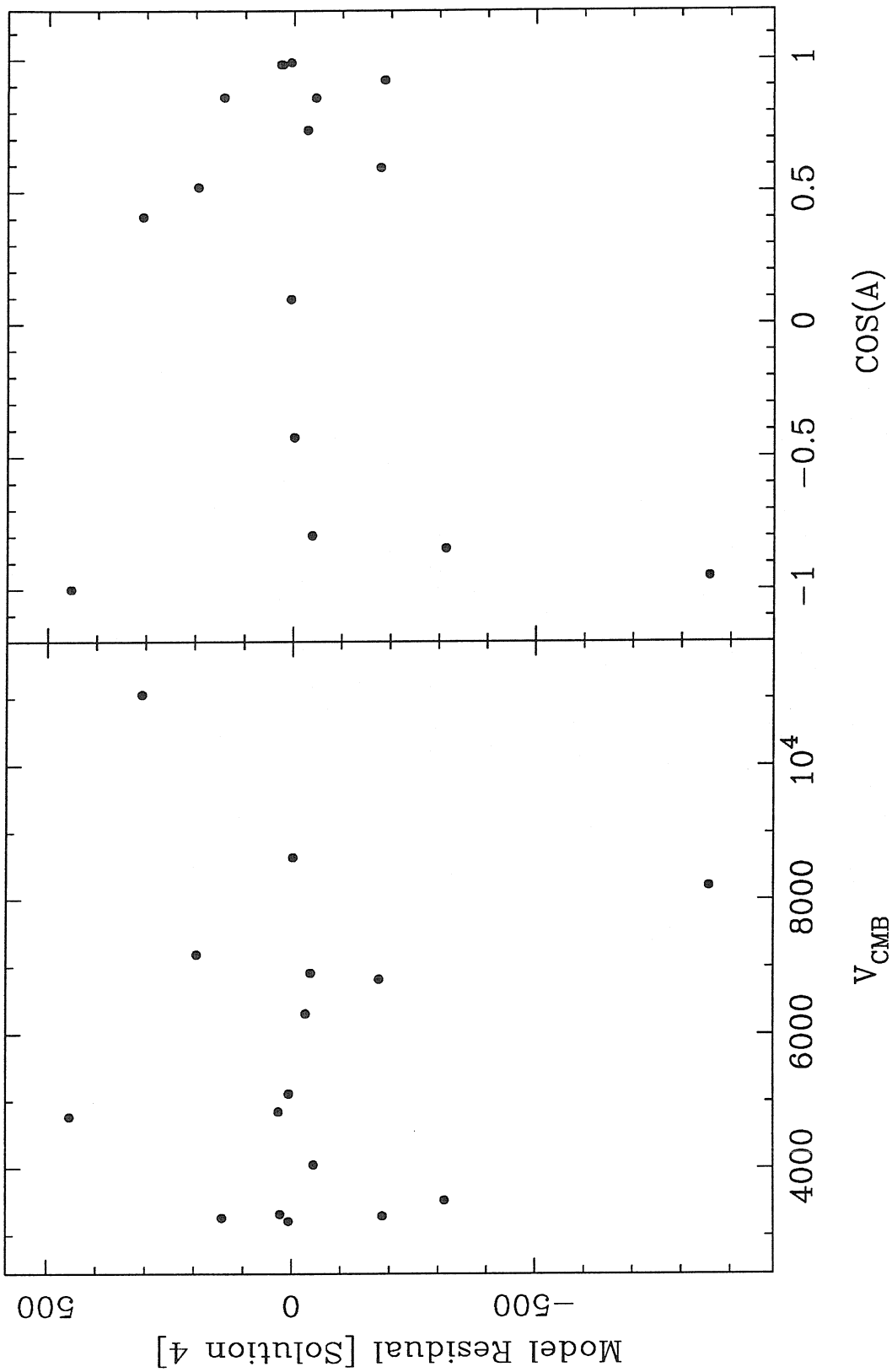
Model Residual [Solution 4]
−500
0
500
4000
6000
8000
10^4
V_{CMB}
−1
−0.5
0
0.5
1
COS(A)

Figure 8.7

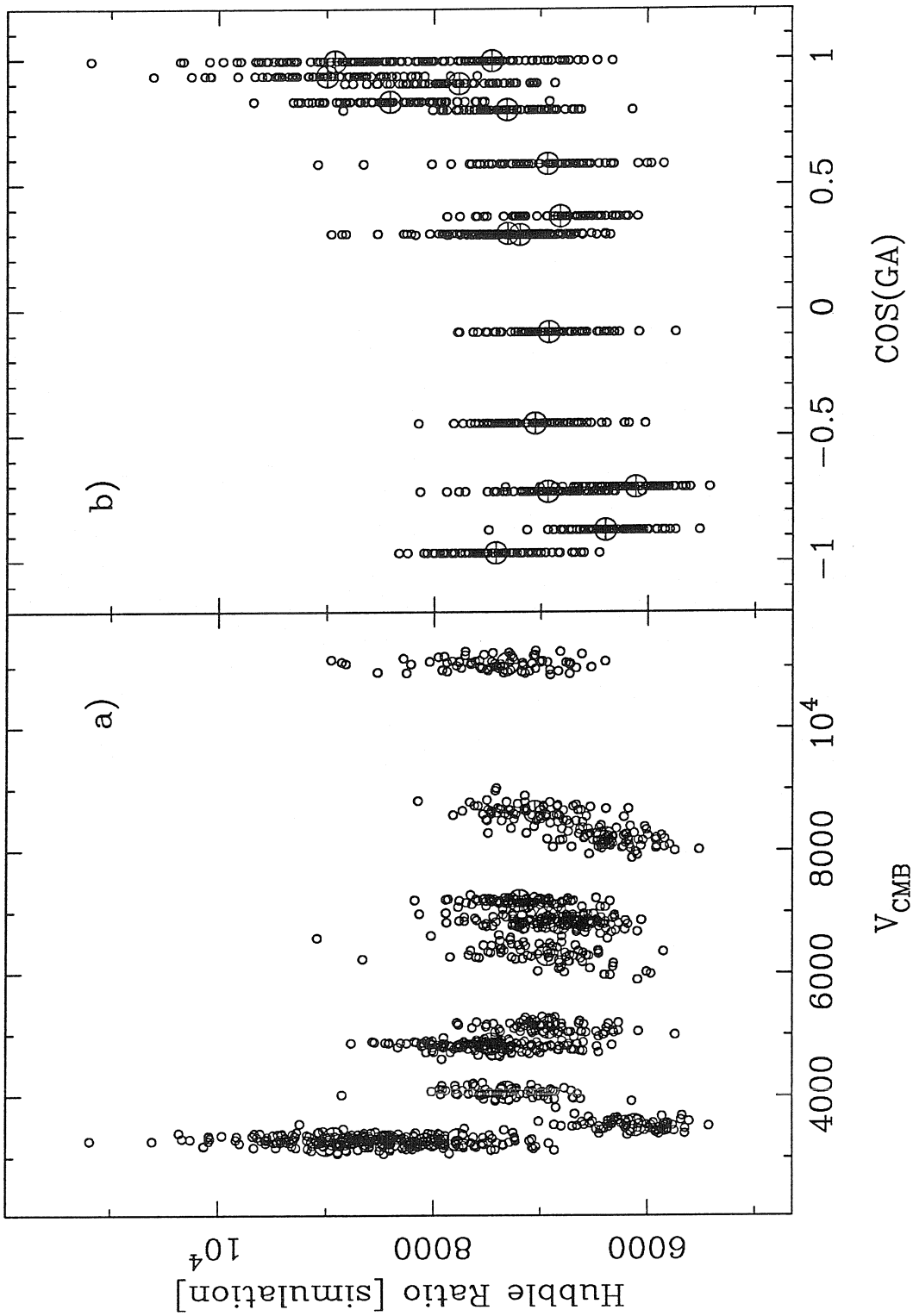
a)
b)
Hubble Ratio [simulation]
10^4
8000
6000
4000
6000
8000
10^4
V_{CMB}
COS(GA)
1
0.5
0
−0.5
−1

Figure 8.8

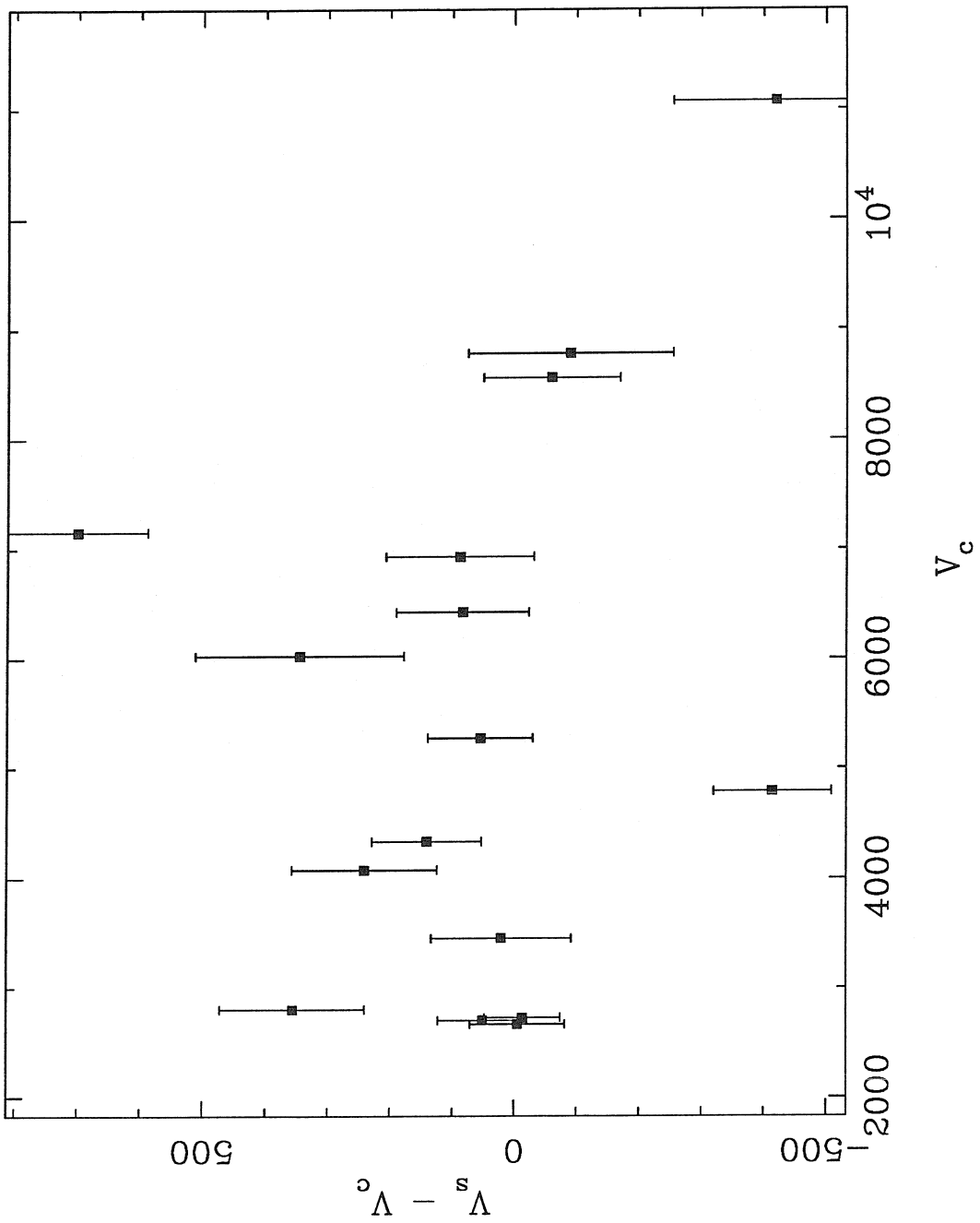

Figure 8.9

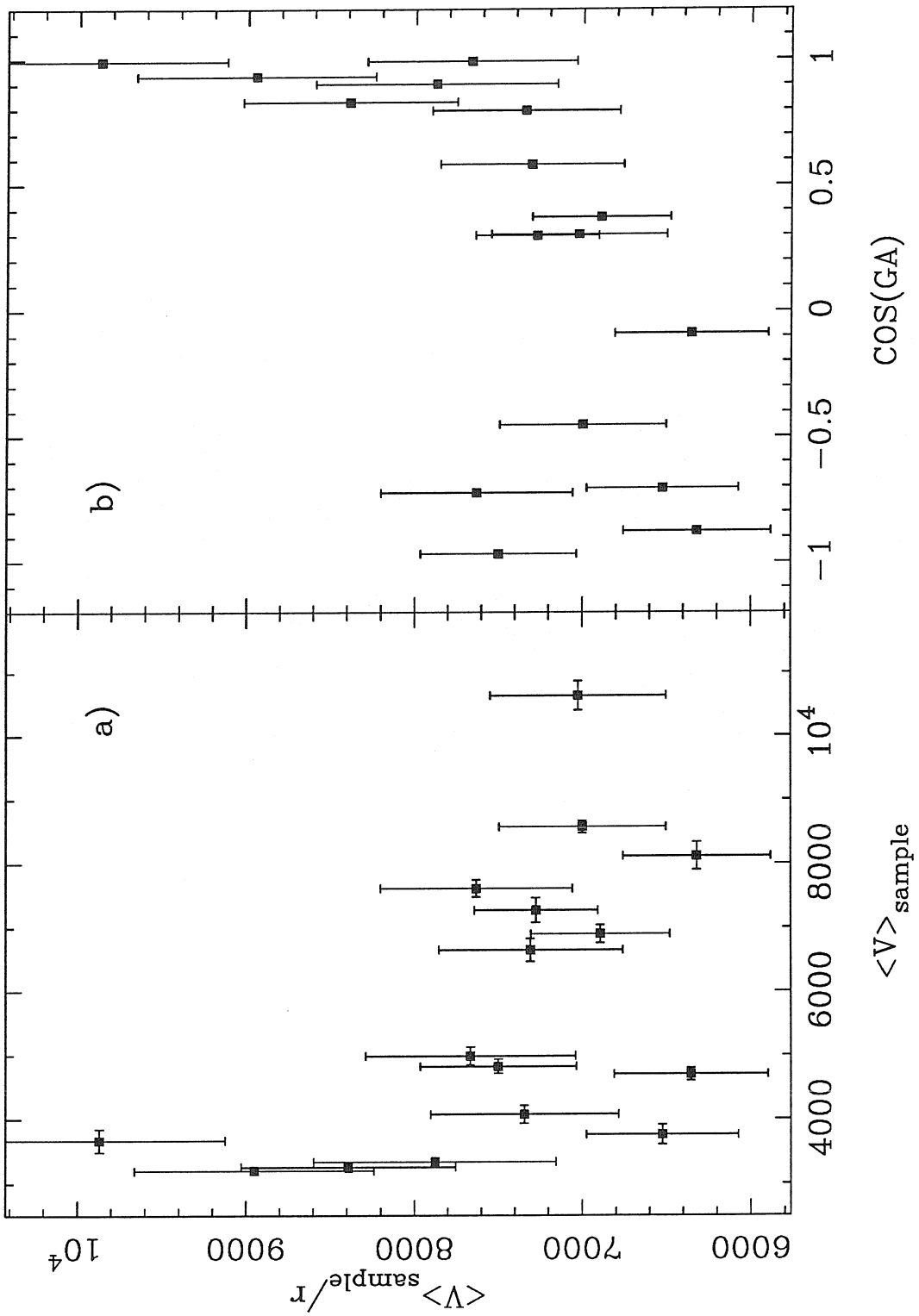
a)
b)
<V>sample/r
<V>sample
COS(GA)
6000
7000
8000
9000
10^4
4000
6000
8000
10^4
−1
−0.5
0
0.5
1

APPENDIX

SFOTO MANUAL

SFOTO

SURFACE-PHOTOMETRY AND IMAGE PROCESSING

Mingsheng Han

November 1990

1. GENERAL OUTLINE

SFOTO is a highly interactive program, it does *Surface Photometry*, as its name tells. It can also be used for some general image processing purposes. Below is an outline of what SFOTO does, more specifically.

1) **Surface Photometry**: for this purpose, SFOTO can be regarded as a complementary program of the ellipse-fitting routine, of either FIGARO _EFIT, or GASP _PROF. SFOTO first prepares the input files for FIGARO _EFIT (or GASP_PROF), and then, after EFIT (or PROF) produces the best fitting ellipses contained in a file IMAGE.ELL (or NAME.PRF), SFOTO reads this file and converts the raw ellipses into astronomically meaningful quantities, such as, surface-brightness profile, isophotal magnitudes, color gradients and inclination of the galaxy, and so on.

2) **Image Processing**: SFOTO can also be used, very conveniently, for the following purposes.

a). Visually check a CCD picture (in your favorite color); and repair the defects on it (e.g., interpolating bad lines, bad regions, and removing stars).

b) Make grey-scale plot of a portion of the picture.

c) Make contour map of a portion of the picture.

d) Measure seeing and CCD scale (arcseconds/pixel).

SFOTO makes an extensive use of FIGARO subroutines. The format of image required by SFOTO is the standard FIGARO HDS format. The way SFOTO works is also very similar to most of the FIGARO interactive routines.

2. USE OF SFOTO

SFOTO has two major levels, the top control level, SFOTO>, and the image processing level, DISP>. Once you start the program, you enter the SFOTO> level first, and you will see the following help information displayed on your terminal, which tells you what you can do in this level.

******** SURFACE PHOTOMETRY ********

********** IMAGE PROCESSING **********

N	–	input image files
A	–	display primary image /repair/stats/efit/prof
B	–	display secondary image /repair/stats/efit/prof
F	–	FIGARO/EFIT —⟩ SFB
G	–	GASP/PROF —⟩ SFB
S	–	subtract two images & display the difference
T	–	back to play image game
O	–	superpose ellipses on image
D	–	set pgplot device
P	–	superplot — check F/G results
E	–	draw ellipses
C	–	draw contours
H	–	help
Q	–	quit

SFOTO ⟩

The SFOTO⟩ prompt accepts one of the above characters (case blind), and does the desired work.

N : This is the first key you should hit, it tells the program which image you are

going to work on. You may, but not necessarily, input (or map) two images at the same time (usually two images of same object observed with different filters). The two images are discriminated by *primary* and *secondary*. After the images are mapped, SFOTO writes, on your terminal, the real object names, filter names and the observing dates, which were extracted from the files headers. It then asks you to enter a physical name, **NAME** (better to use the real object name). If **a** is the filter name of primary image, and **b** is that of the secondary image, then the two images will be named as **NAMEa** and **NAMEb**, respectively, just for I/O purposes. **N** can also be used to re-define the physical name of the already mapped images. To do this, just skip the primary and secondary image-input prompts, you are then asked for a new name.

A : This is to display the primary image on the image-display device. After image is displayed on the device, the program enters a sublevel, named DISP. It is in this mode, all the image processing work is done. Detailed description of DISP mode is given in next section.

B : This is to display the secondary image on the image-display device, and enter the DISP mode.

F : This is the command that does surface photometry using the FIGARO_EFIT ellipse-fitting results, i.e., to convert the output of EFIT (the raw ellipses parameters contained in file **IMAGE.ELL**), into SB profile, isophotal magnitudes ..... The results are written into a file named **NAMEa.SFB**, or **NAMEb.SFB**, depending on which image the surface-photometry is performed on (see Appendix A for more about the output file). **F** is such a magic loop that will leads you, step by step, to go through all the necessary stages, until everything is done and returns you to the prompt SFOTO ⟩. Once you enter the **F** loop, you will be asked to do the following:

1) First you are asked if "Including color term ?" If your answer is 'No,' the color term in mag transformation will be dropped, and the secondary image will not be used in the loop. The final output will also be slightly different (see Appendix A). Dropping color term in mag transformation will obviously cause the isophotal mag and SB over- or under- estimated. So it is not recommended to ignore color term, unless you don't have a secondary image, or the corresponding coefficient in the mag transformation is small.

2) You are then asked which image (primary or secondary) has been used by EFIT for the ellipse-fitting, i.e., upon which image the surface-photometry is to be performed. Usually, surface photometry is performed only on the primary image. Here, it should be pointed out that, for the purpose of doing surface-photometry, the "primary" and "secondary" were not given just as symbol names. The very difference between *primary* (filter **a**) and *secondary* (filter **b**) is that the photometric transformation must be given for the magnitude **a** and color **b-a**, rather than any other combinations (see Appendix C for more).

3) To do the photometric transformation, SFOTO needs to know the exposure time, airmass, CCD scale, and the magnitude and color (optional) transformation coefficients. The exposure time and airmass are read in from the image file header, and will be print on your terminal, you are given the chance to correct them, if there is such need. While the CCD scale and transformation coefficients can be obtained either from terminal or from an external file named TRANSF.COE (see Appendix C for its format).

4) Once the SFOTO receives all kinds of information it needs from the above three steps, it will automatically display the images (only primary image, if no color term included) on the image-display device, and will ask you to

clean up the images and to estimate sky values (these are done in the DISP mode as described in next section). If color term was included, you are also to be asked to mark a couple of reference stars, in order to coordinate the two images, and also to estimate the seeing of the two images.

5) Now, SFOTO performs the very surface photometry. When finished, it will plot some of the results on a user-specified device, and asks you some simple questions; you are also given the opportunity to make comments. All the results and your comments will be written to the file **NAMEa.SFB**, or **NAMEb.SFB**. Finally, you are asked whether to "produce a standard plot set?" (This plot set is also dependent on whether or not you include color term in the transformation). An example of the standard plot is given in Appendix B.

G : G does the same thing as F does, except utilizing the GASP_PROF ellipse-fitting results.

S : This command coordinates the two images by shifting the images in X and Y directions (no rotation), and rescale them according to exposure times, and then subtract one by another and displays the result. It functions only when both primary and secondary images are mapped.

O : This is to draw ellipses on the displayed image from the top SFOTO level. Ellipse-drawing can also be performed in the DISP mode (see next section), with the same command. It should be note that, because there are two different ellipse-fitting programs (EFIT, PROF), and two images of the same object, thus there are up to 4 possible sets of ellipses for one object, namely, *primary ellipse by EFIT, primary ellipse by PROF, secondary ellipse by EFIT*, and *secondary ellipse by PROF*. The program can hold only one set of ellipses at a time. So

when you pressed **O**, you will be asked, either to specify which of the four sets you like to see, if no ellipses has been read in before; or whether to switch to a different fit, if there is already a set of ellipses in the ellipse-buffer.

T : This allows you to quickly jump from SFOTO ⟩ into DISP ⟩, provided you have previously displayed an image on the device.

D : This is to set the PGPLOT device, on which you will make some plots using commands **P, E or C**. If you forget to do **D**, before go to **P, E or C**, you will be asked to do so without jumping back to the SFOTO ⟩ prompt.

P : This goes to a plotting mode, in which, you can check the results of **F** or **G**, by plotting them out on the device defined by **D**. If you have not gone through **F** or **G** for the current mapped images, SFOTO will assume you have done this before, and attempt to read **NAMEa.SFB** (or other files you specify) from your working directory. If no device has yet been defined by **D**, it will ask you to do so.

E : This is to draw ellipses on the device defined by **D**. It can also (optionally) superpose the corresponding real contours on the fitting ellipses. If no device has been defined by **D**, it will ask you to do so. If the ellipses parameters have not been read in, it will attempt to do so.

C : This is to draw contours on the device defined by **D**. This requires that the mag transformation coefficients and CCD scale have already been known by SFOTO. The SFOTO obtains these values from **F** or **G**, but if this has not been done, it will assume you had done this before, and attempt to read **NAMEa.SFB** (or other file you specify) from the current directory. If no device has been defined by **D**, it will ask you to do so.

H : Erase screen and display the help list.

Q : Exit SFOTO.

3. DISP MODE

As explained in section 2, there are five channels to enter the DISP level from the top SFOTO level, that is, **A, B, F, G,** and **T.** In DISP level, you can directly talk to the picture displayed on the image display device. DISP is the heart of SFOTO, and you will spend most of your time in this mode.

The prompt of DISP is DISP⟩, it accepts single characters predefined in the program. Press **H**, you will have a list of DISP recognized characters and their functions, which looks like

```
————————***** Repair/Stats/PROF/EFIT *****————————

H – help                          Q  – quit DISP
K – repair image                  F  – prepare FIGARO_EFIT input
S – measure sky                   G  – prepare GASP_PROF input
X – measure CCD scale             O  – ellipses on/repair/add
W – measure seeing                B  – make gray-scale plot
N – name reminder                 ⟨ sp ⟩ – cursor position & count

————————********** Display **********————————

PF1– step 1    PF2– step 2    PF3 – step 4    PF4– step 8
L – left       R – right      U – up          D – down
T – lookup     Z – stretch    P – redraw
E – expand     C – compress   M – E/C factor

DISP ⟩
```

Explanations for some of these commands are given below, although most of

them have straightforward meanings.

3.1 The Display Commands

The **PFn** is to set the length of cursor moving step. **L, R, U**, and **D** are for moving picture on the display device **left, right, up**, and **down**, respectively. **P** is to redraw the picture. **E** is to expand the picture by a factor of 2, **C** is to compress it by a factor of 2, and **M** is to expand or compress it by a factor of any number you like.

Z is for setting stretch. To do this, it is helpful to know the count level of the image, using the space-bar.

T adds color to the picture, and changes the lookup. A variety of color tables are avaliable to meet different purposes and to satisfy different users. Instructions of doing this will show on your terminal, upon your pressing **T**.

3.2 K

K leads you to a sublevel DISP_K⟩, in which, the displayed image can be repaired in your wish. Again, **H** will give you a hint, by writing the following on your terminal.

——— Master Image Repair ———

Move cursor then do the following

C	–	search & interpolate bad column
R	–	search & interpolate bad row
I	–	interpolate/restore column
N	–	interpolate/restore row
W	–	cursor position and count there

B – interpolate a box

S – interpolate a star (*)

O – restore "S" deleted region (#)

H – help

Q – quit current mode

* max interpolating radius = 50 pixels

only the 50 latest deleted regions can be restored

DISP_K)

C : Automatically search *bad* columns within the range of 20 pixels around the cursor, and to interpolate the *bad* ones, if found. A *bad* column is defined by a parameter q (default 3), such that the mean count, in a short piece of the column, deviates from the average of the 20 columns, by more than q standard deviations. If you input 0 for q, however, the bad column is defined as that of the 20, which has extreme sigma, for example, a dotted column can be interpolated with $q = 0$.

R : Similar to **C**, except that **R** is for rows.

I : Also for interpolating columns, but different from **C**, **I** can interpolate any column, not just *bad* one, and can also restore the interpolated columns by itself. **I** is often used in the case when a bad column goes through an object center or some other "sensitive" regions, or the column is not too *bad* that **C** might not be appropriate.

N : Similar to **I**, except that **N** is for rows.

B : Interpolate a box linearly, in either X-direction or Y-direction. The box is defined by indicating two diagonal points on the image with cursor. This operation

is not restorable.

S : Interpolate a star and make the interpolated region more or less follow the background pattern of sky variation. To do this, you need to tell the program two parameters. One is the radius (maximum 50 pixels) of the region to be interpolated (a circle will be drawn on the image); the other parameter controls the sky fitting, in the sense that a value of 0 corresponds to a uniform fit, and higher values attempt to make the fit follow the background variation to different degrees. The deleted regions can be restored by **O**, this allows you to try different values for the two parameters to delete a star, until you are visually satisfied.

O : Restore the regions deleted by **S**. Only the 50 latest deleted regions can be restored. To use, simply move cursor close to the center of a deleted region and press the key.

It should be noted that the interpolations made in this mode left permanent changes in your image file.

3.3 S

S does the sky statistics, and is very easy to use. First, specify the size of "sky-sample box" (default = 10 pixels), then just move cursor to where you think the sky is, and hit the space-bar to sample the sky at the position, where the sample box will be drawn, and the result of the sampling will be shown on the screen (i.e., the position and the area of the box, the mean intensity in the box, and the sigma value). You may need to do dozens of samplings at different positions for better statistics. To terminate the sampling, just hit **Q**, then the value of ensemble mean sky, sigma, average sigma, and sky variation will be printed out. If you are

not happy with the result, you can go back and do more sampling, which will be combined with the previous samples to yield a new result. The process can be repeated as many times as you like, till you are satisfied. Note that you are not able to change stretch and magnification within **S**, it is thus wise to choose the right stretch and magnification before using **S**.

3.4 F

F brings you to a sublevel DISP_F⟩, in which, you can prepare the file, IMAGE.EIN, required by the FIGARO ellipse-fitting routine EFIT. Upon your entering DISP_F⟩, the following help information will show on your terminal.

========== Prepare EFIT input file ==========

********** Display **********

H – help	E – expand	C – compress	M –E/C factor
L – left	R – right	U – up	D –down
T – lookup	Z – stretch	P – redraw	

****** Select (move cursor then press the right key) ******

O – define object	⟨ sp ⟩– select bad regions
W – write and exit	Q – quit without writing

DISP_F ⟩

The display commands do the same thing as they do in the DISP⟩ mode. Command **O** is to select the program galaxy, on which the surface photometry is to be performed. At the moment, the program allows only one galaxy to be selected on each picture. To select a galaxy, move the cursor to the center of the galaxy, and press **O**. You are then queried for the values of the starting and the maximum semi-major axes, and an axis-increasing factor. The program then roughly estimate

an ellipse using the starting radius, and writes the ellipse parameters (center, eccentricity, position angle) on your terminal, and draws the ellipse on the image. If you don't think that is a right selection, you can modify it, or abort it, otherwise the parameters will be accepted as the EFIT initial values. You can practise with **O** as many times as you like, but only the last selection is finally accepted.

The space-bar defines the regions to be ignored by EFIT, when doing the ellipse fitting. To select such a region, move the cursor to the right position, hit space-par, and specify the size of the region, i.e., radius. The program then draws a circle with that radius on the displayed image. Then it is up to you as whether to accept the selection, or to change the size, or even to abort it. Note that the maximum number of regions that EFIT can ignore is 30.

After the selections of both galaxy and bad-regions are done, **W** is then used to exit the current level and to produce the file, IMAGE.EIN required by EFIT. But after pressing **W**, you are first lead to the sky-statistics mode (see section 3.3) for a sky estimation, and are then queried for the value of sky threshold, above which ellipses-fitting will be done by EFIT on the image. All these parameters are then written to the file IMAGE.EIN. On the other hand, if, for some reason, you decided not to make the file IMAGE.EIN, you can quit the current mode using **Q**, and everything you have selected will be totally lost.

Note that you don't have to work in the order as described above, you may sample a couple of ignored regions first, and then select the program galaxy, and then some more ignored regions. You can even quit DISP_F\) without doing any of these, but the program will warn you. During the process of selection, you may need to have the image redrawn (e.g., expand or compress), every time you do this, the previously selected regions will be marked on the new picture. So you don't have to worry about an unnecessary double selection of the same bad thing.

3.5 G

G brings you to a sublevel DISP_G⟩, in which, you can prepare the 4 input files required by the GASP ellipse-fitting routine PROF. Upon your entering DISP_G⟩, the following help information will show on your terminal.

========== Prepare GASP_PROF input files ==========

********** Display **********

H –help	E –expand	C –compress	M –E/C factor
L –left	R –right	U –up	D –down
T –lookup	Z –stretch	P –redraw	

****** Select (move cursor then press the right key) ******

O –define object ⟨ sp ⟩–select bad regions

Q –header/GASP_file/exit

DISP_G ⟩

The DISP_G⟩ mode almost a duplication of the DISP_F⟩ mode, but there are also minor differences.

O is also for selecting the program galaxy. You need to enter the initial semi-major axis, from which PROF will start the fitting. The program then roughly estimates an ellipse with this radius, and prints its parameters (center, eccentricity, position angle) on your terminal, and draws the ellipse on the image. These parameters, if accepted, will be written to a file **NAMEa.GAL** (or **NAMEb.GAL**, if you are on secondary image), and will serve as the initial guess values for PROF (see GASP manual).

The space-bar defines the regions to be ignored by PROF, You also need to specify the size of the region, by entering the value of radius. Different from the

DISP_F⟩ mode, the program now estimate an *ellipse* with that radius, because PROF recognizes ellipse as an ignored region. The estimated ellipse is drawn on the image, and you can choose either to accept it as the ignored region, or to change the size/shape of the ellipse. These ellipse parameters, if accepted, will be written to file **NAMEa.DEL** (or **NAMEb.DEL**, for secondary image).

Now, you have the **.GAL** and **.DEL** files produced. The PROF, however, needs more than these. The other two are produced on the way of escaping from the current level. Press **Q** to escape DISP_G⟩, you are then asked to estimate the sky value, which will be written to the header file **NAMEa.HDR** (or **NAMEb.HDR**, for secondary image); and finally, the image file in GASP format, **NAMEa.GSP** (or **NAMEb.GSP**, for secondary image) is (optionally) produced.

Same as in DISP_F⟩ mode, you don't have to work in the order as described above in the current mode. You will be warned, however, if you missed something before escaping from DISP_G⟩. Every time you redraw the image, the previously selected regions will be marked on the new picture.

3.6 O

O is an ellipse-drawing command in DISP mode, like that in the SFOTO level. This **O**, however, has an additional function, that is, to modify the existing ellipses, which you don't think be the best fits; or to add more ellipses. **O** is often used to draw the outermost ellipse on the picture, before you clean it for the purpose of photometry. Because, this tells you where you really need to do the hard cleaning work, and where you don't have to bother yourself to do.

3.7 B

B is to make grey-scale plot of the picture. It first asks you to define the portion, from which you want to make the plot. This is done by indicating two diagonal points on the displayed picture. The program then does statistics in the defined box, and displays the result on your screen. Based on the statistics, you can define the black and white levels for the plot, and also define the plot device, as the program queries. Everything else is then left to the program.

3.8 W and X

W measures the FWHM of Point Spread Function in both X and Y directions, using a star at the current cursor position. The results, in units of pixels, will be displayed on your terminal.

X is used to measure the CCD scale (arcsec/pixel). This is done by indicating a couple of reference stars on the image. Of course, you have to enter the (equatorial or galactic) coordinates of each star. The scale value calculated using each pair of the stars, and the mean scale value will be displayed on your terminal.

Appendix A

An example of the SFOTO output file, **NAMEa.SFB**, is given below, which is produced using command **F**, with color term included.

The header part lists some general information about the observation, and photometric transformation: **EXT.T** = exposure time; **SECZ** = airmass; **A/DA** = zero-point and its rms error of mag, and color transformations; **B/DB** = the color term coefficient in the mag, and color transformations; **Kx** = extinction coefficient; **Xcen & Ycen** = object center (i.e., the center of the innermost ellipse); **Sky(counts) & Sky(SFB)** = sky value in counts and in mag/arcsec^2, respectively; **Xsee & Ysee** = the FWHM of point-spreading function in X and Y direction; **Band** = filter name of the primary and secondary images, or color name; **Date** = observing date of the form **yymmdd**; **Instrument** = a character string indicating the instrument used for the observation (from file TRANSF.COE, or from terminal); **CCD Scale** = the pixel size in arcseconds; **Ellipse** = ellipse-fitting program used: FIGARO_EFIT or GASP_PROF.

The second part of the file is the main output of SFOTO, which is tabulated in 10 columns.

Column 1. **R**$''$, major axis of the isophotal ellipses in arcseconds.

Column 2. **SB(mag/[]**$''$**)**, isophotal brightness, and its rms error.

Column 3. M_{iso}, isophotal magnitude, and its rms error.

Column 4. **COLOR**$_{int}$, integrated color within an isophotal ellipse, and its rms error.

Column 5. **COLOR**$_{dif}$, differential color (the color of an 3-pixel wide annulus at the isophotal ellipse), and its rms error.

Column 6. **COLOR**$_{asm}$, the color asymmetry and its rms error. This is simply the color difference between one side of the major axis and the other side of it, calculated using the annulus of column 5, in the sense that the upper half minus the lower half.

Column 7. **ecc**, eccentricity of the ellipse.

Column 8. **P.A.**, position angle of the ellipse (from -90° to +90°), i.e. the angle between major axis and the X-axis.

Column 9. **Xcen**, X coordinates of the ellipse-centers.

Column 10. **Ycen**, Y coordinates of the ellipse-centers.

The third part of the file gives the inclination, light concentration and mean color asymmetry of the galaxy. These parameters were calculated using the *disk range* you have specified in the **F** (or **G**) loop. The SB level and the radii of the range are given in the first two lines. The inclination, in line 3, is calculated using the median eccentricity of those ellipses in the *disk range*, and assuming an intrinsic axial ratio of 5. The concentration parameters (C20, C30, C50, C70 and C80) are given in line 4, where Cm is defined as the semi-major axis of an isophotal ellipse, which encloses m% of the *total* light, in units of the radius of the galaxy, identified as the outer disk edge. Line 5 gives the averaged color asymmetry parameters within, respectively, the inner galaxy (containing 50% light), the outer galaxy (containing 50% light), and the whole galaxy. Line 6 lists the index numbers of those ellipses, which have been modified; it will be blank, if no modification was done.

Finally, the last part of the file is your comments about the galaxy, the observation, and the processing . . .

The output file produced without using the color term, has the same structure

as above, except that all the color information is gone, and the column 4 and 5 list, respectively, the magnitudes of the two half annuli (of three pixel wide), on both side of major axis.

I band surface photometry for N4062

EXP.T	SECZ	A / DA	B / DB	Kx	Xcen	Ycen	Sky(counts)	Sky(SFB)	Xsee	Ysee	Band
100.	1.19	21.223,0.012	-0.023,0.010	0.050	366.65	410.84	343., 1.	18.825	2.37	2.56	I
50.	1.19			0.140	364.90	411.42	203., 1.	20.122	2.28	2.56	V
		1.594,0.014	1.055,0.012	0.090							V-I

Date : 89FEB12 Instrument : P60/CCD4/R CCD scale : 0.640 Ellipse : FIGARO_EFIT

R"	I_SB(mag/[]")	I_iso	(V-I)_int	(V-I)_dif	(V-I)_asm	ecc	PA.	Xc	Yc
0.64	17.976,0.023	17.760,0.025	1.316,0.034	1.395,0.033	0.027,0.065	0.538	19	366.7	410.8
0.77	17.982,0.022	17.732,0.026	1.344,0.035	1.389,0.033	-0.098,0.064	0.578	17	366.5	410.8
0.93	18.001,0.022	17.748,0.027	1.328,0.037	1.370,0.024	-0.031,0.039	0.520	16	366.4	410.8
.	.	.	.	.	.	.	.	.	.
.	.	.	.	.	.	.	.	.	.
.	.	.	.	.	.	.	.	.	.
75.13	20.811,0.028	10.421,0.019	1.169,0.020	1.089,0.036	0.110,0.055	0.622	-7	363.4	410.2
90.91	21.283,0.037	10.241,0.020	1.153,0.022	1.018,0.050	0.093,0.075	0.619	-7	365.7	410.8
110.00	22.037,0.066	10.091,0.022	1.135,0.026	0.904,0.089	0.351,0.135	0.613	-6	366.1	410.6
121.00	22.347,0.086	10.031,0.024	1.125,0.028	0.998,0.119	0.278,0.177	0.613	-6	366.0	410.4

Disk in/out SB levels SB1,SB2 = 20.000 22.347
Corresponding radius R1, R2 = 52.04 121.00
Inclination = Med(isophotes with R1<R<R2) : 70/ 0.9
Concentration(with R2=1) C(20,30,50,70,80) : 0.195 0.298 0.473 0.624 0.726
Color assymetry(H-L) [<in>,<out>,<total>] : -0.003/0.005 0.138/0.035 0.017/0.007

a faint star removed from disk.

Appendix B

A standard plot-set includes 9 separate diagrams (see the example), the contents of the plots depends on whether you have included color term (case 1, below) in the magnitude transformation, or not (case 2).

diagram 1 : surface-brightness (column 2 in file NAME.SFB) vs radius (column 1).

diagram 2 : isophotal magnitude (column 3) vs radius.

diagram 3 : integrated color (column 4) vs radius, for case 1; and isophotal magnitude vs surface-brightness, for case 2.

diagram 4 : differential color (column 5) vs radius, for case 1; and eccentricity (column 7) vs radius, for case 2.

diagram 5 : color asymmetry (column 6) vs radius, for case 1; and X-coordinate (column 9) of ellipse-center vs radius, for case 2.

diagram 6 : isophotal magnitude vs surface-brightness, for case 1; and Y- coordinate (column 10) of ellipse-center vs radius, for case 2.

diagram 7 : eccentricity (column 7) vs radius, for case 1; and position angle vs radius, for case 2.

diagram 8 : a grey-scale picture of the object, with white level = sky, and black level = 80% of the object peak intensity.

diagram 9 : drawing of all the ellipses.

N4062: /P60/CCD4
I_SB (mag/[]")
R (arcsec)
(V–I) dif
R (arcsec)
ecc
R (arcsec)
I Mag
R (arcsec)
(V–I) asm
R (arcsec)
Y (pixel)
X (pixel)
(V–I) int
R (arcsec)
I Mag
R (arcsec)
SB (mag/[]")
Y (pixel)
X (pixel)

Appendix C

TRANSF.COE is an external file, containing the coefficients of the photometric transformation of different observing nights. In the following demonstration, it is assumed the program galaxy has been observed in **B** and **V** bands.

It is very important to note that SFOTO sets two *regulations*, regarding to the transformation. First, the pair of *magnitude* and *color* referred in SFOTO must be either **(V, B-V)**, or **(B, V-B)**, and can not be **(B, B-V)**, or **(V, V-B)**. Second, once the *magnitude* and *color* are specified, e.g., **V** and **B-V**, then you must use the **V** image as the *primary* image, and **B** image as the *secondary* image, when loading the images to SFOTO.

The magnitude and color transformation equations are assumed to take the following forms.

$$\mathbf{V} = a + V_i + b(\mathbf{B} - \mathbf{V}) - k_V X$$
$$(\mathbf{B} - \mathbf{V}) = c + d(B_i - V_i) - k_{B-V} X$$

where B_i and V_i are, respectively, the instrument B and V magnitudes; X is airmass; a, b, c, d, k_V and k_{B-V} are the coefficients we are talking about. Different observing night may have different transformation coefficients; each night is given one line in the TRANSF.COE file, with the following formats:

Column	Content	Format
1	Observing date (**yymmdd**)	A8, X
2	Instrument	A10, X
3	CCD Scale	F7.3
4	a and σ_a	2F7.3
5	b and σ_b	2F7.3

6	k_V	F7.3
7	c and σ_c	2F7.3
8	d and σ_d	2F7.3
9	k_{B-V}	F7.3

The information in TRANSF.COE is required only by the **F**, **G**, and **C** in the top SFOTO level. If you don't have such a file in your directory, or the file does not contain the information on the date your galaxy was observed, then you will have to input the above information from terminal.